

Solid-state NMR and  
DNP-Enhanced Solid-state NMR  
Analysis of Sustainable Materials

by

Alison Daly M<sup>c</sup>Lellan

Thesis

submitted to The University of Nottingham

for the degree of

Doctor of Philosophy


School of Chemistry

March 2023



# Declaration

The work in this thesis is based on research carried out at the Solid-state NMR Group in the School of Chemistry at The University of Nottingham. All work in this thesis is the original work of the author, except where specific reference has been made to the work of others. No part of this thesis has been submitted for any other degree or professional qualification.

Signed: 

Date: 30/03/2023

Alison Daly McLellan

The work in this thesis has been carried out by the author, with the following exceptions:

In Chapter 4

- All MAPbI<sub>3</sub> and MAPbI<sub>3</sub> on ZnO samples were synthesized by Dr Lei Lei.

In Chapter 5

- The sample preparation and DNP experiments of the sample of PS seen in Table 5.3 and Figure 5.3 were performed by Dr Marco Mais.

In Chapter 6

- The PS and 1:1 PS:PMMA core-shell samples were synthesized by Dr Kristoffer Korsten.
- The 1:2, 1:4, and 1:8 core-shell samples were synthesized by Morgan Reynolds-Green.
- The DNP experiments of the sample of PEO which had been impregnated with TEKPol in scCO<sub>2</sub> at 34 °C and 200 bar for 3 hours (Figure 6.2), were performed by Dr Marco Mais.
- The simulation of TEKPol and AMUPol Q-band EPR spectra and analysis of the experimental data were performed by Prof. Eric M<sup>c</sup>Innes and Prof. David Collinson.
- The EPR relaxation data was collected and analysed by Adam Brookfield.

*For my grandpa who encouraged me to take any and all opportunities to learn,  
and for my gran who then reminded me to enjoy them.*

# Abstract

In the drive for more sustainable chemistry, a thorough understanding of the relationship between the structure and properties of any given product is essential. Molecular level characterization is key for optimization of desired properties and synthesis. For many materials, this can be done with high-resolution solution-state techniques or X-ray crystallography. However, to fully understand their structural-property relationships, materials must be studied in the state in which they will be used. Often this state is not amenable to these techniques. In these cases, solid-state NMR provides this vital information. In this work, solid-state NMR analysis has been applied to two classes of materials.

Firstly, solid-state NMR was used to probe the defects in hybrid organic-inorganic perovskite materials with potential applications in solar cells. Structural defects in these materials can improve their function but also reduce their stability. To make these perovskite solar cells commercially viable, a thorough understanding of the relationship between the material properties and the dynamics and structural differences caused by these defects is essential. Static and MAS variable temperature  $^1\text{H}$  NMR has been used to identify possible diffusion of protonic defects in  $\text{MAPbI}_3$ .

The second class of materials studied were polymers. For these materials, dynamic nuclear polarization (DNP) enhanced solid-state NMR was used. The low sensitivity of NMR limits its capability to analyse intrinsically dilute aspects of high molecular weight polymers, such as cross-links, chain-ends, and interfaces. DNP-enhanced solid-state NMR has not had the same impact on polymer analysis as it has in biological and materials science. This may be attributed to the discouragingly low enhancements seen and difficult sample handling encountered when using traditional DNP methods on polymers. In this work, the benefits, and disadvantages of two sample impregnation methods for polymer DNP have been shown. Additional benefits of polymer DNP have also been demonstrated. Beyond a simple sensitivity enhancement, DNP has been shown to provide insight to the dynamics of polymer chains and functional groups.

# Acknowledgements

First and foremost, I would like to thank my supervisor Dr Jeremy Titman for the opportunity to start this PhD with the vague plan of “let’s do some DNP and see if we can relate it to sustainability.” I have truly valued the chance to explore and find projects that I am passionate about, and the great variety of experiences that this has led to. Although there was a certain unprecedented experience that I probably could have done without, I am grateful for all the support and guidance I received throughout.

Dr Marco Mais, Dr Subhradip Paul, Dr Paolo Cerreia Vioglio, and Dr Huw Williams have provided immeasurable assistance in all things practical NMR. I would like to thank them for keeping the DNP and BDI facilities running, their practical contributions to this work and their expertise. I would also like to thank Marco and Charles Mitchell-Thurston for always being receptive to and enthusiastic about having a good complain.

For their guidance, training, encouragement, and good ideas, I would like to thank Dr Kristoffer Korsten, Dr Vincenzo Taresco, and Prof. Steve Howdle. Without them, the supercritical CO<sub>2</sub> work in this thesis would not have been possible.

I am grateful to Bruker and the EPSRC CDT in Sustainable Chemistry for funding. I extend my thanks to everyone involved in the CDT, particularly Prof. Pete Licence, Peri Williams, Mandy Broniewski, for the support, guidance, and opportunities they have provided me. I would like to thank all of Cohort 5 for injecting fun into so many CDT activities. Special thanks go to Mandeep Singh Dhak and Lydia Barnes for making Wednesdays less Lonely.

Outwith the confines of the university, I will forever be grateful to Julie Woodford, Jemma Blackford, and Emily Potter for creating an adult team at Nottingham Synchronized Skating Academy just months before I moved here. All members and supporters of Ice Diamonds, past and present, have played a vital role in maintaining my sanity over the past 5 years. I have very much

enjoyed writing the final parts of this thesis with the British Championship trophy on my desk to remind myself that I can do difficult things!

There are not enough synonyms for grateful on the planet to express my appreciation of the support that I have received from my partner, Ivan. I find comfort and encouragement in his unwavering belief in me and my abilities. As he reminds me, he is always right.

I thank my family for their love and support over the past 5 years (and the 23 before that). In particular, I must acknowledge the thoughtfulness of Bob and Kate to buy a house within a 30-minute drive of The University of Nottingham 34 years ago. I am grateful for their foresight and company. I wish to thank the PhD for the opportunity to spend more time than ever with my cousin, Hannah. My 8 year-old self would be giddy with excitement at the great friendship we have been able to develop.

Of course, none of this would have been possible if not for the unconditional support and belief of my wonderful parents. I was blessed to have an upbringing that instilled in me that I could achieve whatever I set my mind to. Turns out, that includes all of this!



# Contents

<b>Abstract.....</b>	<b>i</b>
<b>Acknowledgements .....</b>	<b>ii</b>
<b>Contents .....</b>	<b>iv</b>
<b>List of Tables .....</b>	<b>viii</b>
<b>List of Figures.....</b>	<b>x</b>
<b>Glossary .....</b>	<b>xiv</b>
<b>1. Introduction .....</b>	<b>1</b>
1.1. Perovskites .....	1
1.2. Polymers .....	1
1.3. Thesis Overview .....	2
<b>2. Theory .....</b>	<b>3</b>
2.1. Solid-state NMR .....	4
2.1.1. <i>The Practical NMR Experiment</i> .....	4
2.1.2. <i>The Zeeman Interaction</i> .....	4
2.1.3. <i>The Quantum Mechanical Approach</i> .....	6
2.1.4. <i>Angular Momentum Operators</i> .....	7
2.1.5. <i>The Density Matrix</i> .....	8
2.1.6. <i>The Time-dependence of the Density Operator</i> ..	11
2.1.7. <i>Hamiltonians and Interactions</i> .....	12
2.1.8. <i>Internal Interactions</i> .....	15
2.1.9. <i>Magic Angle Spinning</i> .....	22
2.1.10. <i>Spin Diffusion</i> .....	24

2.1.11.	<i>Relaxation</i> .....	24
2.2.	Dynamic Nuclear Polarization .....	30
2.2.1.	<i>Electron Paramagnetic Resonance</i> .....	31
2.2.2.	<i>DNP Mechanisms</i> .....	32
2.2.3.	<i>DNP Radicals</i> .....	38
2.2.4.	<i>Sample Preparation</i> .....	39
2.2.5.	<i>Evaluating the DNP Effect</i> .....	40
<b>3.</b>	<b>Experimental Techniques in Solid-state NMR .</b>	<b>42</b>
3.1.	Phase Cycling .....	43
3.2.	Spin Echo .....	44
3.3.	Double-Quantum NMR .....	45
3.4.	Heteronuclear Decoupling.....	47
3.5.	Cross Polarization.....	48
3.6.	Experimental Techniques Used for DNP- Enhanced Solid-state NMR.....	49
3.6.1.	<i>Polarization Transfer</i> .....	49
3.6.2.	<i>SCREAM-DNP</i> .....	51
<b>4.</b>	<b>Hydrogen Defects in MAPbI<sub>3</sub> .....</b>	<b>52</b>
4.1.	Abstract.....	52
4.2.	Introduction.....	53
4.2.1.	<i>Perovskites</i> .....	53
4.2.2.	<i>Defects in MAPbI<sub>3</sub></i> .....	54
4.2.3.	<i>Solid-state NMR Spectroscopy of MAPbX<sub>3</sub></i> <i>Perovskites</i> .....	58
4.2.4.	<i>Probing Diffusion by NMR</i> .....	60
4.3.	Experimental Details .....	62

4.3.1.	<i>Materials</i> .....	62
4.3.2.	<i>Sample Preparation</i> .....	62
4.3.3.	<i>NMR</i> .....	63
4.4.	Results and Discussion .....	64
4.4.1.	<i>MAPbI<sub>3</sub></i> .....	64
4.4.2.	<i>MAPbI<sub>3</sub> on Zinc Oxide</i> .....	74
4.5.	Summary .....	78
<b>5.</b>	<b>DNP-Enhanced Solid-state NMR of Polymers..</b>	<b>79</b>
5.1.	Abstract.....	79
5.2.	Introduction.....	80
5.2.1.	<i>Polymers</i> .....	80
5.2.2.	<i>DNP-Enhanced Solid-state NMR of Polymers</i> ....	81
5.2.3.	<i>DNP Sample Preparation of Polymers</i> .....	84
5.3.	Experimental Details .....	87
5.3.1.	<i>Materials</i> .....	87
5.3.2.	<i>Sample Preparation</i> .....	87
5.3.3.	<i>DNP-Enhanced Solid-state NMR</i> .....	88
5.3.4.	<i>Double-Quantum NMR</i> .....	89
5.4.	Results and Discussion .....	91
5.4.1.	<i>Polymer Swelling</i> .....	92
5.4.2.	<i>Role of a ‘Glass-former’</i> .....	97
5.4.3.	<i>Measuring the Effect of Swelling on DNP Enhancement</i> .....	103
5.4.4.	<i>RDC in Swollen Polymers</i> .....	109
5.5.	Summary .....	115

<b>6.</b>	<b>Supercritical Carbon Dioxide DNP Sample</b>	
	<b>Preparation.....</b>	<b>116</b>
6.1.	Abstract.....	116
6.2.	Introduction.....	117
6.2.1.	<i>Supercritical Fluids.....</i>	<i>117</i>
6.2.2.	<i>Supercritical CO<sub>2</sub> Impregnation of Polymers ...</i>	<i>118</i>
6.3.	Experimental Details .....	120
6.3.1.	<i>High Pressure Equipment .....</i>	<i>120</i>
6.3.2.	<i>Materials.....</i>	<i>121</i>
6.3.3.	<i>Supercritical CO<sub>2</sub> Impregnation .....</i>	<i>121</i>
6.3.4.	<i>DNP-Enhanced Solid-state NMR.....</i>	<i>122</i>
6.3.5.	<i>EPR.....</i>	<i>123</i>
6.4.	Results and Discussion .....	124
6.4.1.	<i>Poly(ethylene oxide) .....</i>	<i>124</i>
6.4.1.	<i>Polystyrene .....</i>	<i>132</i>
6.4.2.	<i>Core-Shell Structures .....</i>	<i>137</i>
6.4.3.	<i>EPR Measurements .....</i>	<i>148</i>
6.5.	Summary .....	155
<b>7.</b>	<b>Summary and Outlook .....</b>	<b>157</b>
	<b>References.....</b>	<b>160</b>

# List of Tables

Table 3.1: Phase shifts of $\pm 2$ coherences .....	44
Table 4.1: $^1\text{H}$ static chemical shift of the $\text{CH}_3$ signal of $\text{MAPbI}_3$ recorded at increasing temperatures .....	67
Table 5.1: Radical solutions used for sample preparation.....	88
Table 5.2: DNP enhancements, linewidths, and SNR enhancements for two samples of PEO impregnated in an aqueous solution (glycerol- $\text{d}_8/\text{D}_2\text{O}/\text{H}_2\text{O}$ ) or organic solvent (TCE).....	92
Table 5.3: DNP enhancements, linewidths, and SNR enhancements for two samples of PS impregnated in an aqueous solution (glycerol- $\text{d}_8/\text{D}_2\text{O}/\text{H}_2\text{O}$ ) or organic solvent (TCE). .....	93
Table 5.4: Sample preparation details of two samples of PEO prepared with different volumes of a radical solution .....	95
Table 5.5: DNP enhancements, linewidths, and SNR enhancement factors for $^1\text{H}$ - $^{13}\text{C}$ CP DNP experiments of $\sim 30$ mg of PEO impregnated with AMUPol.....	99
Table 5.6: DNP enhancements, linewidths, and SNR enhancement factors for $^1\text{H}$ - $^{13}\text{C}$ CP DNP experiments of $\sim 30$ mg of PHEMA impregnated with AMUPol.....	100
Table 5.7: DNP enhancements, linewidths, and SNR enhancement factors for $^1\text{H}$ - $^{13}\text{C}$ CP DNP experiments of $\sim 30$ mg of NaPA impregnated with AMUPol.....	101
Table 5.8: Sample preparation details for the impregnation of NaPA with AMUPol.....	104
Table 5.9: Observed $^1\text{H}$ - $^{13}\text{C}$ CP DNP enhancements and MW on SNR per gram of polymer of NaPA. ....	108
Table 5.10: DNP enhancements for the $\text{COO}^-$ signal of samples of NaPA....	109
Table 5.11: Sample reference, relating to the volume of radical solution added to the equivalent sample studied by DNP-enhanced NMR in Section 5.4.3, and the water content of the swollen polymer, $Q$ . ....	110

Table 6.1: DNP build-up times and DNP enhancements of samples of PEO impregnated in scCO <sub>2</sub> with ~11 μmol g <sup>-1</sup> TEKPol at temperatures of 34 °C for 3 hours at different pressures.....	125
Table 6.2: DNP build-up times and DNP enhancements of samples of PEO impregnated with ~5-6 μmol g <sup>-1</sup> TEKPol in scCO <sub>2</sub> at temperatures of 34 °C and pressures of 241 bar for different lengths of time.....	127
Table 6.3: DNP build-up times and DNP enhancements of samples of PEO impregnated with different concentrations of TEKPol.....	128
Table 6.4: Radical concentrations, effective sample weights, DNP enhancements, signal to noise ratios, and linewidths of samples of PEO impregnated with AMUPol using the swelling method and the scCO <sub>2</sub> method. ....	129
Table 6.5: DNP build-up times, DNP enhancements, and SNR enhancement factors of samples of PEO impregnated with AMUPol using the swelling method and the scCO <sub>2</sub> method. ....	131
Table 6.6: PS signal <sup>1</sup> H- <sup>13</sup> C CP DNP build-up times, CP DNP enhancements, and DP DNP enhancements of core-shell polymers with increasing shell thicknesses. ....	141
Table 6.7: PMMA signal <sup>1</sup> H- <sup>13</sup> C CP DNP build-up times, CP DNP enhancements, and DP DNP enhancements of core-shell polymers with increasing shell thicknesses. ....	143
Table 6.8: Direct (ε +) and cross-relaxation (ε -) DNP enhancements of representative signals of PS and PMMA in a 1: 1 core-shell sample.....	146
Table 6.9: Experimental HFEPER parameters for AMUPol and TEKPol radicals from Ref [ <sup>203</sup> ], used to calculate rigid-limit Q-band EPR spectra. ....	153
Table 6.10: <i>T1e</i> , <i>T2e</i> and DNP enhancements for 3 samples of PEO impregnated with nitroxide radicals by different methods. ....	154

# List of Figures

Figure 2.1: Principal axis system in polar coordinates. ....	17
Figure 2.2: Dipolar interaction between two spins .....	19
Figure 2.3: Schematic representation of the set-up of a sample in MAS NMR. .....	23
Figure 2.4: Energy level diagram for possible relaxation induced transitions .	27
Figure 2.5: a) Pulse sequence used for $T_1$ saturation recovery experiments. ..	30
Figure 2.6: Energy level diagram for the solid effect DNP mechanism.....	33
Figure 2.7: Energy level diagram for the Overhauser effect DNP mechanism. .....	35
Figure 2.8: Energy level diagrams for three stages of the cross effect DNP mechanism. ....	37
Figure 2.9: Structures of the nitroxide biradicals used for DNP .....	38
Figure 3.1: Schematic representation of a simple single-pulse NMR experiment and FID. ....	42
Figure 3.2: Pulse sequence and coherence order pathway of a double-quantum filtered COSY experiment. ....	43
Figure 3.3: Pulse sequence of a spin echo experiment. ....	45
Figure 3.4: Pulse sequence used for static $^1\text{H}$ DQ build up experiments .....	47
Figure 3.5: Pulse sequence for a cross polarization experiment.....	49
Figure 3.6: Schematic representation of the direct and indirect polarization transfer pathways from electrons to the bulk $^{13}\text{C}$ . ....	50
Figure 3.7: a) Direct polarization (DP) and b) cross polarization (CP) DNP pulse sequences.....	50
Figure 3.8: Pulse sequence for interleaved SCREAM-DNP experiments.....	51
Figure 4.1: Schematic representations of the perovskite, $\text{ABX}_3$ crystal structure. ....	53
Figure 4.2: Fits of the spectral density function .....	61
Figure 4.3: $^1\text{H}$ single-pulse MAS spectrum of $\text{MAPbI}_3$ . ....	64
Figure 4.4:a) $^1\text{H}$ static spin echo spectrum of $\text{MAPbI}_3$ .....	65
Figure 4.5: $^1\text{H}$ static spin echo spectra of $\text{MAPbI}_3$ recorded at different temperatures.....	66

Figure 4.6: $^1\text{H}$ MAS spin echo spectra of $\text{MAPbI}_3$ recorded at different temperatures.....	69
Figure 4.7: $^1\text{H}$ MAS spin echo spectra of $\text{MAPbI}_3$ with different recycle delays and spin echo delays. ....	70
Figure 4.8: $^1\text{H}$ MAS spin echo spectra of $\text{MAPbI}_3$ recorded at different temperatures.....	71
Figure 4.9: $^1\text{H}$ - $^{13}\text{C}$ CP spectrum of $\text{MAPbI}_3$ .....	72
Figure 4.10: $^1\text{H}$ MAS spin echo spectra of dry $\text{MAPbI}_3$ (Red) and wet $\text{MAPbI}_3$ (Blue). ....	73
Figure 4.11: Example architecture of a solar cell.....	74
Figure 4.12: $^1\text{H}$ MAS spin echo spectra of $\text{MAPbI}_3$ on $\text{ZnO}$ .....	76
Figure 4.13: $^1\text{H}$ MAS spin echo spectra of $\text{MAPbI}_3$ (Red) and $\text{MAPbI}_3$ on $\text{ZnO}$ (Blue).....	77
Figure 5.1: $^1\text{H}$ - $^{13}\text{C}$ CP spectra a) without and b) with MW irradiation of the polymer samples used here. ....	91
Figure 5.2: $^1\text{H}$ - $^{13}\text{C}$ CP spectra a) without and b) with MW irradiation of PEO93	
Figure 5.3: $^1\text{H}$ - $^{13}\text{C}$ CP spectra a) without and b) with MW irradiation of PS ..	94
Figure 5.4: $^1\text{H}$ - $^{13}\text{C}$ CP spectra a) without and b) with MW irradiation of two samples of PEO impregnated with different volumes of radical solution	95
Figure 5.5: $^1\text{H}$ - $^{13}\text{C}$ CP spectra with MW irradiation of PEO impregnated with a) 14 $\mu\text{L}$ and b) 50 $\mu\text{L}$ of 10 mM AMUPol in $\text{D}_2\text{O}$ (100 %). ....	97
Figure 5.6: $^1\text{H}$ - $^{13}\text{C}$ CP spectra recorded with MW irradiation of PEO.....	98
Figure 5.7: $^1\text{H}$ - $^{13}\text{C}$ CP spectra, intensities scaled to match, recorded with MW irradiation of PEO impregnated with 10 mM AMUPol.....	99
Figure 5.8: $^1\text{H}$ - $^{13}\text{C}$ CP spectra, intensities scaled to match, recorded with MW irradiation of PHEMA impregnated with 10 mM AMUPol .....	100
Figure 5.9: $^1\text{H}$ - $^{13}\text{C}$ CP spectra, intensities scaled to match, recorded with MW irradiation of NaPA impregnated with 10 mM AMUPol.....	101
Figure 5.10: $^1\text{H}$ - $^{13}\text{C}$ CP spectra of NaPA samples without MW irradiation. .	105
Figure 5.11: Plots demonstrating the trends in the change of $\text{H}_2\text{O}$ volume (green) and polymer mass (red) in the rotor and the change in SNR .....	106
Figure 5.12: Plot of the evolution of the SNR per gram and unit of square time .....	107



Figure 5.13: $^1\text{H}$ - $^{13}\text{C}$ CP spectra with MW irradiation of samples <b>1</b> (front) to <b>8</b> (back) .....	107
Figure 5.14: DQ coherence build up curves .....	111
Figure 5.15: DQ coherence curves representing the fit of experimental data to an A-1 build-up function for samples of NaPA.....	112
Figure 5.16: Distributions of RDC constants, $D_{res}$ , calculated from the A-1 fits of $\ln DQ$ build-up, of samples of NaPA.....	113
Figure 6.1: Schematic pressure-temperature phase diagram showing the supercritical fluid region.....	117
Figure 6.2: $^1\text{H}$ - $^{13}\text{C}$ CP spectra a) without and b) with MW irradiation of PEO impregnated with AMUPol (Left) and TEKPol (right) in $\text{scCO}_2$ .....	124
Figure 6.3: Plot of the fraction of the slow component of fitted DNP build-up time as function of $\text{scCO}_2$ impregnation a) pressure and b) time. ....	126
Figure 6.4: $^1\text{H}$ - $^{13}\text{C}$ CP spectra with MW irradiation of PEO impregnated with AMUPol using the swelling method (Red) and the $\text{scCO}_2$ method (Blue). .....	130
Figure 6.5: $^1\text{H}$ - $^{13}\text{C}$ CP spectra a) without and b) with MW irradiation of PEO (Left) and PS (Right) impregnated in $\text{scCO}_2$ .....	133
Figure 6.6: $^1\text{H}$ - $^{13}\text{C}$ CP (Left) and $^{13}\text{C}$ DP (Right) spectra a) without and b) with MW irradiation of PS impregnated with TEKPol in $\text{scCO}_2$ .....	134
Figure 6.7: $^1\text{H}$ - $^{13}\text{C}$ CP spectra a) without and b) with MW irradiation of PS impregnated with $105 \mu\text{mol g}^{-1}$ of TEKPol in $\text{scCO}_2$ .....	136
Figure 6.8: $^1\text{H}$ - $^{13}\text{C}$ CP spectrum of a PS:PMMA core-shell polymer with a 1:1 PS:PMMA ratio. ....	138
Figure 6.9: $^1\text{H}$ - $^{13}\text{C}$ CP spectra of PS:PMMA core-shell polymers with PS:PMMA ratios of a)1: 8, b) 1: 4, c) 1: 2, and d)1: 1. ....	140
Figure 6.10: $^1\text{H}$ - $^{13}\text{C}$ CP DNP build-up curve fits for the PS signal of 1:4 (Red) and 1:2 (Blue) ratios of PS:PMMA core-shell polymers.....	142
Figure 6.11:Schematic representation of the competing polarization transfer pathways during a $^{13}\text{C}$ DP DNP experiment .....	144
Figure 6.12:a) $\text{DP}_{\text{sat}}$ , b) $\text{DP}_{\text{off}}$ , c) $\text{DP}_{\text{on}}$ , and d) $\Delta\text{DP}_{\text{sat}}$ spectra for a 1:1 PS:PMMA core-shell polymer .....	146

Figure 6.13: $\Delta DP_{\text{sat}}$ spectra (with a $180^\circ$ phase change) obtained at increasing polarization build-up delay times .....	148
Figure 6.14: Experimental data for PEO impregnated by swelling in a solution of 10 mM AMUPol in glycerol- $d_8$ /D $_2$ O/H $_2$ O (60/30/10 vol%) (Blue) and calculated spectrum of AMUPol based on HFEP data (Red). .....	149
Figure 6.15: Experimental spectra of PEO impregnated by swelling in a solution of 10 mM AMUPol in glycerol- $d_8$ /D $_2$ O/H $_2$ O (60/30/10 vol%) (Blue) and PEO impregnated with $9 \mu\text{mol g}^{-1}$ concentration of AMUPol in scCO $_2$ (Red). .....	150
Figure 6.16: Comparisons of the experimental data of the scCO $_2$ impregnated PEO sample (Blue) and the calculated Q-band spectrum (Red).....	151
Figure 6.17: Experimental data for PEO impregnated with $6 \mu\text{mol g}^{-1}$ concentration of TEKPol in scCO $_2$ (Blue), experimental data for PS impregnated with $5 \mu\text{mol g}^{-1}$ of TEKPol in scCO $_2$ (Green), and the calculated Q-band spectrum of TEKPol .....	152

# Glossary

API	Active Pharmaceutical Ingredient
ASR	Absolute Sensitivity Ratio
CE	Cross Effect
CP	Cross Polarization
CS	Chemical Shielding
CSA	Chemical Shielding Anisotropy
CW	Continuous Wave
DD	Dipolar Coupling
DNP	Dynamic Nuclear Polarization
DP	Direct Polarization
DQ	Double Quantum
EPR	Electron Paramagnetic Resonance
FC	Film Casting
FID	Free Induction Decay
FWHM	Full Width at Half Maximum Height
GF	Glass Forming
HFEPR	High Field Electron Paramagnetic Resonance
IWI	Incipient Wetness Impregnation
MA	Methylammonium ion
MAPbI <sub>3</sub>	Methylammonium Lead Iodide
MAS	Magic Angle Spinning
MW	Microwave
NaPA	Sodium polyacrylate
NMR	Nuclear Magnetic Resonance
OE	Overhauser Effect
PAS	Principal Axis System
PDMS-MA	Monomethacrylate terminated poly(dimethylsiloxane)
PEO	Poly(ethylene oxide)
PHEMA	Poly(2-hydroxyethyl methacrylate)
PMMA	Poly(methyl methacrylate)

PS	Polystyrene
RDC	Residual Dipolar Coupling
RF	Radio Frequency
RNA	Ribonucleic Acid
scCO <sub>2</sub>	Supercritical Carbon Dioxide
SCERAM-DNP	Specific Cross-Relaxation Enhancement by Active Motions under DNP
SCF	Supercritical Fluid
SE	Solid Effect
SNR	Signal to Noise Ratio
SWf-TPPM	Swept-frequency Two-Pulse Phase Modulation
TCE	Tetrachloroethane
TM	Thermal Mixing
VT	Variable Temperature
ZQ	Zero Quantum



# 1. Introduction

Reducing our global dependency on finite resources is a vital step in achieving climate neutrality in the coming decades. Chemistry and materials research is at the forefront of this drive for sustainability. The ability to improve the performance of materials which can harness renewable, solar energy or develop more sustainable manufacturing processes for materials made from renewable, plant-based sources, requires a deep understanding of the relationships between the structure, dynamics, and properties of these new innovative materials. Solid-state nuclear magnetic resonance (NMR) is an incredibly powerful and versatile tool which can provide this detailed analysis.

## 1.1. Perovskites

The burning of fossil fuels is not only environmentally damaging due to the release of greenhouse gasses, it also relies on finite resources and is not a sustainable long-term energy source. To harness renewable, solar energy, solar cells are used to convert the light energy into electricity. These solar cells already provide some of the cheapest energy generation available in many countries<sup>1</sup> and the global power generation from solar energy continues to increase year on year. However, to meet the targets set to reach Net Zero Emissions by 2050,<sup>2</sup> there must continue to be more investment and development in solar energy technology.

Hybrid perovskite materials have, in recent years demonstrated their potential as solar cells. Although the photoconversion efficiencies of hybrid perovskite based solar cells were initially low, recent developments have seen a rapid increase in the efficiencies of these materials, reaching close to the theoretical limit.<sup>3</sup> These hybrid perovskite materials have the potential to be a high-scale and low-cost competitor to traditional Si-based solar cells. However, overcoming key issues related to their sustainability must be addressed before they are commercially viable.

## 1.2. Polymers

In the early 20<sup>th</sup> century the development of synthetic plastics from polymers was heralded as a great revolution with many benefits. Indeed, the diversity of polymers provides an incredibly versatile array of plastics with desirable properties. What was not anticipated at the time, were the problems associated with an overreliance of plastic and poor waste management. Towards the latter half of the 20<sup>th</sup> century, concerns of the environmental impact of plastic began to arise. 1969 saw the first reports of plastic debris in the guts of seabirds,<sup>4</sup> and since then, reporting on plastic contamination in the ocean and the impact of plastics on wildlife and humans intensified.<sup>5-7</sup>

Despite the harm caused by plastics, it is unrealistic to expect that they will be replaced by a different class of material given so much of the modern world has

been moulded by the availability of plastic. Without these materials many recent technological advances would not be possible. A solution to avoiding the growing pollution by plastic materials is to develop alternative polymer feedstocks which are derived from a cleaner, renewable source, and which are biodegradable or more easily recycled.

### 1.3. Thesis Overview

A theoretical overview of the principals of NMR which pertain to this thesis is given in Chapter 2. This includes an introduction of the internal and external interactions which make NMR such a powerful technique, the phenomenon of relaxation, and the theory and practical aspects of DNP.

Chapter 3 provides an overview of some of the theoretical concepts and practical details of the experimental procedures used in this thesis. Details of phase cycling, spin echoes, double-quantum NMR, heteronuclear decoupling cross polarization, and DNP experiments are covered in this chapter.

The experimental results of this thesis are presented in Chapters 4, 5, and 6. Chapter 4 presents  $^1\text{H}$  NMR investigations of  $\text{MAPbI}_3$  which are focused on identifying the presence and diffusion of hydrogen defects. This involves the use of static and MAS NMR, VT NMR, and spectral editing.

Chapters 5 and 6 are focused on sample preparation for DNP-enhanced NMR of polymers. Chapter 5 is centred on optimizing the radical solution used for polymer DNP. This optimization includes selecting the appropriate radical and solvent combination, the importance of deuteration of the solvent, the role of a ‘glass-former’, and crucially the ideal volume of radical solution. Chapter 6 introduces a new matrix-free method of sample preparation using supercritical  $\text{CO}_2$ . The use of  $\text{scCO}_2$  impregnation for poly(ethylene oxide), polystyrene, and more complex core-shell polymer particles is demonstrated and the conditions of  $\text{scCO}_2$  impregnation are investigated. The different domains of the  $\text{scCO}_2$  impregnated core-shell polymers are investigated by exploiting the cross-relaxation induced by methyl dynamics of the shell portion.

In Chapter 7, general conclusions of the work presented are summarized and the outlook related to this work are considered.



## 2. Theory

The work in this thesis is focused on using solid-state NMR and DNP-enhanced solid-state NMR as the main experimental techniques. In this chapter, some of the basic theory behind these techniques is presented. A full, in-depth review of all aspects of NMR theory is not needed here, instead the main concepts which are applicable to the experimental work in this thesis are the focus. The material here is based on the theory presented in *Understanding NMR Spectroscopy* (J. Keeler),<sup>8</sup> *Spin Dynamics: Basics of Nuclear Magnetic Resonance* (M. H. Levitt),<sup>9</sup> *Solid-State NMR spectroscopy: Principles and Applications* (M. J. Duer),<sup>10</sup> and *Solid-State NMR: Basic Principles and Practice* (D. C. Apperley, R. K. Harris and P. Hodgkinson).<sup>11</sup>

## 2.1. Solid-state NMR

### 2.1.1. The Practical NMR Experiment

In a standard NMR experiment, a sample is positioned within a coil of conducting wire, which is placed within an external magnetic field,  $B_0$ . In the presence of  $B_0$  the energies of the nuclear spin states are no longer degenerate, and their populations are determined by the Boltzmann distribution. This distribution leads to a bulk magnetization which lies parallel to  $B_0$ .

This magnetization is perturbed by a second magnetic field,  $B_1$ , which is generated by applying a current to the coil which generates a radiofrequency field. This RF pulse rotates the bulk magnetization into the plane perpendicular to  $B_0$ . Precession of magnetization in this plane will induce a corresponding oscillating current in the coil. Once the applied current is removed and the bulk magnetization returns to be parallel to  $B_0$ . The induced current in the coil is detected and recorded as a *Free Induction Decay* (FID). The FID is a time domain signal of the measured alternating current in the coil and contains all the information of the NMR experiment. However, the oscillations in the FID are too fast to resolve in the time domain and so the FID is converted from the time domain to a frequency spectrum by Fourier transform.

### 2.1.2. The Zeeman Interaction

Intrinsic properties of matter such as mass and charge have clear, measurable impact on the physical and chemical properties of nuclei. Spin does not have such a physical impact on a given nucleus, but it is this intrinsic property which is exploited by NMR to investigate the structures and dynamics of systems at an atomic level.

Nuclear spin angular momentum,  $I$ , is an intrinsic property of matter which is determined by the number of protons and neutrons within a nucleus and is described by the spin quantum number,  $I$  which takes positive integer or half-integer values. A nucleus with spin  $I$  has  $2I + 1$  degenerate spin states which are described by the magnetic quantum number,  $m$

$$m_I = -I, -I + 1, \dots, I - 1, I \quad [2.1.2.1]$$

The z-component of  $I$  can be quantized as

$$I_z = m_I \hbar \quad [2.1.2.2]$$

For a nucleus with  $I = \frac{1}{2}$ ,  $m$  can take values of  $+\frac{1}{2}$  or  $-\frac{1}{2}$  and so

$$I_z = \pm \frac{1}{2} \quad [2.1.2.3]$$

Nuclei with  $I > 0$ , have an intrinsic magnetic moment and are described as ‘NMR active’. The magnetic dipole moment,  $\boldsymbol{\mu}$ , is related to  $\mathbf{I}$  as

$$\boldsymbol{\mu} = \gamma \mathbf{I} \quad [2.1.2.4]$$

where  $\gamma$  is the gyromagnetic ratio which is an intrinsic property of each type of nucleus. The interaction of the magnetic moment with an external magnetic field,  $\mathbf{B}_0$  is known as the *Zeeman interaction* and induces a loss of degeneracy of the nuclear spin states. The energy associated with this is

$$E = -\boldsymbol{\mu} \mathbf{B}_0 \quad [2.1.2.5]$$

By convention,  $B_0$  is considered to lie on the z-axis and so if we consider the z-component of a  $I = \frac{1}{2}$  nucleus, the energy of the nuclear spin states can be described as

$$E = \pm m_I \gamma B_0 \quad [2.1.2.6]$$

$$E = \pm \frac{1}{2} \gamma B_0 \quad [2.1.2.7]$$

As transitions between these energy levels are only visible in NMR if  $\Delta m_I = \pm 1$ , the observable transitions are all degenerate with an energy

$$\Delta E = -\gamma B_0 \quad [2.1.2.8]$$

This is equal to the difference in energy between the two Zeeman states and can be described in terms of angular frequency as

$$\Delta E = \omega_0 \quad [2.1.2.9]$$

where  $\omega_0 = -\gamma B_0$  is the *Larmor frequency* which is the frequency of precession of bulk magnetization measured in an NMR experiment. As the gyromagnetic ratio is constant and intrinsic to a particular nuclear species, at any given field strength, the Larmor frequency is also an intrinsic characteristic.

The Zeeman interaction, giving rise to the measurable Larmor frequency, provides insight to distinguish between different nuclear species. However, NMR would not be a particularly interesting spectroscopic tool if this was the only knowledge it provided. Interactions between neighbouring spins result in subtle shifts in the Zeeman energy and provide the valuable insight to the local environment of a nucleus which makes NMR such a powerful technique.

### 2.1.3. The Quantum Mechanical Approach

When nuclear spins interact with one another it is necessary to use a quantum mechanical description of the NMR experiment.

In quantum mechanics the physical state of any system can be represented by a wavefunction  $\psi$ . The value of some observable of this system can be extracted from the wavefunction by an operator  $\hat{A}$ , which represents the desired observable,  $A$ .

$$\hat{A}|\psi\rangle = A \quad [2.1.3.1]$$

The average value of the observable is the expectation value  $\langle A \rangle$

$$\langle A \rangle = \langle \psi | \hat{A} | \psi \rangle \quad [2.1.3.2]$$

The energy levels of a wavefunction are given by the time dependent Schrödinger equation

$$i\hbar \frac{d|\psi\rangle}{dt} = \hat{H}|\psi\rangle \quad [2.1.3.3]$$

where  $\hat{H}$  is the Hamiltonian, or energy operator for the system. It is possible to simplify this description if the system is closed and all energy is conserved. In this case the energy of the system can be described by the time independent Schrödinger equation

$$\hat{H}|\psi\rangle = E|\psi\rangle \quad [2.1.3.4]$$

The Hamiltonian for a nuclear spin system can be represented as a linear combination of the Hamiltonians for individual interactions of the spin system

$$\hat{H} = \hat{H}_Z + \hat{H}_{RF} + \hat{H}_{CS} + \hat{H}_{DD} + \hat{H}_J + \hat{H}_Q \quad [2.1.3.5]$$

where  $\hat{H}_Z$  is the Zeeman Hamiltonian,  $\hat{H}_{RF}$  is the radiofrequency Hamiltonian,  $\hat{H}_{CS}$  is the chemical shielding Hamiltonian,  $\hat{H}_{DD}$  is the dipolar coupling Hamiltonian,  $\hat{H}_J$  is the J-coupling Hamiltonian and  $\hat{H}_Q$  is the quadrupolar coupling Hamiltonian.

Analogous to Equation [2.1.2.5], the Zeeman Hamiltonian describes the interaction of a magnetic moment and a magnetic field

$$\hat{H}_Z = -\hat{\mu} \cdot \hat{B} = -\hat{\mu}_z B_0 = -\gamma \hat{I}_z B_0 \quad [2.1.3.6]$$

where  $\hat{I}_z$  is the  $z$  component of the spin angular momentum operator. To solve the Zeeman Hamiltonian, it is necessary to first consider the spin angular momentum operators.

## 2.1.4. Angular Momentum Operators

A spin system is described by nuclear spin wavefunction,  $|I, m\rangle$ , where  $I$  is the spin angular momentum operator and  $m$  is the magnetic quantum number. The operators representing spin angular momentum are  $\hat{I}_z, \hat{I}_x, \hat{I}_y$  and  $\hat{I}^2$ , the first three representing the  $z, x$  and  $y$  components of nuclear spin angular momentum and the final is the total spin. The wavefunction  $|I, m\rangle$  is an eigenstate of the operators  $\hat{I}^2$  and  $\hat{I}_z$

$$\hat{I}^2 |I, m\rangle = I(I + 1) |I, m\rangle \quad [2.1.4.1]$$

$$\hat{I}_z |I, m\rangle = m |I, m\rangle \quad [2.1.4.2]$$

For  $I = \frac{1}{2}$ , the eigenstates are labelled as  $|\alpha\rangle$  and  $|\beta\rangle$  such that

$$\hat{I}_z |\alpha\rangle = \frac{1}{2} |\alpha\rangle \quad \hat{I}_z |\beta\rangle = -\frac{1}{2} |\beta\rangle \quad [2.1.4.3]$$

$\hat{I}_x$  and  $\hat{I}_y$  operators correspond to the  $x$  and  $y$  components of angular momentum but are often expressed as *raising* and *lowering* operators,  $\hat{I}_+$  and  $\hat{I}_-$

$$\hat{I}_x = \frac{1}{2}(\hat{I}_+ + \hat{I}_-) \quad \hat{I}_y = -\frac{i}{2}(\hat{I}_+ - \hat{I}_-) \quad [2.1.4.4]$$

so called because of their effect on the eigenstate  $|m\rangle$

$$\hat{I}_+|\alpha\rangle = 0 \quad \hat{I}_+|\beta\rangle = |\alpha\rangle \quad \text{and} \quad \hat{I}_-|\alpha\rangle = |\beta\rangle \quad \hat{I}_-|\beta\rangle = 0 \quad [2.1.4.5]$$

To describe the total wavefunction of a spin  $I = \frac{1}{2}$ , a linear combination of the two eigenstates is used. This is known as a superposition state

$$|\psi\rangle = c_\alpha|\alpha\rangle + c_\beta|\beta\rangle \quad \langle\psi| = c_\alpha^*\langle\alpha| + c_\beta^*\langle\beta| \quad [2.1.4.6]$$

where  $c_\alpha$  and  $c_\beta$  are time-dependant coefficients which define the weighting of each state and  $c_\alpha^*$  and  $c_\beta^*$  are their complex conjugates.

The expectation values for the spin operators are therefore

$$\begin{aligned} \langle I_z \rangle &= c_\alpha c_\alpha^* \langle \alpha | \hat{I}_z | \alpha \rangle + c_\alpha c_\beta^* \langle \alpha | \hat{I}_z | \beta \rangle + c_\beta c_\alpha^* \langle \beta | \hat{I}_z | \alpha \rangle + c_\beta c_\beta^* \langle \beta | \hat{I}_z | \beta \rangle \\ \langle I_z \rangle &= \frac{1}{2} (c_\alpha c_\alpha^* - c_\beta c_\beta^*) \end{aligned} \quad [2.1.4.7]$$

$$\langle I_x \rangle = \frac{1}{2} (c_\alpha c_\beta^* + c_\beta c_\alpha^*) \quad [2.1.4.8]$$

$$\langle I_y \rangle = \frac{1}{2} (c_\alpha c_\beta^* - c_\beta c_\alpha^*) \quad [2.1.4.9]$$

## 2.1.5. The Density Matrix

When the spin system is small a linear combination of states can be useful, however for large spin systems and when  $I > \frac{1}{2}$ , this approach can become overwhelming, and it is easier to work with a matrix notation.

For  $I = \frac{1}{2}$ , an operator  $\hat{A}$  in the eigenbasis of  $\hat{I}_z$ , can be described by the matrix

$$\mathbf{A} = \begin{pmatrix} A_{\alpha\alpha} & A_{\beta\alpha} \\ A_{\alpha\beta} & A_{\beta\beta} \end{pmatrix} = \begin{pmatrix} \langle \alpha | \hat{A} | \alpha \rangle & \langle \beta | \hat{A} | \alpha \rangle \\ \langle \alpha | \hat{A} | \beta \rangle & \langle \beta | \hat{A} | \beta \rangle \end{pmatrix} \quad [2.1.5.1]$$

The superposition states for  $|\alpha\rangle$  and  $|\beta\rangle$  may be described as vectors

$$|\psi\rangle = \begin{pmatrix} c_\alpha \\ c_\beta \end{pmatrix} \quad \langle\psi| = (c_\alpha^* \quad c_\beta^*) \quad [2.1.5.2]$$

The expectation value of an operator using these definitions is

$$\begin{aligned}
\langle A \rangle &= \langle \psi | \hat{A} | \psi \rangle \\
&= \begin{pmatrix} c_\alpha^* & c_\beta^* \end{pmatrix} \begin{pmatrix} A_{\alpha\alpha} & A_{\alpha\beta} \\ A_{\beta\alpha} & A_{\beta\beta} \end{pmatrix} \begin{pmatrix} c_\alpha \\ c_\beta \end{pmatrix} \\
&= c_\alpha c_\alpha^* A_{\alpha\alpha} + c_\beta c_\beta^* A_{\beta\beta} + c_\alpha c_\beta^* A_{\beta\alpha} + c_\beta c_\alpha^* A_{\alpha\beta}
\end{aligned} \tag{2.1.5.3}$$

As this expression includes the products of coefficients, rather than the coefficients themselves, it suggests it is possible to represent the wavefunction in terms of these products as

$$|\psi\rangle\langle\psi| = \begin{pmatrix} c_\alpha \\ c_\beta \end{pmatrix} \begin{pmatrix} c_\alpha^* & c_\beta^* \end{pmatrix} = \begin{pmatrix} c_\alpha c_\alpha^* & c_\alpha c_\beta^* \\ c_\beta c_\alpha^* & c_\beta c_\beta^* \end{pmatrix} \tag{2.1.5.4}$$

For an ensemble of spins, this description of the system is known as the *density operator*

$$\hat{\rho} = \overline{|\psi\rangle\langle\psi|} \tag{2.1.5.5}$$

where the overbar refers to the ensemble average of the spins.

The density operator is a more complete and effective method to describe the bulk magnetization of a system with a large number of spins than a linear superposition state.

In the same way as for an isolated spin, the expectation value can be found for an ensemble of spins by applying the density operator to the system. The product of the density operator and the operator acting on the system for an ensemble of isolated  $I = \frac{1}{2}$  nuclei is

$$\begin{aligned}
\rho A &= \begin{pmatrix} c_\alpha c_\alpha^* & c_\alpha c_\beta^* \\ c_\beta c_\alpha^* & c_\beta c_\beta^* \end{pmatrix} \begin{pmatrix} A_{\alpha\alpha} & A_{\beta\alpha} \\ A_{\alpha\beta} & A_{\beta\beta} \end{pmatrix} \\
&= \begin{pmatrix} c_\alpha c_\alpha^* A_{\alpha\alpha} + c_\alpha c_\beta^* A_{\beta\alpha} & c_\alpha c_\alpha^* A_{\alpha\beta} + c_\alpha c_\beta^* A_{\beta\beta} \\ c_\beta c_\alpha^* A_{\alpha\alpha} + c_\beta c_\beta^* A_{\beta\alpha} & c_\beta c_\alpha^* A_{\alpha\beta} + c_\beta c_\beta^* A_{\beta\beta} \end{pmatrix}
\end{aligned} \tag{2.1.5.6}$$

The trace (Tr) of this matrix corresponds to the expectation value in Equation [2.1.5.3] and so the expectation value of an ensemble of spins can be defined as

$$\langle A \rangle = Tr\{\rho A\} \tag{2.1.5.7}$$

Examining the density matrix,  $\rho$ , and comparing to Equations [2.1.4.7-9], it can be seen that  $\langle \hat{I}_z \rangle$  is determined by the diagonal elements of the matrix, and  $\langle \hat{I}_x \rangle$  and  $\langle \hat{I}_y \rangle$  are determined by the off-diagonal elements.

Representing the coefficients as the product of a coefficient and a *phase constant*,  $\phi$ , allows for a clearer understanding of what these diagonal and off-diagonal elements represent. If  $c_\alpha = a_\alpha e^{i\phi_\alpha}$  and  $c_\beta = a_\beta e^{i\phi_\beta}$  the density matrix is

$$\rho = \begin{pmatrix} a_\alpha^2 & a_\alpha a_\beta e^{i(\phi_\alpha - \phi_\beta)} \\ a_\alpha a_\beta e^{i(\phi_\beta - \phi_\alpha)} & a_\beta^2 \end{pmatrix} \quad [2.1.5.8]$$

The dependence of the off-diagonal elements on the phase indicates that for a system of spins that exist in different states, these off-diagonal terms will average to zero. In this case, only the diagonal elements remain and represent the *populations* for the state. In an ensemble of spins which exist in the same state,  $e^{i(\phi_\beta - \phi_\alpha)}$  has a non-zero value and the off-diagonal elements are retained. This is known as a *phase coherence* between states, and it is these coherence states which are observable in an NMR experiment.

The *coherence order* of a density matrix,  $p_{\alpha\beta}$ , characterizes the phase coherence and is defined as

$$p_{\alpha\beta} = m_\alpha - m_\beta \quad [2.1.5.9]$$

where  $m_\alpha$  and  $m_\beta$  are the magnetic quantum numbers for states  $|\alpha\rangle$  and  $|\beta\rangle$ .

Considering the off-diagonal elements of the density matrix which represent both the coherence of states and the expectation values of the  $x$  and  $y$  components of  $\hat{I}$ , it becomes clear that the observation of coherence requires magnetization to be in the  $xy$ -plane.



## 2.1.6. The Time-dependence of the Density Operator

The generation of transverse magnetization and the evolution of the precession are time-dependent, and so it is appropriate to consider the density operator as a time-dependent function. Differentiating  $\rho$  with respect to time gives

$$\begin{aligned}\frac{d\hat{\rho}(t)}{dt} &= \frac{d}{dt}(|\psi\rangle\langle\psi|) \\ &= \left( \left( \frac{d}{dt}|\psi\rangle \right) \langle\psi| \right) + \left( |\psi\rangle \left( \frac{d}{dt}\langle\psi| \right) \right)\end{aligned}\quad [2.1.6.1]$$

The time-dependent Schrödinger equations (TDSE) for  $|\psi\rangle$  and  $\langle\psi|$  are

$$\frac{d}{dt}|\psi\rangle = -i\hat{H}|\psi\rangle \quad [2.1.6.2]$$

$$\frac{d}{dt}\langle\psi| = i\langle\psi|\hat{H} \quad [2.1.6.3]$$

Substituting these into Equation [2.1.6.1] gives

$$\begin{aligned}\frac{d\hat{\rho}(t)}{dt} &= -i\hat{H}|\psi\rangle\langle\psi| + i|\psi\rangle\langle\psi|\hat{H} \\ &= -i(\hat{H}, \hat{\rho}(t))\end{aligned}\quad [2.1.6.4]$$

This is known as the *Liouville von-Neumann* equation. The solution to this equation for a time-independent Hamiltonian is

$$\hat{\rho}(t) = e^{-i\hat{H}t} \hat{\rho}(0) e^{i\hat{H}t} \quad [2.1.6.5]$$

where  $\hat{\rho}(t)$  and  $\hat{\rho}(0)$  are the density operators at time  $t$  and time zero. If the density operator at  $t = 0$  and the Hamiltonian are known, the density operator at  $t = t$  can be calculated.

If during the time-period between 0 and  $t$ , the Hamiltonian remains constant a *propagator*,  $\hat{U}(t)$  can be defined as

$$\hat{U}(t) = e^{-i\hat{H}t} \quad [2.1.6.6]$$

If the Hamiltonian does not remain constant during this time-period, the propagator can be divided into a series of Hamiltonians in chronological order

$$\hat{U}(t) = e^{-i\hat{H}_n t_n} \dots e^{-i\hat{H}_1 t_1} \quad [2.1.6.7]$$

In either case, the Liouville von-Neumann equation can be expressed in terms of these propagators as

$$\hat{\rho}(t) = \hat{U}(t)\hat{\rho}(0)\hat{U}(t)^{-1} \quad [2.1.6.8]$$

Using this equation allows the effect of an NMR pulse sequence to be followed during a specified time period.

## 2.1.7. Hamiltonians and Interactions

Each Hamiltonian can be represented by a general form by a *Cartesian* tensor

$$\hat{H} = \hat{\mathbf{I}} \cdot \tilde{\Lambda} \cdot \hat{\mathbf{S}} = \begin{pmatrix} \hat{I}_x & \hat{I}_y & \hat{I}_z \end{pmatrix} \begin{pmatrix} \Lambda_{xx} & \Lambda_{xy} & \Lambda_{xz} \\ \Lambda_{yx} & \Lambda_{yy} & \Lambda_{yz} \\ \Lambda_{zx} & \Lambda_{zy} & \Lambda_{zz} \end{pmatrix} \begin{pmatrix} \hat{S}_x \\ \hat{S}_y \\ \hat{S}_z \end{pmatrix} \quad [2.1.7.1]$$

where  $\tilde{\Lambda}$  is a second rank tensor,  $\hat{\mathbf{I}}$  is a spin operator and  $\hat{\mathbf{S}}$  can be either another spin operator or an external field.

Expressed in these terms, the Zeeman Hamiltonian which describes the interaction between the spin operator  $\hat{\mathbf{I}}$  and an external magnetic field  $\hat{B}_0$  is

$$\hat{H}_Z = \hat{\mathbf{I}} \cdot \tilde{Z} \cdot \hat{B}_0 \quad [2.1.7.2]$$

where

$$\tilde{Z} = -\gamma \begin{pmatrix} 1 & 0 & 0 \\ 0 & 1 & 0 \\ 0 & 0 & 1 \end{pmatrix} \quad [2.1.7.3]$$

The Zeeman Hamiltonian defines the ‘Laboratory frame’ in which the experiment takes place and that all other interactions are referenced to. The magnetic field and the magnetization of the spins are aligned with the z-axis such that the familiar Zeeman Hamiltonian is

$$\hat{H}_Z = -\gamma B_0 \hat{I}_z = \omega_0 \hat{I}_z \quad [2.1.7.4]$$

Visualization of the other interactions relative to the laboratory frame can be complex and the preferred frame of reference is the *principal axis system* (PAS). For each Hamiltonian, there is a PAS in which the second rank tensor,  $\tilde{\Lambda}$ , only has diagonal non-zero elements

$$\tilde{\Lambda}^{PAS} = \begin{pmatrix} \Lambda_{xx} & 0 & 0 \\ 0 & \Lambda_{yy} & 0 \\ 0 & 0 & \Lambda_{zz} \end{pmatrix} \quad [2.1.7.5]$$

However, this PAS does not coincide with the laboratory frame and must undergo frame rotation to bring them into coincidence. To define this transformation in three-dimensions, three angles must be used. These are known as *Euler angles* and are expressed as  $\alpha$ ,  $\beta$  and  $\gamma$ .

Transformation from the PAS frame to the laboratory frame is achieved by three successive rotations of the Euler angles about the original PAS axes. Assigning the PAS axes to be  $X,Y,Z$  and the laboratory frame axes to be  $x,y,z$  the transformation is performed by an initial rotation of  $X,Y,Z$  by  $\gamma$  about  $Z$ ; followed by a rotation by  $\beta$  about  $Y$ ; and finally a rotation by  $\alpha$  about  $Z$  bringing it to the laboratory frame  $x,y,z$ .

The expression of this complete rotation is

$$\hat{R}(\alpha, \beta, \gamma) = \hat{R}_Z(\gamma)\hat{R}_Y(\beta)\hat{R}_Z(\alpha) \quad [2.1.7.6]$$

where  $\hat{R}_Z(\gamma)$  is a rotation of angle  $\gamma$  about the  $Z$ -axis and is defined as

$$\hat{R}_Z(\gamma) = e^{-i\gamma I_z} \quad [2.1.7.7]$$

The Euler angles  $\alpha$  and  $\beta$  are of particular interest as they define the polar angles  $\theta$  and  $\phi$  of the  $z$ -axis in the PAS of chemical shielding anisotropy, which will be covered in Section 2.1.8.1.

### 2.1.7.1. Radiofrequency Interaction

The other external, user controlled, component of an NMR experiment is the radiofrequency (RF) pulse which generates the transverse magnetization. The transverse magnetization is generated because the RF pulse creates a secondary, oscillating magnetic field,  $B_1$ , perpendicular to  $B_0$ . If the oscillation frequency

of this RF field,  $\omega_{RF}$ , is close to  $\omega_0$  magnetic resonance occurs. An oscillating magnetic field aligned along the  $x$ -axis is described as

$$\begin{aligned}\mathbf{B}_1(t) &= 2B_1(\cos(\omega_{rf}t + \phi))\mathbf{i} \\ &= B_1(e^{i\omega_{RF}t} + e^{-i\omega_{RF}t})\mathbf{i} \quad \text{if } \phi = 0\end{aligned}\quad [2.1.7.8]$$

where  $+\omega_{RF}$  and  $-\omega_{RF}$  are the frequencies of two counter rotating magnetic fields. To simplify this, the effects of the RF pulse can be considered in the *rotating frame* which is a coordinate system in which the  $z$ -axis remains aligned with  $B_0$  but the  $xy$ -plane rotates around the  $z$ -axis at a frequency of  $\omega_{RF}$ . In this rotating frame, the  $+\omega_{RF}$  component appears to be static, and the second component becomes  $-2\omega_{RF}$ . This allows for a simplified first-order approximation where the rotating component has no effect, and only the static component interacts with the nuclear spins.

The Hamiltonian for an RF pulse can be considered as another Zeeman interaction applied along a different axis and can be expressed as

$$\begin{aligned}\hat{H}_{RF} &= -\gamma\hat{I}_xB_1 \\ &= \omega_1\hat{I}_x\end{aligned}\quad [2.1.7.9]$$

Using the Liouville von Neumann equation to follow the effect of this RF pulse with a duration,  $t$ , starts with the expression

$$\hat{\rho}(t) = e^{-i\omega_1\hat{I}_xt}\hat{\rho}(0)e^{i\omega_1\hat{I}_xt}\quad [2.1.7.10]$$

Assuming that the system starts at thermal equilibrium,  $\hat{\rho}(0) = \hat{I}_z$ , the resulting density matrix is

$$\boldsymbol{\rho}(t) = \frac{1}{2}\begin{pmatrix} \cos(\omega_1t) & i\sin(\omega_1t) \\ -i\sin(\omega_1t) & -\cos(\omega_1t) \end{pmatrix}\quad [2.1.7.11]$$

The expectation values for the spin angular momentum operators can then be calculated using Equation [2.1.5.7]

$$\langle I_x \rangle = Tr\{\boldsymbol{\rho}I_x\} = 0\quad [2.1.7.12]$$

$$\langle I_y \rangle = Tr\{\boldsymbol{\rho}I_y\} = -\frac{1}{2}\sin(\omega_1t)\quad [2.1.7.13]$$

$$\langle I_z \rangle = Tr\{\boldsymbol{\rho}I_z\} = \frac{1}{2}\cos(\omega_1t)\quad [2.1.7.14]$$

If the nutation frequency of the applied pulse is specified by a *flip angle*,  $\beta$ , where

$$\beta = \omega_1 t = \frac{\pi}{2} \quad [2.1.7.15]$$

it becomes clear that this will result in the population term becoming zero, and the coherence term is non-zero. This shows that the RF pulse along the  $x$ -axis has rotated the bulk magnetization away from the  $z$ -axis and the magnetization now resides in the  $xy$ -plane.

## 2.1.8. Internal Interactions

$$\hat{H}_{int} = \hat{H}_{CS} + \hat{H}_{DD} + \hat{H}_J + \hat{H}_Q \quad [2.1.8.1]$$

The internal spin interactions which are of interest and will be discussed here are the *chemical shielding* (CS), *dipolar coupling* (DD), and *scalar coupling* (J) interactions. The quadrupolar interaction only becomes relevant for nuclei with  $I > \frac{1}{2}$  and so will not be discussed further here as it has no relevance to the experimental work presented.

In modern NMR experiments, the magnetic fields used are large and so the Zeeman interaction will be significantly larger than the internal interactions. This allows the internal Hamiltonians to be simplified using the *secular approximation*. The simplified Hamiltonians become a first-order perturbation of the Zeeman Hamiltonian and only terms which commute with the Zeeman Hamiltonian are retained.

### 2.1.8.1. Chemical Shielding Hamiltonian

Chemical shifts and chemical shielding are the corner stones of NMR spectroscopy applications. The chemical shielding interaction is a result of the external magnetic field inducing currents within the sample. The local magnetic field of any given nuclear spin is a combination of the external magnetic field,  $B_0$ , and the magnetic field induced by the local electronic environment,  $B_{ind}$

$$B_{loc} = B_0 + B_{ind} \quad [2.1.8.2]$$

This local magnetic field '*shields*' the nucleus from  $B_0$  and is highly dependent on the electronic structure of a nucleus and its surroundings.

The induced magnetic field is defined as

$$B_{ind} = -\tilde{\sigma}B_0 \quad [2.1.8.3]$$

where  $\sigma$  is the *chemical shielding tensor*, a second-order tensor which describes the variation of this field. As the distribution of electrons around a nucleus is not necessarily spherical the shielding will be anisotropic.  $\sigma$  is expressed as

$$\tilde{\sigma} = \begin{pmatrix} \sigma_{xx} & \sigma_{xy} & \sigma_{xz} \\ \sigma_{yx} & \sigma_{yy} & \sigma_{yz} \\ \sigma_{zx} & \sigma_{zy} & \sigma_{zz} \end{pmatrix} \quad [2.1.8.4]$$

This results in an expression for  $B_{ind}$  where,

$$\begin{pmatrix} B_{ind,x} \\ B_{ind,y} \\ B_{ind,z} \end{pmatrix} = - \begin{pmatrix} \sigma_{xx} & \sigma_{xy} & \sigma_{xz} \\ \sigma_{yx} & \sigma_{yy} & \sigma_{yz} \\ \sigma_{zx} & \sigma_{zy} & \sigma_{zz} \end{pmatrix} \begin{pmatrix} 0 \\ 0 \\ B_0 \end{pmatrix}$$

$$B_{ind} = -(\sigma_{xz}B_0 + \sigma_{yz}B_0 + \sigma_{zz}B_0) \quad [2.1.8.5]$$

assuming that  $B_0$  is along the z-axis of the laboratory frame. In this expression,  $\sigma_{yz}B_0$  describes the induced field created in the y direction. Thanks to the secular approximation, all components which are not parallel to the external field can be disregarded and so  $B_{ind}$  is simplified to

$$B_{ind} = -\sigma_{zz}B_0 \quad [2.1.8.6]$$

The chemical shielding Hamiltonian is then defined as

$$\hat{H}_{CS} = \gamma \hat{I}_z \sigma_{zz} B_0 \quad [2.1.8.7]$$

The shielding tensor element,  $\sigma_{zz}$ , is expressed within the laboratory frame as

$$\sigma_{zz} = \frac{1}{3} \left\{ \sum_{j=x,y,z} \sigma_j + \sum_{j=x,y,z} (3 \cos^2 \theta_j - 1) \sigma_j \right\} \quad [2.1.8.8]$$

where  $\sigma_j$  describes the diagonal components of the shielding tensor in the principal axis system and  $\theta_j$  is the angle between the shielding principal axis  $j$  and  $B_0$  (the z-axis in the laboratory frame).

The PAS for the chemical shielding tensor is

$$\tilde{\sigma}^{PAS} = \begin{pmatrix} \sigma_{XX}^{PAS} & 0 & 0 \\ 0 & \sigma_{YY}^{PAS} & 0 \\ 0 & 0 & \sigma_{ZZ}^{PAS} \end{pmatrix} \quad [2.1.8.9]$$

The diagonal elements of this PAS can be expressed in terms of three important parameters: the isotropic chemical shielding,  $\sigma_{iso}$ , the chemical shielding anisotropy (CSA),  $\zeta$ , and asymmetry,  $\eta$ . These parameters are defined as

$$\sigma_{iso} = \frac{1}{3}(\sigma_{XX}^{PAS} + \sigma_{YY}^{PAS} + \sigma_{ZZ}^{PAS}) \quad [2.1.8.10]$$

$$\zeta = \sigma_{ZZ}^{PAS} - \sigma_{iso} \quad [2.1.8.11]$$

$$\eta = \frac{\sigma_{XX}^{PAS} - \sigma_{YY}^{PAS}}{\zeta} \quad [2.1.8.12]$$

using the Häberlen-Mehring-Speiss convention. It is often more useful to consider these parameters in the laboratory frame which requires that the PAS is rotated using the rotation matrix presented in Section 2.1.7. By expressing the orientation of the PAS with respect to the laboratory frame using the polar coordinates,  $\theta$  and  $\phi$ , the expression for  $\sigma_{zz}$  becomes

$$\sigma_{zz} = \sigma_{iso} + \frac{\zeta}{2}(3 \cos^2 \theta - 1 + \eta \sin^2 \theta \cos 2\phi) \quad [2.1.8.13]$$

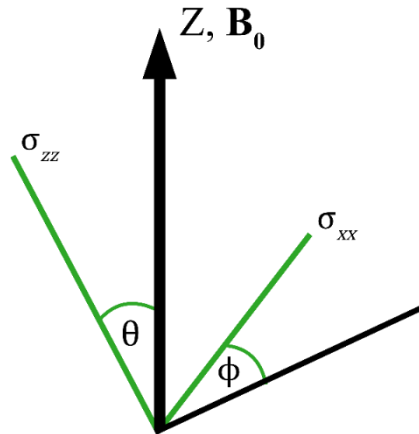


Figure 2.1: Principal axis system in polar coordinates.

It is more common in experiments to describe the effects of chemical shielding in terms of a *chemical shift*,  $\delta$ , which is a measurement of deshielding. It is more convenient to refer to the isotropic chemical shift,  $\delta_{iso}$ , experimentally as it describes the frequency of precession under the induced magnetic field, with respect to a reference sample. This results in a measured value that is field independent and therefore is ideal for comparison across many types of NMR experiment. The chemical shift is related to chemical shielding by

$$\delta_{iso} = \frac{\nu - \nu_{ref}}{\nu_{ref}} \times 10^6 = \frac{\sigma_{ref} - \sigma}{1 - \sigma_{ref}} \times 10^6 \quad [2.1.8.14]$$

where  $\nu$  is the precession frequency of the sample and  $\nu_{ref}$  is the precession frequency of a reference sample. The chemical shift is conventionally quoted in *parts per million (ppm)* as the perturbation of the Larmor frequency due to chemical shielding is very small.

### 2.1.8.2. Dipolar Coupling Hamiltonian

Dipolar coupling is the effect of a through-space interaction between the magnetic moments of two nuclei. Dipolar coupling can occur between two of the same nuclei (*homonuclear*) or between two different nuclei (*heteronuclear*). This interaction is dependent on the internuclear distance and the orientation of the internuclear vector relative to  $B_0$ .



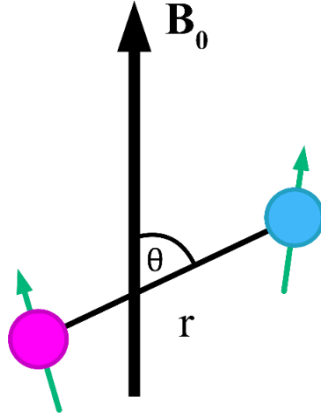


Figure 2.2: Dipolar interaction between two spins which are separated by the distance  $r$  and the internuclear vector is positioned at angle  $\theta$  to the external magnetic field  $B_0$ .

The dipolar coupling Hamiltonian for two coupled spins,  $\hat{I}$  and  $\hat{S}$ , is

$$\hat{H}_{DD} = \sum \hat{I} \tilde{D}_{IS} \hat{S} \quad [2.1.8.15]$$

where  $\tilde{D}$  is the traceless and axially symmetric dipolar coupling tensor which describes how the magnetic field which spin  $I$  experiences due to the field of spin  $S$ , varies depending on the orientation of the  $I$ - $S$  internuclear vector. In the PAS,  $\tilde{D}_{IS}$  is expressed as

$$\tilde{D}_{IS}^{PAS} = \begin{pmatrix} -\frac{d_{IS}}{2} & 0 & 0 \\ 0 & -\frac{d_{IS}}{2} & 0 \\ 0 & 0 & d_{IS} \end{pmatrix} \quad [2.1.8.16]$$

The *dipolar coupling constant*,  $d_{IS}$ , is defined as

$$d_{IS} = \frac{\mu_0 \gamma_I \gamma_S}{4\pi r^3} \quad [2.1.8.17]$$

where  $\mu_0$  is the permeability constant and  $r$  is the internuclear distance.

It is possible and simpler to consider this interaction in classical terms, where the energy of interaction between two magnetic dipoles  $\mu_I$  and  $\mu_S$  is defined as

$$E = \frac{\mu_0}{4\pi} \left( \frac{\boldsymbol{\mu}_I \cdot \boldsymbol{\mu}_S}{r^3} - 3 \frac{(\boldsymbol{\mu}_I \cdot \mathbf{r})(\boldsymbol{\mu}_S \cdot \mathbf{r})}{r^5} \right) \quad [2.1.8.18]$$

Where  $\mu_0$  is the permeability constant,  $\mathbf{r}$  is the *I-S* internuclear vector and  $r$  is the internuclear distance.

The Hamiltonian is then defined by using the definition of  $\boldsymbol{\mu}$  given in Equation [2.1.2.4]

$$\hat{H}_{DD} = \frac{\mu_0 \gamma_I \gamma_S}{4\pi r^3} \left( \hat{\mathbf{I}} \cdot \hat{\mathbf{S}} - 3 \frac{(\hat{\mathbf{I}} \cdot \mathbf{r})(\hat{\mathbf{S}} \cdot \mathbf{r})}{r^2} \right) \quad [2.1.8.19]$$

Using polar coordinates to represent the vector  $\mathbf{r}$

$$\mathbf{r} = (r_x, r_y, r_z) = (r \sin\theta \cos\phi, r \sin\theta \sin\phi, r \cos\theta) \quad [2.1.8.20]$$

The Hamiltonian can be rewritten as

$$\begin{aligned} \hat{H}_{DD} = d_{IS} & \left( \hat{I}_x \hat{S}_x + \hat{I}_y \hat{S}_y + \hat{I}_z \hat{S}_z \right. \\ & - 3(\hat{I}_x \sin\theta \cos\phi + \hat{I}_y \sin\theta \sin\phi \\ & + \hat{I}_z \cos\theta)(\hat{S}_x \sin\theta \cos\phi + \hat{S}_y \sin\theta \sin\phi \\ & \left. + \hat{S}_z \cos\theta) \right) \end{aligned} \quad [2.1.8.21]$$

In a strong external magnetic field, the secular approximation means that this can be simplified considerably to

$$\hat{H}_{DD}^{HOM} = \frac{d_{IS}}{2} (1 - 3 \cos^2 \theta) (3 \hat{I}_z \hat{S}_z - \hat{\mathbf{I}} \cdot \hat{\mathbf{S}}) \quad [2.1.8.22]$$

where  $\theta$  is the angle between the internuclear vector and  $B_0$ . This result is the secular dipolar coupling Hamiltonian for two *homonuclear* coupled spins.

If the homonuclear dipolar Hamiltonian is expanded slightly using the expression where  $\hat{\mathbf{I}} \cdot \hat{\mathbf{S}} = \hat{I}_x \hat{S}_x + \hat{I}_y \hat{S}_y + \hat{I}_z \hat{S}_z$ ,

$$\hat{H}_{DD}^{HOM} = \frac{d_{IS}}{2} (1 - 3 \cos^2 \theta) \left( 2 \hat{I}_z \hat{S}_z - (\hat{I}_x \hat{S}_x + \hat{I}_y \hat{S}_y) \right) \quad [2.1.8.23]$$

The matrix representations for the spin angular momentum operators in this equation are

$$2\mathbf{I}_z\mathbf{S}_z = \begin{pmatrix} \frac{1}{2} & 0 & 0 & 0 \\ 0 & -\frac{1}{2} & 0 & 0 \\ 0 & 0 & -\frac{1}{2} & 0 \\ 0 & 0 & 0 & \frac{1}{2} \end{pmatrix} \quad \mathbf{I}_x\mathbf{S}_x + \mathbf{I}_y\mathbf{S}_y = \begin{pmatrix} 0 & 0 & 0 & 0 \\ 0 & 0 & \frac{1}{2} & 0 \\ 0 & \frac{1}{2} & 0 & 0 \\ 0 & 0 & 0 & 0 \end{pmatrix} \quad [2.1.8.24]$$

For *heteronuclear* dipolar coupling, only the  $2\mathbf{I}_z\mathbf{S}_z$  term is present, and the Hamiltonian has the form

$$\hat{H}_{DD}^{HET} = \frac{d_{IS}}{2} (1 - 3 \cos^2 \theta) 2\hat{I}_z\hat{S}_z \quad [2.1.8.25]$$

In solid-state NMR, measuring the homonuclear dipolar coupling can provide valuable information about the structure and dynamics of a sample. The presence of the  $\hat{I}_x\hat{S}_x + \hat{I}_y\hat{S}_y$  term in the secular homonuclear dipolar coupling Hamiltonian results in broad spectral lines which cannot be fully removed. In an anisotropic sample – such as a solid - there will be a range of preferred molecular orientations. The *residual dipolar coupling* (RDC) is a measurement of an average of the dipolar coupling of a range of orientations and is expressed as

$$d_{res} = d_{IS} \overline{(1 - 3 \cos^2 \theta)} \quad [2.1.8.26]$$

The degree of order of a sample,  $S$ , can be calculated from the RDC and the dipolar coupling constant defined in Equation [2.1.8.17]

$$S^2 = \left( \frac{d_{res}}{d_{IS}} \right)^2 \quad [2.1.8.27]$$

### 2.1.8.3. Scalar Coupling Hamiltonian

In addition to the ‘through-space’ dipolar interaction, nuclear spins can also interact with each other via their shared electron density, or ‘through-bonds’. This through-bond interaction is known as *scalar*, *indirect*, or *J-coupling*.

This coupling is a result of one nuclear spin polarizing an electron spin, this results in polarization of the other electron spin in the bond (due to the Pauli exclusion principal) and this in turn polarizes the second nuclear spin. This indirect interaction of nuclei along with the chemical shift, is what links NMR

directly to chemistry, as it provides a spectroscopic view of chemical bonds. In the solid state, scalar coupling is rarely observed directly as the linewidths are typically too broad. Nevertheless, scalar coupling can be used in the solid state to transfer polarization which is a valuable technique to improve spectral resolution and to indirectly identify chemical bonds.

The Hamiltonian for the scalar coupling of two spins,  $\hat{\mathbf{I}}$  and  $\hat{\mathbf{S}}$ , takes a similar form to the dipolar Hamiltonian

$$\hat{H}_J = \sum \hat{\mathbf{I}} \tilde{J}_{IS} \hat{\mathbf{S}} \quad [2.1.8.28]$$

Similar to the dipolar interaction, scalar coupling has both isotropic and anisotropic components. However, the *J-anisotropy* is usually disregarded due to its small magnitude in comparison to the dipolar coupling. The isotropic scalar coupling of course has no orientational dependence and it is equal to the average of the trace of the tensor,  $\tilde{J}_{IS}$

$$J_{IS} = \frac{1}{3} (J_{xx} + J_{yy} + J_{zz}) \quad [2.1.8.29]$$

## 2.1.9. Magic Angle Spinning

In solution-state NMR the rapid, internal motion of a sample averages out any anisotropic interactions which results in spectra with high-resolution signals making solution-state NMR an excellent tool for detailed chemical structural elucidation. In the solid state there is no such internal motion of the sample and so the CSA and dipolar couplings give rise to broad, featureless spectra. To average these anisotropic interactions in solids, macroscopic motion is used. In *magic angle spinning* (MAS), the spin system is rotated about an axis at the *magic angle*,  $\theta_m = 54.74^\circ$ , with respect to the magnetic field,  $B_0$ .

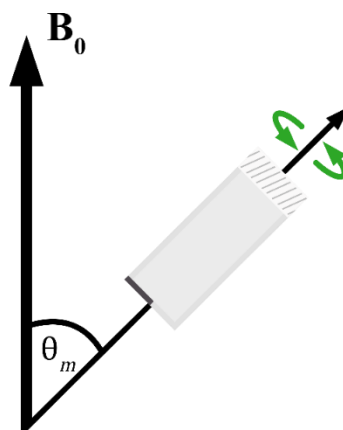


Figure 2.3: Schematic representation of the set-up of a sample in MAS NMR. Green arrows represent the rotation of the sample around an axis which is aligned at an angle  $\theta_m$  to the external magnetic field,  $B_0$ .

All internal NMR interactions have a common dependency on the orientation of the system with respect to the magnetic field which is proportional to  $(3 \cos^2 \theta - 1)$ . If a sample is spun about an axis at the angle  $\theta_m$ , then the angle describing the orientation of the molecule is constantly varied by this motion. The average of  $(3 \cos^2 \theta - 1)$  in this situation is

$$\langle 3 \cos^2 \theta - 1 \rangle = \frac{1}{2} (3 \cos^2 \theta_m - 1) (3 \cos^2 \beta - 1) \quad [2.1.9.1]$$

where  $\beta$  is the angle between the axis of rotation and the principal shielding tensor z-axis which can take all possible values in a powdered sample.  $\theta_m$  on the other hand is a fixed, user defined value meaning that  $(3 \cos^2 \theta_m - 1)$  is a scaling factor for all values of  $\theta$ . When  $\theta_m = 54.74^\circ$ , the scaling factor is zero and so the secular chemical shielding Hamiltonian becomes

$$\hat{H}_{CS}^{MAS} = -\gamma \hat{I}_z B_0 \sigma_{iso} \quad [2.1.9.2]$$

And thus, only the isotropic chemical shift is influential.

MAS is also capable of partially reducing the effect of dipolar, scalar and quadrupolar coupling on a spectrum as these internal spin interactions also have a dependency on the orientation of the molecule in the magnetic field.

## 2.1.10. Spin Diffusion

The exchange of energy between spins during a flip-flop transition is spin diffusion. The rate of spin diffusion,  $W$ , between two identical spins,  $I$  and  $S$  separated by distance  $r_{IS}$  is given by

$$W_{IS} = \frac{1}{8\sqrt{2}} \hbar^2 \gamma^4 T_2 [1 - 3 \cos^2 \theta_{IS}]^2 r_{IS}^{-6} \quad [2.1.10.1]$$

Since the rate of flip-flop transitions diminishes with  $r^{-6}$ , it can be assumed that this exchange of energy only happens with nearest neighbours and so can be represented by a random walk. The spin diffusion is then represented by a differential equation

$$\frac{d\mathbf{M}}{dt} = D \cdot \Delta \mathbf{M} \quad [2.1.10.2]$$

where  $D$  is the *nuclear spin diffusion coefficient* and is defined as

$$D = \sum_{S \neq I} W_{IS} \cdot r_{IS}^2 \quad [2.1.10.3]$$

Spin diffusion is a vital process in many solid-state NMR experiments, and particularly in dynamic nuclear polarization.

## 2.1.11. Relaxation

Relaxation is responsible for the return of the bulk magnetization to equilibrium after perturbation of the system. There are two major relaxation mechanisms: *spin-lattice* (or *longitudinal*) relaxation which has a time constant  $T_1$  and *spin-spin* (or *transverse*) relaxation which has time constant  $T_2$ . Relaxation is driven by fluctuations in the local magnetic field due to molecular motion. For a  $I = \frac{1}{2}$  nucleus, it is primarily the dipolar coupling and the CSA which contribute most to the fluctuating magnetic field.

The simplest way to describe this is by using the phenomenological Bloch equations. If an ensemble of nuclei is placed within an external magnetic field, the magnetization is described by

$$M_z(t) = M_{eq} \left(1 - e^{-t/T_1}\right) \quad [2.1.11.1]$$

$$M_x(t) = M_{eq} \sin(\omega_0 t) \left(e^{-t/T_2}\right) \quad [2.1.11.2]$$

$$M_y(t) = M_{eq} \cos(\omega_0 t) \left(e^{-t/T_2}\right) \quad [2.1.11.3]$$

where  $M_i(t)$  is the bulk magnetization along the  $i$ -axis at time  $t$  and  $M_{eq}$  is the bulk magnetization at equilibrium. The key parameters in these equations are  $T_1$  and  $T_2$ , the spin-lattice and spin-spin relaxation times. It can be seen from the Bloch equations that spin magnetization builds up along the  $z$ -axis exponentially with  $T_1$ . This decay is the result of a return of the magnetization to the equilibrium state. Magnetization in the  $xy$ -plane decays exponentially with  $T_2$ , this relaxation is a result of the dephasing of magnetization as it precesses in the transverse plane at different frequencies.

The local magnetic fields which cause relaxation of the  $z$  magnetization, also affect the  $x$  and  $y$  components and cause transverse relaxation. This contribution to transverse relaxation is the *non-secular* relaxation. The *secular* contribution to transverse relaxation is the relaxation due to inhomogeneity of the  $z$ -component of the local magnetic field. This results in slight differences of the Larmor frequencies of individual spins and causes dephasing of the  $xy$  magnetization.

This description of relaxation is sufficient if the system only contains one nuclear species as  $T_1$  and  $T_2$  here describe the *auto-relaxation* of a nuclear spin. In a multi-nuclear system, there are additional *cross-correlated* and *cross-relaxation* mechanisms which require a more detailed description but allows the NMR relaxation to be coupled to the underlying molecular motion.

### 2.1.11.1. Spectral Density

To understand how molecular motions contribute to relaxation, these random motions must first be defined. The time-dependence of random molecular motion is described by the correlation function,  $G(\tau_c)$ , where  $\tau_c$  is the *correlation time*. The Fourier transform of the correlation function is the *spectral*

density,  $J(\omega)$ . The spectral density describes the amount of motion which occurs at a particular frequency,  $\omega$ .

The most common form of correlation function is a mono-exponential loss of correlation so that  $J$  is a Lorentzian

$$G(\tau_c) = B_{loc}^2 e^{\frac{-t}{\tau_c}} \quad [2.1.11.4]$$

$$J(\omega) = B_{loc}^2 \frac{2\tau_c}{1 + \omega^2\tau_c^2} \quad [2.1.11.5]$$

The reduced correlation function and spectral density can be written to only represent the time dependent parts

$$G(\tau_c) = e^{\frac{-t}{\tau_c}} \quad [2.1.11.6]$$

$$J(\omega) = \frac{2\tau_c}{1 + \omega^2\tau_c^2} \quad [2.1.11.7]$$

The spectral density can be used to describe the factors which influence the rate of relaxation in the equation

$$W_{\alpha\beta} = A_{\alpha\beta} Y^2 J(\omega_{\alpha\beta}) \quad [2.1.11.8]$$

where  $W_{\alpha\beta}$  is the rate constant for transitions between levels  $\alpha$  and  $\beta$ ,  $Y$  is the *size factor* and is a measure of how large the interaction is – to describe a dipolar interaction, this term depends on the gyromagnetic ratios of two nuclei and the distance between them, and  $A_{\alpha\beta}$  is the *spin factor* which acts as a ‘selection filter’, resulting in only allowed transitions having a non-zero value, since it depends on the quantum mechanical detail of the interaction.

### 2.1.11.2. Dipolar Relaxation

The relaxation rate constants for dipolar coupling between two spins  $I$  and  $S$  are

$$\begin{aligned} W_1^I &= \frac{3}{40} b^2 J(\omega_{0,I}) & W_1^S &= \frac{3}{40} b^2 J(\omega_{0,S}) \\ W_2 &= \frac{3}{10} b^2 J(\omega_{0,I} + \omega_{0,S}) & W_0 &= \frac{1}{20} b^2 J(\omega_{0,I} - \omega_{0,S}) \end{aligned} \quad [2.1.11.9]$$



where  $b = \frac{\mu_0 \gamma_I \gamma_S}{4\pi r^3}$  is the size factor and  $W_1$ ,  $W_2$ , and  $W_0$  are the relaxation rate constants for the single, double, and zero-quantum transitions, respectively as seen in Figure 2.4.

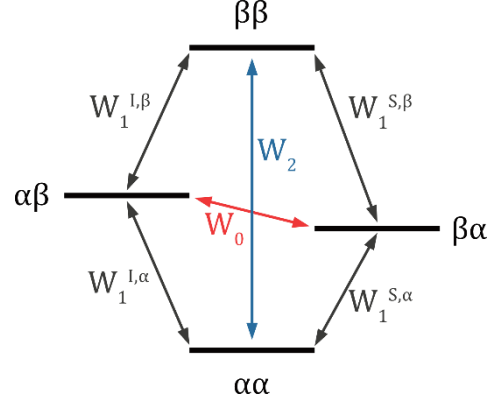


Figure 2.4: Energy level diagram for possible relaxation induced transitions for a two-spin system. Single-quantum transitions are labelled as  $W_1$ , the double-quantum transition is labelled as  $W_2$  and the zero-quantum transition is labelled as  $W_0$ .

The relaxation rate constants associated with spin-lattice relaxation due to dipolar coupling can be written in terms of these relaxation rates

$$\begin{aligned} R_1^I &= W_1^{I,\alpha} + W_1^{I,\beta} + W_2 + W_0 \\ &= b^2 \left[ \frac{3}{20} J(\omega_{0,I}) + \frac{3}{10} J(\omega_{0,I} + \omega_{0,S}) + \frac{1}{20} J(\omega_{0,I} - \omega_{0,S}) \right] \end{aligned} \quad [2.1.11.10]$$

$$\begin{aligned} R_1^S &= W_1^{S,\alpha} + W_1^{S,\beta} + W_2 + W_0 \\ &= b^2 \left[ \frac{3}{20} J(\omega_{0,S}) + \frac{3}{10} J(\omega_{0,I} + \omega_{0,S}) + \frac{1}{20} J(\omega_{0,I} - \omega_{0,S}) \right] \end{aligned} \quad [2.1.11.11]$$

$$\begin{aligned} R_1^{IS} &= W_1^{I,\alpha} + W_1^{I,\beta} + W_1^{S,\alpha} + W_1^{S,\beta} \\ &= b^2 \left[ \frac{3}{20} J(\omega_{0,I}) + \frac{3}{20} J(\omega_{0,S}) \right] \end{aligned} \quad [2.1.11.12]$$

$$\begin{aligned} \Delta^I &= W_1^{I,\alpha} - W_1^{I,\beta} \\ &= b^2 \left[ \frac{3}{40} J(\omega_{0,I\alpha}) - \frac{3}{40} J(\omega_{0,I\beta}) \right] \end{aligned} \quad [2.1.11.13]$$

$$\begin{aligned}
\Delta^S &= W_1^{S,\alpha} - W_1^{S,\beta} \\
&= b^2 \left[ \frac{3}{40} J(\omega_{0,S\alpha}) - \frac{3}{40} J(\omega_{0,S\beta}) \right]
\end{aligned}
\tag{2.1.11.14}$$

$$\begin{aligned}
\sigma_{IS} &= W_2 - W_0 \\
&= b^2 \left[ \frac{3}{10} J(\omega_{0,I} + \omega_{0,S}) - \frac{1}{20} J(\omega_{0,I} - \omega_{0,S}) \right]
\end{aligned}
\tag{2.1.11.15}$$

where  $R_1^I$  and  $R_1^S$  are the self-relaxation rate constants for longitudinal relaxation.  $R_1^{IS}$  is the longitudinal auto-relaxation constant.  $\Delta^I$  and  $\Delta^S$  are the relaxation constants which describe *cross-correlation* which occurs when the rate constants for the allowed transitions of a spin are not the same.  $\sigma_{IS}$  is the relaxation constant which describes *cross-relaxation* which is the rate at which magnetization is transferred from spin  $S$  to  $I$ . This transfer of magnetization occurs when  $S$  is perturbed.

Relaxation time is related to these rate constants as

$$R_1 = \frac{1}{T_1} \tag{2.1.11.16}$$

The relaxation rate constants associated with transverse relaxation mediated by dipolar couplings are

$$\begin{aligned}
R_2^I &= \frac{1}{10} J(0) + 2W_1^S + \frac{W_1^I + W_2 + W_0}{2} \\
&= b^2 \frac{1}{10} J(0)
\end{aligned}
\tag{2.1.11.17}$$

$$R_2^S = \frac{1}{10} J(0) + 2W_1^I + \frac{W_1^S + W_2 + W_0}{2} \tag{2.1.11.18}$$

These relaxation constants differ to the  $T_1$  constants in that they have a component which represents the relaxation of the *other* spin. This dependence describes the effect that one spin has on the other. If  $I$  is in the  $\alpha$  spin state, spin  $S$ , will experience a different local magnetic field than if  $I$  was in the  $\beta$  spin state.

### 2.1.11.3. CSA Relaxation

The origin of relaxation due to chemical shift anisotropy is a result of the local magnetic field being varied because the magnetic moments are in different orientations in the magnetic field.

The relaxation constants associated with CSA are

$$R_1 = c^2 \left[ \frac{1}{15} J(\omega_0) \right] \quad [2.1.11.19]$$

$$R_2 = c^2 \left[ \frac{2}{45} J(0) + \frac{1}{30J(\omega_0)} \right] \quad [2.1.11.20]$$

where  $c = \gamma B_0 \zeta$ , is the CSA size factor.

### 2.1.11.4. Measuring $T_1$ relaxation

Determining the relaxation processes taking place in a system is key to taking experimental measures of the sample.

A saturation recovery experiment (Figure 2.5a) is used to measure longitudinal  $T_1$  relaxation. This experiment begins with a series of RF pulses which generate a randomly distributed ensemble of spin polarization. After a time  $\tau$ , where the spins experience relaxation to the equilibrium state, a  $\frac{\pi}{2}$  RF pulse is applied, and a signal is detected. This set of pulses is repeated multiple times while varying the time  $\tau$ , and as  $\tau$  is increased, the intensity of the signal measured increases until it reaches a maximum. Once the signal reaches a maximum, the  $T_1$  relaxation can be measured as the signal intensity depends upon the amount of magnetization that has relaxed to equilibrium during time  $\tau$ . Longitudinal relaxation is calculated by fitting the signal intensities to the equation

$$I(\tau) = I_0 \left( 1 - e^{-\frac{\tau}{T_1}} \right) \quad [2.1.11.21]$$

where  $I_0$  is the equilibrium magnetization.

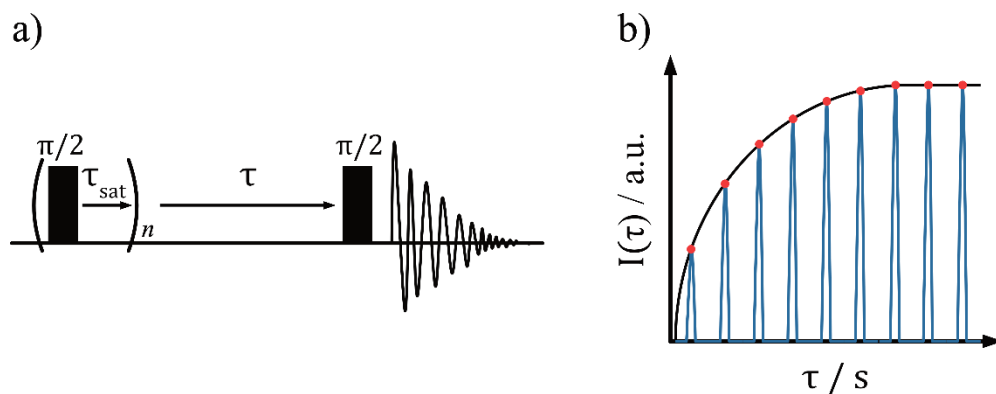


Figure 2.5: a) Pulse sequence used for  $T_1$  saturation recovery experiments. b) Representation of the relative signal intensity as the delay  $\tau$  increases for the saturation recovery experiment.

## 2.2. Dynamic Nuclear Polarization

*Dynamic nuclear polarization* (DNP) enhanced solid-state NMR is a powerful tool for boosting the sensitivity of an NMR experiment by increasing the available bulk magnetization of a sample. DNP makes use of the significantly larger  $\Delta E$  experienced by electrons in a magnetic field, thus consequently the large polarization of electron spins. This electron spin polarization is transferred to a nucleus, improving the sensitivity. A DNP experiment is generally performed at low temperatures of  $\sim 100\text{ K}$ .

Although the theory of DNP has been known since the 1950s,<sup>12-14</sup> it is due to recent technical advancements, such as the introduction of the high-frequency *gyrotron* as a microwave source in the early 1990s,<sup>15</sup> that DNP has become a feasible high field solid-state NMR enhancement technique. The large signal enhancements achieved by DNP have opened many doors for the application of solid-state NMR to materials that were previously unrealistic due to the insensitivity of NMR.

The process of DNP involves using a gyrotron as a continuous-wave microwave source, to irradiate a sample and saturate the energy transition of an electron in a radical implanted into the sample and facilitate the transition of polarization to a nucleus. Typically, this will be a transfer from  $e \rightarrow {}^1\text{H}$ , the proton polarization will then dissipate throughout the sample *via* spin diffusion and can be

transferred to another nucleus of interest such as  $^{13}\text{C}$  by NMR techniques such as cross polarization.

## 2.2.1. Electron Paramagnetic Resonance

*Electron paramagnetic resonance* (EPR) is to electrons, as NMR is to nuclei.

The magnetic dipole moment for an electron is

$$\begin{aligned}\mu_S &= -g_e\mu_B\mathbf{S} \\ &= -\gamma_e\mathbf{S}\end{aligned}\quad [2.2.1.1]$$

where  $\mathbf{S}$  is the spin angular momentum,  $g_e$  is the  $g$ -factor for a free electron,  $\gamma_e = g_e\mu_B$  is the gyromagnetic ratio of a free electron, and  $\mu_B$  is the Bohr magneton ( $\mu_B = 9.274 \cdot 10^{-24}\text{JT}^{-1}$ ).

When unpaired electrons are subjected to an external magnetic field, the Zeeman energy of the electronic spin states is

$$\begin{aligned}E &= \pm\gamma_e m_S B_0 \\ &= \pm\mu_S B_0\end{aligned}\quad [2.2.1.2]$$

where  $m_S$  is the magnetic quantum number of spin  $S$ .

The electron gyromagnetic ratio,  $\gamma_e$ , is almost one thousand times larger than the  $^1\text{H}$  nuclear gyromagnetic ratio, this means that the transition energy between electronic Zeeman levels lies in the microwave region of the electromagnetic spectrum, rather than the radio frequency region.

There are two methods of performing an EPR experiment: *continuous-wave* (CW) EPR and *pulse* EPR.

In a pulse EPR experiment a sample is placed inside a constant external magnetic field and pulses are applied to the system to generate transverse magnetization. This is followed by relaxation and the resulting FID is recorded. The pulses in this EPR method are high-power microwave pulses which can be varied in length to excite different bandwidths.

In a CW EPR experiment the sample is placed inside a constant microwave irradiation field and the external magnetic field is swept until the resonance condition is met.

The total energy of an electron spin system is described by a Hamiltonian made up of the following interactions

$$\hat{H} = \hat{H}_{EZ} + \hat{H}_{NZ} + \hat{H}_{HFI} + \hat{H}_{NQI} + \hat{H}_{ZFS} + \hat{H}_{EE} \quad [2.2.1.3]$$

where  $\hat{H}_{EZ}$  and  $\hat{H}_{NZ}$  are the electron and nuclear Zeeman Hamiltonians.  $\hat{H}_{HFI}$  is the *hyperfine interaction* Hamiltonian which describes the interaction between an electron and a nucleus.  $\hat{H}_{NQI}$  is the *nuclear quadrupole* Hamiltonian which originates from the interaction between the electric quadrupolar moment of a nucleus with  $I > \frac{1}{2}$  and the electric field gradient.  $\hat{H}_{ZFS}$  is the *zero-field splitting* term which describes dipole-dipole interactions between electrons.  $\hat{H}_{EE}$  is the *electronic exchange* Hamiltonian which describe the weak inter-electronic interactions.

When considering the phenomenon of EPR in the context of DNP, the hyperfine interaction is of particular interest. It is this interaction which facilitates the transfer of electron polarization to a nucleus that it is hyperfine coupled to.

The hyperfine interaction Hamiltonian has the form

$$\hat{H}_{HFI} = \hat{\mathbf{S}} \cdot \tilde{\mathbf{A}} \cdot \hat{\mathbf{I}} \quad [2.2.1.4]$$

where  $\hat{\mathbf{S}}$  is the electron spin operator,  $\hat{\mathbf{I}}$  is the nuclear spin operator and  $\tilde{\mathbf{A}}$  is the hyperfine coupling tensor which is determined by an EPR experiment. The result of hyperfine coupling is to perturb the energies of the electron and nuclear Zeeman states, this happens because the orientation of the nuclear magnetic moment relative to the electron magnetic moment can either increase or decrease the local magnetic field experienced by the electron.

## 2.2.2. DNP Mechanisms

There are four primary mechanisms for DNP enhancement: the *Overhauser Effect* (OE),<sup>12</sup> the *Solid Effect* (SE),<sup>16-18</sup> the *Cross Effect* (CE),<sup>19-21</sup> and *Thermal Mixing* (TM).<sup>22</sup>

The major mechanism used in solid-state DNP NMR of organic materials at high fields is the cross effect<sup>23</sup> and the experimental conditions and electron sources used in the experimental work presented here have been chosen to facilitate the CE. The aim to transfer polarization *via* the CE however, does not necessarily prevent the transfer happening *via* another mechanism. The Overhauser effect is conventionally thought of as only important in systems with mobile electrons such as liquids or conducting solids, however it is now known that the OE can be present in insulating solids in combination with other mechanisms.<sup>24,25</sup>

### 2.2.2.1. The Solid Effect and Thermal Mixing

The solid effect occurs in a two-spin system,  $|m_S m_I\rangle$ , where  $m_S$  is the electron spin and  $m_I$  is the nuclear spin. Due to the mixing caused by the hyperfine coupling of the nuclear and electron spins, it is possible to irradiate the usually forbidden zero-quantum (ZQ) and double-quantum (DQ) transitions (Figure 2.6).

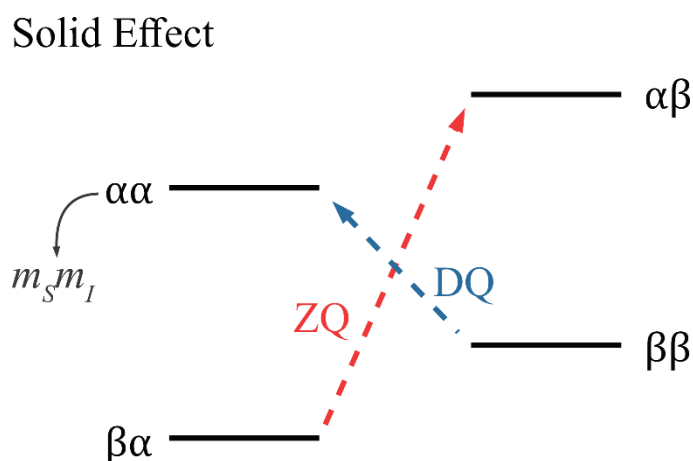


Figure 2.6: Energy level diagram for the solid effect DNP mechanism. The dashed lines indicate the transitions driven by microwave irradiation.

This mechanism is observed when the polarizing agent has a narrow homogenous EPR linewidth,  $\delta$ , and inhomogeneous spectral breadth,  $\Delta$ , such that

$$\delta, \Delta \ll \omega_{0I} \quad [2.2.2.1]$$

This is necessary to ensure that only the correct transition is excited. For the SE the polarizing agents used are usually mono-radicals with high molecular symmetry such as trityl derivatives.

Thermal mixing also uses mono-radicals as polarizing agents however, the process occurs when there is a high concentration of free electrons and the EPR linewidth is broad so that

$$\delta \gg \omega_{0I} \quad [2.2.2.2]$$

The polarization transfer in TM is a multi-electron process, where the polarization is transferred from an ensemble of electron spins to the nuclear spin ( $|m_S m_I\rangle$ ). The TM process is not efficient at high magnetic fields and the high radical concentrations required results in bleaching of the NMR signal.

#### 2.2.2.2. The Overhauser Effect

The Overhauser effect is a two-spin process of polarization transfer from an electron to a nuclear spin ( $|m_S m_I\rangle$ ) which is achieved through cross-relaxation. The OE proceeds by electron polarization being generated by the saturation of electron spin transitions by applied microwave irradiation, followed by cross-relaxation *via* the ZQ and DQ transitions (Figure 2.7). Enhancement of the nuclear polarization happens if the rates of ZQ and DQ relaxation are different.

This electron-nuclear Overhauser effect is similar to the nuclear Overhauser effect observed in solution where molecular motions drive cross-relaxation in dipolar-coupled spin systems. The cross-relaxation in the electron-nuclear Overhauser Effect is mediated by fluctuations in the hyperfine interaction. In metals this can be due to the motion of conduction electrons and in liquids this can be caused by molecular motion. In insulating solids, the exact reason for this cross-relaxation is still under investigation.



## Overhauser Effect

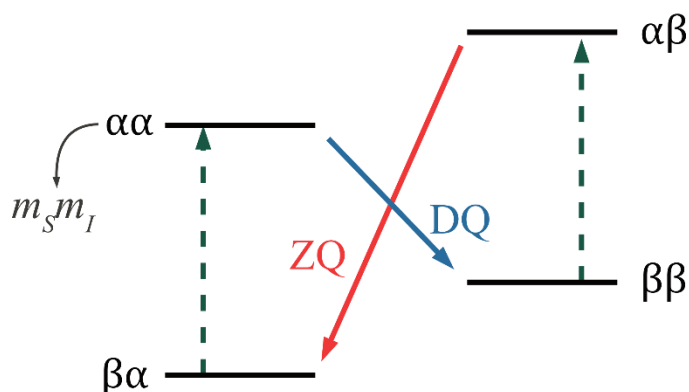


Figure 2.7: Energy level diagram for the Overhauser effect DNP mechanism. Dashed lines indicate transitions induced by applied microwave irradiation. Solid lines indicate spontaneous cross-relaxation transitions caused by rotational and translational modulation of the electron-nucleus hyperfine coupling.

### 2.2.2.3. The Cross Effect

The cross effect is a three-spin process involving two coupled electrons and one hyperfine coupled nuclear spin ( $|m_{S1}m_{S2}m_I\rangle$ ). The mechanism for polarization transfer involves a three-spin flip-flop-flip transition such as  $|\beta\alpha\alpha\rangle \leftrightarrow |\alpha\beta\beta\rangle$  or  $|\alpha\beta\alpha\rangle \leftrightarrow |\beta\alpha\beta\rangle$  (Figure 2.8). Under static conditions, the CE polarization transfer proceeds if the difference of the two electron Larmor frequencies is equal to the nuclear Larmor frequency.

$$\omega_{0S1} - \omega_{0S2} \sim \pm\omega_{0I} \quad [2.2.2.3]$$

This condition ensures that either the  $|\alpha\beta\alpha\rangle$  and the  $|\beta\alpha\beta\rangle$  or the  $|\beta\alpha\alpha\rangle$  and the  $|\alpha\beta\beta\rangle$  energy levels are degenerate. The microwave irradiation is set at a frequency that saturates the transition for just one of the electrons in the system, this results in a population difference between the two electron spins. If the condition in Equation [2.2.2.3] is met, this population difference is transferred to the nuclear spin *via* the hyperfine interaction.

It is essential for the CE to take place, that the inhomogeneous spectral breadth of the polarizing agent is larger, and the homogeneous linewidth is smaller, than the nuclear Larmor frequency so that

$$\delta < \omega_{0I} < \Delta \quad [2.2.2.4]$$

This ensures that one electron transition can be saturated selectively. To achieve these requirements for the polarizing agent, it is most efficient to use bi-radicals with defined inter-electron distances as this ensures there is strong electron dipolar coupling.

Under MAS conditions, the process of CE polarization transfer is more complex, but it does offer increased efficiency. Since the electronic energy has a dependence on orientation, as the sample rotates the energies of the three-spin states will change over the course of a rotor period and can lead to them crossing. However due to the coupling of the spin system and the microwave irradiation, these crossings are avoided and as a result the CE is increased.<sup>26</sup>

There are three points when these avoided crossings are important for the CE process:

- 1 When the microwave frequency matches the Larmor frequency of one of the electrons ( $\omega_{MW} \sim \omega_{0S1,2}$ )
- 2 When the CE matching condition is met ( $\omega_{0S1} - \omega_{0S2} \sim \pm\omega_{0I}$ )
- 3 When the Larmor frequencies of the two electrons match ( $\omega_{0S1} \sim \omega_{0S2}$ )

At some point in the rotor period condition **1** will be met inducing a non-equilibrium spin population. At another point in the rotor period condition **2** will be met and the flip-flop-flip transition will build nuclear polarization. The point at which condition **3** is met is particularly important because this allows an electron flip-flop event which leads to exchange of polarization between the two electron spins. The e-e flip-flop event ensures that the non-equilibrium spin population remains, and the other two events result in an accumulation of net nuclear polarization.

The separation of the microwave and CE matching conditions by MAS means that nuclear polarization can accumulate over many rotor periods during the typical timeframe of nuclear spin-lattice relaxation.

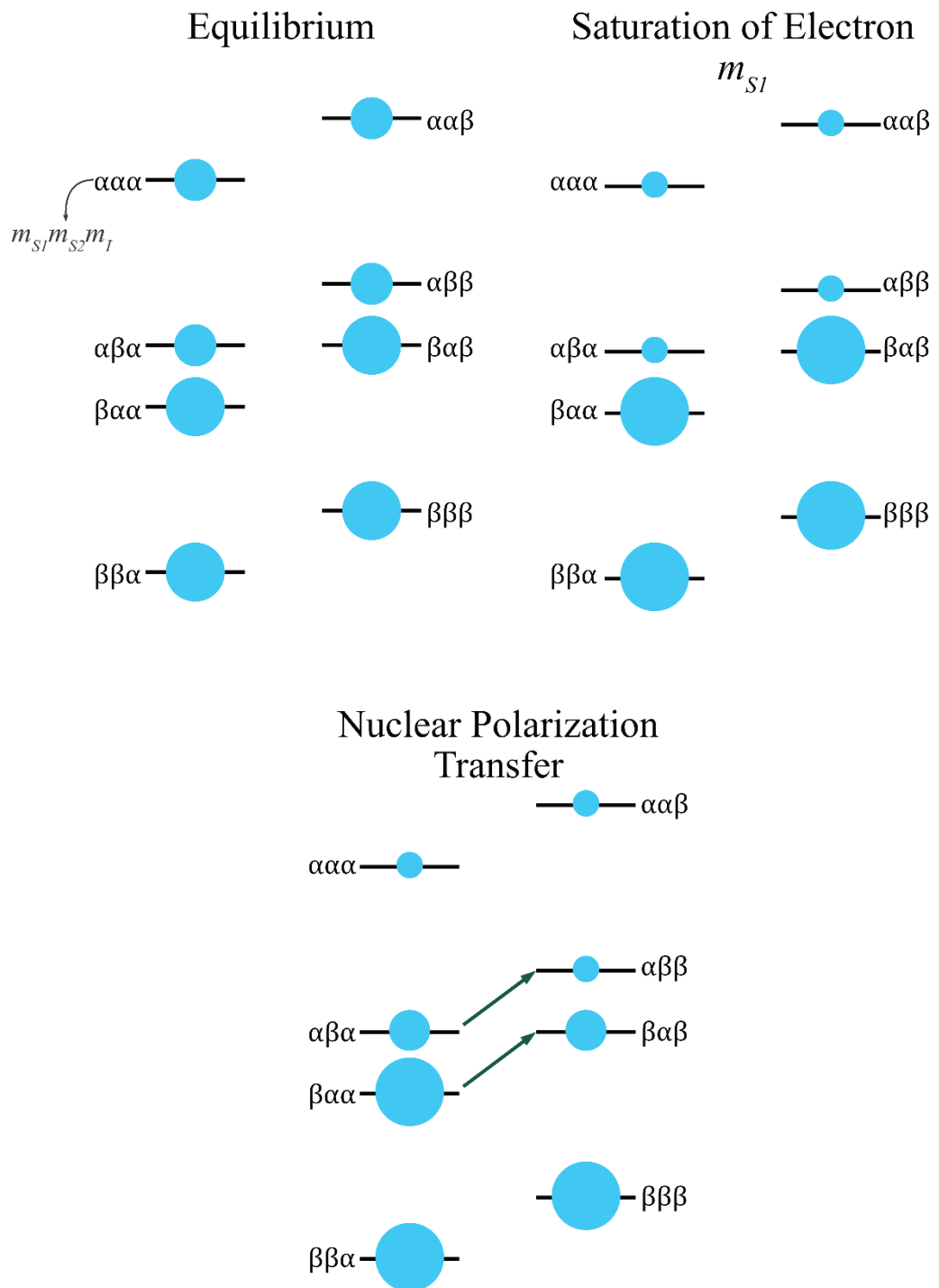
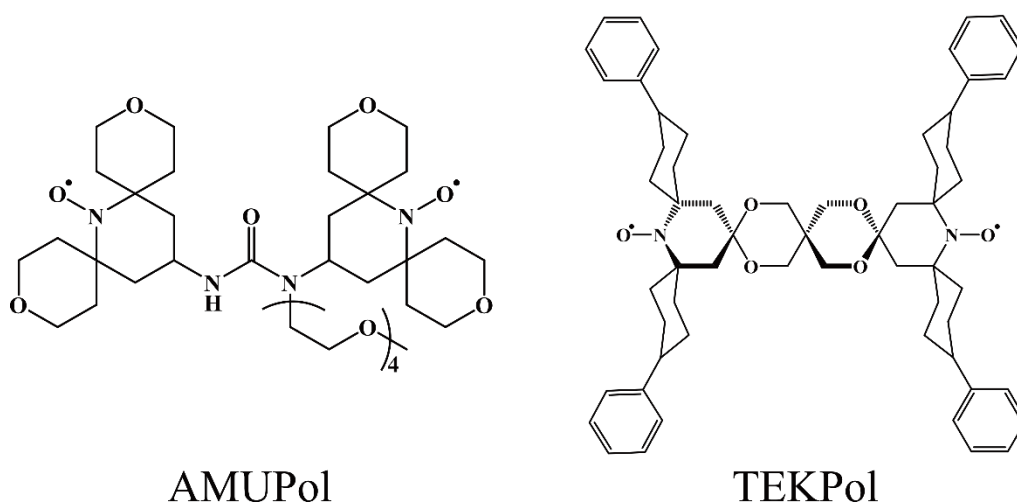


Figure 2.8: Energy level diagrams for three stages of the cross effect DNP mechanism. At equilibrium, the difference of the two electron Larmor frequencies is equal to the nuclear Larmor frequency. Saturation of the transition of one electron results in a population difference between the two electron spins. As the energy of  $|\alpha\beta\alpha\rangle$  and  $|\beta\alpha\beta\rangle$  are equal, magnetization flows across them under the influence of the hyperfine interaction, equalizing their populations. This results in a population difference across the nuclear spin energy levels,  $|\alpha\beta\alpha\rangle$  &  $|\alpha\beta\beta\rangle$  and  $|\beta\alpha\alpha\rangle$  &  $|\beta\alpha\beta\rangle$ . Saturation of  $m_{S_2}$  will result in the same difference of population but in the opposite direction.

### 2.2.3. DNP Radicals

The sources of free electrons used in standard CE DNP experiments are nitroxide bi-radicals which have been specifically designed to facilitate the CE mechanism. As the CE requires two dipolar coupled electrons, the most efficient way to ensure this condition is met is to design a bi-radical with a constant distance between the two electrons.

The most widely used radicals for CE DNP, and the radicals used in the experimental work here, are TEKPOL<sup>27</sup> and AMUPOL.<sup>28</sup> TEKPOL is soluble in organic solvents while AMUPOL is soluble in aqueous solution. Between the two radicals, it is possible to find a radical/solvent system that works for many different types of materials.



*Figure 2.9: Structures of the nitroxide biradicals used for DNP enhanced solid-state NMR. AMUPol (Left) and TEKPol (Right).*

The design and success of these radicals has involved thorough investigations of the most efficient e-e distances and relative orientations and the most effective substituents around the radical centres.

TEKPOL and AMUPOL have large bulky groups surrounding the radical centres as these help to lengthen the electron relaxation times, thereby ensuring that the CE events happen while there is still a substantial non-equilibrium population of the electron spins.

## 2.2.4. Sample Preparation

There are four main methods of incorporating the radical within a sample: *glass forming* (GF),<sup>29</sup> *film casting* (FC),<sup>30</sup> *incipient wetness impregnation* (IWI),<sup>31</sup> and “*matrix free*” techniques. The matrix free techniques often involve incorporating a radical during the synthesis of a material whereas the GF, FC, and IWI techniques involve post-synthesis treatment of a material. The optimal sample preparation technique varies according to the nature of the sample.

The glass forming and film casting preparation techniques both initially involve complete solubilization or suspension of the sample in a radical solution. For GF experiments the sample is then placed directly in the rotor and analysed as a frozen solution. The GF method requires specially selected solvents which will not crystallize when frozen at cryogenic temperatures as crystallization could cause phase separation in the sample, lowering DNP enhancements. Cryoprotectant solvents such as glycerol and dimethyl sulfoxide (DMSO) are added to water to create the glass-forming matrix for aqueous solutions. 1,1,2,2-tetrachloroethane (TCE) can act as a GF solvent for use with the TEKPOL radical.

The film casting method involves a further step where the solvent is evaporated from the sample which is then ground and packed into the rotor. This approach has the benefit of improved sample filling factor – without the excess solvent, an effective larger volume of the sample can be analysed. Drawbacks to the FC method include the potential for the polarizing agent to organize itself into crystalline domains during the evaporation of the solvent, resulting in lower DNP enhancements.

The incipient wetness impregnation method uses the minimum amount of radical solution needed to impregnate the sample which is then instantly frozen as in the GF method. The sample is not dissolved in the solution, rather the solvent is just used as a transporter to carry the polarizing agent throughout the sample, this is particularly useful in porous materials. The IWI method helps homogeneously distribute the polarizing agent without resulting in the reduction of analyte sample volume.

Additional sample preparation methods used in the experimental work presented here will be described and discussed in the context of the relevant experiments later.

## 2.2.5. Evaluating the DNP Effect

The simplest method of confirming if there is any DNP enhancement of a spectrum is to perform two experiments with the same conditions, but one is done with microwave irradiation *off* and one with microwave irradiation *on*. By comparing these two spectra and measuring the ratio of the intensities of equivalent signals gives an enhancement factor,  $\varepsilon_{DNP}$  which is defined as

$$\varepsilon_{DNP} = \frac{I_{on}}{I_{off}} \quad [2.2.5. 1]$$

Although this method of measuring DNP enhancement is convenient and useful in an experimental setting to confirm whether the sample preparation has been successful, it is not a good measure of whether DNP has provided an enhancement compared to a standard NMR experiment. In practice, a DNP enhancement is only useful if the signal to noise ratio (SNR) of a spectrum obtained in a set time is improved by DNP.

The sensitivity per scan,  $\chi$ , can be experimentally obtained using the equation

$$\chi_{DNP} = \frac{SNR}{NS\sqrt{T_{DNP}}} \quad [2.2.5. 2]$$

where  $NS$  is the number of scans and  $\sqrt{T_{DNP}}$  is the square root of the DNP build-up time. The DNP build-up time is calculated using the same process as for longitudinal relaxation (Equation [2.2.5. 3]). By substituting  $T_{DNP}$  for  $T_1$ , it is possible to calculate  $\chi$  for a conventional NMR experiment and a more realistic calculation of DNP enhancement can be done. This comparison of DNP to a standard NMR experiment gives a practical measurement of the *Absolute Sensitivity Ratio* (ASR) which can be used as a measure of whether DNP is a useful tool for a particular sample.<sup>32,33</sup> The experimentally obtained ASR can be considered a representation of eight factors which determine the effectiveness of a DNP enhancement. The eight factors contributing to the ASR are

$$ASR = \varepsilon_{DNP} \cdot \varepsilon_T \cdot \eta_{T1} \cdot \chi_{bleach} \cdot \chi_{LW} \cdot \chi_{weight} \cdot \chi_{seq} \cdot \chi_{ex} \quad [2.2.5. 4]$$

where  $\varepsilon_{DNP}$  is the measured enhancement defined in Equation [2.2.5.1],  $\varepsilon_T$  is the enhancement achieved by performing the DNP experiment at low temperature,  $\eta_{T1}$  considers the different relaxation times and total experiment lengths of the DNP and standard NMR experiments,  $\chi_{bleach}$  is a signal bleaching factor,  $\chi_{LW}$  is the ratio of the linewidths,  $\chi_{weight}$  is the ratio of the effective sample weights,  $\chi_{seq}$  is the factor allowing for any difference of signal decay during the experiments, and  $\chi_{ex}$  is a factor accounting for any extra differences between the DNP and standard NMR experiments.

### 3. Experimental Techniques in Solid-state NMR

The simplest NMR experiment involves a single  $90^\circ$  (or  $\frac{\pi}{2}$ ) RF pulse to generate transverse magnetization and then observing the precession of the magnetization as a free induction decay (FID) (Figure 3.1).

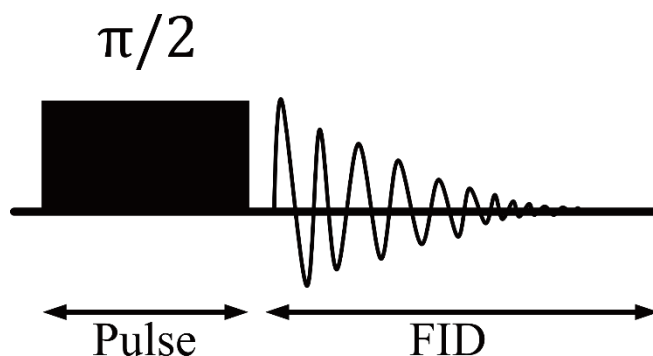


*Figure 3.1: Schematic representation of a simple single-pulse NMR experiment and FID.*

However, not all NMR experiments are simple. This chapter will set out the potential applications and practical details of some commonly used NMR techniques and experiments.



## 3.1. Phase Cycling

All RF pulses have a duration ( $t_p$ ), a power level and a *phase* ( $\phi$ ). By repeating a pulse sequence a number of times and varying the phase of the RF pulses and the receiver for each repetition, it is possible to select specific *coherence pathways*. This process is known as *phase cycling*.

The zero quantum coherence order,  $p = 0$ , represents the equilibrium, population state (before any RF pulse is applied) and  $p = \pm 1, \pm 2, \pm 3, \dots$  represent the single, double, and triple quantum coherence orders respectively. In an NMR experiment  $p = -1$  is the only directly observable coherence state, but by selecting the appropriate coherence pathways it is possible to indirectly observe interactions which rely on higher order coherences such as homonuclear dipolar coupling.

An intuitive way to understand the selected coherence pathway for an experiment is to visually represent the effect of each pulse in a coherence pathway diagram underneath a pulse diagram as demonstrated in Figure 3.2.

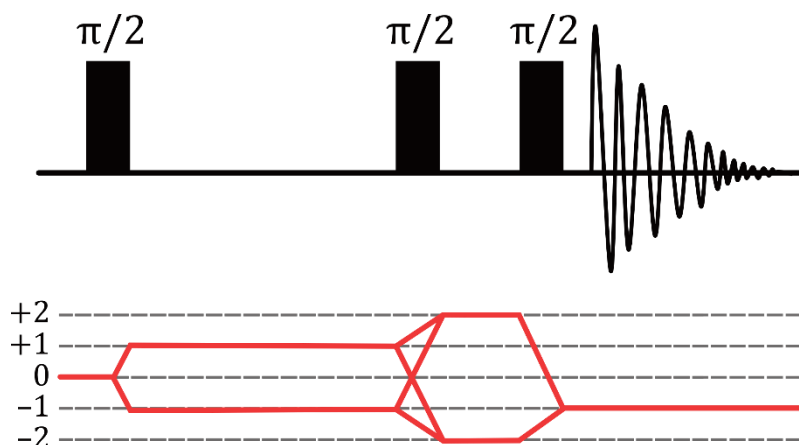


*Figure 3.2: Pulse sequence and coherence order pathway of a double-quantum filtered COSY experiment.*

The rules of phase cycling which allow a specific pathway to be selected are

- A pulse's phase must be cycled through a complete  $360^\circ$  cycle. This can be done in steps of  $90^\circ$  resulting in a 4-step phase cycle

- A shift in the pulse phase,  $\Delta\phi$ , adds a phase shift of  $-\phi\Delta p$ , to the coherence, where  $\Delta p$  is the desired change in coherence
- The receiver phase,  $\phi_R$ , must follow the phase shift of the desired coherence. If the phase cycle is completed through  $360^\circ$ , the other coherences should be subtracted away

To select a coherence change  $p = \pm 2$ , the coherence phase will shift by  $-\phi_A\Delta p$  where  $\phi_A$  is the phase of the pulse. A 4-step phase cycle to select the  $\pm 2$  coherences will be

Step	$\phi_A$	$-\phi_A\Delta P = \pm 2\phi_A$
1	0	0
2	90	180
3	180	0
4	270	180

Table 3.1: Phase shifts of  $\pm 2$  coherences

To ensure that the  $\pm 2$  coherences are selected, and all others are eliminated, the receiver phase must be synchronized with the phase shifts

$$\phi_R = -\phi_A\Delta p \quad [2.2.5.1]$$

$$\phi_R = 0, 180, 0, 180$$

Although in theory, this phase cycle would also select the  $\pm 6$  coherences, it is safe to disregard these as it is assumed that not much 6-order coherence is formed.

## 3.2. Spin Echo

A *spin echo* (or *Hahn echo*)<sup>34</sup> experiment is a two-pulse sequence which is commonly used to maximize the amount of signal that is acquired in an experiment by reducing the effects of inhomogeneous dephasing of the signal.

The pulse sequence is structured as follows:

- An initial  $\frac{\pi}{2}$  pulse with phase  $\phi$ , which generates transverse magnetization
- A delay,  $\tau$ , which can be considered the *evolution time* during which  $T_2$  relaxation occurs
- A  $\pi$  pulse with phase  $\phi + 180^\circ$ , which flips the spins in the  $xy$ -plane
- A second  $\tau$  delay, during which the magnetization in the  $xy$ -plane is refocused
- Acquisition

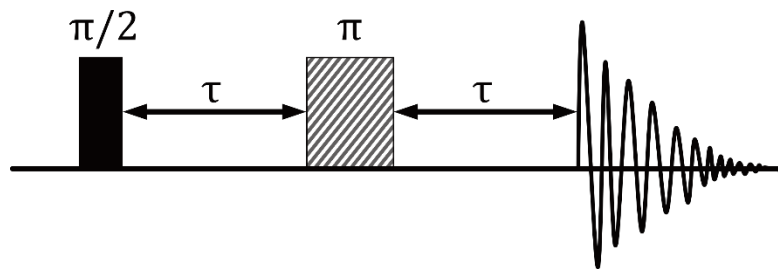


Figure 3.3: Pulse sequence of a spin echo experiment.

During the evolution time, the bulk magnetization begins to de-phase during  $T_2$  relaxation as some spins move faster and some move slower than the bulk magnetization in the  $xy$ -plane. When the  $\pi$  pulse is applied, the magnetization is flipped and this results in the faster spins being flipped to be ‘behind’ the slower components and bulk magnetization. During the second delay the faster spins, bulk magnetization, and the slower spins will realign, and an ‘echo’ can be recorded.

The most common use of the spin echo experiment is to maximize the signal intensity however, by varying the evolution time it is also possible to deduce information about the spin-spin relaxation process of a sample.

### 3.3. Double-Quantum NMR

An experiment which causes excitation of coherence order  $p = \pm 2$  is a *double-quantum* (DQ) experiment. By exciting the higher-order coherences, it is possible to access information on internuclear interactions. DQ experiments are used widely to understand the homonuclear dipolar coupling between  $^1\text{H}$  spins

in organic solids. DQ coherences are created when there is significant dipolar coupling, which is the case in many organic materials due to the high concentration of  $^1\text{H}$ .

Since DQ coherence is not observable, it must be detected *via*  $p = -1$  coherence. This is done exciting the DQ coherence and then reconverting this to observable magnetization such as in the pulse sequence in Figure 3.4a, which shows the general form of a DQ experiment.

The steps of this DQ experiment are:

- An ‘*excitation*’ block, which consists of multiple pulses of appropriate pulse length and phase to generate DQ coherence
- A delay  $\tau_e$ , during which the DQ coherence evolves
- A ‘*reconversion*’ block, which is equivalent to the excitation block but with an additional phase shift
- A  $\frac{\pi}{2}$  ‘read-out’ pulse which generates the detectable transverse magnetization

For a static solid, the excitation and reconversion blocks are both complex trains of twelve pulses: eight  $\frac{\pi}{2}$  pulses and four  $\pi$  pulses.<sup>35</sup> The twelve-pulse block can be seen in Figure 3.4b. The twelve-pulse train differs from the original *Baum-Pines* pulse sequence to improve the stability of the sequence.<sup>36</sup> For a DQ experiment under MAS, the dipolar coupling is suppressed by MAS and so the excitation and reconversion blocks involve *recoupling* of the dipolar interaction.

The phase of the excitation block  $\phi_0$  is a combination of phases for these twelve pulses  $\{\phi_0 = xyx, xyx, -x - y - x, -x - y - x\}$ , where  $x, y, -x$ , and  $-y$  are the axes along which the pulse is applied. The reconversion block has the same pulse structure, but the phase is shifted by  $\Delta\phi = n \cdot 90^\circ$ , which results in a four-step phase cycle of the reconversion block pulse, where the phase of the reconversion block is  $\phi_0 + \Delta\phi$ , as  $\Delta\phi = 0^\circ, 90^\circ, 180^\circ, 270^\circ$ .<sup>37</sup>

The lengths of the excitation and reconversion blocks are

$$\tau_{DQ} = n_c t_c \quad [2.2.5.1]$$

where  $n_c$  is the number of times the twelve-pulse block is cycled and  $t_c$  is the duration of one cycle. This time,  $\tau_{DQ}$  is the DQ evolution time and can be varied

so that a ‘DQ build-up curve’ is obtained which can be used to probe the strength of  $^1\text{H}$ - $^1\text{H}$  dipolar coupling.

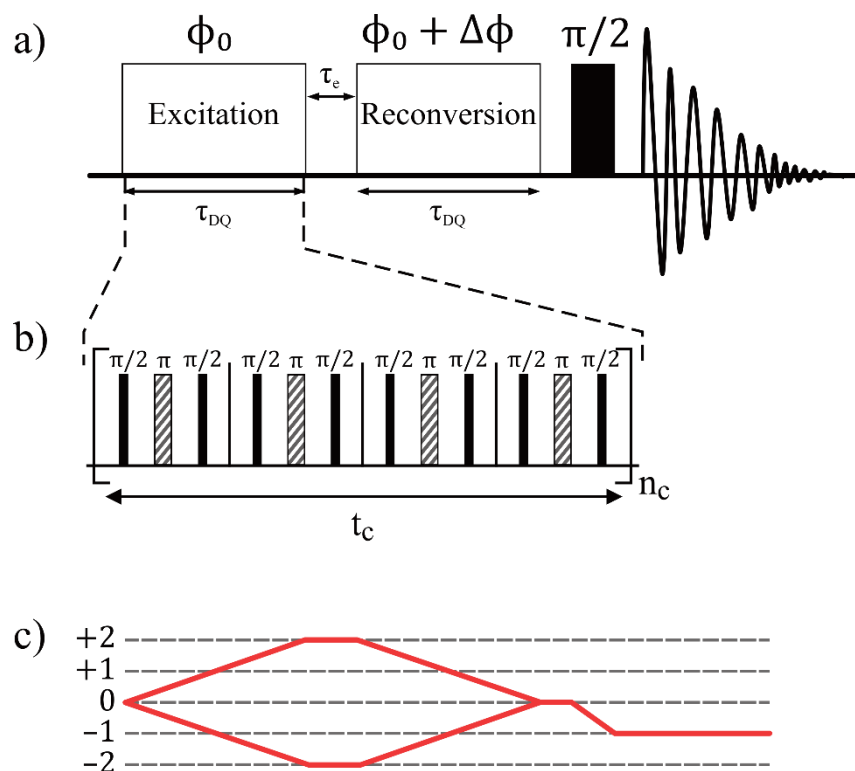


Figure 3.4: Pulse sequence used for static  $^1\text{H}$  DQ build up experiments, a) General form of DQ experiment including an excitation and reversion block, DQ evolution time and  $\pi/2$  ‘read-out’ pulse. b) twelve-pulse excitation and reversion block used for DQ experiments of static solids. Consisting of eight  $\pi/2$  pulses and four  $\pi$  pulses. The total duration of one twelve-pulse block is  $t_c$ . The total duration of the DQ excitation or reversion block,  $\tau_{\text{DQ}}$  is  $t_c$  multiplied by the number of repetitions of the twelve-pulse block,  $n_c$ . c) The coherence pathway selected during the experiment.

### 3.4. Heteronuclear Decoupling

For a dilute species like  $^{13}\text{C}$  which often experiences heteronuclear dipolar coupling to  $^1\text{H}$ , removing any residual coupling that is not averaged by MAS can greatly reduce the linewidth of  $^{13}\text{C}$  resonances and thus improve the resolution of the experiment. This is known as *heteronuclear decoupling*.

Heteronuclear decoupling is applied by continuous RF irradiation on the more abundant species such as  $^1\text{H}$  which excites transitions between the  $^1\text{H}$   $|\alpha\rangle$  and  $|\beta\rangle$  states. If the power of the RF irradiation is sufficient, these transitions will be faster than the magnitude of the heteronuclear dipolar coupling and the coupling will be averaged out.

### 3.5. Cross Polarization

A second technique to increase the signal of an experiment of dilute nuclei is to use *cross polarization* (CP). CP uses the heteronuclear dipolar coupling between dilute ( $S$ ) and abundant ( $I$ ) spins to transfer the larger magnetization of  $I$  to  $S$  thereby increasing the bulk magnetization of the dilute spin and improving the signal intensity.<sup>38</sup>

The magnetization transfer occurs when a *spin lock* pulse is applied to spins  $I$  and  $S$  for a duration known as the *contact time* which typically lasts for a few milliseconds.

A spin lock pulse is a pulse which ‘locks’ the magnetization in the transverse plane along  $B_1$  for the duration of the contact time.

The transfer of magnetization proceeds during this spin lock time as long as the amplitudes of the pulses are set so that they satisfy the *Hartmann-Hahn matching condition*<sup>39</sup> which under static conditions is

$$\gamma_I B_{1,I} = \gamma_S B_{1,S} \quad [2.2.5.1]$$

Under MAS, the HH matching condition is

$$\gamma_I B_{1,I} = \gamma_S B_{1,S} \pm n\omega_r \quad [2.2.5.2]$$

where  $\omega_r$  is the MAS frequency and  $n$  can be  $\pm 1$  or  $\pm 2$ . At fast MAS achieving the correct matching conditions can be difficult so a *ramped* spin lock pulse is used on one of the spins as shown in Figure 3.5. This ramped pulse varies the nutation frequency for the duration of the pulse and improves the chances of the matching condition being achieved at some point during the ramp.

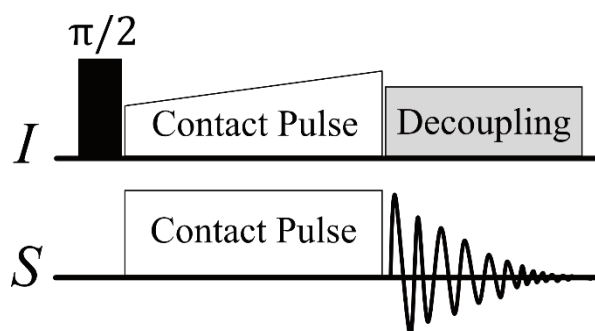


Figure 3.5: Pulse sequence for a cross polarization experiment from abundant spin,  $I$  to dilute spin,  $S$ . An FID is acquired on the  $S$  channel while heteronuclear decoupling is applied to the  $I$  channel.

## 3.6. Experimental Techniques Used for DNP-Enhanced Solid-state NMR

### 3.6.1. Polarization Transfer

In a dynamic nuclear polarization enhanced NMR experiment, electron polarization is generated by the saturation of electron spin transitions by applied microwave irradiation and this polarization is then transferred to the nucleus of interest *via* a direct or indirect pathway.

The direct polarization (DP) transfer involves a simple transfer from electron to nucleus as shown by the (Blue) arrow in Figure 3.6. Indirect polarization transfer (Red arrows) involves an additional step. Generally, electron polarization initially transferred to an abundant nucleus, such as  $^1\text{H}$ , is further transferred to the nucleus of interest, such as  $^{13}\text{C}$  *via* cross polarization (CP).

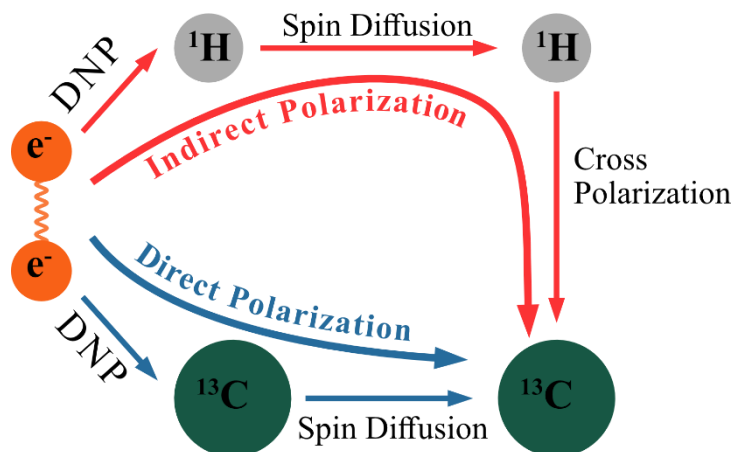
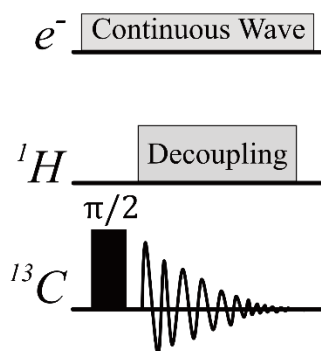


Figure 3.6: Schematic representation of the direct and indirect polarization transfer pathways from electrons to the bulk  $^{13}\text{C}$ . The indirect pathway involves initial DNP of  $^1\text{H}$  in close proximity to the radical, this polarization is then dispersed to the bulk  $^1\text{H}$  via spin diffusion and is then transferred to the  $^{13}\text{C}$  nucleus via cross polarization. The direct pathway involves initial DNP of  $^{13}\text{C}$  in close proximity to the radical, which can then be transferred to the bulk  $^{13}\text{C}$  via spin diffusion given a high enough abundance of  $^{13}\text{C}$ .

The pulse sequences used to achieve direct and indirect polarization transfer are shown in Figure 3.7.

a) DP



b) CP

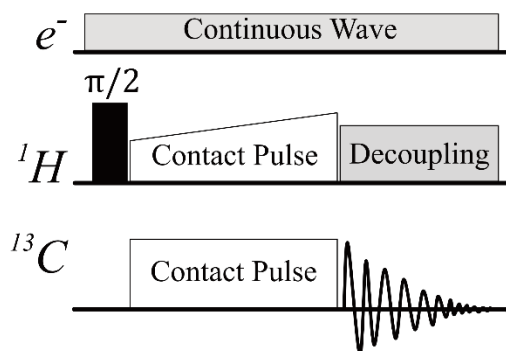


Figure 3.7: a) Direct polarization (DP) and b) cross polarization (CP) DNP pulse sequences used for the acquisition of indirect and direct  $^{13}\text{C}$  DNP-enhanced spectra, respectively. MW irradiation used to induce polarization from electrons is represented by a long continuous wave pulse.



### 3.6.2. SCREAM-DNP

An additional possible polarization transfer pathway is *via*  $^1\text{H}$ - $^{13}\text{C}$  cross-relaxation, which is mediated by fast dynamics such as methyl rotations. This cross-relaxation polarization transfer can obscure DP transfer as it is a much faster process, due to being dissipated through the sample by  $^1\text{H}$ - $^1\text{H}$  spin diffusion. The DP relies on much slower spin diffusion of less abundant nuclei such as  $^{13}\text{C}$ .

*Specific cross-relaxation enhancement by active motions under DNP* (SCREAM-DNP)<sup>40</sup> is a method which enables the separation of the effects of DP and cross-relaxation polarization.

The pulse sequence used to study the SCREAM-DNP process can be seen in Figure 3.8. Interleaved experiments are performed, alternating between a pulse sequence where  $^1\text{H}$  and  $^{13}\text{C}$  polarization is allowed to build-up during a set delay ( $\tau$ ) and a pulse sequence where  $^{13}\text{C}$  polarization is allowed to build-up, but  $^1\text{H}$  spins are saturated by a train of pulses during the same duration of delay.

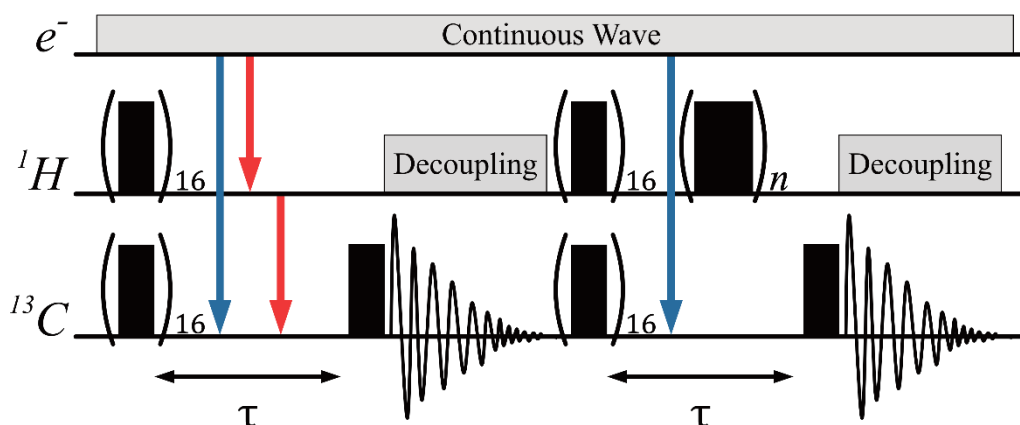


Figure 3.8: Pulse sequence for interleaved SCREAM-DNP experiments. The polarization transfer pathways active during each step are indicated. Indirect polarization (Red arrows) occurs via methyl  $^1\text{H}$ - $^{13}\text{C}$  cross-relaxation. Direct polarization (Blue arrows).

# 4. Hydrogen Defects in MAPbI<sub>3</sub>

*All MAPbI<sub>3</sub> and MAPbI<sub>3</sub> on ZnO samples in this chapter were synthesized by Dr Lei Lei in the research group of Dr Ming Li, Faculty of Engineering, University of Nottingham.*

## 4.1. Abstract

In this work, static and Magic Angle Spinning solid-state NMR has been used to investigate possible defects and diffusion in a Methylammonium lead iodide perovskite (MAPbI<sub>3</sub>). Methylammonium Lead Halide perovskites, MAPbX<sub>3</sub> (X = Br<sup>-</sup>, Cl<sup>-</sup>, I<sup>-</sup>) are important functional materials with promising applications in solar cells and their properties and stability are impacted by defects in the structures.

At low resolution, the <sup>1</sup>H spectrum of MAPbI<sub>3</sub> shows just the two expected signals for CH<sub>3</sub> and NH<sub>3</sub>, at 3.3 ppm and 6.3 ppm respectively. At higher resolution, however, it becomes clear that there are additional signals from some impurity at 0-2 ppm. Intentional wetting of the MAPbI<sub>3</sub> sample suggests that these impurities are present in dry MAPbI<sub>3</sub> and are not due to moisture. Variable temperature experiments of MAPbI<sub>3</sub> provide evidence that these impurity signals could be involved in some diffusion throughout the sample.

## 4.2. Introduction

### 4.2.1. Perovskites

The term *perovskite* was first used as a name for the mineral  $\text{CaTiO}_3$ . Today the term is used more broadly to describe crystal structures which are analogous to  $\text{CaTiO}_3$ . Figure 4.1 shows a simplified, schematic representation of a perovskite structure which has the general formula  $\text{ABX}_3$ , where the A-site cation sits within the free space between  $\text{BX}_6$  octahedra.

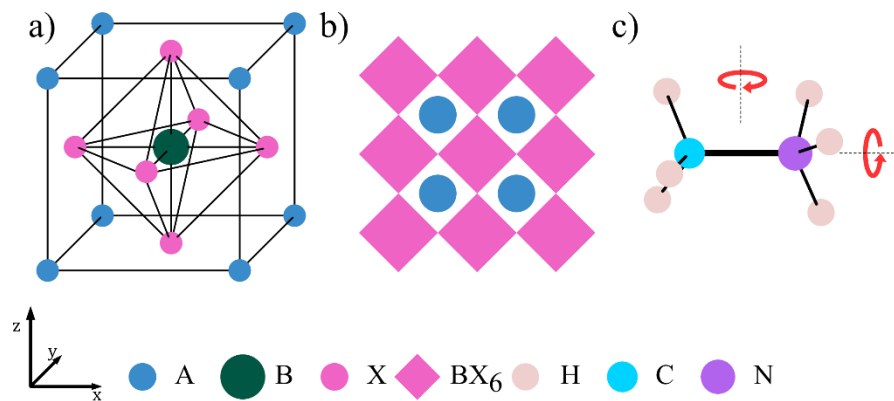


Figure 4.1: Schematic representations of the perovskite,  $\text{ABX}_3$  crystal structure. a) The ideal cubic unit cell, viewed along the y-axis. pink circles represent the X atoms at the face-centred position, blue circles represent the A atoms in the cube corner position, and the green circle represents the B atom in the body centred position. b) shows a view along the z-axis, where the pink diamonds represent the  $\text{BX}_6$  octahedra and the blue circles are the A atom in the free space between them. c) shows the axes of rotation of a methylammonium ion.

When the A-site cation is an organic molecule such as the methylammonium ion, the material is described as a *hybrid perovskite*. In  $\text{MAPbX}_3$  ( $\text{X}^- = \text{Br}^-$ ,  $\text{Cl}^-$ ,  $\text{I}^-$ ) hybrid perovskites, the A-site cation is not a perfect sphere and so it exhibits mobility and reorients over time. For the iodide perovskite, at room temperature, the MA ion “hops” between four different orientations with the average time between these hops being just 3 ps.<sup>41</sup> The structure of  $\text{MAPbI}_3$  at room temperature is considered to be *tetragonal*. At temperatures below 161 K the structure has *orthorhombic* symmetry, and there is no MA reorientation. At temperatures above 330 K the structure has *pseudocubic* symmetry and the MA ion is fully disordered to reflect this symmetry.<sup>42</sup>

The transitions between the different phases of hybrid perovskites are similar to those seen for inorganic perovskites, such as caesium lead halide perovskites, which have an orthorhombic structure at room temperature and cubic structure at high temperatures.<sup>43</sup> The asymmetry of the *A*-site cation in hybrid perovskites allows for the extra phase transition and the hydrogen bonding which exists between the MA ion and the framework further affects the phase transitions and distortion of the crystal structure. These structural distortions affect the physical properties and stability of the hybrid perovskites. This is what leads to significant differences in the properties and performance of the three MAPbX<sub>3</sub> perovskites.

The synthesis and structures of MAPbX<sub>3</sub> hybrid perovskites were first described in 1978,<sup>44</sup> however in 2009 the use of hybrid perovskites as photovoltaic solar cells was first reported.<sup>45</sup> This initiated widespread study of both inorganic and hybrid perovskites. Although the photoconversion efficiencies of hybrid perovskite based solar cells were initially low, recent years have seen a rapid increase in the efficiencies of these materials, reaching close to the theoretical limit.<sup>3</sup> The properties which make these perovskites promising candidates for widespread use in solar cells are numerous and include long charge carrier lifetimes, tuneable bandgap properties, and relatively simple synthesis.

The iodide perovskite MAPbI<sub>3</sub> is of particular interest due to its favourable direct bandgap (1.55 – 1.6 eV)<sup>46,47</sup> and was the first hybrid perovskite to show promise for solar cell applications.<sup>45</sup>

### 4.2.2. Defects in MAPbI<sub>3</sub>

The optoelectronic properties and efficiency of MAPbI<sub>3</sub> are greatly influenced by ion diffusion and migration. The phenomenon of ion migration in halide perovskites has been known for many years,<sup>48</sup> however interest in understanding the implications of this migration is more recent, initiated by the presence of hysteresis in the current-voltage curves of hybrid perovskite based cells.<sup>49,50</sup>

Ion migration in solid-state structures is facilitated by either a vacancy or interstitial defect. In perovskite-based structures, vacancy-mediated diffusion is the most common process.<sup>51</sup> This is a result of Schottky disorder where equal

numbers of cations and anions are absent from their normal sites, leaving an equal number of anion and cation vacancies. Interstitial migration is less likely due to the tight packing of the perovskite structure.

It is reasonable to believe that the ion migration most likely to occur in MAPbI<sub>3</sub> and thus most likely to be the cause of the hysteresis is I<sup>-</sup> migration. In the PbI<sub>6</sub><sup>4-</sup> octahedron, the I<sup>-</sup> ions have a shorter distance to travel to reach a I<sup>-</sup> vacancy than the MA<sup>+</sup> or Pb<sup>2+</sup> ions do. The calculated activation energy for I<sup>-</sup> migration is also the lowest of the three ions.<sup>51,52</sup> Although theoretically, I<sup>-</sup> migration is most likely, it has not been observed experimentally at room temperature. MA<sup>+</sup> ions were the first experimentally observed migrating species at room temperature using photothermal induced resonance (PTIR) microscopy.<sup>53</sup> Evidence of I<sup>-</sup> migration has only been experimentally observed at elevated temperatures of 330 K.<sup>54</sup>

Although ion migration *via* interstitial vacancies is unlikely for larger ions like I<sup>-</sup> and MA<sup>+</sup>, the migration of interstitial hydrogen is a possibility. The presence of hydrogen ions (H<sup>+</sup>, H<sup>0</sup>, and H<sup>-</sup>) in MAPbI<sub>3</sub> could be a result of extrinsic defects, resulting from partial decomposition in the presence of H<sub>2</sub>O, or intrinsic defects resulting from deprotonation of the MA<sup>+</sup> ion.<sup>55</sup> It has been shown that the performance of hybrid halide perovskite solar cells can be improved by mild moisture.<sup>56</sup> This is analogous to oxide perovskites (ABO<sub>3</sub>) which are known to form protonic defects by adsorption of water and have high proton conductivities.<sup>57-59</sup> The theoretical model of hydrogen migration in MAPbI<sub>3</sub> shows the migration barriers to be comparable to those calculated for oxide perovskites.<sup>60</sup>

H<sup>+</sup> being the smallest hydrogen ion is most likely to migrate through interstitial vacancies. A theoretical study by Egger et al.<sup>60</sup> shows that H<sup>+</sup> is calculated to be stable in a bridging position between two iodides, the presence of the H<sup>+</sup> ion in this position results in a rearrangement of the iodide sites. They suggest that there are two possible mechanisms of H<sup>+</sup> ions through the MAPbI<sub>3</sub> structure. The Bourgoin-Corbett mechanism is an ionization-enhanced pathway of migration. As the equilibrium position for the H ion is different depending on the charge state, a change in charge state of an ion will result in a shift in its position.<sup>61</sup>

When an interstitial  $H^+$  ion captures an electron and becomes an  $H^0$  ion, the position of the ion migrates from the iodide bridging site of  $H^+$ , to the lead-iodide interstitial site of  $H^0$  to minimize the total energy of the system. This process can also occur for the  $H^0$  and  $H^-$  ions, which upon changing their charge state will change their position. The cumulative effect is a net migration of defects.

The second mechanism for  $H^+$  ion migration is thermally activated diffusion. During this process, the  $H^+$  ion migrates along the transient hydrogen bond between two equatorial iodides which causes rearrangement of both iodide positions. The proton now closely attached to the iodide then stabilizes in a local minimum and the  $H^+$  ion is now in an equatorial-apical bridging position.<sup>60,62</sup> The calculated energy barrier for this migration of  $H^+$  between two iodide positions is relatively low, suggesting the possibility of these mobile  $H^+$  defects in MAPbI<sub>3</sub>. However, the calculations did not consider the effects of possible quantum tunnelling which would be likely to reduce the energy barrier even further.

Experimental evidence of  $H^+$  migration in MAPbI<sub>3</sub> solar cells has been shown by studying the change in the kinetic isotope effect (KIE) when selectively deuterating the MA<sup>+</sup> ion.<sup>63</sup> While investigating MA<sup>+</sup> ion rotations and their relationship to the dielectric response of MAPbI<sub>3</sub>, Chen *et al.* unexpectedly found that selective deuteration of the ammonium group resulted in a large *inverse* KIE. An inverse KIE can be caused by several different mechanisms, including the occurrence of an ionic hydrogen bond between two electronegative atoms.<sup>64</sup> Given the ionic nature of the material, they concluded the origin of the intermediate dielectric response they observed was actually a result of  $H^+$  migration *via* A---H<sup>+</sup>---A ionic bonding, where A is an electronegative atom. Since the same inverse KIE was not seen when the methyl group was deuterated, it can be concluded that it is the labile protons on the ammonium group that are the source of the  $H^+$  ions. When evaluating the mechanism of this  $H^+$  migration, they found that the process was active at 90 K which suggests that the migration occurs *via* quantum tunnelling.<sup>65</sup> Although the results from this study only demonstrate local movement between two iodide sites at an interfacial region of a MAPbI<sub>3</sub> solar cell architecture, Feng *et al.* were able to confirm the quantum tunnelling behaviour of  $H^+$  migration at low temperature and classical hopping

at room temperature in MAPbI<sub>3</sub> in a combined experimental and theoretical study.<sup>66</sup>

H<sup>+</sup> migration in MAPbI<sub>3</sub> was further studied by Sadhu *et al.* by *polarization-modulated infrared reflection-absorption spectroscopy* (PM-IRRAS).<sup>67</sup> They were able to indirectly follow the migration of H ions by exploiting the difference in vibrational frequencies of X-H and X-D bonds, where X is a heavier element. PM-IRRAS was used to follow the process of D/H exchange of the ammonium group in MAPbI<sub>3</sub> while the sample was irradiated by a 450 nm LED for several hours. Although this experiment was performed in a controlled, dry environment, the D/H exchange was easily observed as the signal corresponding to CH<sub>3</sub>ND<sub>3</sub><sup>+</sup> decreases while the signal for CH<sub>3</sub>NH<sub>2</sub>D<sup>+</sup> first increases then decreases in intensity and the signal for CH<sub>3</sub>NH<sub>3</sub><sup>+</sup> appears and increases in intensity. For this complete D/H exchange, there must be diffusion of water or protons through the sample.

While Chen *et al.* conclude that the mechanism of H<sup>+</sup> migration follows the thermally activated mechanism suggested by Egger *et al.*, Sadhu *et al.* conclude from their experimental results that it is the ionization-enhanced mechanism. Their results show that the partial dissociation of water at the surface of the material and initial diffusion of protons into the sample is the rate determining step in the D/H exchange as the rate is dependent on the intensity of light used and concentration of water present. However, this does not facilitate the total exchange as the rate is independent of the thickness of the material and there is no evidence of H<sub>2</sub>O or D<sub>2</sub>O in the PM-IRRAS spectra. They propose that there is ionization-enhanced migration through the sample and at any location where H<sup>+</sup> is generated, H<sup>+</sup>/D<sup>+</sup> exchange may occur.

There has been significant recent discussion in the literature on how best to measure the diffusion coefficient of proton defects in MAPbI<sub>3</sub>.<sup>67-70</sup> The discrepancies in reported proton diffusion values suggests that the H<sup>+</sup> migration mechanism is more complex than the pathways proposed thus far and further investigation is required to understand this important process.

### 4.2.3. Solid-state NMR Spectroscopy of MAPbX<sub>3</sub> Perovskites

MAPbX<sub>3</sub> perovskites have been extensively studied by solid-state NMR, including <sup>1</sup>H, <sup>13</sup>C, <sup>14</sup>N, <sup>15</sup>N <sup>2</sup>H, and <sup>207</sup>Pb NMR. These studies provide structural information as well as a method to study the dynamic processes of these materials.<sup>71</sup>

<sup>207</sup>Pb NMR can be a useful probe for any dynamics of the halide ions. The large chemical shift range of <sup>207</sup>Pb NMR makes it sensitive to subtle structural changes including any changes in Pb–X bonding which result from halide dynamics.<sup>72</sup> The phase of the system and rotational and reorientation dynamics of the MA<sup>+</sup> ion have been studied by the quadrupolar splitting and relaxation behaviour of <sup>2</sup>H and <sup>14</sup>N NMR.<sup>73–76</sup>

<sup>13</sup>C and <sup>15</sup>N NMR both suffer from very low sensitivity at natural abundance, but they can still be useful for elucidation of the cation structure and identification of unwanted impurities.<sup>76–79</sup> <sup>1</sup>H NMR is also mainly used to study the structure of the cation and any interactions with organic dopants. However, <sup>1</sup>H NMR of MAPbI<sub>3</sub> can also be a useful tool to probe the phase transition of the structure at high temperature.<sup>80</sup>

There are several examples of solid-state NMR being used to probe the defects in hybrid halide perovskite structures including ion diffusion.<sup>81</sup> Halide diffusion in mixed halide perovskites has been identified using <sup>207</sup>Pb 2D exchange spectroscopy (EXSY).<sup>82,83</sup> These studies by Askar *et al.* and Karmakar *et al.* concluded that mixed halide perovskites with the formula MAPb(Cl<sub>x</sub>Br<sub>1-x</sub>)<sub>3</sub>, showed solid-solution behaviour. As the ratio of Cl to Br changed, the local environment of Pb in the structure was changed and the <sup>207</sup>Pb chemical shift and line shape could be used to identify the halide composition. <sup>207</sup>Pb EXSY spectra of MAPb(Cl<sub>0.5</sub>Br<sub>0.5</sub>)<sub>3</sub> and FAPb(Cl<sub>0.5</sub>Br<sub>0.5</sub>)<sub>3</sub> showed evidence of exchange cross-peaks with seven distinct <sup>207</sup>Pb environments. The mixing times used to probe this halide exchange and the insensitivity of the EXSY experiment to <sup>207</sup>Pb-<sup>207</sup>Pb spin diffusion, indicate that these cross-peaks are due to chemical exchange of the halides rather than spin diffusion.



Senocrate *et al.* used variable temperature  $^{14}\text{N}$  linewidths and  $^1\text{H}$  relaxation and linewidths to demonstrate that there was no discernible diffusion of the  $\text{MA}^+$  ion in the temperature range of 193-503 K.<sup>84</sup> Contrary to these conclusions, Franssen *et al.* suggest that there is ion mobility at relatively low temperatures.<sup>85</sup> They measured the  $^{14}\text{N}$  quadrupolar coupling constant ( $C_Q$ ) of  $\text{MAPbI}_3$  in the cubic phase which should be averaged to zero by the fast rotation of the cation. However, they found that in the cubic phase there is a residual quadrupolar interaction indicated by unusual line shapes. Heating the sample results in narrowing of the linewidth until reaching a minimum at  $\sim 393$  K, however cooling the sample does not reintroduce the broad line. From this observation, Franssen *et al.* suggest that this annealing behaviour is a result of structural defects and ion mobility.

The evidence of interstitial hydrogen defects and diffusion<sup>63,66,67</sup> in  $\text{MAPbI}_3$  is more recent than these NMR studies of  $\text{MA}^+$  diffusion. There are several examples of  $^1\text{H}$  NMR spectroscopy being used to identify interstitial and substitutional hydrogen defects in oxide perovskites and other metal oxide materials.<sup>86-91</sup>

The presence of hydrogen impurities in  $\text{ZnO}$  can be seen clearly from  $^1\text{H}$  NMR.<sup>86,88,92</sup> Wang *et al.* were able to assign the  $^1\text{H}$  signals in  $\text{ZnO}$  to interstitial  $\text{H}^+$  and substitutional H in an oxygen vacancy,  $\text{H}_\text{O}$  using deuteration of a model  $\text{Zn}(\text{OH})_2$  sample and  $^1\text{H} - ^{17}\text{O}$  correlations.<sup>88</sup> They assigned the signal at  $\sim 4.2$  ppm at low temperatures to sorbed water and at high temperatures to  $\text{H}^+$ . The signals at 0-2 ppm were assigned to  $\text{H}_\text{O}$  defects.

By minimizing exposure to moisture and treating samples of lead zirconate titanate (PZT) and barium titanate (BTO) with high-pressure  $\text{H}_2$  gas, Alvine *et al.*<sup>87</sup> confirmed by  $^1\text{H}$  NMR that signals at  $\sim 4$  ppm and  $\sim 7$  ppm for both samples can be assigned to contamination due to moisture but the three signals around  $-1$  to  $1$  ppm result from internal hydrogen species, likely interstitial defects in the perovskite lattice. Their results are consistent with structural models of these materials which indicate that there could be three possible locations of interstitial hydrogen defects.

The  $^1\text{H}$  NMR studies of these purely inorganic materials benefit from a lack of native hydrogen in the structure and so any  $^1\text{H}$  signal is guaranteed to be some impurity in the sample. The simpler spectra allow for easier identification of the nature of the hydrogen impurity. However, if there are interstitial or substitutional hydrogen defects in  $\text{MAPbI}_3$  it may still be possible to identify them by  $^1\text{H}$  NMR. If these defects are identified, it may also be possible to determine whether there is any diffusion of these species through the structure.

#### 4.2.4. Probing Diffusion by NMR

Diffusion in solids can be probed *via* NMR by measuring the diffusion induced relaxation at different temperatures. Relaxation is driven by fluctuations in the local magnetic field due to molecular motion. As the temperature changes, the rate of molecular diffusion through a structure will change and as a result the average local magnetic field will also change. Both spin-spin relaxation and spin-lattice relaxation can be used to measure diffusion.

As the temperature increases, and the diffusion of ions throughout a sample increases, the local magnetic field becomes more averaged. The increased homogeneity of the local magnetic field reduces the dephasing of magnetization in the  $xy$  plane. The measurable result of this is a slower  $T_2$  relaxation rate at higher temperatures.

As  $T_2^*$  relaxation is inversely proportional to the linewidth at half height,  $\nu_{\frac{1}{2}}$  of a signal,

$$\nu_{\frac{1}{2}} = \frac{1}{\pi T_2} \quad [4.2.4. 1]$$

The narrowing of the linewidth of a signal as temperature increases is an efficient indicator that a species could be involved in diffusion.

The fluctuations of the magnetic field that are a result of diffusion can be described by the correlation function,  $G(\tau_c)$ , and spectral density function,  $J(\omega)$ , as in Section 2.1.11.1. The spectral density function (Equation [2.1.11.7]) describes the amount of motion happening at a particular frequency. Figure 4.2 shows the plots of the spectral density function at different correlation times.

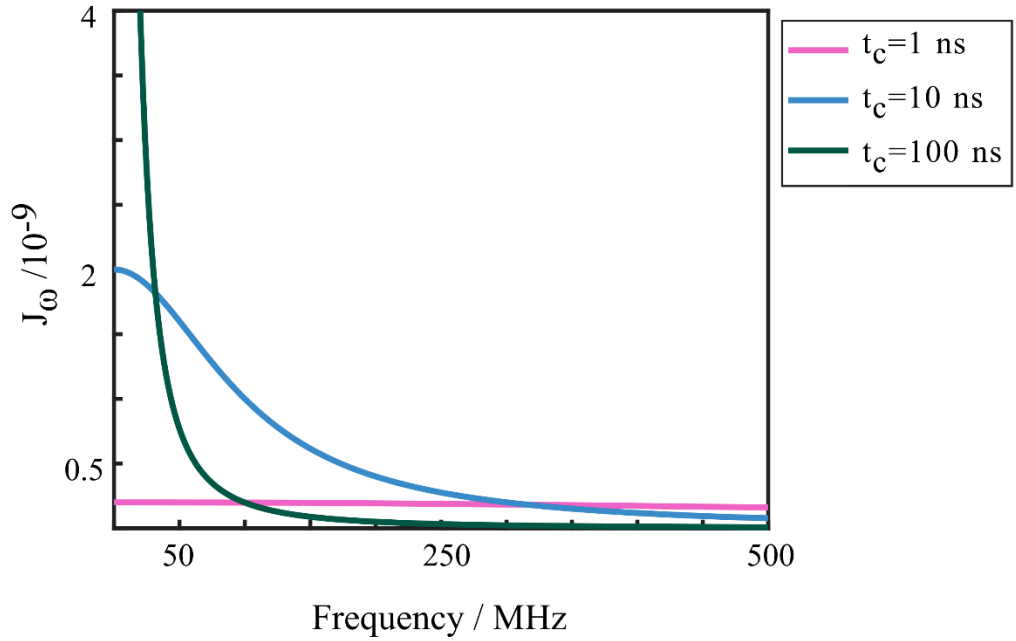


Figure 4.2: Fits of the spectral density function at correlations times,  $\tau_c$ , of 1 ns (Pink), 10 ns (Blue), and 100 ns (Green).

At short correlation times, relating to fast molecular motion, there is a broad range of frequencies sampled. Slow molecular motion has long correlation times and samples a narrow range of frequencies. For a given frequency such as the Larmor frequency,  $\omega_0$ , the spectral density function will have a maximum when  $\omega_0\tau_c \cong 1$ .

The correlation time associated with the spectral density can be considered equal to the residence time of a diffusing species,  $\tau$ .  $\tau$  is a measure of how long a species rests in an energy minimum as it diffuses through a structure. The temperature dependence of  $\tau$  follows Arrhenius behaviour

$$\tau = \tau_0 e^{\frac{E_A}{k_B T}} \quad [4.2.4.2]$$

where  $\tau_0$  is a pre-exponential factor,  $E_A$  is the activation energy of the diffusion process in J,  $k_B$  is the Boltzmann constant in  $\text{J K}^{-1}$ , and T is temperature.

As the temperature increases,  $\tau$  will decrease and the spectral density function will change. By measuring the  $T_1$  times of a sample at different temperatures, it is possible to extract information about  $\tau$ .

As  $J(\omega) \propto T_1^{-1}$ , a plot of  $T_1^{-1}$  against  $T^{-1}$  will also have a maximum when  $\omega_0\tau \cong 1$ . From this plot it is possible to extract information about the diffusion residence time and the activation energy of diffusion.

## 4.3. Experimental Details

### 4.3.1. Materials

Hydroiodic acid (47 wt%) and ethanol ( $\geq 99.5\%$ ) were obtained from Honeywell. Methylammonium ethanol solution (33 wt%), diethyl ether (99+ %, anhydrous), and lead iodide ( $\text{PbI}_2$ , 99 %) were obtained from Acros Organics.

### 4.3.2. Sample Preparation

#### 4.3.2.1. Methylammonium Iodide Synthesis

Hydroiodic acid was mixed with methylammonium ethanol solution with a molar ratio of 1: 1 in a round flask under an ice water bath. After reacting for two hours, the product was crystallized by removing the solvent with a rotary evaporator. The solid was dissolved in a minimal volume of ethanol and recrystallized with diethyl ether. The product was collected by vacuum filtration and washed three times with diethyl ether. The white salt was dried in a vacuum oven at 60 °C for 12 h.

#### 4.3.2.2. $\text{CH}_3\text{NH}_3\text{PbI}_3$ synthesis

To prepare  $\text{CH}_3\text{NH}_3\text{PbI}_3$ , 1.383 g  $\text{PbI}_2$  and 0.477 g above synthesized  $\text{CH}_3\text{NH}_3\text{I}$  powder were dissolved in 2 mL dimethyl formamide in a vial by stirring for 12 hours. The solution was firstly filtered by a 0.22  $\mu\text{m}$  syringe filter and then precipitated with 500 mL diethyl ether. The yellow precipitate was collected by vacuum filtration and dried in a 65 °C vacuum oven for 12 h.

### 4.3.2.3. ZnO Synthesis

ZnO nanoparticles were synthesized by reacting a zinc acetate solution (42 mL, 0.069 molL<sup>-1</sup> in ethanol) with a potassium hydroxide solution (23 mL, 0.1 molL<sup>-1</sup> in ethanol). The above solutions were mixed at room temperature by stirring (600 rpm) for 15 min and left still on a 60 °C hotplate for 2 hours. The suspension was cooled down to room temperature and centrifuged to obtain the wet product. ZnO nanopowder was finally obtained by drying the about white powder in a 60 °C vacuum oven for 12 h.

### 4.3.2.4. Preparation of Solid-state NMR Samples

For the reference CH<sub>3</sub>NH<sub>3</sub>PbI<sub>3</sub> sample, the as synthesized powder was used. The water incorporation was conducted by expose the CH<sub>3</sub>NH<sub>3</sub>PbI<sub>3</sub> powder to water bubbled argon flow for 8 hours with a flow rate of ~60 ml min<sup>-1</sup>. For the mixed CH<sub>3</sub>NH<sub>3</sub>PbI<sub>3</sub>-ZnO sample, 0.0968 g CH<sub>3</sub>NH<sub>3</sub>PbI<sub>3</sub> was mixed with 0.0032 g ZnO by grinding with a mortar and pestle for 30 min.

## 4.3.3. NMR

Static and MAS NMR experiments were performed on a Bruker Avance III spectrometer operating at a <sup>1</sup>H Larmor frequency of  $\nu_{0H} = 600$  MHz (14.1 T) using a 2.5 mm triple-resonance MAS probe and a 1.3 mm double-resonance MAS probe, and a Bruker Avance NEO spectrometer operating at a <sup>1</sup>H Larmor frequency of  $\nu_{0H} = 800$  MHz (18.8 T) using a 1.3 mm double-resonance MAS probe. Spinning frequencies ranged from 0-60 kHz, most experiments were performed at 0 or 20 kHz. The temperature due to frictional heating during MAS VT experiments was monitored by the chemical shift change of <sup>79</sup>Br in KBr powder.<sup>93</sup> The temperature was allowed to equilibrate for at least 10 minutes between experiments.

<sup>1</sup>H experiments were performed using a spin echo pulse sequence. The interpulse delay,  $\tau$ , was varied from 0.17 to 5 ms. <sup>1</sup>H  $T_1$  experiments were performed using a saturation recovery pulse sequence. 32 transients were co-added and a recycle delay of 100 ms was used. 32 points were recorded with variable delays ranging from 1 ms to 200 s.

## 4.4. Results and Discussion

### 4.4.1. MAPbI<sub>3</sub>

MAPbI<sub>3</sub> was packed in a 2.5mm MAS rotor inside of a glovebox to limit any contamination with moisture in the air. The single-pulse <sup>1</sup>H NMR spectrum of this sample is shown in Figure 4.3.

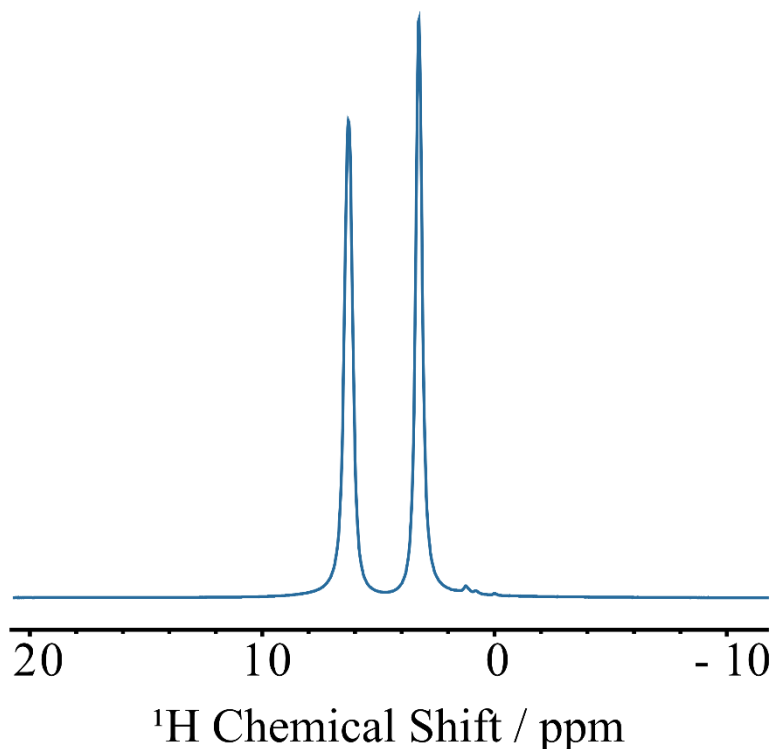


*Figure 4.3: <sup>1</sup>H single-pulse MAS spectrum of MAPbI<sub>3</sub>. Recorded on a 14.1 T spectrometer with spinning frequency of 20 kHz. Signal at 6.3 ppm assigned to NH<sub>3</sub>, signal at 3.3 ppm assigned to CH<sub>3</sub>, multiple small signals around 0-2 ppm are not assigned for this spectrum due to low intensity.*

As expected, there are two clear peaks with equal integrals corresponding to the CH<sub>3</sub> and NH<sub>3</sub> of the MA<sup>+</sup> cation, at 3.3 ppm and 6.3 ppm respectively. There are however other unexpected signals present in the spectrum. In examples of <sup>1</sup>H NMR of MAPbI<sub>3</sub> in the literature, these signals are also often present and are tentatively assigned to be water or other impurities in the sample.<sup>75,80,94–96</sup> The location of these impurity signals around 0-2 ppm is similar to the locations of interstitial and substitutional hydrogen defects in oxide perovskites and metal

oxide materials.<sup>86-91</sup> Given the potential of any impurity or defect in the perovskite structure having an important effect on the performance of the material, it is important to properly investigate and understand these regularly appearing anomalies in the  $^1\text{H}$  NMR of  $\text{MAPbI}_3$ . If there is any significant diffusion of H containing ions through the  $\text{MAPbI}_3$  structure, the linewidths of the  $^1\text{H}$  spectrum at varying temperatures should be affected by this diffusion and allow some identification of the process.<sup>97,98</sup>

The resolution of a  $^1\text{H}$  spectrum of  $\text{MAPbI}_3$  at moderate magnetic field strength and MAS frequency is sufficient to analyse the large  $\text{CH}_3$  and  $\text{NH}_3$  signals however the smaller impurity signals are overpowered by the MA signals. Improving the resolution and separating the impurity signals further from the MA signals using very fast MAS can be difficult when working with hybrid perovskite materials due to their sensitivity to temperature. Frictional heating from MAS limits the range of temperatures that can be reached by variable temperature measurements and thus limits the possibility of studying the different phases of these materials.

#### 4.4.1.1. Static VT Experiments

The static, room temperature  $^1\text{H}$  spectrum of  $\text{MAPbI}_3$  at 18.8 T field strength features a broad signal centred around 4.6 ppm and a second overlapping signal with a maximum around 1.5 ppm as shown in Figure 4.4.

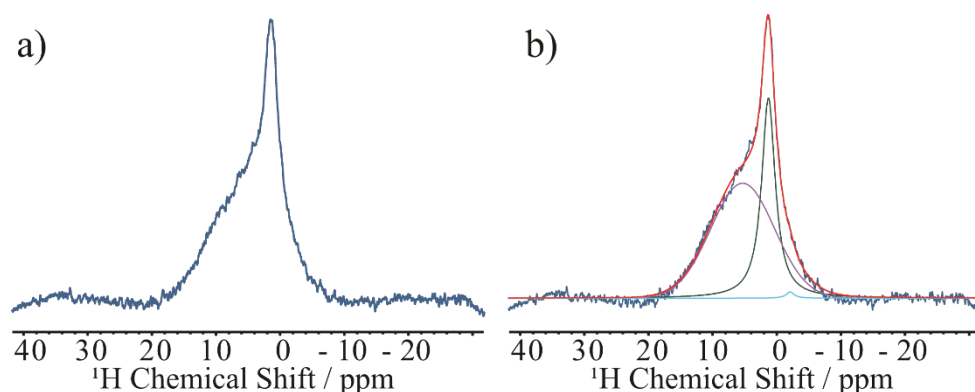


Figure 4.4: a)  $^1\text{H}$  static spin echo spectrum of  $\text{MAPbI}_3$  recorded on a 18.8 T spectrometer with 0 kHz MAS. b) Fitting and deconvolutions of signals at approximately 4.6 ppm, 1.5 ppm, and -1.5 ppm. Ratios of these signals are 63 %, 36 %, and 1 % respectively.

Assuming only two species, the linewidths of these signals was estimated after deconvolution of the spectrum using DMfit software.<sup>99</sup> The signal at 4.6 ppm has a linewidth of 10 kHz and the signal at 1.5 ppm has a linewidth of 2 kHz. This static spectrum of MAPbI<sub>3</sub> sample differs from the static spectrum recorded at a 9.4 T magnetic field strength by Senocrate *et al.* who observed just one broad signal with a linewidth of 8 kHz.<sup>96</sup> This difference is likely due to the significant improvement of the resolution at higher field strengths.

Where Senocrate *et al.* were unable to observe any change in the line shape, linewidth or position of the static <sup>1</sup>H signal of MAPbI<sub>3</sub> between 183 and 503 K, at higher field strength, the higher resolution of the spectrum does show that the signals change in this temperature range.

Technical limitations restricted the temperature range that could be explored. However, it was possible to observe the phase change from tetragonal to pseudocubic MAPbI<sub>3</sub> at 330 K. In Figure 4.5, the static <sup>1</sup>H spectra of MAPbI<sub>3</sub> at temperatures between 298 and 338 K are shown.

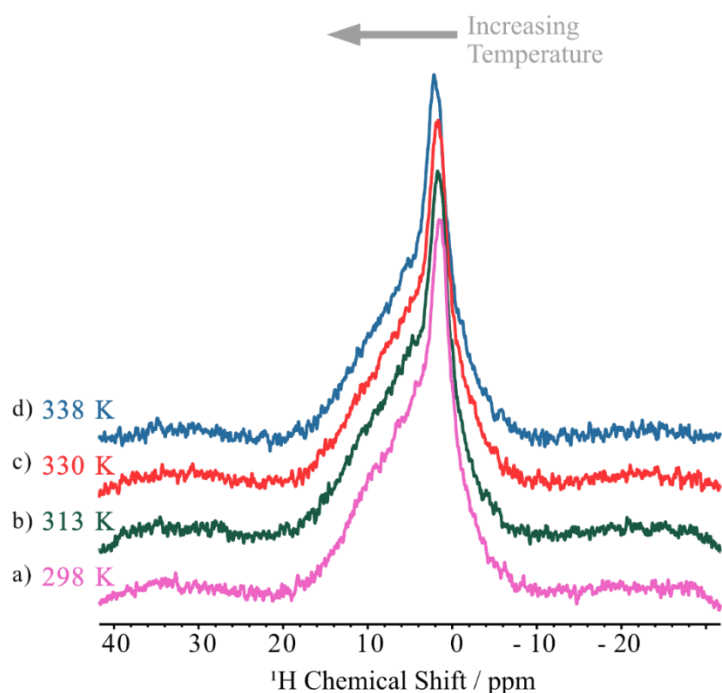


Figure 4.5: <sup>1</sup>H static spin echo spectra of MAPbI<sub>3</sub> recorded at different temperatures. a) T = 298 K, b) T = 313 K, c) T = 330 K, and d) T = 338 K.



Temperature	CH <sub>3</sub> <sup>1</sup> H chemical shift
298 K	1.41 ppm
313 K	1.58 ppm
330 K	1.65 ppm
338 K	1.94 ppm

Table 4.1: <sup>1</sup>H static chemical shift of the CH<sub>3</sub> signal of MAPbI<sub>3</sub> recorded at increasing temperatures. Chemical shifts have been obtained by fitting and deconvolution of the broad spectrum using DMFit.

There is no observable change of the NH<sub>3</sub> signal but despite the poor SNR, the second signal does show a clear change in position as the temperature increases and the phase change of the perovskite cage is instigated, as demonstrated by the arrow in Figure 4.5 . This is consistent with results for well-resolved MAS VT experiments on hybrid halide perovskites.<sup>80,100</sup>

The change of the spin-lattice relaxation with temperature can also be a good measure of diffusion, however the limited temperature range available and poor sensitivity resulting in very long experiment times meant that it was not feasible to undertake these measurements. The static <sup>1</sup>H T<sub>1</sub> relaxation times as a function of temperature were recorded by Senocrate *et al.* over a range from 183 - 310 K.<sup>96</sup> The behaviour that they observed was characteristic of spin-lattice relaxation which was dominated by dipolar coupling and spin-rotation mediated relaxation and showed no signs of diffusion induced relaxation. The activation energy of  $\Delta E_a = 0.13$  eV that they were able to extract from the VT T<sub>1</sub> experiments was in agreement with that expected of rotational motion of the MA<sup>+</sup> ion. The calculated activation barriers for MA<sup>+</sup> or H<sup>+</sup> diffusion are estimated to be much larger.<sup>60,101</sup>

These results indicate that the change in the spectrum as the phase changes from tetragonal to pseudocubic which is likely a result of changes in the interaction between the MA<sup>+</sup> ion and the perovskite lattice as the phase changes.<sup>100</sup> Considering the lack of narrowing of either of the signals and the observations

of Senocrate *et al.* it is unlikely that there is diffusion of the MA<sup>+</sup> ion in MAPbI<sub>3</sub> under the conditions and timescales measurable by static <sup>1</sup>H NMR.

#### 4.4.1.2. MAS VT Experiments

MAS <sup>1</sup>H NMR provides the spectral resolution required to separate the NH<sub>3</sub> and CH<sub>3</sub> signals. Where in the static case, only the CH<sub>3</sub> signal showed a change in chemical shift as the temperature increased, using 60 kHz MAS shows that the NH<sub>3</sub> signal also moves to higher chemical shift as the temperature increases as seen in Figure 4.6.

Using a change of linewidth with respect to temperature to identify any ion diffusion in MAPbI<sub>3</sub> is complicated by the already narrow linewidths due to fast rotation of the MA<sup>+</sup> ion within the perovskite cage. Although in this case MAS allows for better observation of changes of signals as a function of temperature, it is not useful for identifying ion diffusion as MAS induces further unnatural narrowing of the signals. Additionally, the frictional heating which occurs during MAS severely limits the temperature range which can be investigated. This limits the usefulness of  $T_1$  relaxation as function of temperature as a measurement of diffusion.

Static and MAS <sup>1</sup>H NMR can be useful tools to identify the phase change of MAPbI<sub>3</sub> as the temperature changes however neither have been able to identify any ion diffusion.

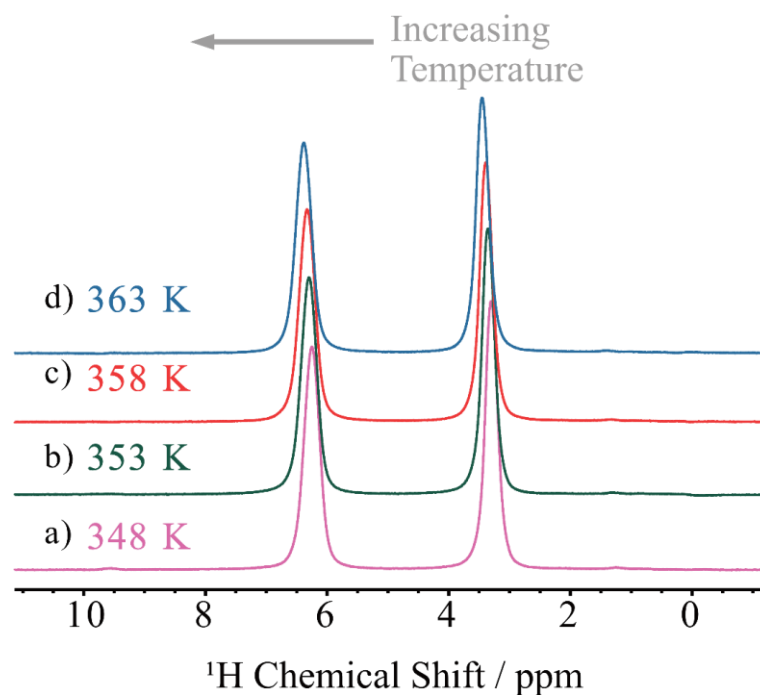


Figure 4.6:  $^1\text{H}$  MAS spin echo spectra of  $\text{MAPbI}_3$  recorded at different temperatures. a)  $T = 348\text{ K}$ , b)  $T = 353\text{ K}$ , c)  $T = 358\text{ K}$ , and d)  $T = 363\text{ K}$ . Spectra are recorded with a spinning frequency of  $60\text{ kHz}$ .

## Impurities

MAS  $^1\text{H}$  NMR can also provide the spectral resolution needed to investigate the unassigned impurity signals of  $\text{MAPbI}_3$ , however the intensity of these signals is significantly lower than for the  $\text{CH}_3$  and  $\text{NH}_3$  signals and some resolution is lost. Using spectral editing techniques to preferentially remove the MA signals, the unassigned signals can be resolved in greater detail. For these experiments a MAS frequency of  $20\text{ kHz}$  was used as this was sufficient to provide the necessary resolution.

Spectral editing can refer to any technique which simplifies a spectrum, such as water suppression. In this case, careful selection of inter-pulse delay lengths in the spin echo sequence, results in the suppression of signals with short spin-spin,  $T_2$ , relaxation times. This means that the MA signals which have strong homonuclear couplings which drive the  $T_2$  relaxation will be preferentially suppressed.

As the echo delay time increases, all signals decrease in intensity, but the MA signals decrease much faster to the point where they disappear completely. The  $T_1$  relaxation time for the MA signals is  $\sim 14$  s, compared to 10 s for the unassigned signals so to further emphasize the unassigned signals short recycle delays can be used. Figure 4.7 demonstrates the difference of the spectra of MAPbI<sub>3</sub> acquired with different echo delays and recycle delays.

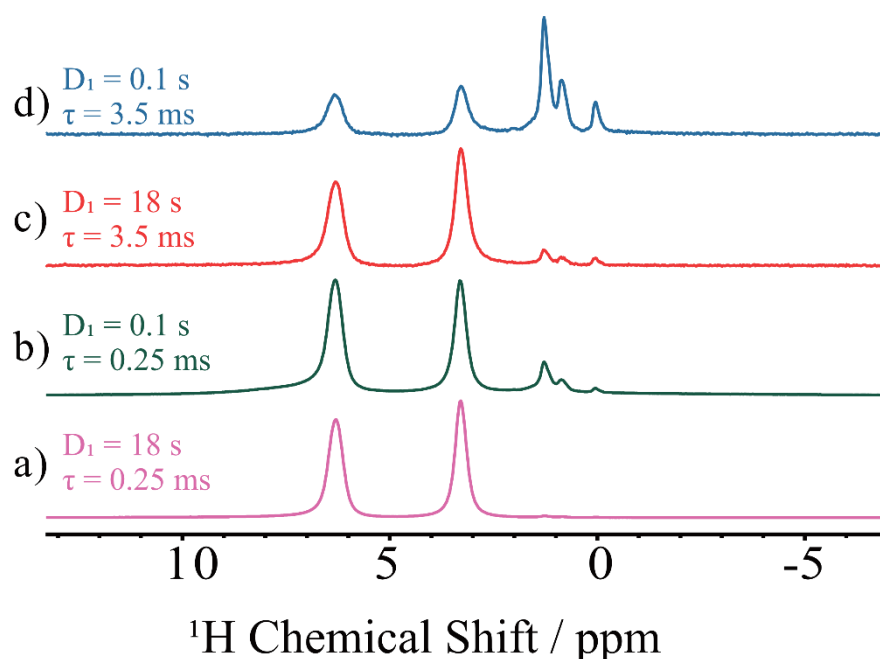


Figure 4.7:  $^1\text{H}$  MAS spin echo spectra of MAPbI<sub>3</sub> with different recycle delays and spin echo delays. a) Recycle delay = 18 s, spin echo delay = 0.25 ms. b) Recycle delay = 0.1 s, spin echo delay = 0.25 ms. c) Recycle delay = 18 s, spin echo delay = 3.5 ms. d) Recycle delay = 0.1 s, spin echo delay = 3.5 ms. Spectra are recorded with a spinning frequency of 20 kHz. Spectra are normalized to the maximum intensities.

Additional VT MAS experiments were performed at 20 kHz spinning frequency to investigate the impurity. For these experiments, an echo delay time and a recycle delay time which resulted in the MA and smallest of the unassigned signals being similar intensities, such as in Figure 4.7d) were chosen ( $D_1 = 0.1$  s,  $\tau = 3.5$  ms).

Across the temperature range investigated (331 - 346 K), the notable difference in the spectrum as the temperature changes is the change in intensity of the signals as seen in Figure 4.8. As the temperature increases, the intensity of the

MA signals decreases slightly, and the intensity of the unassigned signals increases. In particular, the most intense impurity signal at 1.2 ppm increases by 28 %. The change in intensity of the MA signals is less pronounced than the impurity signals. At 346 K the NH<sub>3</sub> signal has decreased by 5 % and the CH<sub>3</sub> by 6 % compared to at 331 K.

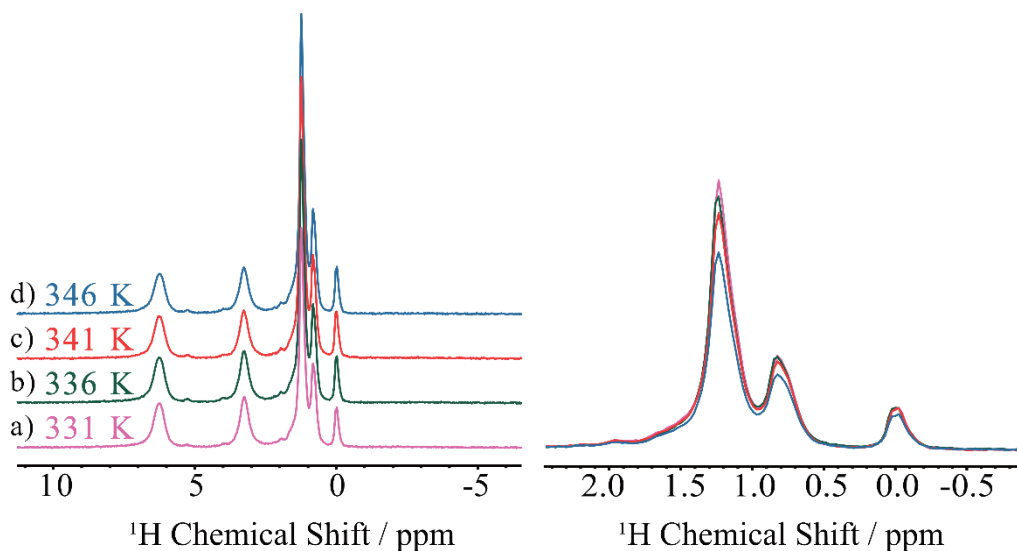


Figure 4.8: <sup>1</sup>H MAS spin echo spectra of MAPbI<sub>3</sub> recorded at different temperatures. a)  $T = 331$  K, b)  $T = 336$  K, c)  $T = 341$  K, and d)  $T = 346$  K. Spectra are recorded with a spinning frequency of 20 kHz. A magnification of the region -1 to 2.5 ppm (Right) shows the differences in the intensities of the signals in this region.

The observation of this behaviour during a spin echo experiment with a long evolution time suggests that the  $T_2$  relaxation time of the unassigned signals increases as temperature increases. This increase of  $T_2$  relaxation time as the temperature increases could indicate diffusion of these species.

It would be expected that the  $T_2$  relaxation of the MA<sup>+</sup> ions would also increase as the speed of reorientation of the MA<sup>+</sup> ion increases at higher temperatures. This anomaly could be due to other factors such as changes in the homogeneity of the external magnetic field as temperature increases. If all signals are normalized so that there is no change in the CH<sub>3</sub> signal, there is still an increase in intensity of the impurity signals.

While it has not been possible to determine any increased motion or diffusion quantitatively, the results from the spin echo experiments show qualitative evidence of increased motion or diffusion.

#### 4.4.1.3. $^{13}\text{C}$ NMR

To ensure the signals at 0-2 ppm were not from any residual solvent or dimethylammonium impurities,<sup>102,103</sup> a  $^{13}\text{C}$  NMR spectrum of  $\text{MAPbI}_3$  was recorded. The spectrum shown in Figure 4.9 exhibits one singular signal at 31.3 ppm which corresponds to the  $\text{CH}_3$  of the MA cation. From this spectrum it is also possible to confirm that there is unlikely to be any significant difference in the nitrogen group of the cation such as the presence of any formamidinium ions, as this would result in a change in the  $^{13}\text{C}$  chemical shift.<sup>104</sup>

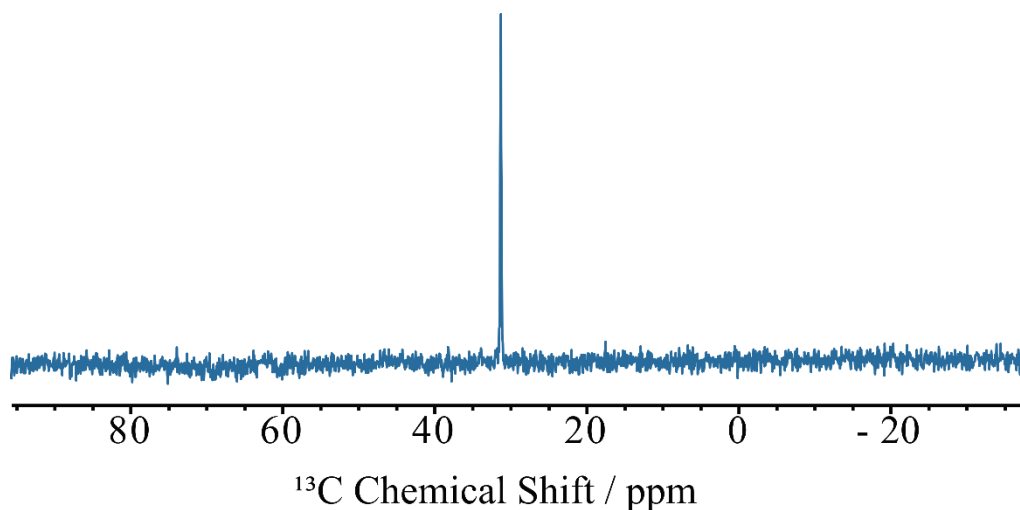


Figure 4.9:  $^1\text{H}$ - $^{13}\text{C}$  CP spectrum of  $\text{MAPbI}_3$  recorded at a spinning frequency of 20 kHz. The signal at 31 ppm is assigned to  $\text{CH}_3$  of the MA ion.

#### 4.4.1.4. Spectral Assignment

The short  $T_1$  relaxation time, line shape, and behaviour of the signals during spin echo experiments with long  $\tau$  delays, indicates that the signals at 0-2 ppm come from a mobile environment. A sample of  $\text{MAPbI}_3$  intentionally washed with water was prepared to determine whether these signals were likely to be due to water. Figure 4.10 shows the comparison between the  $^1\text{H}$  spectra of wet  $\text{MAPbI}_3$  and pristine, dry  $\text{MAPbI}_3$ .

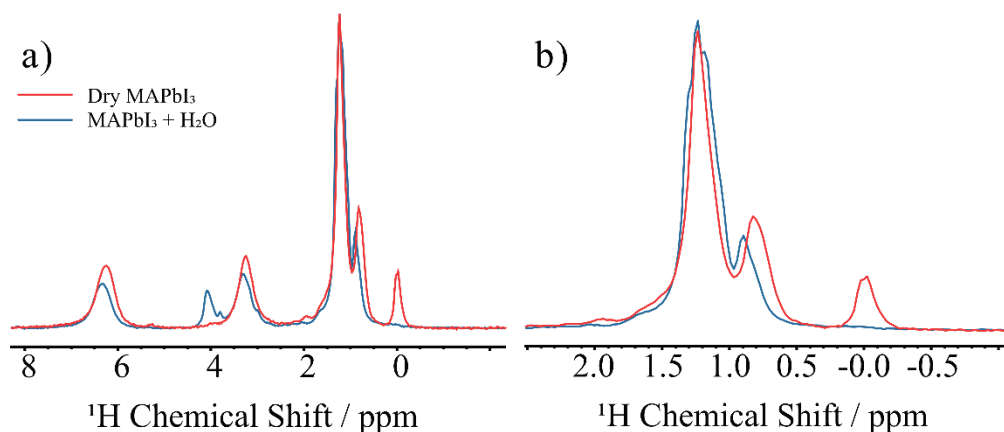


Figure 4.10:  $^1\text{H}$  MAS spin echo spectra of dry  $\text{MAPbI}_3$  (Red) and wet  $\text{MAPbI}_3$  (Blue). Additional signals at 4 and 4.7 ppm of the spectrum of wet  $\text{MAPbI}_3$  are assigned to water. A magnification of the region -1 to 2.5 ppm (Right) shows the differences in the line shape of the signals in this region. On the right, spectra are normalized to the maximum intensity. On the right, spectra are normalized to the same  $\text{CH}_3$  signal intensity.

In the spectrum of wet  $\text{MAPbI}_3$  there are additional peaks at 4 and 4.7 ppm, and the signal at 0 ppm has disappeared. The signals around 0.5-2 ppm have also changed, after deconvolution and fitting of these signals, there are at least two additional signals in the wet sample.

The signals at 4 and 4.7 ppm are only present in the sample which has been exposed to water. Therefore, these signals can be assigned to water which may be present on the surface or within the perovskite cage structure or other H species in water rich environments. These assignments are consistent with the assignment of surface water in oxide perovskite structures.<sup>80,87</sup>

As the signal at 0 ppm disappears in the wet sample, it is unlikely that this signal is due to any strongly bonded hydrogen impurity. This signal is tentatively assigned to some surface impurity. Very dilute impurities of water or -OH could be present in a preferential environment on the surface. When  $\text{MAPbI}_3$  is exposed to moisture it will absorb and uptake water. The controlled exposure of  $\text{MAPbI}_3$  to moisture results in the concentration of -OH and  $\text{H}_2\text{O}$  increasing in the sample. As this happens, water penetrates further into the bulk of the sample by tens of  $\mu\text{m}$ .<sup>105</sup>

Around 0.5-2 ppm the signals which are present in pristine MAPbI<sub>3</sub> remain but there are additional signals overlapping when the sample is exposed to moisture.

The  $T_1$  relaxation measurement of wet MAPbI<sub>3</sub> requires two components to achieve a good fit for the overlapping signals around 0.5-2 ppm. This indicates that there are two distinct species in this group of signals. Fitting the relaxation curve of the wet sample gives  $T_1$  relaxation times of 9.4 and 0.6 s. The signals around this are of pristine MAPbI<sub>3</sub> had a  $T_1$  time of 10 s which corresponds well with one component of the wet sample.

When MAPbI<sub>3</sub> is exposed to moisture for prolonged periods the sample will absorb and uptake moisture which eventually will result in its decomposition:



The signals at 1.2 ppm and 0.8 ppm could be due to a decomposition product, although there is no evidence for this in the <sup>13</sup>C spectrum. It is likely that there are signals in this range which can be assigned to water. However, the signals at 1.2 ppm and 0.8 ppm which remain largely unchanged after exposure to moisture could be some other hydrogen containing impurity or interstitial hydrogen.

#### 4.4.2. MAPbI<sub>3</sub> on Zinc Oxide

The typical structure for a solar cell includes a cathode, an electron transport layer (ETL), an absorber, a hole transport layer (HTL), and an anode. In hybrid perovskite based solar cells, the ETL is often a metal oxide, such as ZnO.<sup>106-108</sup>

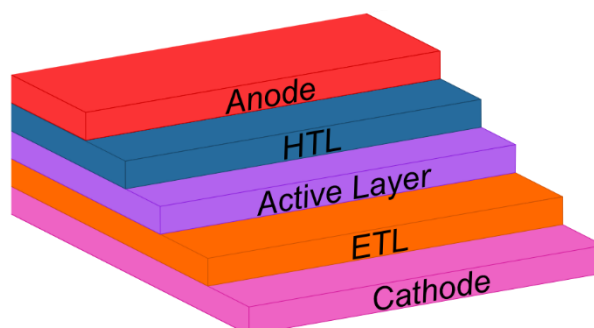


Figure 4.11: Example architecture of a solar cell



The electron transport properties of ZnO have been studied extensively. It exhibits unintentional n-type conductivity, the origins of which have been widely debated. A possible explanation for this n-type conductivity is the presence of hydrogen defects in the ZnO structure.<sup>109</sup> First-principles calculations show that positively charged interstitial hydrogen,  $H^+$  is thermodynamically stable and can act as a shallow donor in ZnO.<sup>110</sup> Substitutional H defects,  $H_O$ , where hydrogen replaces an oxygen and is equally bonded to four Zn neighbours, has also been shown to be possible in ZnO. The  $H_O$  impurities also act as shallow donors.<sup>111</sup> Experimentally, the introduction of hydrogen into ZnO has been shown to increase the n-type conductivity. The solubility of H in ZnO has been determined by measuring the conductivity as a function of temperature, and the value of this corresponds to the calculated formation energy of interstitial  $H^+$ .<sup>112</sup>

The likelihood of sorbed water,  $H^+$ , and  $H_O$  impurities in the ZnO layer of a sample of MAPbI<sub>3</sub> deposited on ZnO, means that the <sup>1</sup>H NMR spectrum of this sample is likely to be different to that of pure MAPbI<sub>3</sub>.

Recently, Nitta *et al.* assigned a <sup>1</sup>H NMR spectrum of ZnO with four species of incorporated hydrogen – water present in the crystal lattice, interstitial  $H^+$ , substitutional  $H_O$ , and  $V_{Zn}-H_3$ , three O-H bonds in a zinc vacancy.<sup>91</sup> They assigned the broad signal in their spectrum at 4.9 ppm to water, a sharp signal largely obscured by water at 4.1 ppm to  $H^+$ , and signals between 0-2.5 ppm to  $H_O$  and  $V_{Zn}-H_3$ . Their assignment is largely in agreement with the assignments of Wang *et al.*<sup>88</sup> who concluded that a signal at 4.2 ppm at low temperatures was the result of sorbed water and at high temperatures could be assigned to  $H^+$ . They assigned the signals at 0-2 ppm to several  $H_O$  defects in slightly different local environments.

There are several studies which assign the signals around 0-2 ppm to -OH groups on the surface of ZnO rather than any structural defect.<sup>86,92,113,114</sup> However, more recently Li *et al.* used MQ NMR to differentiate between these signals and assigned the signals at lower chemical shift to surface -OH species and the signal towards 2 ppm to three O-H bonds in a zinc vacancy ( $V_{Zn}-H_3$ ) due to their close proximity to one another.<sup>115</sup>

The spectrum seen for MAPbI<sub>3</sub> on ZnO in Figure 4.12 appears to be very similar to that of pristine MAPbI<sub>3</sub>.

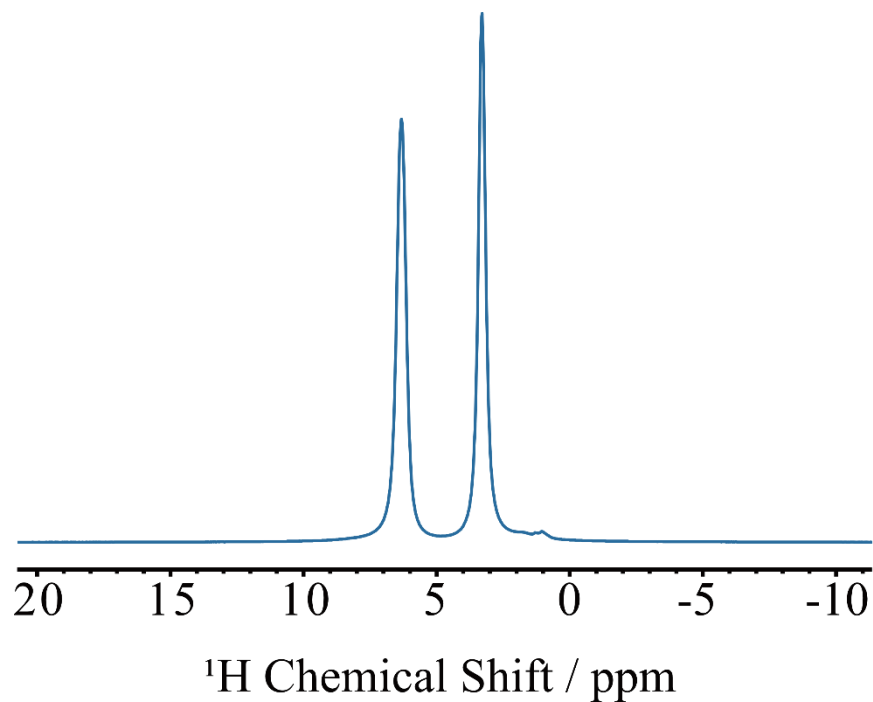


*Figure 4.12: <sup>1</sup>H MAS spin echo spectra of MAPbI<sub>3</sub> on ZnO recorded on a 14.1 T spectrometer at a spinning frequency of 20 kHz.*

This spectrum exhibits the intense CH<sub>3</sub> and NH<sub>3</sub> signals at 3.3 and 6.3 ppm respectively as well as additional sharp signals at 3.9 ppm and between 0.5-2 ppm. However, by using short recycle delays and long echo delays again, the difference of the unassigned signals in the spectrum of MAPbI<sub>3</sub> on ZnO compared to pristine MAPbI<sub>3</sub> can be seen more clearly (Figure 4.13).

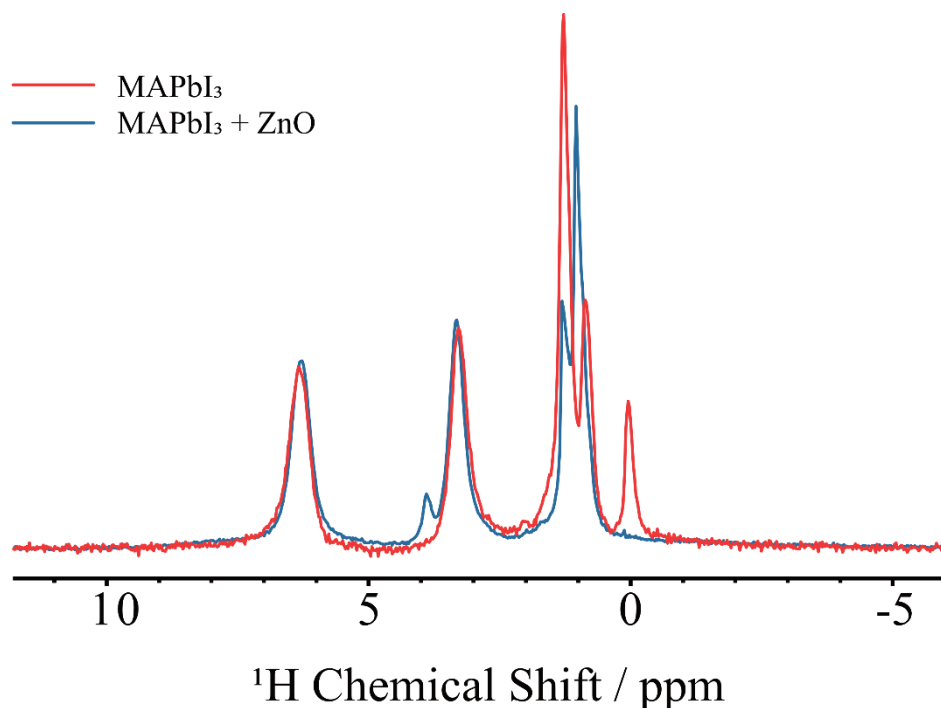


Figure 4.13:  $^1\text{H}$  MAS spin echo spectra of  $\text{MAPbI}_3$  (Red) and  $\text{MAPbI}_3$  on  $\text{ZnO}$  (Blue) recorded with a recycle delay of 0.1 s and a spin echo delay of 3.5 ms. Additional signal on the spectrum of  $\text{MAPbI}_3$  on  $\text{ZnO}$  at 4 ppm is assigned to water. Spectra are normalized to the same  $\text{CH}_3$  signal intensity.

Consistent with the published  $^1\text{H}$  spectra of  $\text{ZnO}$ <sup>91,114</sup> and the spectrum of wet  $\text{MAPbI}_3$  in Section 4.4.1.4, the signal at around 4 ppm can be assigned to water. The absence of a signal at 0 ppm in the spectrum of  $\text{MAPbI}_3$  on  $\text{ZnO}$  is also consistent with the same observation of the intentionally wetted sample of  $\text{MAPbI}_3$ . The behaviour of this group of impurity signals as the temperature of the measurement is increased is the same as for pristine  $\text{MAPbI}_3$ .

Given the overlap of signals which could be due to water, defects in the  $\text{ZnO}$  component or defects or impurities in the  $\text{MAPbI}_3$  component, it is not possible to differentiate or assign any of these signals in this spectrum. The deposition of  $\text{MAPbI}_3$  on  $\text{ZnO}$  may create additional interfacial defects in the structure which may further complicate the assignment of these signals.

## 4.5. Summary

Methylammonium lead halide perovskites are important functional materials with promising applications in solar cells. MAPbI<sub>3</sub> is an extensively studied perovskite with well understood properties. However, to increase the stability and photoconversion efficiency a more thorough understanding of defects present in the structure is required. MAPbI<sub>3</sub> and MAPbI<sub>3</sub> on ZnO were characterized by <sup>1</sup>H NMR to identify possible structural defects which could indicate proton diffusion in these materials.

The phase change between tetragonal and pseudocubic MAPbI<sub>3</sub> has been identified by a change in chemical shift of the CH<sub>3</sub> and NH<sub>3</sub> resonances in static and MAS <sup>1</sup>H NMR. However, there has been no observed evidence of diffusion of the MA<sup>+</sup> ion in this temperature range.

Additional signals in the <sup>1</sup>H spectrum of MAPbI<sub>3</sub> and MAPbI<sub>3</sub> on ZnO have been identified between 0.5 ppm and 2 ppm. Intentional wetting of the MAPbI<sub>3</sub> sample was used here to aid in the assignment of these signals and showed that although there is some overlap with the chemical shift of water on the surface and within the pores of MAPbI<sub>3</sub>, these impurity signals remain largely unchanged by exposure to moisture and could be evidence of some other hydrogen impurity. The behaviour of these signals during spin echo experiments with long inter-pulse delays at different temperatures suggests that there is possibly some increased diffusion or other motion of these species as the temperature increases, both in the tetragonal and pseudocubic phases.

Given the very small concentration of these additional hydrogen species and the inherent insensitivity of NMR, <sup>1</sup>H NMR of the as synthesized materials alone is not sufficient to assign these signals.

# 5. DNP-Enhanced Solid-state NMR of Polymers

## 5.1. Abstract

In this work, investigation of the optimum sample preparation conditions for DNP enhanced solid-state NMR of polymers has been carried out. The enhancement that DNP provides allows intrinsically dilute aspects of polymers such as cross-links, chain ends, and interfaces to be identified. For DNP of polymers, finding the correct sample preparation technique is key to ensuring an even distribution of radical throughout the material.

Analysis of the effects of the choice of radical solution, the volume and extent of polymer swelling, and the role of glycerol in aqueous radical solutions has shown that the extent of swelling of a polymer is important in achieving good DNP enhancements. It is also shown that the use of a glass-former or cryoprotectant is not always necessary due to the amorphous nature of polymer gels. However, the negative aspects of polymer swelling have also been shown in the changed spectral line shapes.

## 5.2. Introduction

### 5.2.1. Polymers

The unsustainable overconsumption of non-biodegradable petroleum derived plastics is a major contributor to the current climate emergency. The polymer-based materials are present in almost all facets of the modern world and play an integral role in 21<sup>st</sup> century life. However, the manufacturing of plastics from petroleum and the pollution of the eco-system caused by discarded plastic waste have long lasting, negative impacts on the health of humans, animals, and nature.

A solution to avoiding continual pollution by plastic materials is to develop alternative polymer feedstocks which are derived from a cleaner, renewable source, and which are biodegradable or more easily recycled. The work of developing these alternative polymers has progressed to the point where many polymers originally prepared from petroleum sources now have viable synthetic routes from renewable sources.<sup>117,118</sup>

To ensure that a new “green plastic” from a renewable and/or biodegradable polymer source is a worthy replacement for a traditional plastic already in circulation, the properties of the new plastic must match or exceed those of the existing plastic. The development of plastics with specific properties requires a detailed understanding of the structure-property relationship of existing and new materials. There are many analytical techniques used to study polymer properties such as *gel permeation chromatography* (GPC)<sup>119</sup> which determines molecular weight distributions; *differential scanning calorimetry* (DSC)<sup>120</sup> which measures melting and glass transitions, as well as the degree of crystallinity, and *thermal gravimetric analysis* (TGA)<sup>121</sup> to measure thermal stability. However, for structural characterization, the amorphous or semi-crystalline nature of polymers means that the common technique of *X-ray diffraction* (XRD) cannot always be used.

It is still important to have a detailed understanding of the structure of polymers as, if the structural features responsible for the desired property can be fully understood, it becomes possible to design new materials with better properties

for any given application. For this type of analysis, solid-state NMR is the optimal choice as it can provide information on the structure and dynamics of amorphous and insoluble materials. Beyond simple confirmation of the chemical structure of a polymer, solid-state NMR has been used to investigate the macro-structure of polymer materials such as domain sizes in block co-polymers,<sup>122,123</sup> packing and chain conformations,<sup>124</sup> and the structure of interfaces in core-shell polymer morphologies.<sup>125</sup>

The ability of solid-state NMR to probe molecular motion on a series of timeframes with excellent specificity makes it an appealing technique to study dynamic processes of polymers even in the solid state.<sup>126</sup> Relaxation time measurements such as  $T_{1\rho}$  experiments can provide insight to molecular motions happening on a millisecond timescale such as rotation of bulky substituents<sup>127</sup> or rotation about the axis of inline aromatic groups.<sup>128</sup> The analysis of these types of molecular motions is important as they can have an impact on the compatibility of a polymer for a particular use. When considering appropriate plastic packaging in the food and beverage industry, significant attention is paid to the oxygen permeation characteristics of the polymer.<sup>129</sup> These characteristics are linked to the dynamic motions which can be identified by solid-state NMR.<sup>130</sup>

### 5.2.2. DNP-Enhanced Solid-state NMR of Polymers

Dynamic Nuclear Polarization (DNP) enhanced solid-state NMR of polymers is a useful technique when the inherent insensitivity of solid-state NMR is a barrier to analysis of the material. DNP may be necessary when working with very small volumes of a material, or to analyse intrinsically dilute aspects of a polymer such as cross-links or chain ends.

When analysing functional materials, it is important to study the structure of the material in the state it will be used as this can explain the characteristic properties of conjugated polymers including their semi-conductor abilities and favourable mechanical properties. Due to the nature of their sample as a thin film, allowing

them only a small quantity of analyte, Chaudhari *et al.* used a combination of DNP experiments and simulations to analyse the backbone structure of the donor-acceptor conjugated polymer diketopyrrolo-pyrrole-dithienylthieno[3,2-b] thiophene (DPP-DTT).<sup>131</sup> A <sup>1</sup>H DNP enhancement of around 15 to 45, depending on the film deposition technique, allowed the authors to analyse just 0.1 mg of the donor-acceptor stacking in thin films of DPP-DTT. The DNP enhancement made it possible to obtain high resolution two-dimensional <sup>1</sup>H-<sup>13</sup>C NMR data in a reasonable time frame. This data provided an insight to the modes of charge transport *via* the backbone of these materials.

Another photocatalytic material that requires improved structural analysis before performance can be optimized are polymeric carbon nitrides (PCNs). The photocatalytic properties of PCNs are of great interest and it is generally believed that good photocatalytic activity can be attributed to disorder in structure. It is however incredibly difficult to analyse this disorder in PCNs. Li *et al.* employed DNP to analyse the structural defects of PCNs to determine where these defects affect the photocatalytic activity.<sup>132</sup> The authors compared two PCNs prepared in different ways PCN-P prepared via templating and PCN-B which is prepared thermally. Tests show that PCN-B has a photocatalytic activity 17 times lower than PCN-P. DNP-enhanced NMR allowed Li *et al.* to perform several correlation experiments including a natural abundance <sup>13</sup>C-<sup>15</sup>N double CP correlation experiment. The high resolution of these spectra allowed for a full structural assignment, including information on structural defects.

Ouari *et al.* have shown the application of DNP to end group analysis of polymers.<sup>133</sup> This is of particular interest in *living polymers*, where the end groups may go on to react further. Analysing these end groups is difficult, as they are inherently dilute in comparison to the polymer backbone. DNP again is an obvious choice to enhance the signal intensity and allow for identification of any signals which could be attributed to the end groups. Using the film casting sample preparation method to prepare samples of living polystyrene (PS) and poly(ethylene oxide) (PEO) in a solution of bCTbK radical in dichloromethane they achieved an enhancement,  $\epsilon_{DNP} \approx 6$ . This enhancement provided a spectrum with high enough resolution to determine the end group location and structure of the living polymers. Additionally, they were able to confirm that the



reaction of the initiator and PEO had not gone to completion as they could see signals characteristic of the acrylate PEO starting material.

Creating chemical libraries can streamline future endeavors to create new materials with less of an iterative approach. However, for polymers their amorphous and generally insoluble nature means their structures cannot be determined by common high throughput analytical techniques. Solid-state NMR is also unfeasible for the creating of libraries due to the extremely long experiment times. Blanc *et al.* used DNP-enhanced NMR with shortened experiment times as a high throughput characterization technique to facilitate the creation of a library of microporous organic polymers (MOPs) prepared by combinatorial chemical methods.<sup>134</sup> The MOPs all follow the structure P1-RX where P1 is the backbone polymer and R is the specific end group, with concentration X. The very low percentage of functionalization of the R groups in these high molecular weight polymers, meant that the identification of these groups was not possible with standard solid-state NMR. Blanc *et al.* achieved a DNP enhancement,  $\epsilon_{DNP} = 13$  on a  $^1\text{H}$ - $^{13}\text{C}$  CP spectrum of P1, this allowed them to fully assign and determine the structure of the polymer backbone. Similar enhancements were achieved for the functionalized P1-RX samples and as such spectra with high enough resolution were obtained that the functional groups could be identified. These spectra were obtained in 256 scans or fewer, corresponding to experiment times of less than 1 hour, compared to over 5 hours for standard solid-state NMR experiments.

While the previous examples of DNP of polymers are excellent examples of the usefulness of the technique, they all benefit from simple and effective sample preparation. Many of the samples presented are *porous* polymer structures which allow the radical to be homogeneously distributed through the pores of the material. In the case of the living polymers studied by Ouari *et al.*, the samples used were able to be solubilized and the film-casting sample preparation was used, this again ensures a homogeneous distribution of the radical. If the material does not allow for such a distribution of the radical and as a result the radical is localized on the surface, the success of the DNP enhancement relies on the relaxation properties of the material. It has been shown by Rossini *et al.* that samples with long  $^1\text{H}$   $T_1$  relaxation values ( $T_1 > 100$  s) can achieve substantial

DNP enhancement factors due to efficient  $^1\text{H}$  spin diffusion carrying the polarization from the radical on the surface to the bulk of the sample during the long relaxation process.<sup>135</sup> For samples which have short  $T_1$  relaxation times the transfer of polarization cannot penetrate as thoroughly in the time available and DNP enhancements can be poor or non-existent. These examples demonstrate the benefits of DNP of polymers but highlight the limitations that current DNP sample preparation techniques impose.

### 5.2.3. DNP Sample Preparation of Polymers

For polymers which are insoluble and non-porous this presents a challenge in finding a suitable sample preparation procedure. Even at the cryogenic temperatures used for DNP experiments, the  $T_1$  values for polymers can be very short due to the presence of methyl groups, acting as relaxation sinks.<sup>136</sup> In addition, the amorphous nature of polymers and short-range order can hinder efficient spin diffusion through the bulk of the material and result in a misrepresentation of the sample. For these reasons, finding a sample preparation technique which is capable of evenly distributing the radical throughout these solid polymers is necessary to ensure effective DNP is possible.

An optimization of the sample preparation procedure was investigated by Le *et al.* for samples of polystyrene (PS) and poly(lactic acid) (PLA).<sup>30</sup> They compared methods of preparing polymer samples using the glass forming and film casting methods using the radicals bCTbK and TEKPol. The overall conclusions of this study show that there can be benefits to both the glass forming and film casting methods in different situations. The greatest DNP enhancement was achieved by the GF technique however, there was also a significant loss of resolution due to increased disorder in the presence of the solvent. While the FC technique gave a smaller enhancement, there was less broadening of the lines and the spectral resolution remained largely unchanged in comparison to a standard solid-state NMR experiment.

To compare the effect of the two techniques, they compared the absolute sensitivity ratios, as described in Section 2.2.5. This allows the authors to

systematically compare the different sample preparation methods for different polymers. They found that the increased enhancement gained with the GF method was most applicable for fully amorphous polymers whose spectral linewidth is broad to begin with, however for polycrystalline polymers where spectral resolution may be of the utmost importance for intricate structural determination, the FC method may be preferred, despite the lesser enhancements. They conclude that the reason for decreased enhancements despite the effective larger volume of sample in the FC method is due to a non-uniform distribution of polarizing agent throughout the sample. This could be a result of the slow evaporation of solvent leaving the polymer time to organize itself into crystalline domains, excluding the polarizing agent from these domains.

Experiments performed by Le *et al.* using the incipient wetness impregnation technique show very little to no enhancement. They determine that the reason for this was the difficulty they had to find a solvent which would solubilize the radical but not the polymer. By using the radical bTbK<sup>137</sup> they were able to find a suitable solvent system, but the resulting DNP enhancements were negligible especially in comparison to those achieved using the FC and GF methods. Their results using the IWI technique are consistent with the observations of Rossini *et al.* that heterogeneously impregnated samples require very long spin-lattice relaxation times to achieve good DNP enhancements.<sup>135</sup>

To limit the negative line broadening effect of the GF method while still ensuring a homogeneous distribution of radical, Tanaka *et al.* combined the principals of the GF and IWI techniques to develop guidelines for sample preparation of cross-linked polymers by swelling.<sup>138</sup> Their procedure involves adding minimal volumes of a radical solution which will swell the polymer sample, without fully dissolving the material. The swollen polymer sample is then packed into the rotor and frozen at  $\sim 100$  K inside the cooled probe.

By analysing the apparent DNP enhancement in the microwave on *vs.* microwave off spectra of their samples,  $\epsilon$ , alongside a signal quenching factor,  $\theta$ , and the ratio of relaxation rates of the sample containing radical solution,

$T_{DNP}$  and a sample with only the solvent,  $T_1$ , the authors compared the overall DNP enhancement of a series of cross-linked polymers.

They compared the overall enhancement achieved with two different radical solutions – one which would swell some of the polymer samples, and a second which would swell the other polymers. They also investigated the effect that how much the polymers swelled had on the resultant overall DNP enhancement.

Tanaka *et al.* presented a very clear set of data showing that the overall DNP enhancement is directly linked to the extent of swelling of a polymer sample. The polymers that swelled in an organic radical solution showed positive DNP enhancements while the polymers that did not swell in that solution showed no DNP enhancement. Conversely, the polymers that did not swell in the organic solvent, did swell in an aqueous radical solution and these samples did show positive DNP enhancements in that case, while the polymers that did not swell in aqueous solutions showed no DNP enhancement. They allowed these samples to stand at room temperature for 2 hours before cooling to 100 K to ensure that they swelled fully in the radical solutions. Experiments done on optimizing this impregnation time showed that there was also a positive correlation between long standing times and higher DNP enhancements. This adds to their conclusions that a more swollen polymer sample results in a better DNP enhancement.

The authors conclude that this relationship between achieved DNP enhancement and the extent of the swelling of a polymer in a radical solution is due to the higher concentration of radical present in more swollen samples. They confirmed this with EPR data which showed that the samples that had higher DNP enhancements also had higher concentration of electron spin.

The authors did consider the effects that the solvents themselves could have on the outcome and were able to show there was no correlation between increased deuteration and increased DNP enhancement. However, they did not present any work relating to the swelling effect of the solvents which was disconnected from radical concentration. Given the reported importance of swelling in achieving any DNP enhancement, it is likely that the extent of swelling is linked to a more thorough dispersion of radical throughout the sample. It follows that there is a

possibility that it is not the radical concentration alone that results in higher DNP enhancements of more swollen polymers. Understanding the impact of swelling alone on the DNP enhancements of polymers will provide the opportunity to better improve the sample preparation techniques used for polymers to optimise sensitivity and resolution.

## 5.3. Experimental Details

### 5.3.1. Materials

Sodium polyacrylate (NaPA, cross-linked), poly(ethylene oxide) (PEO,  $M_v = 1,000,000$ ), and poly(2-hydroxyethyl methacrylate) (PHEMA,  $M_v = 1,000,000$ ) were purchased from Sigma-Aldrich. Polystyrene (PS,  $M_v = 290,000$ ) was purchased from Thermo Fisher Scientific. All chemicals were used as received.

### 5.3.2. Sample Preparation

The general procedure for polymer sample preparation involved impregnation of a powder sample with a radical following a similar protocol to the incipient wetness impregnation technique.<sup>31</sup> Typically a measured amount of polymer was wetted or swollen in the desired volume of radical solution. The samples were mixed thoroughly and re-weighed. The samples were then packed into 3.2 mm sapphire rotors and inserted into the pre-cooled probe and were rapidly cooled to 100 K.

The radical solutions used to prepare samples from Sections 5.4.1 and 5.4.2 are listed in Table 5.1. The details of the radical solution used to prepare samples in Section 5.4.3 are provided in Table 5.8. Specific details of which radical solution, and the volume used for each sample are provided alongside the results. Where possible, samples were impregnated immediately before measuring, rather than in advance. For the DQ build-up experiments, it was not possible to prepare the samples one at a time, so all samples were prepared 7 days in advance of any measurements.

Radical	Solvent
10 mM AMUPol	3 M Ca(NO <sub>3</sub> ) <sub>2</sub> D <sub>2</sub> O/H <sub>2</sub> O (90/10 vol%)
10 mM AMUPol	Glycerol-d <sub>8</sub> /D <sub>2</sub> O/H <sub>2</sub> O (60/30/10 vol%)
10 mM AMUPol	D <sub>2</sub> O/H <sub>2</sub> O (90/10 vol%)
10 mM AMUPol	D <sub>2</sub> O (100 vol%)
17 mM TEKPol	TCE

*Table 5.1: Radical solutions used for sample preparation.*

### 5.3.3. DNP-Enhanced Solid-state NMR

DNP-enhanced solid-state NMR experiments were performed on a Bruker Avance III HD spectrometer operating at a <sup>1</sup>H Larmor frequency,  $\nu_{0H} = 600$  MHz (14.1 T), equipped with a double resonance low-temperature 3.2 mm CP-MAS probe. The microwave source to generate electron polarisation was a 7.2 T gyrotron emitting 395 GHz microwaves at 5 W power.

Polymer samples were packed directly into 3.2 mm sapphire rotors and inserted into the pre-cooled probe and were rapidly cooled to 100 K. Each sample was subjected to multiple freeze-thaw cycles by ejecting and reinserting the rotor. Experiments were performed under low temperature MAS. Temperatures ranged from 98-110 K. Spinning frequencies ranged from 8-10 kHz.

<sup>1</sup>H-<sup>13</sup>C CP was achieved using a 90 to 100 % ramp on the <sup>1</sup>H channel for 2 ms and <sup>1</sup>H decoupling was applied during acquisition using a swept-frequency two-pulse phase modulation (SWf-TPPM) sequence. Recycle delays used were determined for each sample from the <sup>1</sup>H-<sup>13</sup>C CP DNP build-up time.

DNP build-up times were determined using a <sup>1</sup>H-<sup>13</sup>C CP saturation recovery sequence. 8 transients were co-added and a recycle delay of 100 ms was used. Between 16 and 32 points were recorded with variable polarization times ranging from 4 ms to 600 s.

### 5.3.4. Double-Quantum NMR

$^1\text{H}$ - $^1\text{H}$  double-quantum build-up experiments were performed on a Bruker Avance III spectrometer operating at a  $^1\text{H}$  Larmor frequency of  $\nu_{0H} = 600$  MHz (14.1 T) using a double-resonance BBFO+ solution-state probe.

DQ experiments were recorded using the pulse sequence described in Section 3.3 for static solids. The DQ filtered ( $I_{DQ}$ ) and reference ( $I_{ref}$ ) spectra were recorded in an interleaved experiment, resulting in a *pseudo-3D* data set which was split into two 2D data sets containing the  $I_{DQ}$  build-up in one, and the  $I_{ref}$  build-up in the other. The  $^1\text{H}$   $90^\circ$  pulse length was  $25 \mu\text{s}$ , the duration of the twelve-pulse excitation block was  $t_c = 0.5$  ms and the number of times this block was repeated ranged from  $n_c = 0$  to 70. A DQ pre-selection filter was also used which involved applying the DQ excitation and reconversion blocks twice, separated by a z-filter delay,  $\tau_z = 1$  ms. The pre-selection  $\tau_{DQ} = 4$  ms ( $t_c = 0.5$  ms  $n_c = 8$ ). 256 transients were co-added for each of the 46 values of  $\tau_{DQ}$ , for both  $I_{DQ}$  and  $I_{ref}$ , with a recycle delay of 1.5 s.

#### 5.3.4.1. Data Analysis

Experimental data was initially processed in TopSpin by normalizing the integrated intensity of each  $I_{ref}$  and  $I_{DQ}$  1D data slice to the intensity of the first  $I_{ref}$  spectrum. These values were then used to determine the normalized DQ coherence build-up using Equations [5.3.4.1] and [5.3.4.2]:

$$I_{\Sigma DQ} = I_{ref} + I_{DQ} \quad [5.3.4.1]$$

$$I_{nDQ} = \frac{I_{DQ}}{I_{\Sigma DQ} - I_{defect}} \quad [5.3.4.2]$$

Dividing the experimental DQ intensity by  $I_{\Sigma DQ} - I_{defect}$  removes the effect of relaxation.  $I_{defect}$  is a correction applied to the normalized DQ build-up to account for liquid-like components which contribute to  $I_{ref}$ . Since these liquid-like components do not possess any RDC they do not contribute to  $I_{DQ}$  and as a result, without the removal of  $I_{defects}$ , the normalized DQ

build-up,  $I_{nDQ}$ , would be underestimated.  $I_{defect}$  is found by fitting the long  $\tau_{DQ}$  range of  $I_{ref} - I_{DQ}$ .<sup>139</sup>

$$I_{ref} - I_{DQ} = B e^{-\frac{2\tau_{DQ}}{T_{2,B}^*}} \quad [5.3.4.3]$$

where  $B$  is the fraction of isotropic component and  $T_{2,B}^*$  is the apparent transverse relaxation of this component. This correction is necessary to ensure the DQ coherence build-up curve reaches the expected plateau of 50 % intensity.

The normalized DQ coherence build-up curves were then fitted to the ‘‘Abragam-like’’ (A-l) function in Equation [5.3.4.4] and distributions of the RDC constants  $D_{res}$  were calculated using the program *ftikreg*.<sup>140</sup>

$$I_{nDQ}^{A-l}(\tau_{DQ}, D_{res}) = 0.5 \left( 1 - e^{-\{0.378D_{res}\tau_{DQ}\}^{1.5}} \right) \cdot \cos(0.538D_{res}\tau_{DQ}) \quad [5.3.4.4]$$



## 5.4. Results and Discussion

The requirements for successful impregnation of polymers with radicals used for DNP-enhanced solid-state NMR have been investigated. Representative  $^1\text{H}$ - $^{13}\text{C}$  CP DNP spectra for all polymers used in this work and their spectral assignments are presented in Figure 5.1.

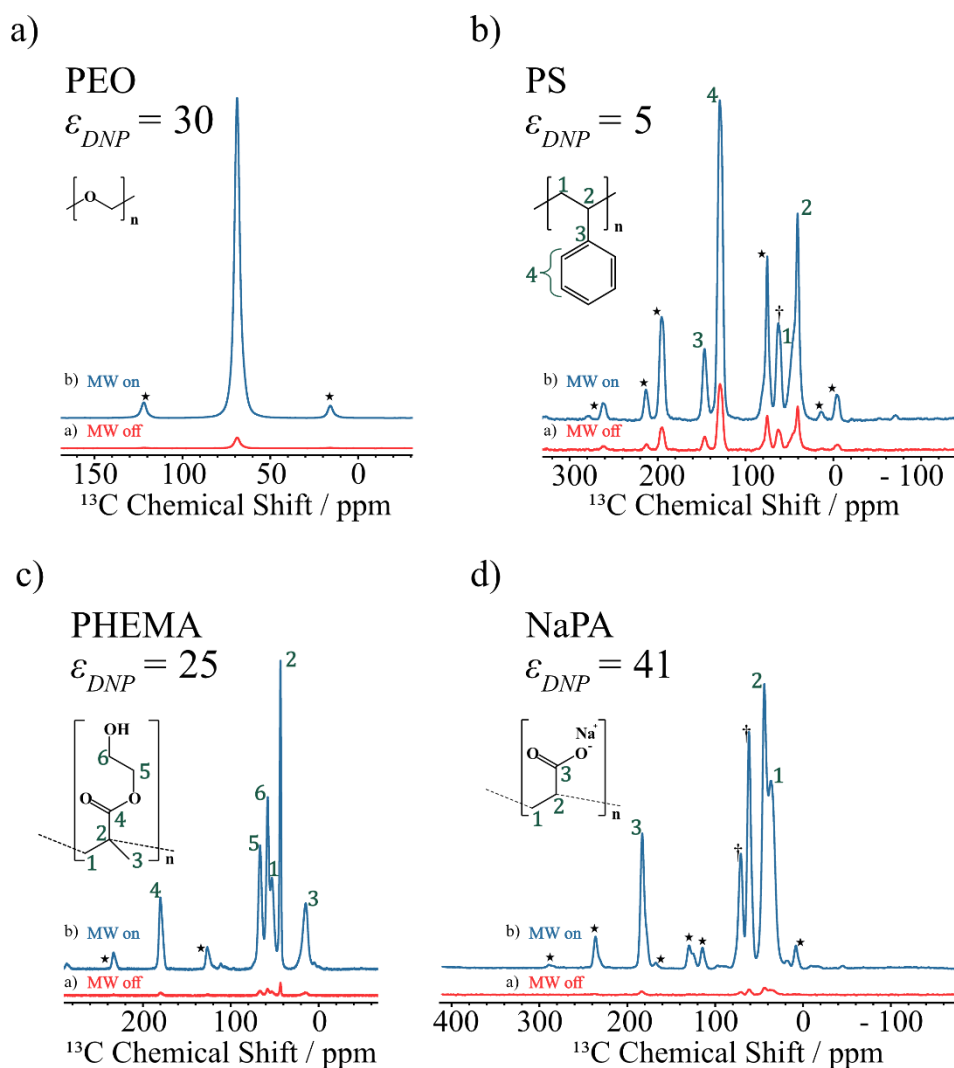


Figure 5.1:  $^1\text{H}$ - $^{13}\text{C}$  CP spectra a) without and b) with MW irradiation of the polymer samples used here. Poly(ethylene oxide) (PEO) (top left), polystyrene (PS) (top right), poly(2-hydroxyethyl methacrylate) (PHEMA) (bottom left), and sodium polyacrylate (NaPA) (bottom right). The polarizing agent used for a), c), and d) was AMUPol, TEKPol was the polarizing agent used for b). † marks signals from solvent used in sample preparation. Spinning sidebands are noted with ★.

## 5.4.1. Polymer Swelling

The requirement for a polymer to swell in the radical solution to ensure a homogeneous distribution of the polarization source was investigated by comparing the enhancements seen for two PEO and PS in radical solutions that would interact one but not the other. PEO is a very hydrophilic polymer that at low molecular weights will be soluble in aqueous solution, but at higher molecular weights will swell. The observed DNP enhancement, measured as the signal intensity of the spectrum with microwave irradiation relative to the intensity without microwave irradiation ( $\epsilon_{DNP} = I_{MWon}/I_{MWoff}$ ), linewidths, and the signal to noise enhancement ( $\chi_{DNP} = SNR/\sqrt{T_{DNP}}$ ) of PEO impregnated with AMUPol in an aqueous solution and TEKPol in organic solvent are presented in Table 5.2.

### PEO

Radical Solution	$\epsilon_{DNP}$	FWHM	$\chi_{DNP}$
10 mM AMUPol in D <sub>2</sub> O/H <sub>2</sub> O (90/10 vol%)	30.2	455 Hz	2711
17 mM TEKPol in TCE	1	379 Hz	145

Table 5.2: DNP enhancements, linewidths, and SNR enhancements for two samples of PEO impregnated in an aqueous solution (glycerol-*d*<sub>8</sub>/D<sub>2</sub>O/H<sub>2</sub>O) or organic solvent (TCE). Linewidths were calculated using the peakw function in TopSpin on data with 0 Hz line broadening applied  $\chi_{DNP} = \frac{SNR}{NS\sqrt{T_{DNP}}}$ .

It can be seen from the observed  $\epsilon_{DNP}$ , that the radical impregnation with aqueous solution has been much more effective for PEO. The aqueous solution sample preparation has however increased the linewidth of the signal in comparison to the sample prepared in TCE. The reduced linewidth of the TCE sample indicates the reduced swelling of this sample. The <sup>1</sup>H-<sup>13</sup>C CP spectra with and without MW irradiation for these samples can be seen in Figure 5.2.

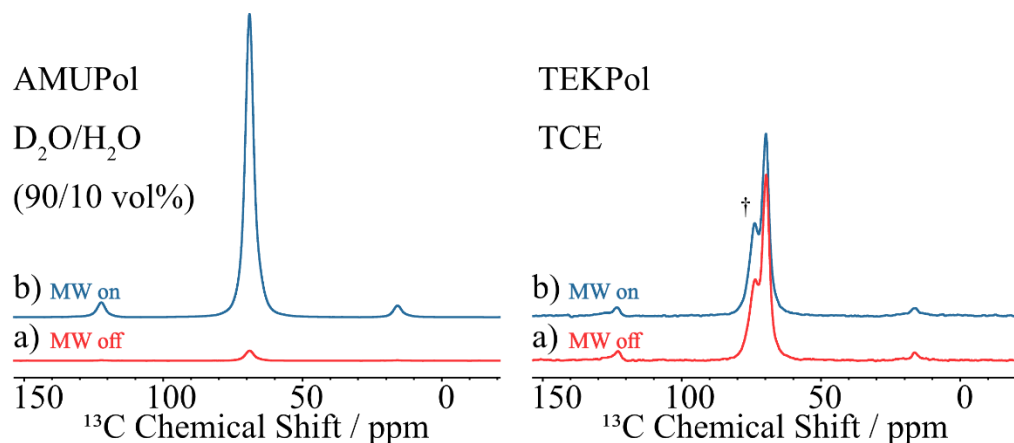


Figure 5.2:  $^1\text{H}$ - $^{13}\text{C}$  CP spectra a) without and b) with MW irradiation of PEO impregnated with AMUPol in  $\text{D}_2\text{O}/\text{H}_2\text{O}$  (90/10 vol%) (Left) and TEKPol in TCE (Right). † marks signals from solvent used in sample preparation.

Conversely to PEO, PS is a hydrophobic polymer. When impregnated with AMUPol in aqueous solution, the PS powder formed a suspension in the solution. The impregnation with TCE resulted in part solubilization and aggregation of the PS powder. The observed enhancements for these samples are presented in Table 5.3.

### PS

Radical Solution	$\epsilon_{DNP}$	FWHM	$\chi_{DNP}$
10 mM AMUPol in glycerol- $\text{d}_8/\text{D}_2\text{O}/\text{H}_2\text{O}$ (60/30/10 vol%)	0.8	909	22
17 mM TEKPol in TCE	4.9	960	112

Table 5.3: DNP enhancements, linewidths, and SNR enhancements for two samples of PS impregnated in an aqueous solution (glycerol- $\text{d}_8/\text{D}_2\text{O}/\text{H}_2\text{O}$ ) or organic solvent (TCE). The values of these observables were taken for the aromatic signal at 130 ppm as it was least obscured by solvent signals. Linewidths were calculated using the peakw function in TopSpin on data with 0 Hz line broadening applied.  $\chi_{DNP} = \frac{\text{SNR}}{NS\sqrt{T_{DNP}}}$ .

The sample of PS suspended in a solution of glycerol- $\text{d}_8/\text{D}_2\text{O}/\text{H}_2\text{O}$  exhibited no enhancement of the PS signals, as seen in Figure 5.3. There was in fact a slight decrease in intensity of the PS signals in the spectrum recorded with MW irradiation, this can be attributed to slight heating of the sample by the

microwaves. The signals arising from the glycerol present in this sample do exhibit significant DNP enhancements. This enhancement can be used as evidence that the lack of enhancement is due to an absence of radical in the polymer phase of the sample.

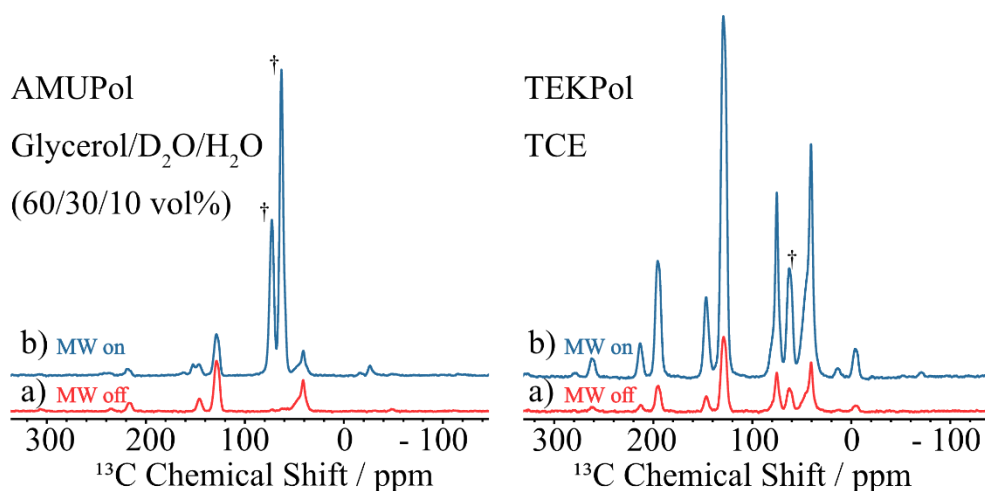


*Figure 5.3:  $^1\text{H}$ - $^{13}\text{C}$  CP spectra a) without and b) with MW irradiation of PS impregnated with AMUPol in glycerol- $d_8$ / $\text{D}_2\text{O}$ / $\text{H}_2\text{O}$  (60/30/10 vol%) (Left) and TEKPol in TCE (Right). The sample prepared in aqueous solution does not exhibit any enhancement of the signals assigned to PS, but there is a large enhancement of the signals assigned to glycerol. This demonstrates that the DNP process is effective in this sample, but the polymer does not experience this. † marks signals from solvent used in sample preparation.*

Although these results show some correlation between the affinity of the solvent and polymer and the observed DNP enhancement, there is a possibility that there is also an influence of the affinity of the radical itself and the polymer.

The effect of swelling alone was further investigated by looking at the impact of the volume of radical solution used. This allowed for a view of the impact of swelling without any potential interference from the effects of different radicals.

The effect of the volume of radical solution was investigated by preparing two samples of PEO with different volumes of 10 mM AMUPol in  $\text{D}_2\text{O}$  (100 %). The sample preparation details are presented in Table 5.4.

Mass of Polymer	Volume of Radical Solution	Polymer Content	$\epsilon_{DNP}$	FWHM	$\chi_{DNP}$
30 mg	50 $\mu\text{L}$	35 wt%	22.8	456 Hz	905
20 mg	14 $\mu\text{L}$	56 wt%	19.5	579 Hz	1362

Table 5.4: Sample preparation details of two samples of PEO prepared with different volumes of a radical solution, 10 mM AMUPol in  $D_2O$  (100 %): mass of polymer, volume of radical solution added, and resulting wt% of polymer content in the final sample; and DNP enhancements, linewidths and SNR enhancement. Linewidths were calculated using the `peakw` function in TopSpin on data with 0 Hz line broadening applied.  $\chi_{DNP} = \frac{SNR}{NS\sqrt{T_{DNP}}}$ .

Following expectations set in the previous results in this work and in the literature, the sample which has been swelled in more of the radical solution results in a higher  $\epsilon_{DNP}$ . However, the higher polymer content in the second sample contributes to a higher SNR of the spectrum without MW irradiation to such an extent that the sensitivity of the less swollen polymer is higher. A comparison of the spectra can be seen in Figure 5.4.

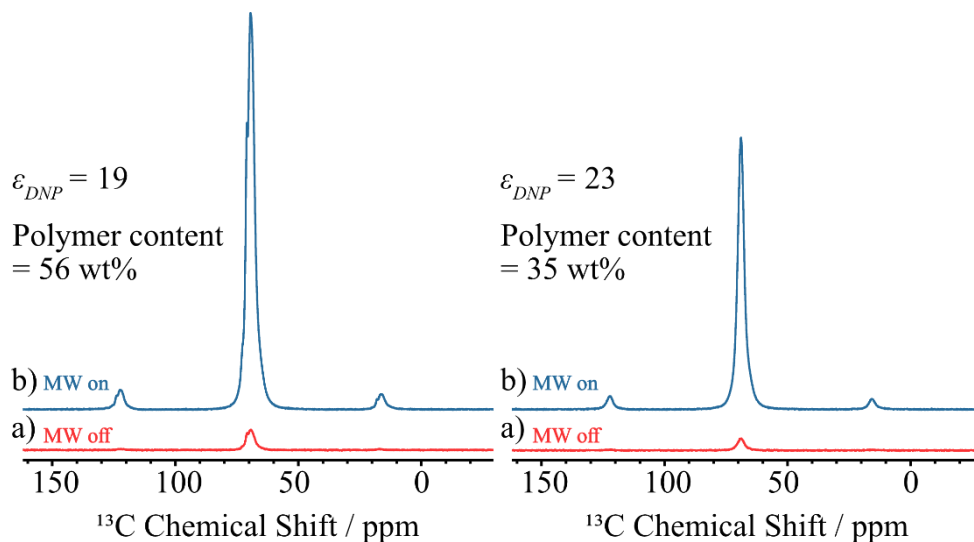


Figure 5.4:  $^1H$ - $^{13}C$  CP spectra a) without and b) with MW irradiation of two samples of PEO impregnated with different volumes of radical solution, 10 mM AMUPol in  $D_2O$  (100 %). The sample with a lower volume of radical solution (Left) exhibits a lower  $\epsilon_{DNP}$  but the higher polymer content of the sample results in an improved resolution.

In this case, the increased volume of radical solution has reduced the linewidth of the spectrum, contrary to what is expected. However, the reduced linewidth does not necessarily afford improved resolution of the spectrum. The low temperature  $^1\text{H}$ - $^{13}\text{C}$  CP standard NMR spectrum of dry PEO shows several distinct maxima, resulting from distortion of the helical structure of the polymer chains.<sup>141,142</sup> 2D solid-state NMR experiments identified, in a 2 ppm range, 14 distinct environments in the repeat unit of crystalline PEO.<sup>143</sup> In amorphous PEO, the C-C bonds take a predominately (~80 %) *gauche* configuration and the C-O bonds are predominately (~70 %) *trans*, and in crystalline PEO all C-C bonds are *gauche* and all C-O bonds are *trans* but with a distortion of torsion angles of these bonds. The semi-crystalline PEO samples used here will therefore have a wide range of distinct  $^{13}\text{C}$  environments.

In aqueous solutions of PEO, it has been seen that the *gauche* conformation of C-C bonds becomes increasingly favourable as the water volume fraction is increased,<sup>144</sup> this may account for the apparent homogeneous linewidth seen here for the sample of PEO with a higher proportion of radical solution. In Figure 5.5, the intensities of the spectra with MW irradiation of these two samples have been matched and the differences in the shape of the spectra is demonstrated. The sample with a lower volume of radical solution added exhibits two additional resolved peaks, although its linewidth does appear to have been broadened, the shape of this spectrum shares more similarities with that of dry, pristine PEO. The narrower, single peak observed in the spectrum of the sample prepared with a higher volume of radical solution indicates that there has been some D<sub>2</sub>O induced change in conformation of the polymer chains.

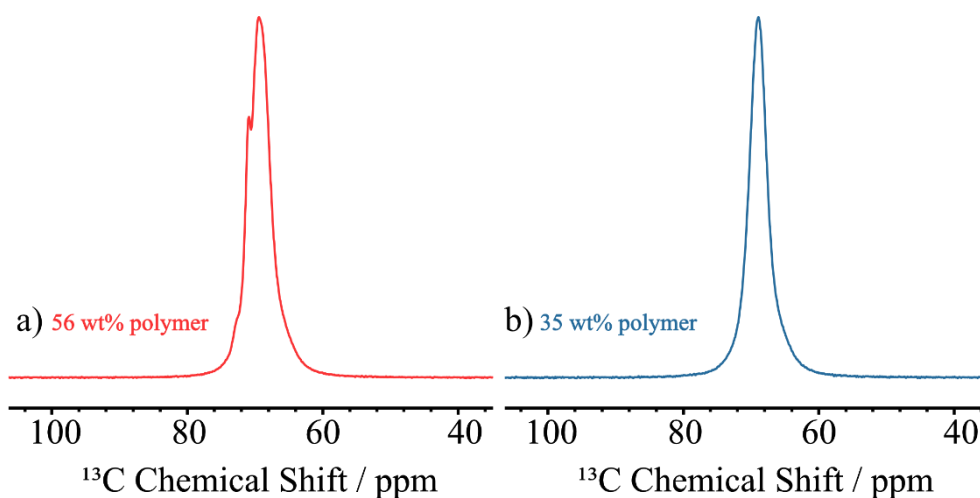


Figure 5.5:  $^1\text{H}$ - $^{13}\text{C}$  CP spectra with MW irradiation of PEO impregnated with a) 14  $\mu\text{L}$  and b) 50  $\mu\text{L}$  of 10 mM AMUPol in  $\text{D}_2\text{O}$  (100 %). Spectrum a) exhibits a larger linewidth but additional resolved peaks indicating a more disordered conformation of polymer chains.

The changes in the spectrum of PEO as the volume of radical solution increases indicates the importance of considering the impact that DNP sample preparation will have on the sample. While good DNP enhancements can be achieved on polymers by swelling them in a radical solution, these enhancements may not be useful if the sample has been changed in the process.

### 5.4.2. Role of a ‘Glass-former’

For DNP sample preparation for most materials the use of a ‘glass-former’ or cryoprotectant, is of utmost importance due to the low temperatures at which DNP experiments are performed. Without a glass-former the radical solution will crystallize and cause aggregation of the radical which limits the achievable DNP enhancement.

The commonly used solvents for DNP sample preparation which provide this glass-forming function (TCE and glycerol- $\text{d}_8/\text{D}_2\text{O}/\text{H}_2\text{O}$  solution) present a limitation in the study of organic materials with DNP. The  $^{13}\text{C}$  signal of these solvents can overlap and obscure the signals of interest. Figure 5.6 demonstrates this overlap for a sample of PEO.

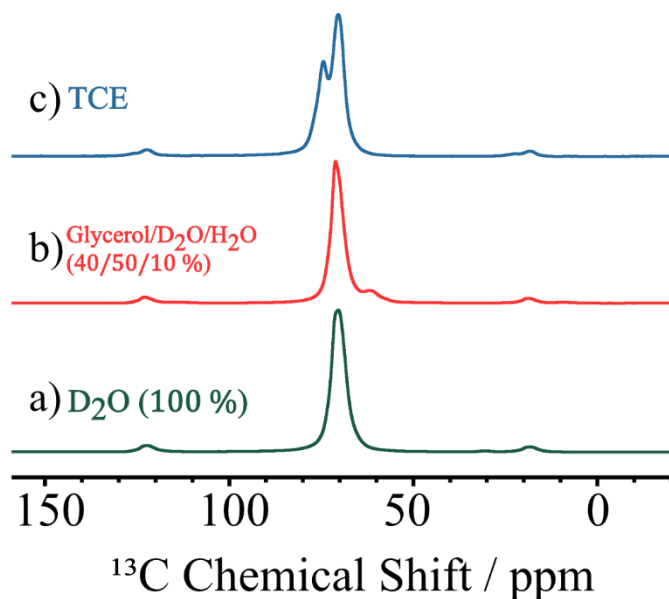


Figure 5.6:  $^1\text{H}$ - $^{13}\text{C}$  CP spectra recorded with MW irradiation of PEO impregnated with 10 mM AMUPol in a)  $\text{D}_2\text{O}$  (100 %), b) glycerol- $d_8$ / $\text{D}_2\text{O}$ / $\text{H}_2\text{O}$  (40/50/10 vol%), and c) with 17 mM TEKPol in TCE. The comparison demonstrates the complete overlap of the PEO resonance by the signals of glycerol and TCE.

Several strategies to overcome this problem exist such as solvent signal suppression<sup>145,146</sup> and the use of inorganic glass-forming agents such as a  $\text{Ca}(\text{NO}_3)_2$  solution. However, for polymers where it appears to be important that the sample swells in the radical solution, the use of glycerol or  $\text{Ca}(\text{NO}_3)_2$  presents an additional limitation as they may reduce the absorbancy of the polymer.<sup>147</sup>

In the effort to improve the sample preparation process for polymers, the requirement to have a glass-forming agent at all was investigated. Samples of PEO, PHEMA, and NaPA were prepared using 30 mg of polymer and 50  $\mu\text{L}$  of a 10 mM AMUPol solution in a range of aqueous solutions. For PEO (Table 5.5, Figure 5.7) and PHEMA (Table 5.6, Figure 5.8) the DNP enhancements and SNR enhancements were higher for samples which did not contain glycerol or  $\text{Ca}(\text{NO}_3)_2$ . For NaPA (Table 5.7, Figure 5.9), the opposite was true and the samples containing glycerol and  $\text{Ca}(\text{NO}_3)_2$  achieved higher DNP and SNR enhancements.



## PEO

Solution	$\epsilon_{DNP}$	FWHM	$\chi_{DNP}$
Glycerol-d <sub>8</sub> /D <sub>2</sub> O/H <sub>2</sub> O (60/30/10 vol%)	15.5	328	615
3 M Ca(NO <sub>3</sub> ) <sub>2</sub> D <sub>2</sub> O/H <sub>2</sub> O (90/10 vol%)	21.4	545	1281
D <sub>2</sub> O/H <sub>2</sub> O (90/10 vol%)	30.2	455	2711
D <sub>2</sub> O (100 vol%)	22.8	456	905

Table 5.5: DNP enhancements, linewidths, and SNR enhancement factors for  $^1\text{H}$ - $^{13}\text{C}$  CP DNP experiments of  $\sim 30$  mg of PEO impregnated with AMUPol using  $50 \mu\text{L}$  of a 10 mM solution in different aqueous solutions. Linewidths were calculated using the `peakw` function in TopSpin on data with 0 Hz line broadening applied.  $\chi_{DNP} = \frac{SNR}{NS\sqrt{T_{DNP}}}$ .

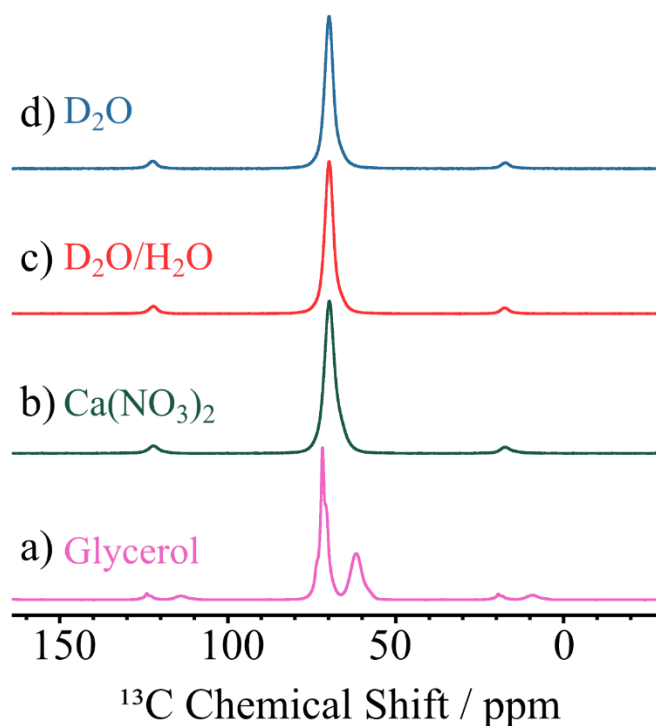


Figure 5.7:  $^1\text{H}$ - $^{13}\text{C}$  CP spectra, intensities scaled to match, recorded with MW irradiation of PEO impregnated with 10 mM AMUPol in a) glycerol-d<sub>8</sub>/D<sub>2</sub>O/H<sub>2</sub>O (60/30/10 vol%), b) 3 M Ca(NO<sub>3</sub>)<sub>2</sub> solution in D<sub>2</sub>O/H<sub>2</sub>O (90/10 vol%), c) D<sub>2</sub>O/H<sub>2</sub>O (90/10 vol%), and d) D<sub>2</sub>O (100 %). Spectrum a) demonstrates the much better resolution of the PEO signal in the sample prepared with glycerol, indicating that there is less swelling of this sample which could be responsible for the lower  $\epsilon_{DNP}$ .

## PHEMA

Solution	$\epsilon_{DNP}$	FWHM	$\chi_{DNP}$
Glycerol-d <sub>8</sub> /D <sub>2</sub> O/H <sub>2</sub> O (60/30/10 vol%)	7.8	865	79
3 M Ca(NO <sub>3</sub> ) <sub>2</sub> D <sub>2</sub> O/H <sub>2</sub> O (90/10 vol%)	18.3	688	66
D <sub>2</sub> O/H <sub>2</sub> O (90/10 vol%)	24.8	706	220
D <sub>2</sub> O (100 vol%)	20.1	717	92

Table 5.6: DNP enhancements, linewidths, and SNR enhancement factors for  $^1\text{H}$ - $^{13}\text{C}$  CP DNP experiments of  $\sim 30$  mg of PHEMA impregnated with AMUPol using  $50 \mu\text{L}$  of a  $10 \text{ mM}$  solution in different aqueous solutions. Linewidths were measured for the carbonyl resonance at  $180 \text{ ppm}$  as this resonance is least impacted by the overlapping solvent signals. Linewidths were calculated using the *peakw* function in TopSpin on data with  $0 \text{ Hz}$  line broadening applied.

$$\chi_{DNP} = \frac{SNR}{NS\sqrt{T_{DNP}}}$$

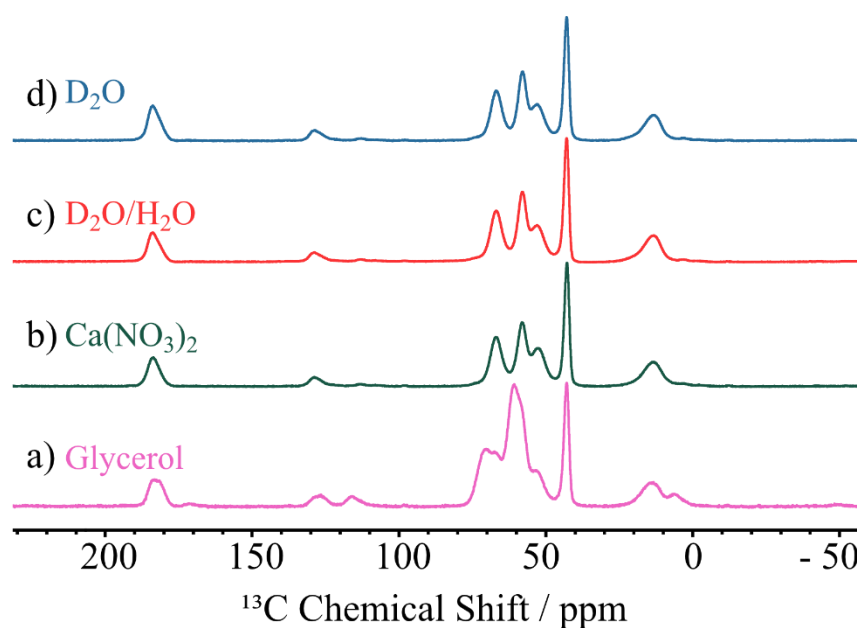


Figure 5.8:  $^1\text{H}$ - $^{13}\text{C}$  CP spectra, intensities scaled to match, recorded with MW irradiation of PHEMA impregnated with  $10 \text{ mM}$  AMUPol in a) glycerol-d<sub>8</sub>/D<sub>2</sub>O/H<sub>2</sub>O (60/30/10 vol%), b)  $3 \text{ M}$  Ca(NO<sub>3</sub>)<sub>2</sub> solution in D<sub>2</sub>O/H<sub>2</sub>O (90/10 vol%), c) D<sub>2</sub>O/H<sub>2</sub>O (90/10 vol%), and d) D<sub>2</sub>O (100 %)

### NaPA

Solution	$\epsilon_{DNP}$	FWHM	$\chi_{DNP}$
Glycerol-d <sub>8</sub> /D <sub>2</sub> O/H <sub>2</sub> O (60/30/10 vol%)	41.0	668	80
3 M Ca(NO <sub>3</sub> ) <sub>2</sub> D <sub>2</sub> O/H <sub>2</sub> O (90/10 vol%)	13.6	754	211
D <sub>2</sub> O/H <sub>2</sub> O (90/10 vol%)	11.3	679	72
D <sub>2</sub> O (100 vol%)	10.9	708	73

Table 5.7: DNP enhancements, linewidths, and SNR enhancement factors for  $^1\text{H}$ - $^{13}\text{C}$  CP DNP experiments of  $\sim 30$  mg of NaPA impregnated with AMUPol using  $50 \mu\text{L}$  of a  $10 \text{ mM}$  solution in different aqueous solutions. Linewidths were measured for the carbonyl resonance at  $180 \text{ ppm}$ . Linewidths were calculated using the peakw function in TopSpin on data with  $0 \text{ Hz}$  line broadening applied.

$$\chi_{DNP} = \frac{SNR}{NS\sqrt{T_{DNP}}}$$

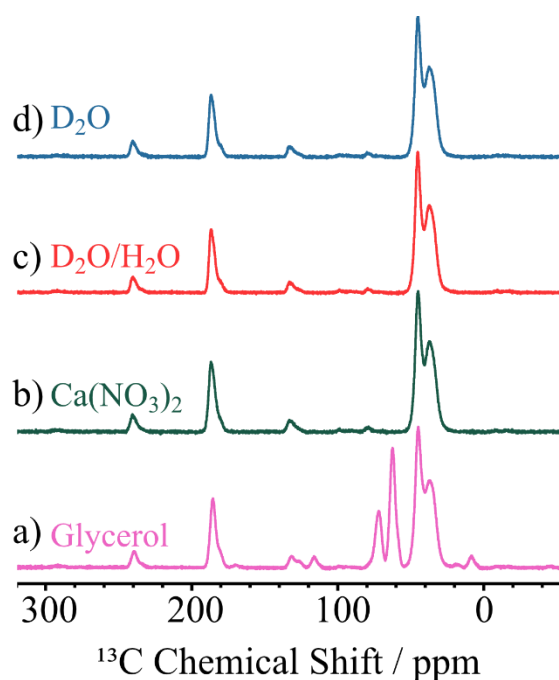


Figure 5.9:  $^1\text{H}$ - $^{13}\text{C}$  CP spectra, intensities scaled to match, recorded with MW irradiation of NaPA impregnated with  $10 \text{ mM}$  AMUPol in a) glycerol-d<sub>8</sub>/D<sub>2</sub>O/H<sub>2</sub>O (60/30/10 vol%), b)  $3 \text{ M}$  Ca(NO<sub>3</sub>)<sub>2</sub> solution in D<sub>2</sub>O/H<sub>2</sub>O (90/10 vol%), c) D<sub>2</sub>O/H<sub>2</sub>O (90/10 vol%), and d) D<sub>2</sub>O (100 %).

The difference in enhancement behaviour seen could be the result of several processes, such as the extent of swelling of the polymers being impacted differently. In Figure 5.7a, although the signal of PEO is expected to be somewhat perturbed by an overlapping glycerol signal, the linewidth is narrower and resolution is better than the other PEO samples. It may be argued that the resolution seen here is the result of a different conformation of the polymer, as seen in Figure 5.5a. However, the significantly narrower linewidth, which is only observed in the samples prepared in TCE and the glycerol solution, leads to the conclusion that this is an observation of reduced swelling of PEO in the glycerol solution. The enhancements seen for PEO prepared with the  $\text{Ca}(\text{NO}_3)_2$  solution and 100 %  $\text{D}_2\text{O}$  are very similar however the enhancement for the sample prepared with  $\text{D}_2\text{O}/\text{H}_2\text{O}$  (90/10) is much higher. The effect of deuteration on the enhancement seen here differs from the observations seen for other polymers in the literature.<sup>30,138</sup> It has been seen that as the concentration of  $^1\text{H}$  in polymers tends to be significantly higher than other types of materials, even at 100 % deuteration of the solvent, there is sufficient  $^1\text{H}$  concentration to mediate efficient spin diffusion. The reduced enhancement seen here for the fully deuterated solvent suggests that the  $^1\text{H}$  concentration of PEO is not sufficiently high to self-mediate the spin diffusion.

For PHEMA, where the enhancement behaviour is the same as PEO, the spectrum in Figure 5.8a is significantly obscured by the glycerol signal, inhibiting a comparison of the spectral linewidths. This precludes an assessment of whether the glycerol solution has had an impact on the swelling of PHEMA. Nevertheless, the good enhancements seen for samples prepared without a glass-forming agent confirm that PHEMA can perform this function itself and facilitate efficient DNP.

Given the function of NaPA as a superabsorbent polymer, it is less likely that the large differences in enhancements seen for different radical solutions is due to changes in swelling behaviour. It is possible that the improvement of enhancements of NaPA with the addition of glycerol or  $\text{Ca}(\text{NO}_3)_2$  is due to a reduced ability for NaPA to act as a glass-former compared to PEO and PHEMA.

For both PHEMA and NaPA, the sample prepared with 100 % D<sub>2</sub>O shows only a slightly lower enhancement than the sample which has 10 % H<sub>2</sub>O content. This is consistent with observations for other polymers presented in the literature.<sup>30,138</sup>

### 5.4.3. Measuring the Effect of Swelling on DNP Enhancement

The research presented by Tanaka *et al.* which showed a positive correlation between the volume of radical solution used, and subsequent extent of polymer swelling, and the DNP enhancement achieved, led them to the conclusion that the increased radical concentration in the more swollen samples was the reason for the larger enhancements.<sup>138</sup> In this work, the extent of polymer swelling has been uncoupled from the radical concentration, to investigate the impact that the swelling itself has on the DNP enhancement.

A series of samples of NaPA were swollen in increasing volumes of a radical solution of AMUPol in D<sub>2</sub>O/H<sub>2</sub>O (90/10). As the volume of radical solution was increased, the concentration of AMUPol in the solution was decreased. This ensured that the radical concentration in the prepared samples was consistent. This was achieved by preparing a highly concentrated solution of 40 mM AMUPol in D<sub>2</sub>O/H<sub>2</sub>O (90/10), of which 5  $\mu$ L was used for each NaPA sample. The concentrated radical solution was then either added to the NaPA sample directly, or further diluted in increasing volumes of D<sub>2</sub>O/H<sub>2</sub>O (90/10) before being added to the polymer. Each sample was left to stand at room temperature for 10 minutes before being packed into a rotor and frozen at 100 K. The samples were each prepared immediately before measurement to eliminate any potential influence of prolonged impregnation time.<sup>138</sup> Details of the sample preparation and resulting radical concentration in the measured sample are presented in Table 5.8.

<b>Sample Reference</b>	<b>Polymer Mass</b>	<b>D<sub>2</sub>O/H<sub>2</sub>O (90/10) Volume</b>	<b>Polymer Mass in Rotor</b>	<b>Total Radical Solution Volume in Rotor</b>	<b>Radical Concentration in Rotor</b>
<b>1</b>	23.4 mg	0 $\mu\text{L}$	23.4 mg	5 $\mu\text{L}$	8.5 $\mu\text{mol g}^{-1}$
<b>2</b>	23.3 mg	10 $\mu\text{L}$	23.3 mg	15 $\mu\text{L}$	8.6 $\mu\text{mol g}^{-1}$
<b>3</b>	23.3 mg	20 $\mu\text{L}$	20.3 mg	22 $\mu\text{L}$	8.6 $\mu\text{mol g}^{-1}$
<b>4</b>	23.1 mg	30 $\mu\text{L}$	15.6 mg	24 $\mu\text{L}$	8.7 $\mu\text{mol g}^{-1}$
<b>5</b>	23.4 mg	40 $\mu\text{L}$	12.3 mg	24 $\mu\text{L}$	8.5 $\mu\text{mol g}^{-1}$
<b>6</b>	23.3 mg	50 $\mu\text{L}$	10.1 mg	24 $\mu\text{L}$	8.6 $\mu\text{mol g}^{-1}$
<b>7</b>	23.7 mg	80 $\mu\text{L}$	6.3 mg	23 $\mu\text{L}$	8.4 $\mu\text{mol g}^{-1}$
<b>8</b>	23.0 mg	100 $\mu\text{L}$	5.3 mg	24 $\mu\text{L}$	8.7 $\mu\text{mol g}^{-1}$

*Table 5.8: Sample preparation details for the impregnation of NaPA with AMUPol. 5  $\mu\text{L}$  of a 40 mM solution of AMUPol in D<sub>2</sub>O/H<sub>2</sub>O (90/10) was added to all samples in addition to the volumes of D<sub>2</sub>O/H<sub>2</sub>O (90/10) noted in this table. The mass of polymer and total radical volume in the rotor were calculated from their respective weight percentages in the prepared sample. The radical concentration represents the concentration of AMUPol per gram of NaPA.*

The  $^1\text{H}$ - $^{13}\text{C}$  spectra of these samples without MW irradiation demonstrate the impact that swelling has on the polymer itself and the  $^1\text{H}$ - $^{13}\text{C}$  CP spectrum. In Figure 5.10, the MW off spectra of samples 1, 2, and 3 are shown. There is a significant increase in the SNR and resolution of the spectra without MW irradiation of samples 2 and 3, in comparison to sample 1, despite their slightly reduced sample weight. This may be the result of the increased volume of  $\text{H}_2\text{O}$  in these samples. The increased  $\text{H}_2\text{O}$  content can improve the efficiency of the CP transfer. However, as the volume of  $\text{H}_2\text{O}$  in the rotor increases, the mass of polymer decreases and the SNR of the spectra without MW irradiation begins to decrease for samples 4-8 due to this decrease in practical sample weight.

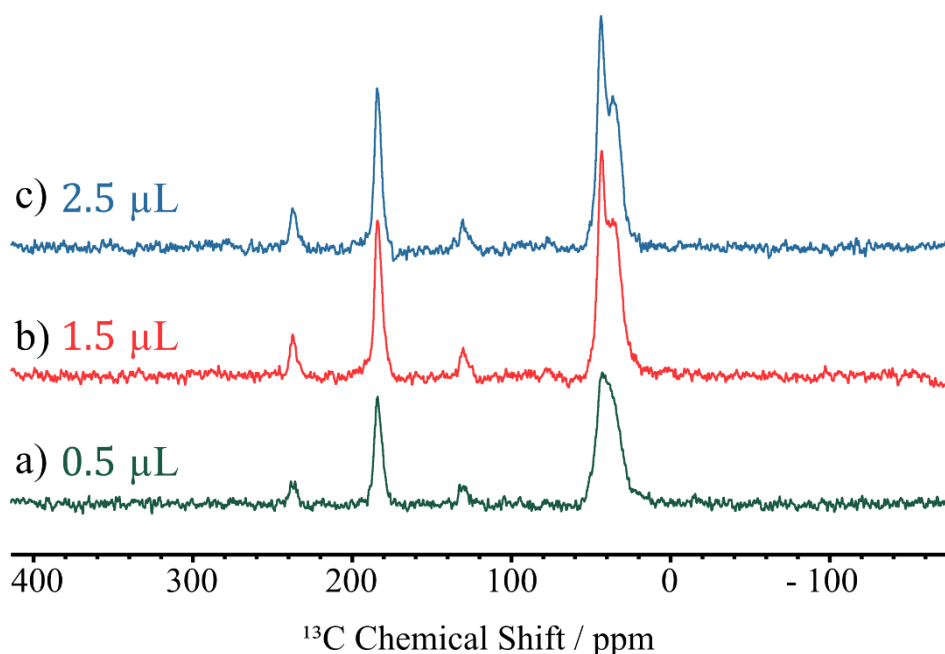


Figure 5.10:  $^1\text{H}$ - $^{13}\text{C}$  CP spectra of NaPA samples without MW irradiation. a) sample 1 impregnated with a radical solution containing 0.5  $\mu\text{L}$  of  $\text{H}_2\text{O}$ , b) sample 2 impregnated with a radical solution containing 1.5  $\mu\text{L}$  of  $\text{H}_2\text{O}$ , and c) sample 3 impregnated with a radical solution containing 2.5  $\mu\text{L}$  of  $\text{H}_2\text{O}$ .

The change in SNR of the  $\text{COO}^-$  signal at 180 ppm and the CH and  $\text{CH}_2$  signals around 40 ppm can be seen in relation to the mass of polymer and volume of  $\text{H}_2\text{O}$  in Figure 5.11a. The change in SNR of both signals of the MW off spectrum initially increases, following a similar trend to the change in  $\text{H}_2\text{O}$  volume. The change in SNR then decreases, following the trend of change in polymer mass, as would be expected.

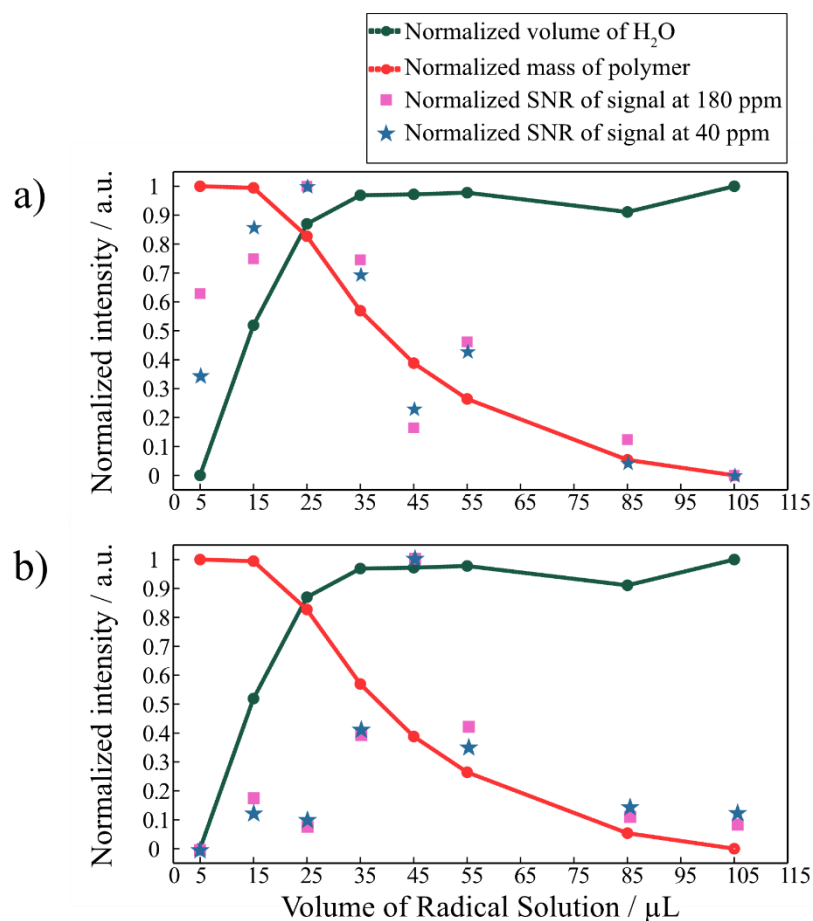


Figure 5.11: Plots demonstrating the trends in the change of  $\text{H}_2\text{O}$  volume (green) and polymer mass (red) in the rotor and the change in SNR of the  $\text{COO}^-$  signal at 180 ppm (pink) and the  $\text{CH}$  and  $\text{CH}_2$  signal around 40 ppm (blue) of a) spectra without MW irradiation and b) spectra with MW irradiation. All values have been standardized to allow for comparison of the trends, lines are included as a guide for the eye.

The change in SNR of the spectra recorded *with* MW irradiation (Figure 5.11b) does not appear to follow these trends as closely, although there is some dependence on the sample weight. This dependence can be seen more clearly in Figure 5.12 which shows the SNR with respect to the mass of polymer in the rotor and the square root of experiment time.



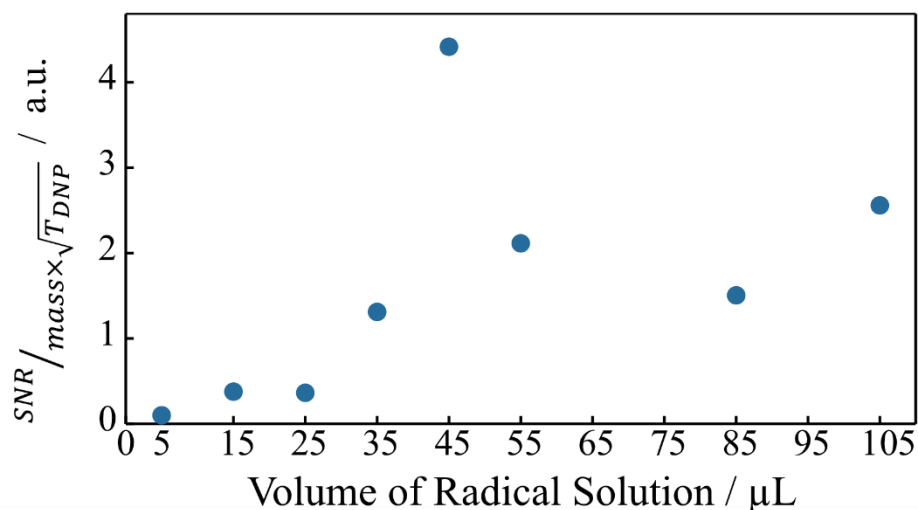


Figure 5.12: Plot of the evolution of the SNR per gram and unit of square time of the  $\text{COO}^-$  signal in the DNP-enhanced  $^1\text{H}$ - $^{13}\text{C}$  CP spectra as a function of the volume of radical solution used to impregnate and swell the sample.

This measure of sensitivity shows a more linear trend as the volume of radical solution changes. However, an anomalously high enhancement is observed for sample **5**. Repetition of the sample preparation yielded the same anomalously high sensitivity of this sample. The dramatic increase in signal intensity for sample **5** can be seen in the overlaid spectra in Figure 5.13 and the details of observed enhancements for all samples are presented in Table 5.9.

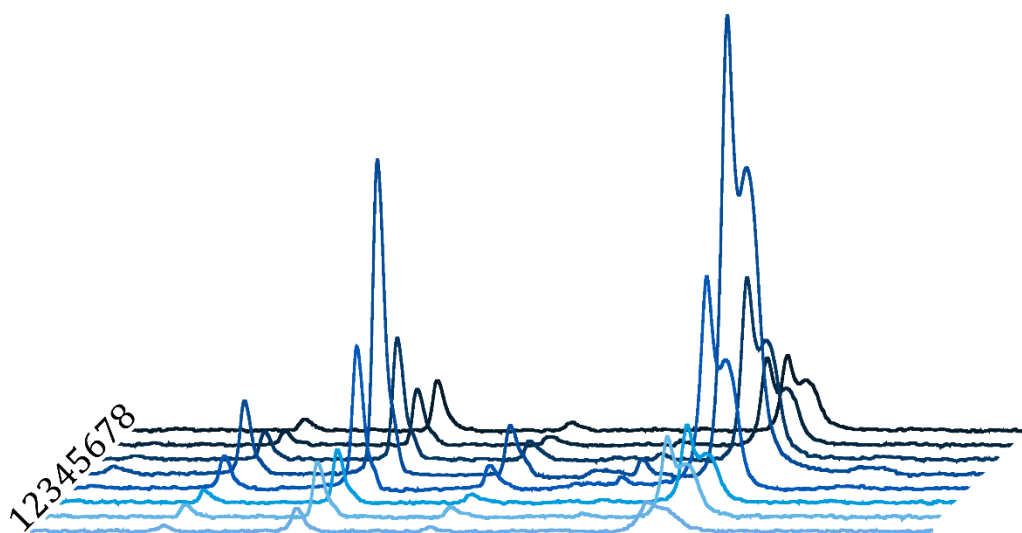


Figure 5.13:  $^1\text{H}$ - $^{13}\text{C}$  CP spectra with MW irradiation of samples **1** (front) to **8** (back), demonstrating the significantly higher signal intensity of sample **5**.

Sample Reference	$\epsilon_{DNP}$	COO <sup>-</sup> SNR g <sup>-1</sup>	CH/CH <sub>2</sub> SNR g <sup>-1</sup>
<b>1</b>	1.1	0.7	1.0
<b>2</b>	1.8	2.8	2.8
<b>3</b>	1.7	1.9	2.9
<b>4</b>	6.6	7.8	10.4
<b>5</b>	19.4	23.0	29.3
<b>6</b>	6.7	12.9	14
<b>7</b>	6.0	7.5	11.7
<b>8</b>	5.5	7.5	12.6

Table 5.9: Observed  $^1\text{H}$ - $^{13}\text{C}$  CP DNP enhancements and MW on SNR per gram of polymer of NaPA. SNRs were measured using the sinocal function in TopSpin on data with 100 Hz line broadening applied.

Given the results from Section 5.4.1 and the literature,<sup>30,138</sup> it can be assumed that the low enhancements of samples **1-3** are due to insufficient swelling of the polymer and subsequently poor radical dispersion. However, the reason for the anomalously high enhancement of sample **5** is not immediately clear. It may be the case that sample **5** represents the ideal conditions for NaPA prepared in D<sub>2</sub>O/H<sub>2</sub>O. The lower enhancements of samples **6-8** could be due to *excessive* swelling which has increased the distances between the polarization source and the polymer. Furthermore, a larger ‘free-volume’ in the more swollen polymers could reduce the ability of the polymer to perform the role of a ‘glass former’ as the free-volume in which the radical solution exists may become too large to impose the necessary geometrical constraints to prevent ice formation.<sup>148</sup> This may relate to the results in Section 5.4.2, which showed that NaPA performed better with an additional glass-forming agent present. Comparing the results of sample preparations with a glass-former to those here (Table 5.10) demonstrates the significant impact that a glass-former can have on the enhancement of NaPA

samples with comparable polymer content. Although these results should not be used as a direct comparison as the radical concentration is not equal across all samples, they provide an insight to the higher enhancements achievable for NaPA if a glass-former is present.

	<b>Radical solution</b>	<b>Polymer content</b>	$\epsilon_{DNP}$
Table 5.7	Glycerol-d <sub>8</sub> /D <sub>2</sub> O/H <sub>2</sub> O (60/30/10 vol%)	45 wt%	41.0
	3 M Ca(NO <sub>3</sub> ) <sub>2</sub> D <sub>2</sub> O/H <sub>2</sub> O (90/10 vol%)	35 wt%	13.6
	D <sub>2</sub> O/H <sub>2</sub> O (90/10 vol%)	38 wt%	11.3
Table 5.8	D <sub>2</sub> O/H <sub>2</sub> O (90/10 vol%)	51 wt%	1.7
	D <sub>2</sub> O/H <sub>2</sub> O (90/10 vol%)	41 wt%	19.4
	D <sub>2</sub> O/H <sub>2</sub> O (90/10 vol%)	35 wt%	6.7

*Table 5.10: DNP enhancements for the COO<sup>-</sup> signal of samples of NaPA prepared with different volumes of different radical solutions, demonstrating the higher  $\epsilon_{DNP}$  of the samples prepared with glycerol and Ca(NO<sub>3</sub>)<sub>2</sub> despite similar polymer content.*

The importance of a glass-former in optimal NaPA sample preparation supports the hypothesis that excessive swelling *without* a glass-former could have the severely negative impact of phase separation of the radical. This speaks to the importance of being able to accurately measure the extent of swelling of such polymers.

#### 5.4.4. RDC in Swollen Polymers

Preliminary attempts were made to quantify the swelling of NaPA samples using double quantum NMR. The extent of swelling of three samples of NaPA swollen in volumes of D<sub>2</sub>O/H<sub>2</sub>O (90/10 vol%) equivalent to samples **5**, **6**, and **7**, without any radical present, was investigated by measuring the residual dipolar coupling (RDC) in these samples.

Polymers with a lower degree of swelling will have larger RDC constants,  $D_{res}$ , as the orientational constraints of the more rigid polymer chains prevent the averaging of the dipolar coupling. Polymers with higher degrees of swelling,

and thus increased mobility in the sample, will better average the dipolar coupling and thus  $D_{res}$  will be lower.

The value of  $^1\text{H}$ - $^1\text{H}$  RDC can be calculated by fitting the build-up behaviour of signal intensity as the DQ excitation time,  $\tau_{DQ}$  is increased (Figure 3.4). This has been previously demonstrated to quantify the swelling of hydrogels by Höpfner *et al.* who measured the RDC in a series of hydrogels with varying degrees of cross-linking,  $\text{Na}^+$  content, and water content.<sup>149</sup> They observed that decreasing the degree of cross-linking or increasing the water content increased the swelling capacity of the hydrogels, and this was reflected in slower  $^1\text{H}$  DQ coherence build-up and lower values of  $D_{res}$ .

The water content in the prepared samples is defined as  $Q$  and these values for the samples used in this work are shown in Table 5.11.

$$Q = \frac{\text{mass}[D_2O] + \text{mass}[H_2O]}{\text{mass}[NaPA]} \quad [5.4.4. 1]$$

Sample Reference	$Q$
5	1.9
6	2.4
7	3.7

*Table 5.11: Sample reference, relating to the volume of radical solution added to the equivalent sample studied by DNP-enhanced NMR in Section 5.4.3, and the water content of the swollen polymer,  $Q$ .*

The experimental data acquired for these samples,  $I_{ref}$  and  $I_{DQ}$ , the sum of these data points,  $I_{\Sigma DQ}$ , the normalized  $^1\text{H}$  DQ build-up data including defect subtraction,  $I_{nDQ}$ , and the fit of the normalized data to an A-1 build-up function (Equation [5.3.4.4]) are shown in Figure 5.14. The experimental data suffered from poor SNR at long  $\tau_{DQ}$  times, likely due to the relatively low polymer content in the samples. The effect of this can be seen in the behaviour of the  $I_{nDQ}$  build-up curves for  $\tau_{DQ} \geq 5$  ms.

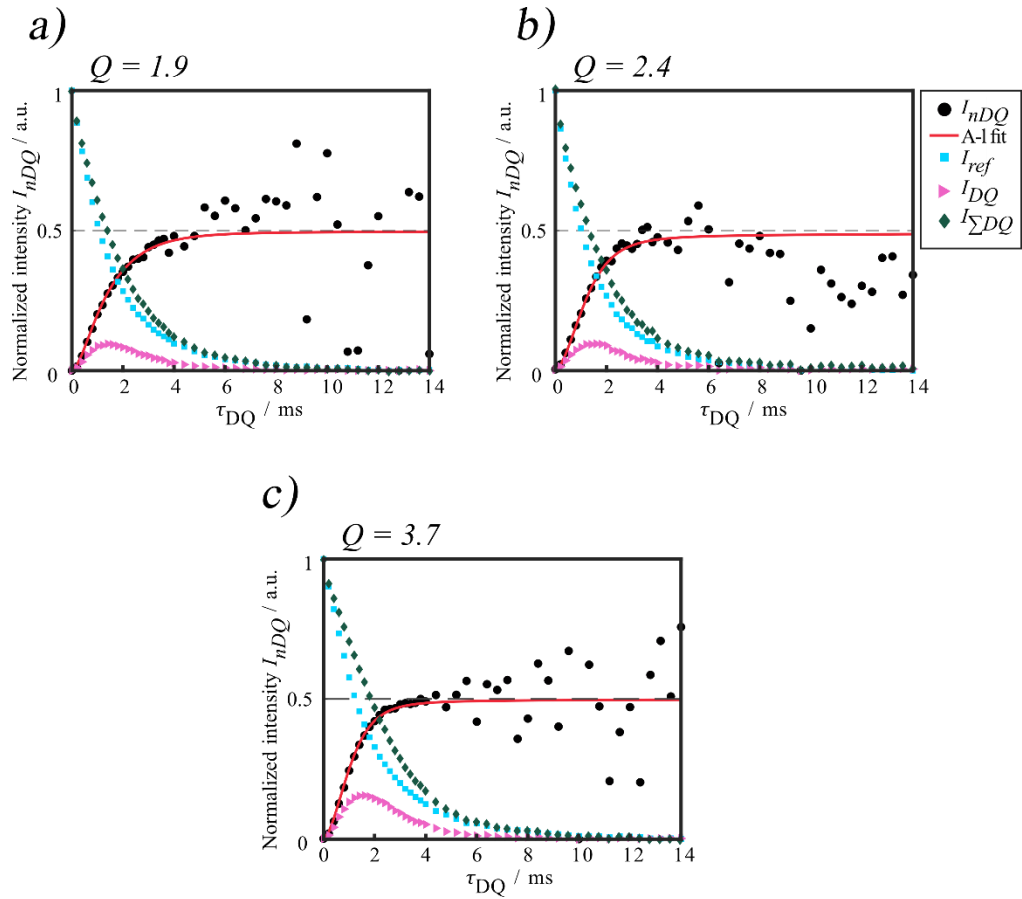


Figure 5.14: DQ coherence build up curves of the experimental data,  $I_{ref}$  and  $I_{DQ}$ , the sum of these data points,  $I_{\Sigma DQ}$ , the normalized  $^1H$  DQ build-up data including defect subtraction,  $I_{nDQ}$ , and the fit of the normalized data to an A-1 build-up function shown with a solid line. a) lowest  $D_2O/H_2O$  content,  $Q = 1.9$ , b)  $Q = 2.4$ , and c) highest  $D_2O/H_2O$  content,  $Q = 3.7$ . An additional dashed line has been added at the expected maximum of  $I_{nDQ}$  at 0.5 as a guide for the eye.

The  $I_{nDQ}$  data points for  $Q = 1.9$  and  $3.7$  reach the maximum of 0.5 after  $\sim 5$  ms and then proceed to oscillate around this value for longer  $\tau_{DQ}$  times, albeit with significant variation and errors due to the lower SNR of the  $I_{ref}$  and  $I_{DQ}$  spectra at these times. For  $Q = 2.4$ , after the maximum is reached the intensity of  $I_{nDQ}$  data points begins to decay. This decay may be attributed to insufficient removal of the liquid-like contributions.

A clearer comparison of the A-1 fits of the experimental data for these samples can be seen in Figure 5.15.

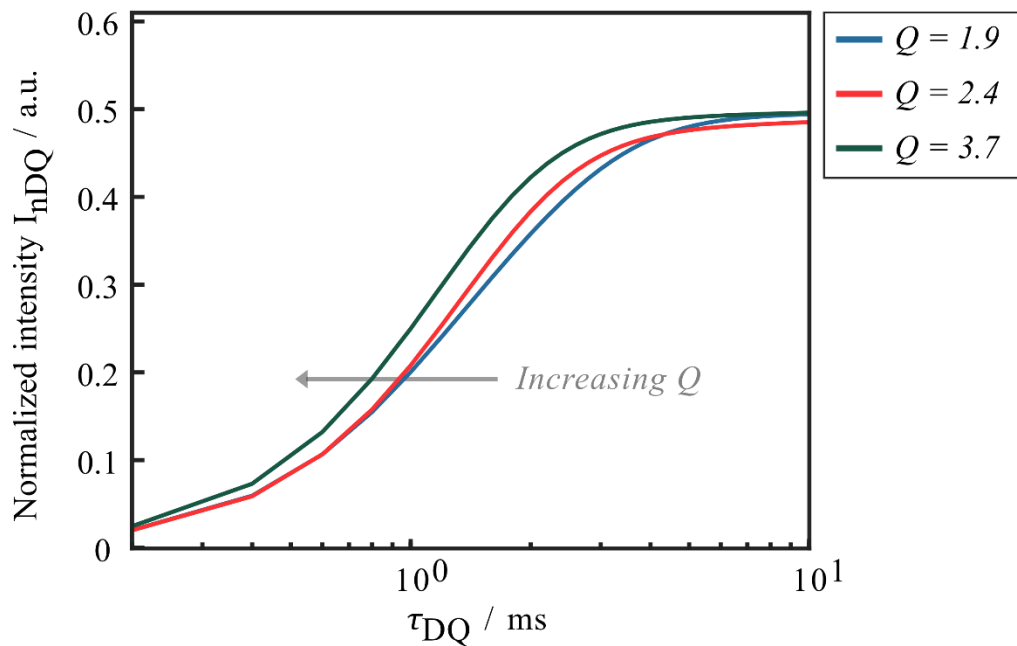


Figure 5.15: DQ coherence curves representing the fit of experimental data to an A-l build-up function for samples of NaPA swollen with different volumes of a D<sub>2</sub>O/H<sub>2</sub>O (90/10 vol%) solution. These fits show a faster build-up for samples swollen in higher volumes ( $Q = 3.7$ ).

The fitted build-up curves seen for these samples do not follow the expected behaviour of slower DQ coherence build up for polymers with higher water content. The sample with  $Q = 3.7$  appears to have the fastest build-up. Although initially, the build-up of the sample with  $Q = 2.4$  appears to be faster than for  $Q = 1.9$ , the best fit of the experimental data for this sample does not reach the expected maximum of 0.5 and thus cannot be considered reliable. This poor fitting may be due to the faster decay of  $I_{nDQ}$  seen for this sample in Figure 5.14b.

The distributions of the  $D_{res}$  of the samples with  $Q = 1.9$  and 3.7 obtained from the regularization of the A-l fits are shown in Figure 5.16.

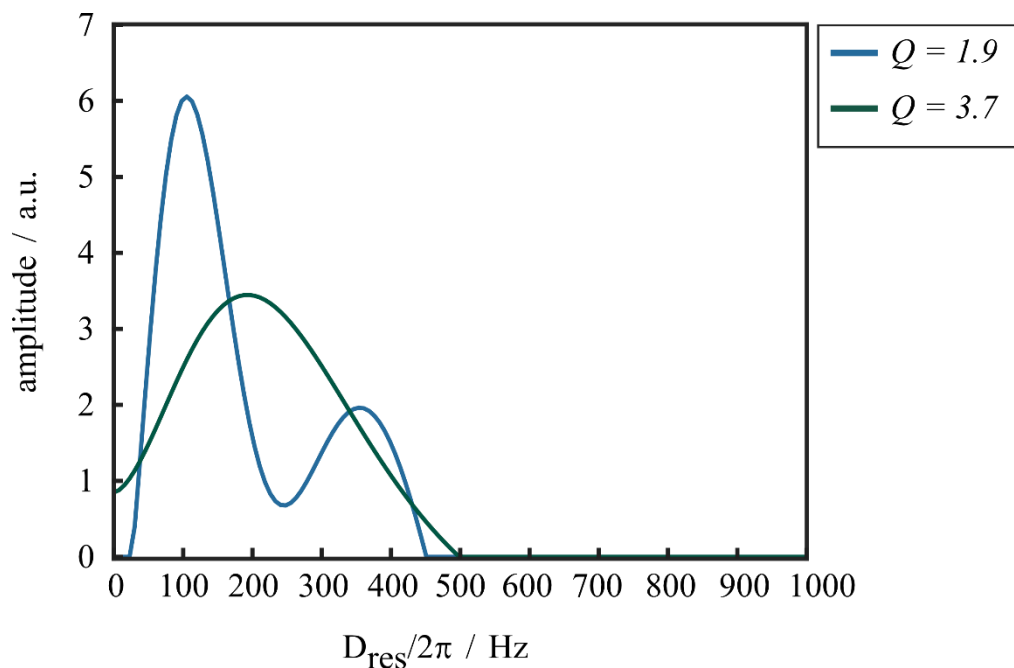


Figure 5.16: Distributions of RDC constants,  $D_{res}$ , calculated from the A-1 fits of  $I_{nDQ}$  build-up, of samples of NaPA swollen with different volumes of a  $D_2O/H_2O$  (90/10 vol%) solution. A bimodal distribution of the sample with  $Q = 1.9$  was required to ensure a good fit of the build-up curve to experimental data. The  $D_{res}$  distribution of the sample  $Q = 2.4$  is not shown due to the unreliability of the data as noted above.

The distributions of  $D_{res}$  for these samples also do not follow the expected behaviour. A significant proportion of the  $D_{res}$  distribution of sample  $Q = 1.9$  is centred at lower  $D_{res}$  values. This conflicts with the expectation that the lower  $D_2O/H_2O$  content in this sample will swell the polymer less and there will be less averaging of the dipolar coupling of the polymer chains.

Although the observed build-up behaviour and values of  $D_{res}$  do not align with those reported by Höpfner *et al.*, the bimodal distribution of  $D_{res}$  seen here in the least swelled sample ( $Q = 1.9$ ) is consistent with the lesser swelled samples reported in the literature. The bimodal distribution of RDC arises from an inhomogeneity in the sample which results in some very mobile domains with high solvent content and separate, more constrained domains.

Höpfner *et al.* were able to identify the source of the bimodal distribution that they observed by performing equivalent experiments on a sample that had undergone drying and extraction of water. The  $D_{res}$  distributions for the sol-

extracted sample saw a reduction in intensity for the component at lower  $D_{res}$  values, confirming that in the wet sample, this component arises from a very mobile fraction of the polymer. They saw a trend, that for *more highly constrained* samples (i.e., samples with low water content and/or high cross-link density) there was a larger difference between the  $D_{res}$  values extracted for the mobile domain and constrained domain. They also noted that the  $D_{res}$  values of the mobile component tended to be lower, the lower the water content was. These findings suggest that the unexpected behaviour of the DQ build-up curves of these samples is an observation of increased inhomogeneity in the sample,  $Q = 1.9$ .

Considering the results presented by Höpfner *et al.*, it may be concluded that the results obtained in this work are not sufficient to quantify the extent of swelling of these samples. Further work must be done to determine whether the unexpected results seen here are a true representation of the RDC in swollen NaPA hydrogels, or whether they are the result of poor fitting due to insufficient data.



## 5.5. Summary

These results have demonstrated that while swelling is an important step in the impregnation of polymers for DNP-enhanced solid-state NMR, careful consideration of the impact of the sample preparation beyond the potential DNP enhancement is necessary. The impact of increased D<sub>2</sub>O content on the structural conformation of PEO was demonstrated by the observed changes in the spectra of PEO swelled in different volumes of radical solution.

The ability of polymers to perform the role of a glass-former at 100 K and prevent significant ice formation and radical phase separation was also shown. This presents a positive step in improving the effectiveness of polymer DNP by removing the risk of obscuring polymer signals with overlapping solvents. Although for NaPA there appears to be a significant advantage in terms of DNP enhancements achievable when using glycerol in the sample preparation, the identification of sample preparation conditions which provide good DNP enhancements without the risk of obscuring relevant signals remains important.

Further improvement of the guidelines for DNP sample preparation of polymers could be gained by gaining a deeper understanding of the reason for the anomalously high DNP enhancement of the sample of NaPA prepared by swelling in 45  $\mu$ L of radical solution.

Despite uncertainty surrounding the reasons for the different DNP enhancements seen here, these results demonstrate the importance of considering all aspects of the sample preparation process when determining the optimal technique. It is essential that the impact of the sample preparation on the structure and conformation of the polymer itself is considered.

# 6. Supercritical Carbon Dioxide

## DNP Sample Preparation

*Polystyrene and polystyrene:poly(methyl methacrylate) core-shell polymer particles were synthesized by Dr Kristoffer Korsten and Morgan Reynolds-Green in the research group of Prof. Steven M. Howdle at The University of Nottingham.*

*Q-band CW EPR spectra were analysed by Prof. David Collinson and Prof. Eric McInnes and EPR relaxation measurements and analysis were performed by Adam Brookfield at the EPSRC National Service for Electron Paramagnetic Resonance Spectroscopy at The University of Manchester.*

### 6.1. Abstract

The impregnation of polymers with nitroxide radicals using supercritical CO<sub>2</sub> (scCO<sub>2</sub>) has the potential to expand the range of materials that can be studied by DNP-enhanced solid-state NMR.

scCO<sub>2</sub> is commonly used to impregnate polymers with dopants such as dyes and pharmaceuticals and has been used here as solvent to impregnate poly(ethylene oxide) (PEO), polystyrene (PS), and complex polystyrene:poly(methyl methacrylate) (PS:PMMA) core-shell particles with the radicals TEKPol and AMUPol. DNP enhancements have been measured on <sup>13</sup>C direct polarization spectra of PS, <sup>1</sup>H-<sup>13</sup>C cross polarization spectra of PEO, and methyl <sup>1</sup>H-<sup>13</sup>C cross-relaxation polarization spectra of PS:PMMA core-shell polymers. The largest DNP enhancement observed of ~5, enabled a spectrum of PEO to be obtained with a higher signal to noise ratio and narrower linewidths than a comparative system using the swelling sample preparation method.

## 6.2. Introduction

### 6.2.1. Supercritical Fluids

Above the *critical point* of a substance, it exists as a *supercritical fluid* (SCF). The critical point of a substance is the temperature and pressure above which the substance does not exhibit a distinct gas or liquid phase but possesses the qualities of both. A phase diagram which demonstrates the critical point and supercritical fluid phase is presented in Figure 6.1. A supercritical fluid can behave as a liquid where it is able to dissolve solids and liquids. A SCF can also behave as a gas where it can readily diffuse through porous materials. All materials have a critical point and can therefore exist as a supercritical fluid. This results in a wide range of SCFs being available to meet the needs of many industrial and research endeavours. The properties and capabilities of any given SCF can be tuned by adjusting its density. It is possible to control the density of a SCF by adjusting the temperature and pressure conditions.<sup>150,151</sup> Control of the density of a SCF allows control of its solvent capacity.

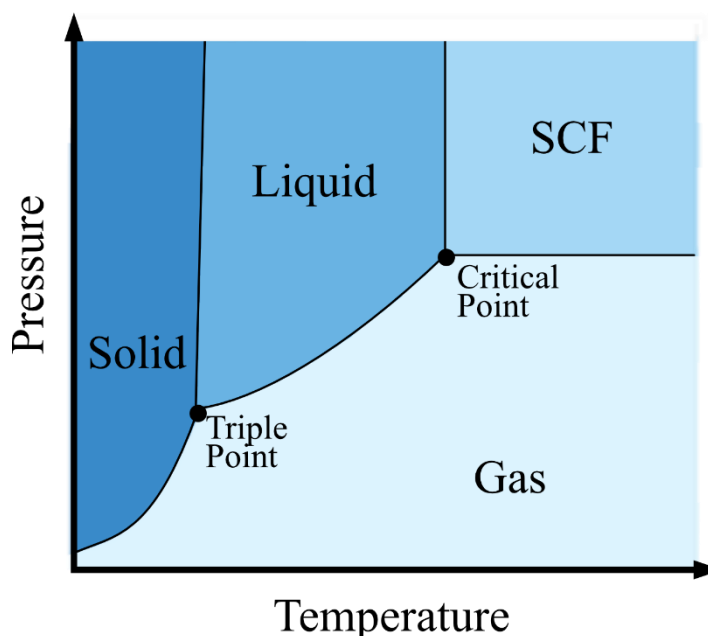


Figure 6.1: Schematic pressure-temperature phase diagram showing the supercritical fluid region, the triple point where the solid, liquid, and gas phases meet, and the critical point where the SCF phase begins.

The relatively mild conditions required to achieve the supercritical state of CO<sub>2</sub> (T = 304.13 K, P = 73.8 bar) have led to supercritical CO<sub>2</sub> (scCO<sub>2</sub>) being a potential sustainable alternative to conventional organic solvents. Benefits of using scCO<sub>2</sub> include the natural abundance of CO<sub>2</sub> as a by-product of several industrial processes as well as the non-toxic, non-flammable and largely inert nature of CO<sub>2</sub>.

The low dielectric constant of scCO<sub>2</sub> ( $\kappa \approx 2$ ) means that it is generally considered to be a non-polar solvent, but it has been observed experimentally that scCO<sub>2</sub> can also be used as a solvent for solutes with significant polarity, such as sugar acetates.<sup>152,153</sup> This dual nature places scCO<sub>2</sub> in a position to be used in a wide variety of processes. In the food industry, scCO<sub>2</sub> is commonly used in extraction processes such as the decaffeination of coffee and tea.<sup>154,155</sup> In chemical processes used in industry and in research, scCO<sub>2</sub> is used as an alternative to organic solvents, notably in polymer synthesis and processing.

scCO<sub>2</sub> polymer processing has many benefits in addition to the reduced toxicity and sustainability of using scCO<sub>2</sub> as a reaction medium. The sorption of scCO<sub>2</sub> into polymer networks has an impact on their physical properties, including reducing the *glass transition temperature* ( $T_g$ ).<sup>156,157</sup> This has the effect of inducing plasticization of polymers at lower temperatures as the sorbed CO<sub>2</sub> allows the polymer chains to move more freely.<sup>158,159</sup> In scCO<sub>2</sub>, the softened polymers are more easily moulded or extruded and there is increased diffusion throughout the polymer matrix. This enhanced diffusion is responsible for the success of scCO<sub>2</sub> in extraction processes and the *impregnation* of polymers.<sup>160–162</sup>

## 6.2.2. Supercritical CO<sub>2</sub> Impregnation of Polymers

The combined ability of scCO<sub>2</sub> to swell polymers and dissolve many small molecules, makes it an excellent tool for polymer impregnation. There are two possible mechanisms for scCO<sub>2</sub> impregnation,<sup>163</sup> the first applies when the additive is soluble in scCO<sub>2</sub> and is distributed through the increased free-volume of the polymer by sorbed CO<sub>2</sub>. On depressurization, the additive precipitates out

and is left trapped in the polymer matrix as gaseous CO<sub>2</sub> is removed. The second impregnation mechanism applies when the additive is poorly soluble in scCO<sub>2</sub> but has a higher affinity for the polymer phase of the reaction system. The result of this is a favourable partitioning of the additive in the polymer matrix over the scCO<sub>2</sub>.<sup>164</sup> It is possible to modify the solubility of additives in scCO<sub>2</sub> by the addition of a cosolvent.<sup>165,166</sup>

Polymer based drug delivery implants are excellent tools for controlled and targeted release of active pharmaceutical ingredients (API). Traditional methods of manufacturing these implants often require high energy input to produce and ensure that any residual solvent has been removed.<sup>167</sup> Using scCO<sub>2</sub> to produce and impregnate these polymeric drug-delivery systems boasts the major advantage of the possibility to recover the final product dry and free of residual solvent. This is particularly important to ensure bio-compatibility of the implants.<sup>168</sup>

Supercritical CO<sub>2</sub> has also been used to impregnate polymers with stable nitroxide radicals. The impregnation of polymers with nitroxide radicals has been used to track the process of impregnation and study the spatial distribution by electron paramagnetic resonance (EPR).<sup>169</sup> EPR as an analytical technique to monitor the process of scCO<sub>2</sub> impregnation offers the ability to monitor the total concentration, spatial distribution, and mobility of dopants. Understanding the distribution of additives in scCO<sub>2</sub> impregnated polymers is vital in drug delivery systems. While the tunable nature of scCO<sub>2</sub> impregnation provides advantages in being able to tune the extent of drug loading which can be measured using gravimetric methods,<sup>170</sup> the spatial distribution of the drug, which can have significant impact on the drug delivery mechanism, can also be easily controlled during scCO<sub>2</sub> impregnation. Golubeva and coworkers have demonstrated the usefulness of this approach through monitoring the impregnation of poly(lactide),<sup>171-173</sup> poly(carbonate),<sup>174</sup> poly(acrylic acid), and poly(ethylene oxide)<sup>175</sup> with stable nitroxide radicals TEMPOL<sup>171,172,174</sup> and TEMPONE.<sup>173,175</sup>

The EPR studies of successful scCO<sub>2</sub> impregnation of polymers with stable nitroxide radicals provide a basis for investigating the possibility of using the same process to impregnate polymers with the larger nitroxide biradicals used

for DNP-enhanced solid-state NMR. The use of these larger radicals may not provide any additional benefit in determining the mechanism of impregnation. However DNP-enhanced NMR of polymeric drug delivery systems could provide insight to any polymer-API interactions.<sup>176,177</sup> The scCO<sub>2</sub> impregnation of these systems with radicals can be preferable compared to traditional sample preparation methods which require the radical to be dissolved in an organic solvent or aqueous solution. In the interest of preserving delicate polymer-API interactions,<sup>178</sup> scCO<sub>2</sub> impregnation of the radical can be included in the existing API impregnation process, or can be carefully tuned to provide an unobtrusive post-synthetic impregnation. For other polymer systems, scCO<sub>2</sub> impregnation provides the advantage of a dry, free flowing powder as opposed to a swollen gel. This solvent-free sample provides benefit for DNP-enhanced NMR measurements as the practical sample volume in the rotor is increased and there is no solvent signal which could interfere with spectral analysis.

## 6.3. Experimental Details

### 6.3.1. High Pressure Equipment

For all high-pressure experiments, liquid carbon dioxide was introduced from a cylinder (Air Products and Chemicals Inc., SCF grade 5.5, 99.9995 %) at a pressure of ~55 bar, to a high-pressure pump. CO<sub>2</sub> was guided through a refrigerated condenser to guarantee liquid phase CO<sub>2</sub> filled the pump. The dual piston pump was driven by compressed air at ~4 bar, ensuring the CO<sub>2</sub> is compressed to the required reaction pressures of up to 300 bar. The high-pressure setup was connected to the CO<sub>2</sub> pump via a series of HiP valves, Swagelok SS316 tubing, and unions.

All high-pressure impregnations were conducted in a high-pressure reactor (autoclave) with a volume of 20 mL, designed and produced at The University of Nottingham. The autoclave consists of two main sections, the head and the base, which are sealed by an O-ring, placed between the matching faces and held together by a stainless-steel clamp. The clamp is secured using a custom key that sits in the head during operation. The autoclave head also features the required ports for CO<sub>2</sub> addition, CO<sub>2</sub> release, and contains an internal thermocouple for

temperature monitoring and heating control. The thermocouple is connected to an external heating jacket surrounding the base, controlled to  $\pm 1^\circ\text{C}$ . Pressure is monitored using a quartz piezoelectric transducer, providing a digital read out in pounds-per-square-inch. A connected electronic trip will disconnect heating in case of pressure exceeding a set value. Furthermore, the head contains a Swagelok SS-4R3A proportional relief valve, that will release pressure in the event of the system exceeding 350 bar. The autoclave is placed on a magnetic hotplate stirrer which drives a magnetic stirrer bar placed in the base of the autoclave.

### 6.3.2. Materials

Poly(ethylene oxide) (PEO,  $M_v = 1,000,000$ ) was purchased from Sigma-Aldrich. Carbon dioxide ( $\text{CO}_2$ , SCF grade 5.5, 99.9995 %) was obtained from Air Products and Chemicals Inc. Polystyrene and polystyrene:poly(methyl methacrylate) core-shell structures were synthesized at The University of Nottingham in the research group of Prof Steven Howdle. All chemicals were used as received.

### 6.3.3. Supercritical $\text{CO}_2$ Impregnation

The general procedure used for the impregnation of polymer powders with a radical (TEKPol or AMUPol) involved adding the dry polymer powder and the radical to the bottom of a 20 mL high-pressure autoclave with a stirrer bar. The autoclave was sealed and heated using a heating jacket while  $\text{CO}_2$  was added until the desired temperature and pressure were reached. The autoclave was left stirring for the desired length of treatment time after which, the heating was stopped, and the autoclave was left to cool to below the critical temperature of  $\text{CO}_2$ . Stirring was continued during this cooling time. Once the temperature of the autoclave reached  $< 30^\circ\text{C}$ , the stirring was stopped, and the system was slowly returned to ambient pressure by releasing gaseous  $\text{CO}_2$ . The product was collected from the base and walls of the autoclave as a dry, free flowing powder.

The initial mass of radical used in the  $\text{scCO}_2$  impregnation was chosen to be equivalent to the radical molar concentration used in a standard incipient

wetness impregnation process, of around 5 to 20  $\mu$ moles of TEKPol or AMUPol per gram of sample. Although it may be possible that following the scCO<sub>2</sub> processing and the actual radical concentration of the impregnated sample will be lower. The concentration of radicals in the impregnated samples can be measured by EPR which will provide insight to the ideal ratio of radical to polymer used in the scCO<sub>2</sub> process. Attempts were made to carry out these EPR spin counting experiments as part of this work. However, technical limitations prevented access to the necessary equipment to complete this work.

### 6.3.4. DNP-Enhanced Solid-state NMR

DNP-enhanced solid-state NMR experiments were performed on a Bruker Avance III HD spectrometer operating at a <sup>1</sup>H Larmor frequency,  $\nu_{0H} = 600$  MHz (14.1 T), equipped with a double resonance low-temperature 3.2mm CP-MAS probe. The microwave source to generate electron polarization was a 7.2 T gyrotron emitting 395 GHz microwaves at 5 W power.

Polymer samples impregnated *via* the scCO<sub>2</sub> impregnation method were packed directly into 3.2 mm sapphire rotors with no further modifications. The filled rotors were inserted into the pre-cooled probe and were rapidly frozen to 100 K. Each sample was subjected to multiple freeze-thaw by ejecting and reinserting the rotor. Experiments were performed under low temperature MAS. Temperatures ranged from 98-110 K. Spinning frequencies ranged from 8-10 kHz.

<sup>1</sup>H-<sup>13</sup>C CP was achieved using a 90 to 100 % ramp on the <sup>1</sup>H channel for 2 ms and <sup>1</sup>H decoupling was applied during acquisition using a SWf-TPPM sequence. Recycle delays used were determined for each sample from the <sup>1</sup>H-<sup>13</sup>C CP DNP build-up time.

<sup>13</sup>C DP DNP experiments were performed using a single pulse experiment with SWf-TPPM <sup>1</sup>H decoupling. The low signal intensity of the <sup>13</sup>C DP spectra, due to the low natural abundance of <sup>13</sup>C (1.1 %) meant that it was not possible to measure the direct <sup>13</sup>C polarization build-up. Therefore, the recycle delays used were based on the <sup>1</sup>H-<sup>13</sup>C CP DNP build-up time for each sample.



DNP build-up times were determined using a  $^1\text{H}$ - $^{13}\text{C}$  CP saturation recovery sequence. 8 transients were co-added and a recycle delay of 100 ms was used. Between 16 and 32 points were recorded with variable polarization times ranging from 4 ms to 1000 s.

SCREAM-DNP experiments were recorded using the pulse sequence described in Section 3.6.2. They were acquired in an interleaved fashion, alternating between a pulse sequence where  $^1\text{H}$  and  $^{13}\text{C}$  polarization is allowed to build-up during a variable delay,  $\tau$ , ( $\text{DP}_{\text{on}}$ ), and a pulse sequence where  $^{13}\text{C}$  polarization is allowed to build-up, but  $^1\text{H}$  spins are saturated by a train of pulses during the same duration of delay ( $\text{DP}_{\text{sat}}$ ). This resulted in a *pseudo-3D* data set which was split into two 2D data sets containing the  $\text{DP}_{\text{on}}$  spectra in one, and  $\text{DP}_{\text{sat}}$  in the other. The spectra were measured using a single  $90^\circ$   $^{13}\text{C}$  pulse preceded by a pre-saturation  $90^\circ$  pulse train applied to both  $^{13}\text{C}$  and  $^1\text{H}$  channels and a polarization delay, which was varied from 50 ms to 18.15 s. For the  $\text{DP}_{\text{sat}}$  experiments, additional  $180^\circ$  pulses were evenly distributed during the polarization delay, separated by 50 ms, to prevent  $^1\text{H}$  polarization build-up. The  $180^\circ$  saturation pulses were chosen to match the original SCREAM-DNP experiments.<sup>179</sup> SWf-TPPM  $^1\text{H}$  decoupling was applied during acquisition of both  $\text{DP}_{\text{on}}$  and  $\text{DP}_{\text{sat}}$ . 128 transients were co-added for each value of  $\tau$ , for both  $\text{DP}_{\text{on}}$  and  $\text{DP}_{\text{sat}}$ , with a recycle delay of 10 s.  $\Delta\text{DP}_{\text{sat}}$  spectra were obtained by subtracting the  $\text{DP}_{\text{sat}}$  spectrum from the equivalent  $\text{DP}_{\text{on}}$  spectrum using the *adsu* function in TopSpin.

### 6.3.5. EPR

Continuous-wave (CW) X-band EPR measurements were performed at room temperature on a Bruker EMX Micro X-band spectrometer. CW Q-band EPR measurements were performed at 100 K on a Bruker EMXPlus spectrometer. Pulsed Q-band EPR measurements were performed at 100 K on a Bruker ELEXSYS E580 spectrometer equipped with a 50 W solid-state amplifier. Relaxation times were measured using a Hahn Echo-Detected Field Sweep.

## 6.4. Results and Discussion

### 6.4.1. Poly(ethylene oxide)

Poly(ethylene oxide) (PEO) was chosen as an initial test sample following the impregnation procedure used by Golubeva et al. which resulted in a high concentration of uniformly distributed radicals in the sample.<sup>175</sup> As PEO was able to be impregnated with both the radicals TEKPol in TCE and AMUPol in D<sub>2</sub>O/H<sub>2</sub>O as presented in Section 5.4.1, it is also the best choice available to compare the effectiveness of the scCO<sub>2</sub> impregnation technique to the swelling impregnation technique.

Initial scCO<sub>2</sub> impregnations were carried out under the conditions found in the literature for the impregnation of PEO with TEMPONE.<sup>175</sup> Figure 6.2 shows the <sup>1</sup>H-<sup>13</sup>C CP spectra of PEO, impregnated with AMUPol and TEKPol using the scCO<sub>2</sub> method for 3 hours at 200 bar and 34 °C. The spectra are recorded with and without microwave irradiation (noted as MW ON and MW OFF respectively). The DNP enhancement ( $\epsilon_{DNP} = \frac{I_{MWON}}{I_{MWOFF}}$ ) observed for the sample impregnated with AMUPol is  $\epsilon_{DNP} = 4.7$ . For the sample impregnated with TEKPol,  $\epsilon_{DNP} = 3.2$ .

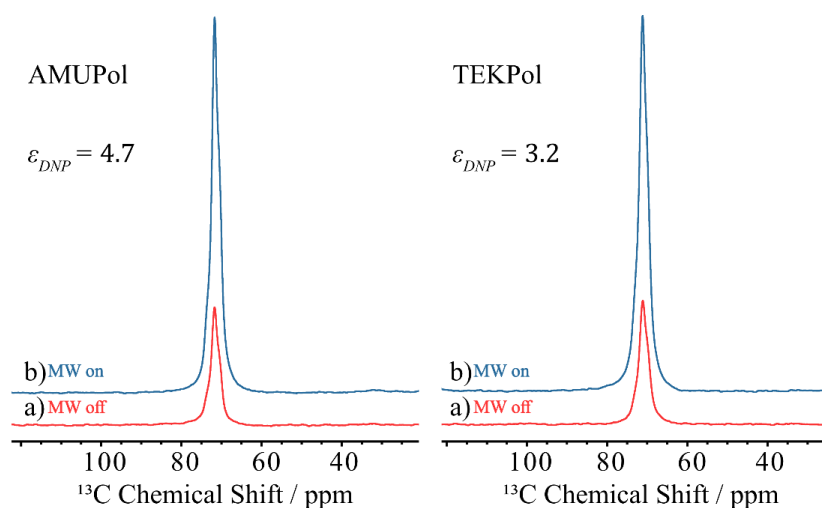


Figure 6.2: <sup>1</sup>H-<sup>13</sup>C CP spectra a) without and b) with MW irradiation of PEO impregnated with AMUPol (Left) and TEKPol (right) in scCO<sub>2</sub> at 34 °C and 200 bar for 3 hours.

These enhancements observed provide a proof of concept, that scCO<sub>2</sub> impregnation of polymers is possible with both radicals, AMUPol and TEKPol.

### 6.4.1.1. Sample Impregnation Conditions

As the solvation properties of scCO<sub>2</sub> change as the temperature and pressure change, the effect of these changes on the resulting DNP enhancement were investigated. Table 6.1 includes details of the DNP build up times ( $T_{DNP}$ ) and DNP enhancements ( $\epsilon_{DNP}$ ) of <sup>1</sup>H-<sup>13</sup>C CP DNP spectra of PEO impregnated with TEKPol using scCO<sub>2</sub> at 34 °C and varying pressures for 3 hours.

scCO <sub>2</sub> Impregnation Pressure	$T_{DNP}$	$\epsilon_{DNP}$
76 bar	38s (68 %)	1.7
	8 s (32 %)	
138 bar	40 s (74%)	2.9
	12 s (26 %)	
200 bar	31 s (78 %)	3.2
	4 s (22 %)	
241 bar	51 s (80 %)	2.0
	12 s (20 %)	

*Table 6.1: DNP build-up times and DNP enhancements of samples of PEO impregnated in scCO<sub>2</sub> with ~11 μmol g<sup>-1</sup> TEKPol at temperatures of 34 °C for 3 hours at different pressures.*

The DNP build up times of the scCO<sub>2</sub> impregnated PEO samples required the use of the biexponential function in Equation [6.4.1.1] to achieve a good fit.

$$I(\tau) = A \left( 1 - f e^{-\frac{\tau}{T_{DNPf}}} - (1 - f) e^{-\frac{\tau}{T_{DNP_s}}} \right) \quad [6.4.1.1]$$

where  $A$  is the signal equilibrium intensity,  $T_{DNPf}$  and  $T_{DNP_s}$  are the build-up time constants representing *fast* and *slow* build-up times respectively, and where  $f$  is the fraction of the population polarized by the first, fast process. This biexponential fit implies that there is an inhomogeneous distribution of radicals in the sample, which contribute to a distribution of build-up times.<sup>180</sup>

For each sample there is a faster component of the polarization build-up, between 4 and 12 s. The slower component ranges between 38 and 51 s. The fraction of the fast component decreases linearly as the pressure of scCO<sub>2</sub> impregnation increases from 80-67 %, as seen in Figure 6.3a. This trend may indicate that the temperature of scCO<sub>2</sub> impregnation has an impact on the radical distribution in the sample.

For samples prepared at 76 bar, the system will reach sub-critical conditions almost instantly as the temperature begins to fall. For systems at 241 bar, the depressurization is a much slower process, and the pressure remains high even when the system has cooled to < 30 °C and the gaseous CO<sub>2</sub> is vented from the system. During the time that the systems at higher pressures are left to cool, there may be some rearrangement or ordering of the polymer which separates the radical into distinct domains. This kind of radical phase separation is seen in solvent-free sample preparation of crystalline materials<sup>180</sup> and polymers that are impregnated using the film casting technique as the slow evaporation of solvent allows time for the polymer chains to rearrange and exclude the radical from certain polymer domains.<sup>30</sup>

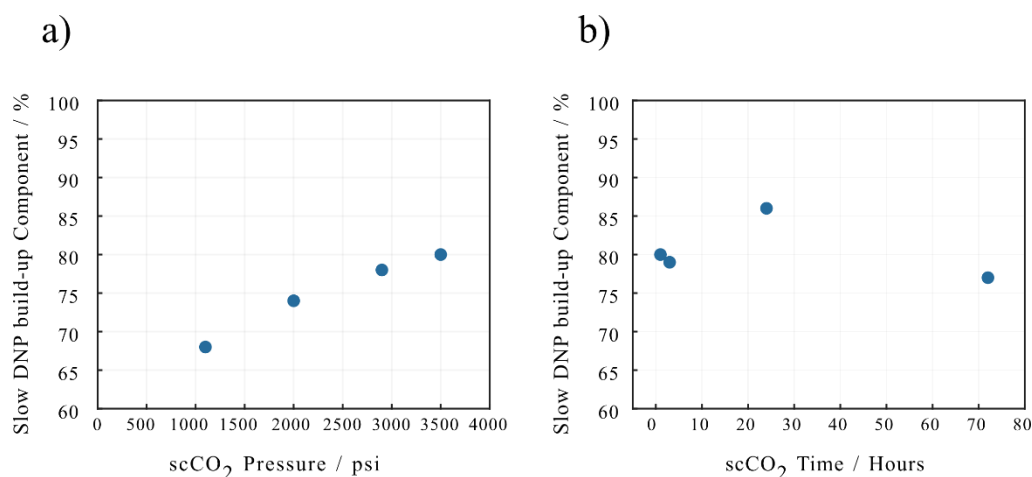


Figure 6.3: Plot of the fraction of the slow component of fitted DNP build-up time as function of scCO<sub>2</sub> impregnation a) pressure and b) time.

The length of time that the polymer and radical are subjected to scCO<sub>2</sub> treatment was also varied. Table 6.2 provides details of the observed  $T_{DNP}$  and  $\epsilon_{DNP}$  of

$^1\text{H}$ - $^{13}\text{C}$  CP DNP spectra of PEO impregnated with TEKPol using  $\text{scCO}_2$  at 34 °C and 241 bar for different lengths of time.

<b>scCO<sub>2</sub> Impregnation Time</b>	<b><math>T_{DNP}</math></b>	<b><math>\epsilon_{DNP}</math></b>
1 Hour	51 s (80 %)	3.0
	13 s (20 %)	
3 Hours	47 s (79 %)	2.9
	14 s (21 %)	
24 Hours	48 s (86 %)	3.0
	8 s (13 %)	
72 Hours	43 s (77 %)	2.6
	14 s (23 %)	

*Table 6.2: DNP build-up times and DNP enhancements of samples of PEO impregnated with  $\sim 5\text{-}6 \mu\text{mol g}^{-1}$  TEKPol in  $\text{scCO}_2$  at temperatures of 34 °C and pressures of 241 bar for different lengths of time.*

As seen for the previous results, the DNP build up times of these samples also requires a biexponential function to fit the experimental data. However, there does not appear to be the same relationship between the impregnation *time* and the resulting DNP build-up time or percentage contribution of the different build-up times, as seen in Figure 6.3b.

Again, the DNP enhancements observed do not change significantly as the  $\text{scCO}_2$  conditions change. On average, the DNP enhancement observed for these samples is higher than the enhancement observed for the samples which were prepared at varying pressures, despite the lower radical concentration used. Table 6.3 shows the DNP build-up times and DNP enhancements of two samples of PEO impregnated with different concentrations of TEKPol under the same  $\text{scCO}_2$  conditions.

<b>Radical Concentration</b>	$T_{DNP}$	$\epsilon_{DNP}$
11 $\mu\text{mol g}^{-1}$	51 s (80 %) 12 s (20 %)	2.0
6 $\mu\text{mol g}^{-1}$	47 s (79 %) 14 s (21 %)	2.9

*Table 6.3: DNP build-up times and DNP enhancements of samples of PEO impregnated with different concentrations of TEKPol at temperatures of 34 °C and pressures of 241 bar for 3 hours.*

The DNP enhancement observed here appears to be higher for the sample with a lower radical concentration. If there is an inhomogeneous distribution which results in the aggregation of radicals, these very localized regions of high electron densities will reduce the DNP efficiency.<sup>181</sup> It therefore follows that a sample with a higher global concentration of radical, will also have a higher local concentration and a reduced DNP enhancement. This further supports the possibility of these polymer samples having a poor distribution of the radical throughout the polymer matrix.

#### 6.4.1.2. Comparison to Swelling Sample Preparation

The DNP enhancements seen of PEO samples impregnated in scCO<sub>2</sub> are lower than those seen in Section 5.4 of PEO impregnated using the swelling method. However, there are additional benefits to the scCO<sub>2</sub> impregnation method, including the increase in the practical volume of the sample compared to the swelling method where over 50 % of the rotor volume is filled with the radical solution. In the case of impregnating samples with TEKPol, the scCO<sub>2</sub> method has the major advantage of eliminating the <sup>13</sup>C signal of the solvent. Observed differences in the <sup>1</sup>H-<sup>13</sup>C CP DNP-enhanced spectra of samples impregnated

with AMUPol *via* the swelling and scCO<sub>2</sub> impregnation methods are summarized in Table 6.4.

<b>Impregnation Method</b>	<b>Radical Concentration</b>	<b>Sample Weight</b>	$\epsilon_{DNP}$	SNR	FWHM
Swelling	17 $\mu\text{mol g}^{-1}$	10.6 mg	22.8	1858	456 Hz
scCO <sub>2</sub>	14 $\mu\text{mol g}^{-1}$	21.6 mg	4.7	2426	262 Hz

*Table 6.4: Radical concentrations, effective sample weights, DNP enhancements, signal to noise ratios, and linewidths of samples of PEO impregnated with AMUPol using the swelling method and the scCO<sub>2</sub> method. SNRs were measured using the sinocal function in TopSpin on data with 100 Hz line broadening applied. Linewidths were calculated using the peakw function in TopSpin on data with 0 Hz line broadening applied.*

A sample of PEO impregnated with an initial molar concentration of 14  $\mu\text{mol g}^{-1}$  of AMUPol in scCO<sub>2</sub> at 200 bar and 34 °C for 3 hours, shows a <sup>1</sup>H-<sup>13</sup>C CP DNP enhancement of  $\epsilon_{DNP} = 4.7$ . A sample of PEO impregnated with a molar concentration of 17  $\mu\text{mol g}^{-1}$  by swelling the polymer in a 10 mM solution of AMUPol in D<sub>2</sub>O shows a <sup>1</sup>H-<sup>13</sup>C CP DNP enhancement of  $\epsilon_{DNP} = 22.8$ .

If the actual radical concentration of the scCO<sub>2</sub> sample is 14  $\mu\text{mol g}^{-1}$ , the slight difference in radical concentration between the two samples should not result in any significant change in the DNP enhancement observed.<sup>30</sup> However, it is possible that the radical concentration in the final impregnated polymer is not 100 % of the starting concentration. In this case, a significantly lower radical concentration in the scCO<sub>2</sub> impregnated sample could also contribute to the lower DNP enhancement.

Based on the values of the DNP enhancement alone, the scCO<sub>2</sub> impregnation method does not seem to offer any advantage over the swelling impregnation method. However, the SNR of the scCO<sub>2</sub> sample is 1858, compared to the swelling sample SNR of 2426. The higher SNR of the scCO<sub>2</sub> sample can be attributed to the higher practical sample weight. The swelling sample

preparation used 50  $\mu\text{L}$  of radical solution to swell 30 mg of PEO, resulting in the PEO making up just 35 wt% of the prepared sample.

Additionally, the linewidth of the  $\text{scCO}_2$  impregnated sample is much smaller. One appealing quality of ‘matrix-free’ sample preparation such as  $\text{scCO}_2$  impregnations is the narrower linewidths that are generally observed.<sup>182,183</sup> In cases where there is a solvent present, there is increased disorder of the polymer chains which when frozen at 100 K results in line broadening.<sup>30</sup> The absence of solvent in the  $\text{scCO}_2$  sample results in a much narrower linewidth and better resolution of the spectrum as can be seen in Figure 6.4. This allows the observation of three  $^{13}\text{C}$  signals indicating the distortion of the PEO structure that has been identified previously for pristine samples of PEO (Section 5.4.1).<sup>141,142</sup>

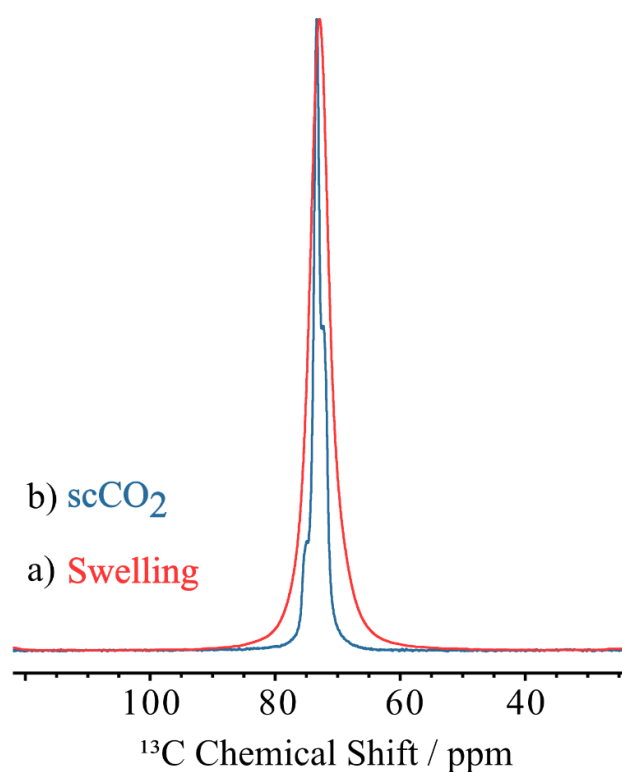


Figure 6.4:  $^1\text{H}$ - $^{13}\text{C}$  CP spectra with MW irradiation of PEO impregnated with AMUPol using the swelling method (Red) and the  $\text{scCO}_2$  method (Blue). Spectra are processed with 0 Hz line broadening and are normalized to the maximum intensities. The line shape of the  $\text{scCO}_2$  sample demonstrates the disordered conformation of polymer chains seen in semi-crystalline PEO at low temperatures.



The DNP build-up times, DNP enhancements, and the SNR enhancement factors,  $\chi_{DNP}$  (Equation [2.2.5.2]), of these two samples are shown in Table 6.5. The SNR enhancement factor provides a better measure of the usefulness of DNP and is most often used to compare the spectrum of a DNP experiment with a ‘standard’ solid-state NMR experiment.<sup>183</sup> Here, it is useful in assessing the benefits of one sample preparation technique over another.

<b>Impregnation Method</b>	$T_{DNP}$	$\epsilon_{DNP}$	$\chi_{DNP}$
Swelling	4.2 s	22.8	115
scCO <sub>2</sub>	19 s (66 %) 4.8 s (33 %)	4.7	70

*Table 6.5: DNP build-up times, DNP enhancements, and SNR enhancement factors of samples of PEO impregnated with AMUPol using the swelling method and the scCO<sub>2</sub> method. The DNP build-up time of the swelling sample was fitted with a monoexponential build-up function:  $I(\tau) = A \left(1 - e^{-\frac{\tau}{T_{DNP}}}\right)$ .  $\chi_{DNP} = \frac{SNR}{NS\sqrt{T_{DNP}}}$ .  $\chi_{DNP}$  of the scCO<sub>2</sub> sample was calculated using  $T_{DNP} = 19$ .*

Calculating  $\chi_{DNP}$  of the two samples allows a comparison of the effectiveness of the two sample preparation methods taking into consideration the shorter DNP build-up time of the swelling method and the higher SNR of the scCO<sub>2</sub> method. If optimal overall sensitivity is the most important factor in determining which sample preparation method to use, the swelling method should be chosen. However, the improved resolution and retention of solid-state conformation of PEO impregnated in scCO<sub>2</sub> are also valuable results.

Additionally, there is scope for improvement of the efficiency of the scCO<sub>2</sub> method by further investigations of the optimum scCO<sub>2</sub> temperature, pressure, and depressurization rate. Any increased homogeneity of the radical distribution in scCO<sub>2</sub> prepared samples from further optimization of the impregnation conditions could reduce the DNP build-up time and improve the SNR enhancement factor. This would result in the scCO<sub>2</sub> sample preparation method providing high sensitivity and resolution.

## 6.4.1. Polystyrene

Polystyrene (PS) does not show the same readiness to swell in scCO<sub>2</sub> as PEO. This reduced swelling behaviour is due to stronger intermolecular interaction in a PS chain due to  $\pi$ -stacking of the phenyl groups. This  $\pi$ -stacking restricts the rotational freedom of PS chains which limits the ability of scCO<sub>2</sub> to affect the structure of the polymer.<sup>184</sup>

Though slight swelling of PS does occur if processed for a significant length of time at sufficiently high temperatures and pressures, the impregnation of PS has been used here as a test of whether it is important to have significant swelling of the polymer to successfully impregnate a polymer with a bulky nitroxide radical. At temperatures and pressures which do not induce significant swelling of PS, there remains diffusion of scCO<sub>2</sub> throughout the polymer network.<sup>185</sup>

The impregnation of PS with a DNP radical in the absence of swelling, could indicate some degree of solubility of the radical in scCO<sub>2</sub>. Following the results in Section 5.4.1, it is necessary for the DNP radical to be dispersed throughout the polymer network to achieve a DNP enhancement. Samples where the radical was concentrated on the surface of the polymer did not show any enhancement. Solubility of the radical in scCO<sub>2</sub> would assist in its dispersion throughout a non-swollen polymer. This could provide a basis for successful scCO<sub>2</sub> impregnation of other non-swelling materials such as zeolites.

### 6.4.1.1. Cross Polarization and Direct Polarization

The <sup>1</sup>H-<sup>13</sup>C CP spectra of PS and PEO, impregnated with TEKPol in scCO<sub>2</sub> at 200 bar and 34 °C for 1 hour, are shown in Figure 6.5. Unlike the PEO samples, the impregnated PS sample shows no DNP enhancement. The intensity of the MW on spectrum of the PS sample is in fact reduced, this is likely due to heating of the sample under MW irradiation.<sup>136</sup> Varying the temperature, pressure, and time of the scCO<sub>2</sub> process did not improve the CP DNP enhancements observed.

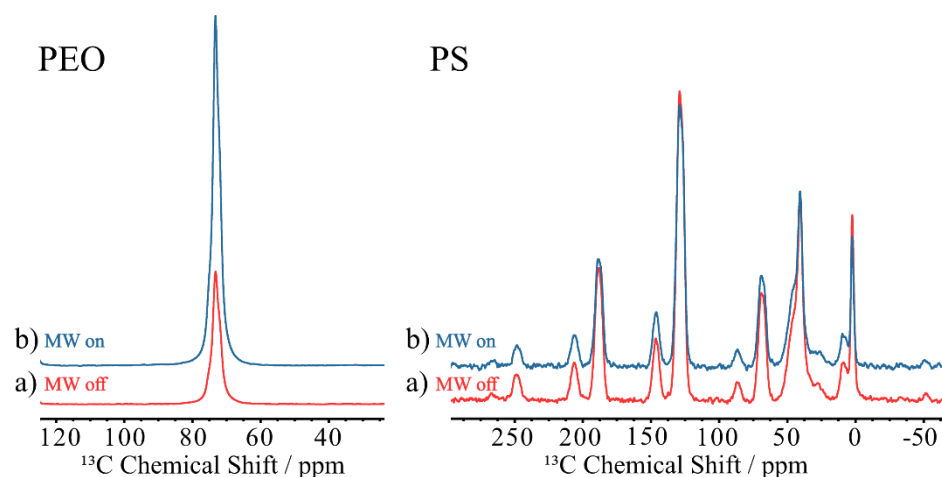


Figure 6.5:  $^1\text{H}$ - $^{13}\text{C}$  CP spectra a) without and b) with MW irradiation of PEO (Left) and PS (Right) impregnated in  $\text{scCO}_2$  with  $11 \mu\text{mol g}^{-1}$  of TEKPol at  $34^\circ\text{C}$  and 200 bar for 1 hour. For PEO,  $\epsilon_{\text{DNP}} = 2.6$ , for PS,  $\epsilon_{\text{DNP}} = 0.8$ .

The hypothesis that the lack of DNP enhancement of the PS signals could be due to reduced swelling of PS in  $\text{scCO}_2$ , and resultant inability of the radical to be distributed throughout the sample, is not supported by EPR measurements. EPR spectra of PS samples show that TEKPol is present in comparable quantities to PEO samples (Figure 6.17).

Figure 6.6 shows the MW on and MW off spectra of  $^1\text{H}$ - $^{13}\text{C}$  CP and  $^{13}\text{C}$  DP experiments of PS, impregnated with TEKPol in  $\text{scCO}_2$  at 207 bar and  $40^\circ\text{C}$  for 2 hours. As seen for other PS samples, there is no DNP enhancement of the CP experiment however, there is an observable DNP enhancement of the DP experiment. The measured enhancement of the phenyl carbons is 2.0 and the enhancement of the polymer backbone carbons is 2.9. The signal at 0 ppm which does not exhibit a CP or DP enhancement is likely to be the  $\text{CH}_3$  groups of the PDMS-MA stabilizer used in the synthesis of PS.<sup>186</sup>

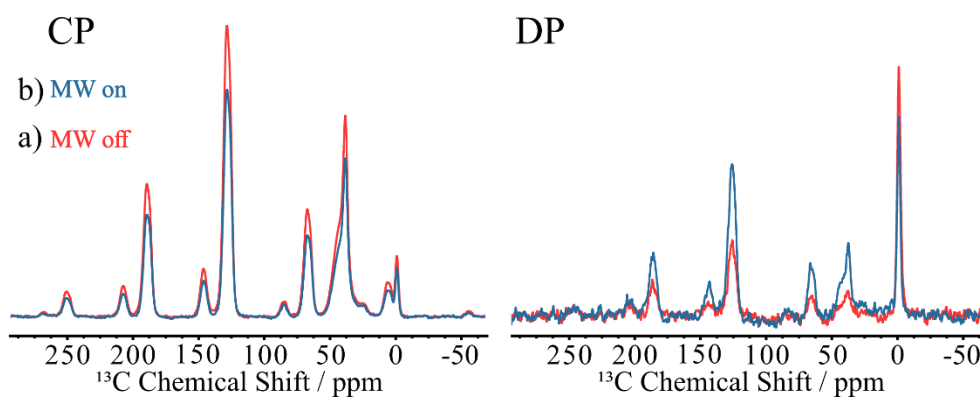


Figure 6.6:  $^1\text{H}$ - $^{13}\text{C}$  CP (Left) and  $^{13}\text{C}$  DP (Right) spectra a) without and b) with MW irradiation of PS impregnated with TEKPol in  $\text{scCO}_2$  at  $40^\circ\text{C}$  and 207 bar for 2 hours. For CP,  $\epsilon_{\text{DNP}} = 0.8$ , for DP,  $\epsilon_{\text{DNP}} = 2.9$ .

Although the observation of a DNP enhancement for the DP  $^{13}\text{C}$  spectrum of PS is a positive sign that the process of  $\text{scCO}_2$  impregnation of PS is possible, the low natural abundance of  $^{13}\text{C}$  and slower homonuclear spin diffusion process means that any benefit that could be drawn from a DNP enhancement, is insignificant in comparison to the time saved by first polarizing  $^1\text{H}$  followed by CP transfer to detect  $^{13}\text{C}$  signals.<sup>187</sup>

#### 6.4.1.2. Radical Concentration

Recently published work by Le *et al.* provides evidence that the radical concentrations used in this work are too low, which could be the reason that there is no DNP enhancement of CP experiments.<sup>188</sup> In the  $\text{scCO}_2$  impregnation of PS by Le *et al.*, the initial concentration they used was between 180 and  $256\ \mu\text{mol}$  of the radical bTbK per gram of PS. This quantity of radical resulted in PS samples which had bTbK loadings of between 5 and  $20\ \mu\text{mol g}^{-1}$ , as measured by CW EPR. The bTbK loading seemed to be dependent on the molecular weight of the polymer with the higher molecular weight polymers having significantly lower bTbK concentrations.

This result indicates that there is significant loss of the radical at some point during the  $\text{scCO}_2$  impregnation process. The radical bTbK is smaller in size than TEKPol and is therefore more likely to be soluble in  $\text{scCO}_2$ , Le *et al.* note that attempts they made to impregnate their samples with TEKPol showed no

improvement in the DNP enhancement achieved, despite TEKPol being a more optimized radical which should provide larger enhancements. They conclude that this is likely due to the reduced solubility of TEKPol in scCO<sub>2</sub>. They do not note the loading of TEKPol in these samples. The reduced solubility of TEKPol in scCO<sub>2</sub> may result in a less efficient distribution of TEKPol throughout the polymer matrix however it may also reduce the amount of radical which is lost during the scCO<sub>2</sub> processing.

Assuming that the loading of TEKPol during scCO<sub>2</sub> impregnation is similar to that of bTbK in the work of Le *et al.*, it is possible that the radical concentration of the PS samples prepared in this work could be as low as 7.4 % of the initial starting concentration. Attempts were made to carry out EPR spin counting experiments as part of this work. However, technical limitations prevented this work from being completed.

Figure 6.7 shows the <sup>1</sup>H-<sup>13</sup>C CP spectra of a PS sample impregnated with an initial concentration of 105 μmol g<sup>-1</sup> of TEKPol in scCO<sub>2</sub> at a pressure of 200 bar and temperature of 40 °C for 24 hours. This initial radical concentration is closer to that used by Le *et al.* and provides a DNP enhancement of 1.2 for all carbon signals in the CP experiment. This result reinforces the theory that the radical concentrations used for all other PS samples are well below the optimum of ~ 10 μmol g<sup>-1</sup> and the DNP enhancements achieved could be improved by increasing this concentration.

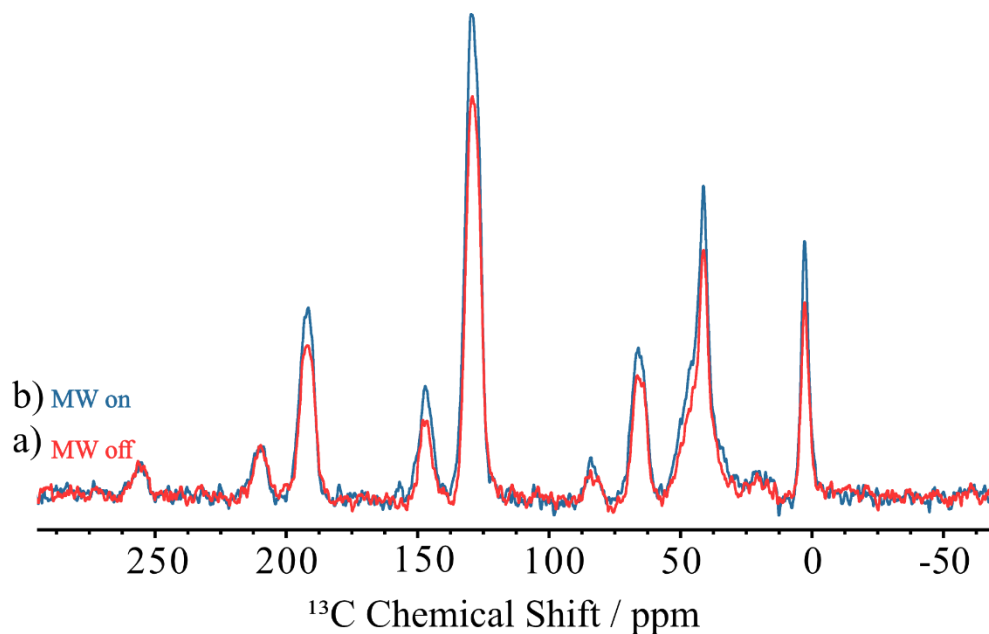


Figure 6.7:  $^1\text{H}$ - $^{13}\text{C}$  CP spectra a) without and b) with MW irradiation of PS impregnated with  $105 \mu\text{mol g}^{-1}$  of TEKPol in  $\text{scCO}_2$  at  $40^\circ\text{C}$  and 200 bar for 24 hours.  $\epsilon_{\text{DNP}} = 1.2$ .

The publication from Le *et al.* is the first to detail a process for supercritical  $\text{CO}_2$  impregnation of polymers with radicals designed for DNP-enhanced solid-state NMR. Their method of impregnation differs slightly from the one used here, the radical and stirrer bar in their set up is never in direct contact with the polymer, which is placed on an aluminium support and covered with filter paper to avoid deposition of the radical on the polymer surface after depressurization. These steps were considered when designing the sample preparation method used in this study however, limited access to the biradicals used meant that a considerably smaller autoclave was used which could not accommodate this set up.

It must be noted that although the PEO samples prepared in this work were also impregnated with lower initial radical concentrations, the DNP enhancements observed for PEO are comparable to the enhancements achieved for PS with very high initial radical concentrations prepared by Le *et al.*<sup>188</sup> It is possible that the nature of PEO results in a more favourable partition of radical in the polymer matrix resulting in a higher impregnated concentration. Additionally, the DNP build-up times for the PS samples prepared in this work and that of Le *et al.* are

significantly shorter than those of PEO. Given the apparent inhomogeneous distribution of radical in PEO and PS, for a longer  $T_{DNP}$ , a higher  $\varepsilon$  should be expected.<sup>30,189</sup>

## 6.4.2. Core-Shell Structures

Core-shell structured impact modifiers are dispersed through engineering plastics to improve toughness, heat resistance, and weather resistance.<sup>190,191</sup> Improving the strength and durability of engineering polymers is necessary to limit the environmental damage resulting from their synthesis and degradation. While core-shell impact modifiers do provide this increased durability, the negative impact of their synthesis must also be considered when determining the overall sustainability of the practice.

Work at The University of Nottingham is ongoing in developing methods of preparing such core-shell systems using scCO<sub>2</sub> as the reaction medium. This method of synthesis encompasses many of the common benefits of scCO<sub>2</sub> synthesis, including eliminating the requirement for the energy and resource intensive processes of drying and separation. The synthesis of conventional two-phase core-shell morphology impact modifiers, which have a “*soft*” rubber core and a “*hard*” glassy shell,<sup>192,193</sup> in scCO<sub>2</sub> is challenging as the scCO<sub>2</sub> induces plasticization and agglomeration of the soft polymer.<sup>194,195</sup> To resolve this issue, three-phase materials which layer a soft polymer between two hard components were investigated. These three-phase hard-soft-hard polymer structures could provide the necessary properties of good impact modifiers with the benefit of more sustainable synthetic routes.

The first step in the development of these structures is the synthesis of hard core-hard shell systems with a polystyrene (PS) core, encased by a poly(methyl methacrylate) (PMMA) shell in scCO<sub>2</sub>. A <sup>1</sup>H-<sup>13</sup>C CP spectrum of a PS:PMMA core-shell polymer and the spectral assignment are shown in Figure 6.8. The aim of this step is to develop pathways to ensure the centre hard plastic core is as small as possible in relation to the overall particle size. The synthesis of PS:PMMA core-shell particles with increasing ratios of PMMA produces particles of expected PS:PMMA ratios, with a single distribution of sizes for

each ratio, as confirmed by  $^1\text{H}$  NMR, dynamic light scattering, dynamic mechanical analysis, tunnelling electron microscopy, and scanning electron microscopy. Although these techniques provide a measurement of the particle size, this is a measurement of the outer shell and thus the size of the core can only be estimated from these measurements and the core:shell ratio. DNP-enhanced solid-state NMR can be used to analyse the structures of multi-component materials such as core-shell systems,<sup>196,197</sup> in particular *relayed* DNP can be used to measure component domain sizes in these complex systems.<sup>198</sup>

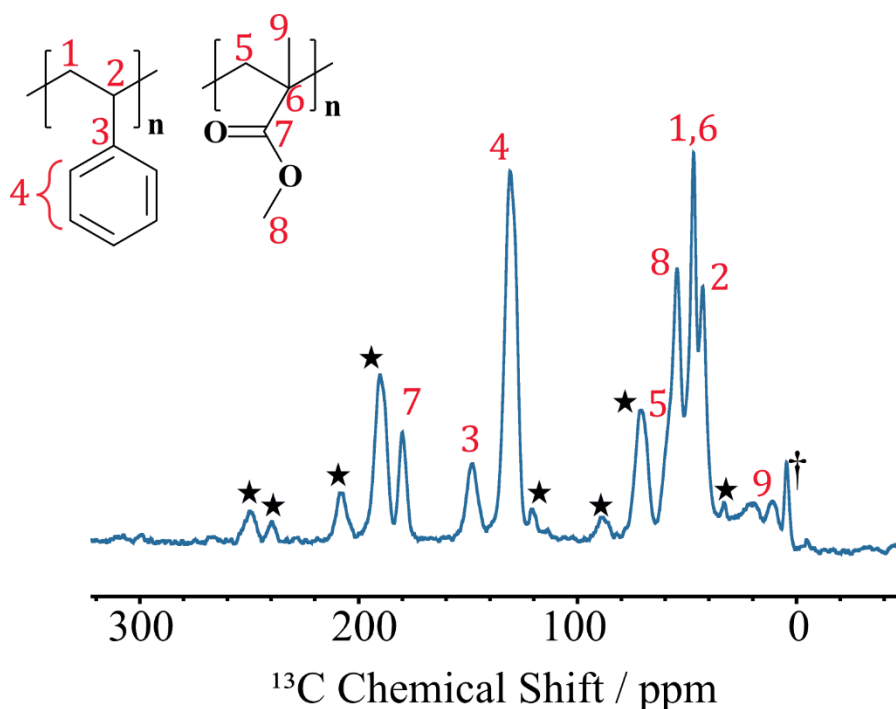


Figure 6.8:  $^1\text{H}$ - $^{13}\text{C}$  CP spectrum of a PS:PMMA core-shell polymer with a 1:1 PS:PMMA ratio. † marks signals from an impurity, tentatively assigned to the  $\text{CH}_3$  group of PDMS. Spinning sidebands are noted with ★.

The relayed DNP effect can be seen in CP DNP measurements of multi-component samples in which the radical is localized in one component, and the other component is radical-free. When the radical source component is hyperpolarized, this polarization is distributed to the radical free component *via*  $^1\text{H}$  spin diffusion. The DNP enhancement of signals in the radical free component is due to  $^1\text{H}$  spin diffusion from the source component and is therefore dependant on the size of the source domain. NMR is a particularly



useful technique for these measurements as the different components can be easily identified by their distinct chemical shifts or relaxation properties.

The application of relayed DNP requires selective radical impregnation of one component of the system which presents a challenge in preparation of PS:PMMA core-shell systems. It is essential that the integrity of the core-shell structure is maintained after impregnation of one component with a radical. Attempts at preparing these systems using a radical solution of TEKPol in TCE were unsuccessful as the PMMA shell in contact with the organic solvent was soluble and the core-shell structure was lost. Attempts to prepare these systems using AMUPol in a glycerol- $d_8$ /D<sub>2</sub>O/H<sub>2</sub>O solution gave no DNP enhancement.

Radical impregnation using scCO<sub>2</sub> as the solvent is an attractive option since the particles are synthesized in scCO<sub>2</sub> there is limited risk of disruption of the core-shell morphology. Given the different swelling properties of PS and PMMA in scCO<sub>2</sub>, it may also be possible to preferentially impregnate either the core or the shell by careful tuning of the scCO<sub>2</sub> conditions.

#### 6.4.2.1. Cross Polarization and Direct Polarization

Core-shell systems with PS:PMMA ratios of 1:1, 1:2, 1:4, and 1:8 were impregnated with 10 to 15  $\mu$ mol of TEKPol per gram of polymer in scCO<sub>2</sub> at 207 bar and 40 °C for 2 hours. The <sup>1</sup>H-<sup>13</sup>C CP spectra of these polymers are presented in Figure 6.9. By normalizing the signal intensities of the intense resonance which corresponds to overlapping signals from the back-bone of both polymers, the change in relative intensities of PS and PMMA signals as the PMMA shell thickness increases, is clear.

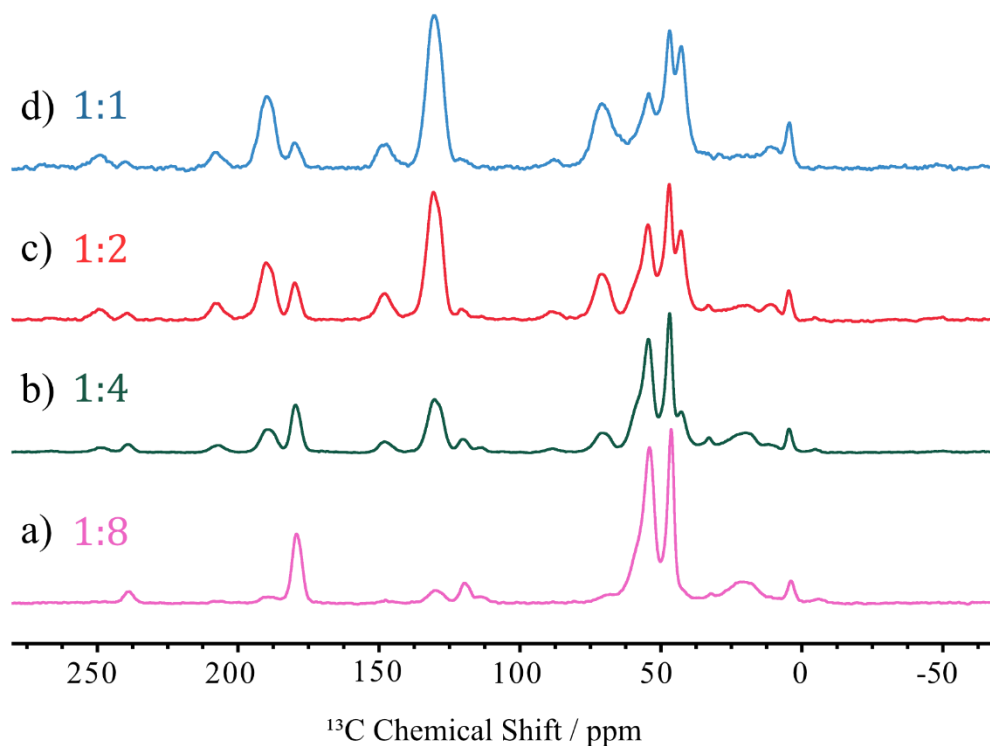


Figure 6.9:  $^1\text{H}$ - $^{13}\text{C}$  CP spectra of PS:PMMA core-shell polymers with PS:PMMA ratios of a) 1: 8, b) 1: 4, c) 1: 2, and d) 1: 1. Intensities are normalized by the back-bone resonance at 45 ppm.

Similarly, to the PS samples prepared in  $\text{scCO}_2$ , the core-shell samples show no DNP enhancement in CP experiments, but the PS resonances do exhibit DNP enhancements in the  $^{13}\text{C}$  DP experiments. The CP DNP build-up times and CP and DP enhancements of the phenyl signal of PS are presented in Table 6.6. The PS signals of the 1: 8 core-shell sample could not be fully analysed due to the low concentration of PS in this sample.

<b>PS:PMMA</b>	<b><math>T_{DNP}</math></b>	<b>CP <math>\epsilon_{DNP}</math></b>	<b>DP <math>\epsilon_{DNP}</math></b>
1:1	1.3 s (79 %) 0.4 s (21 %)	0.7	2.0
1:2	13 s (43 %) 0.8 s (57 %)	0.8	1.8
1:4	3 s (66 %) 0.14 s (34 %)	0.8	0.7
1:8	—	0.6	—

*Table 6.6: PS signal  $^1H$ - $^{13}C$  CP DNP build-up times, CP DNP enhancements, and DP DNP enhancements of core-shell polymers with increasing shell thicknesses.*

As the thickness of the PMMA shell increases, the DNP enhancement observed for the PS core decreases. It is possible that this is an observation of relayed DNP. If selective impregnation of the PMMA shell has been successful, the polarization of PS spins is solely dependent on spin diffusion from the shell. It can be seen in Figure 6.10, that the build-up of polarization of the PS signal of the 1:2 and 1:4 samples is significantly accelerated by MW irradiation, which is a primary indicator of relayed DNP.<sup>198</sup>

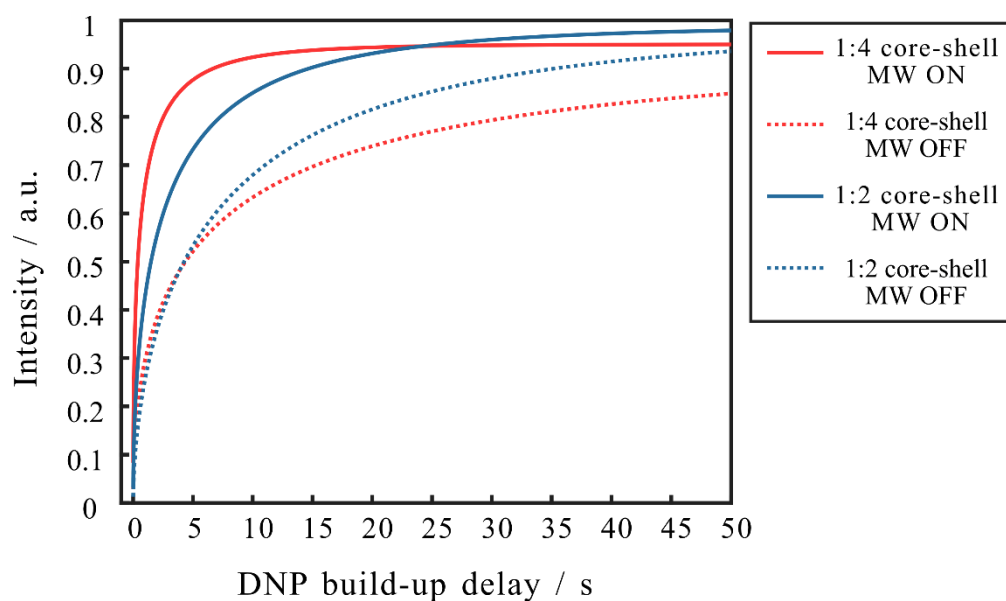


Figure 6.10:  $^1\text{H}$ - $^{13}\text{C}$  CP DNP build-up curve fits for the PS signal of 1:4 (Red) and 1:2 (Blue) ratios of PS:PMMA core-shell polymers measured with (solid line) and without (dashed line) MW irradiation. The polarization build-up is significantly accelerated by MW irradiation.

However, the enhancement of pure PS samples that have been impregnated in  $\text{scCO}_2$  under the same conditions, as seen in Section 6.4.1 means that it cannot be said with certainty that there is no paramagnetic source present in the PS component, without additional investigation. Further investigation of the optimal  $\text{scCO}_2$  conditions preparations, coupled with EPR measurements of spin concentration could provide a route to preferential localization of the radical in the PMMA shell and allow relayed DNP analysis to be used to determine the sizes of the core and shell components.

The CP DNP build-up times and CP and DP enhancements of the OCH<sub>3</sub> signal of PMMA are presented in *Table 6.7*.

PS:PMMA	$T_{DNP}$	CP $\epsilon_{DNP}$	DP $\epsilon_{DNP}$
1:1	0.88 s	0.6	0.7
1:2	5 s (36 %) 0.8 s (64 %)	0.5	0.6
1:4	1.4 s (61 %) 0.27 s (39 %)	0.5	0.6
1:8	1.2 s (76 %) 0.3 s (24 %)	0.5	0.6

*Table 6.7: PMMA signal 1H-13C CP DNP build-up times, CP DNP enhancements, and DP DNP enhancements of core-shell polymers with increasing shell thicknesses.*

The PMMA signals are not enhanced during the <sup>1</sup>H-<sup>13</sup>C CP or <sup>13</sup>C DP experiments, this is potentially due to the very short  $T_{DNP}$  build-up times due to the methyl groups present acting as relaxation sinks. Additionally, the biexponential fitting of the PMMA  $T_{DNP}$  suggests that there is an inhomogeneous distribution of the radical in this domain. Coupled with the intrinsically short relaxation time of PMMA, this prevents efficient spin diffusion of polarization throughout the polymer. As the PMMA shell thickness increases, the DNP enhancement of PMMA shows no significant change despite apparent changes in the homogeneity of the radical distribution. This indicates that the major hindrance to achieving a DNP enhancement of PMMA is the intrinsically short relaxation. The lack of enhancement of the DP spectra despite <sup>13</sup>C DP build-up rates being slower, can also be attributed to the fast dynamics

of the PMMA methyl groups. Even at 100 K, the rotation of methyl groups can lead to a spontaneous  $^1\text{H}$ - $^{13}\text{C}$  polarization transfer due to *cross-relaxation*.<sup>179</sup> The cross-relaxation mediated polarization transfer results in a negative enhancement of  $^{13}\text{C}$  spins which are dipolar coupled to the  $^{13}\text{C}$  of a methyl group. The MW on DP spectrum of a system which is undergoing this cross-relaxation therefore suffers a reduction in intensity which correlates to the increased polarization due to cross-relaxation.

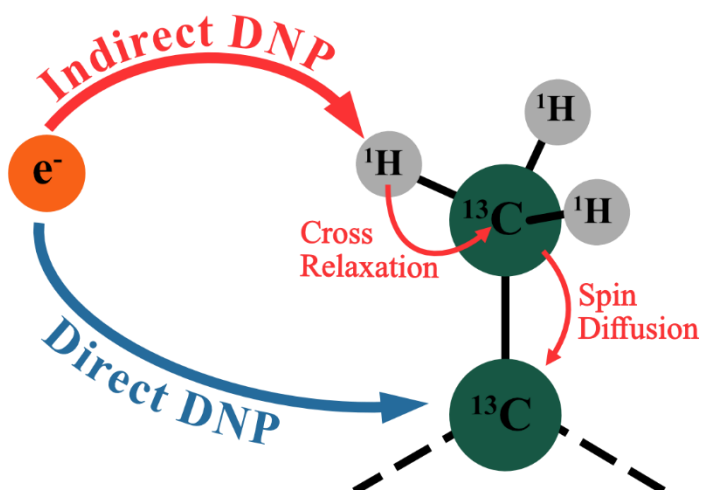


Figure 6.11: Schematic representation of the competing polarization transfer pathways during a  $^{13}\text{C}$  DP DNP experiment (direct  $e$ - $^{13}\text{C}$  polarization (Blue) and indirect polarization via  $^1\text{H}$ - $^{13}\text{C}$  cross-relaxation (Red)) of a sample with hyperpolarized  $^1\text{H}$  methyl spins.

#### 6.4.2.2. SCREAM-DNP

Potential solutions to overcome the negative enhancement due to cross-relaxation are the perdeuteration of methyl groups<sup>199</sup> or the use of novel radicals designed for proton rich samples.<sup>200</sup> However, it is possible to harness the cross-relaxation to derive information about the molecular structure and dynamics using *specific cross-relaxation enhancement by active motions under DNP* (SCREAM-DNP).<sup>40</sup>

SCREAM-DNP is a particularly useful tool for large biomolecules where spectral crowding hinders efficient spectral analysis. SCREAM-DNP allows for selective polarization transfer to  $^{13}\text{C}$  from methyl groups, the absence of any methyl groups in unmodified RNA makes SCREAM-DNP a highly selective

tool to investigate binding sites of RNA with methyl-containing ligands.<sup>40,201</sup> In a  $^{13}\text{C}$  ‘direct’ polarization experiment of a methyl containing system, the total  $^{13}\text{C}$  hyperpolarization is a result of direct polarization transfer from the electron source and spontaneous indirect polarization transfer to the methyl  $^{13}\text{C}$  from hyperpolarized  $^1\text{H}$  (Figure 6.11). Saturation of the  $^1\text{H}$  spins during the DNP build up time suppresses the methyl cross-relaxation and only true direct polarization transfer to  $^{13}\text{C}$  can occur. It is therefore possible to identify which  $^{13}\text{C}$  sites are dipolar coupled to a methyl group. This is useful when the goal is selective enhancement of these sites but, could also provide useful measurements of domain sizes in core-shell systems if only one domain contains methyl groups. By observing the enhancement which is the result of cross-relaxation and the build-up of this enhancement over time, coupled with models of polarization dynamics and  $^{13}\text{C}$ - $^{13}\text{C}$  spin diffusion, distances may be calculated. The measurement of the SCREAM-DNP effect provides a DP equivalent to measure the relayed DNP effect where in this case, the polarization source is hyperpolarized methyl  $^1\text{H}$ .<sup>196</sup>

In Figure 6.12, four spectra of a 1:1 core-shell polymer are presented. The spectrum  $\text{DP}_{\text{sat}}$  was recorded while any  $^1\text{H}$  hyperpolarization was saturated by a train of pulses and as a result this spectrum consists only of direct  $^{13}\text{C}$  polarization. The  $\text{DP}_{\text{off}}$  spectrum was collected with no MW irradiation and no  $^1\text{H}$  saturation. The  $\text{DP}_{\text{on}}$  spectrum represents the  $^{13}\text{C}$  spectrum which results from direct  $^{13}\text{C}$  polarization from electrons and cross-relaxation induced  $^1\text{H}$ - $^{13}\text{C}$  polarization transfer. Subtraction of  $\text{DP}_{\text{sat}}$  from the  $\text{DP}_{\text{on}}$  spectrum results in the  $\Delta\text{DP}_{\text{sat}}$  spectrum which represents the  $^{13}\text{C}$  polarization that has been generated solely by  $^1\text{H}$ - $^{13}\text{C}$  cross-relaxation.

The enhancement factor which describes the direct  $^{13}\text{C}$  polarization,  $\epsilon_+$ , is determined by comparing the  $\text{DP}_{\text{sat}}$  and  $\text{DP}_{\text{off}}$  spectra. The cross-relaxation enhancement factor,  $\epsilon_-$ , is determined by comparing the  $\Delta\text{DP}_{\text{sat}}$  and  $\text{DP}_{\text{off}}$  spectra. These enhancement factors of representative signals of PS and PMMA of the 1:1 core-shell polymer, calculated from spectra obtained with a 15.15 s polarization build-up delay, are presented in Table 6.8.

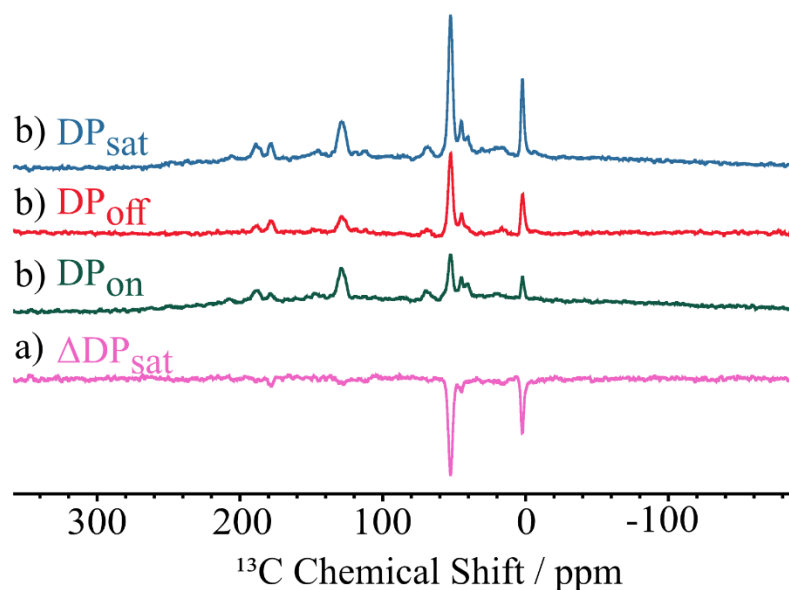


Figure 6.12: a)  $DP_{sat}$ , b)  $DP_{off}$ , c)  $DP_{on}$ , and d)  $\Delta DP_{sat}$  spectra for a 1:1 PS:PMMA core-shell polymer impregnated with TEKPol in  $scCO_2$  at 40 °C and 241 bar for 2 hour.  $DP_{sat}$ ,  $DP_{off}$ , and  $DP_{on}$  spectra were obtained with a 15.15 s polarization build-up delay.  $\Delta DP_{sat} = DP_{on} - DP_{sat}$ .

Polymer	$\epsilon_+$	$\epsilon_-$
PS	1.9	0.1
PMMA	1.7	1.2

Table 6.8: Direct ( $\epsilon_+$ ) and cross-relaxation ( $\epsilon_-$ ) DNP enhancements of representative signals of PS and PMMA in a 1: 1 core-shell sample impregnated with 12  $\mu\text{mol g}^{-1}$  TEKPol in  $scCO_2$  at 241 bar and 40 °C for 2 hours.

These enhancement factors demonstrate strong SCREAM-DNP activity of the OCH<sub>3</sub> PMMA signal. In Figure 6.13,  $\Delta DP_{sat}$  spectra (with a 180 ° phase change) at increasing polarization delay times are overlaid. The OCH<sub>3</sub> signal of PMMA shows very strong SCREAM-DNP behaviour, appearing at just 0.55 s. The quaternary and carbonyl <sup>13</sup>C signals of PMMA and phenyl signals of PS begin to show some SCREAM-DNP behaviour at around 11 s and appear to build-up



much slower. This slower onset of SCREAM-DNP activity for these PMMA signals is evidence of the initial methyl  $^1\text{H}$ - $^{13}\text{C}$  polarization transfer being further diffused through the material by  $^{13}\text{C}$ - $^{13}\text{C}$  spin diffusion.<sup>202</sup> The strong SCREAM-DNP activity of the impurity signal at 0 ppm, confirms that this is a signal corresponding to the  $\text{CH}_3$  groups of the PDMS used as a stabilizer in the synthesis of PS. It is therefore likely, that the slow onset of SCREAM-DNP activity for the PS phenyl signal, is due to polarization transfer from the PDMS methyl cross-relaxation process.

The presence of these methyl groups in the PS core limits the applicability of SCREAM-DNP to the measurement of domain sizes in these PS:PMMA core-shell systems. Even if there is domain specific impregnation of the PMMA shell, the much faster  $^1\text{H}$ - $^1\text{H}$  polarization transfer from PMMA methyl  $^1\text{H}$  to PDMS methyl  $^1\text{H}$  initiating PDMS cross-relaxation and subsequent PDMS methyl  $^{13}\text{C}$ -PS  $^{13}\text{C}$  polarization transfer, will likely obscure the observation of any longer-range PMMA methyl  $^{13}\text{C}$ -PS  $^{13}\text{C}$  transfer.

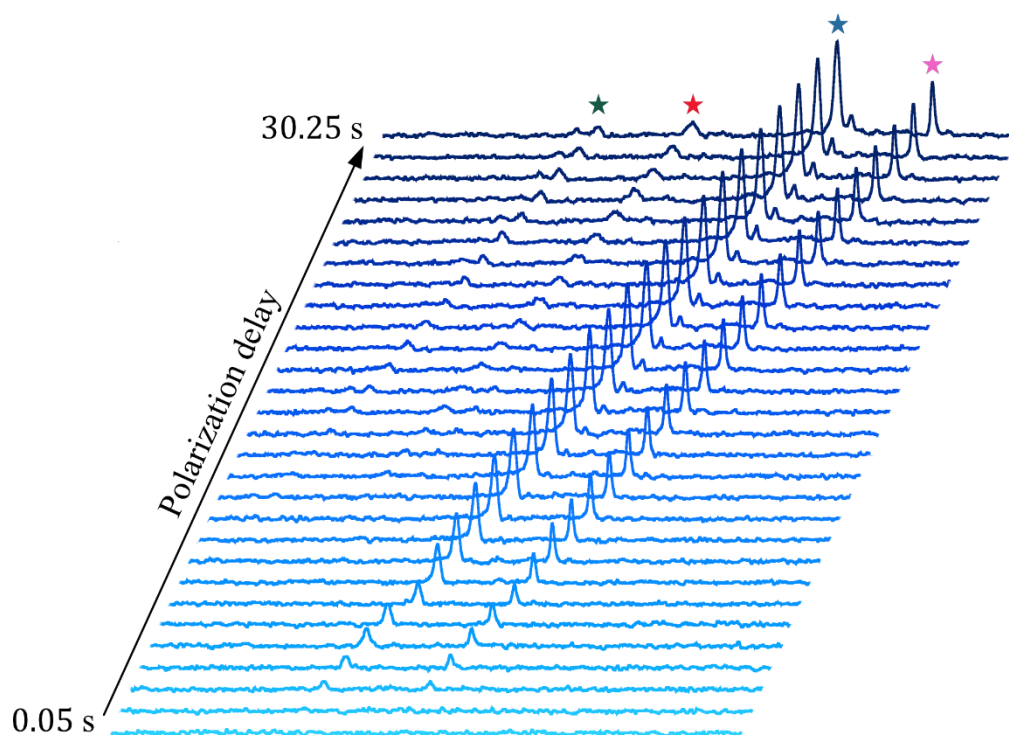


Figure 6.13:  $\Delta DP_{sat}$  spectra (with a  $180^\circ$  phase change) obtained at increasing polarization build-up delay times from 50 ms to 30.25 s demonstrating the very quick cross-relaxation induced polarization of the PMMA (Blue ★) and PDMS (Pink ★) methyl groups. and the PMMA carbonyl (Green ★) and PS phenyl (Red ★) signals experiencing cross-relaxation induced polarization much slower than methyl groups.

### 6.4.3. EPR Measurements

Electron paramagnetic resonance was used to confirm the presence of a radical in samples that showed no signs of DNP enhancement, and to investigate any differences in samples prepared in  $scCO_2$ , and those impregnated by swelling.

The Q-band spectra recorded at 100 K show MW saturation effects due to an electron spin relaxation effect. This results in distorted line shapes and complicates the analysis of the spectra. Due to the poor resolution, it was not possible to simulate the spectra well. However, it was possible to use spin Hamiltonian parameters reported in the literature,<sup>203</sup> to calculate the Q-band spectra for these radicals. The literature parameters were obtained from high-field EPR (HF-EPR) spectra and were tested by reproducing the HF-EPR spectra seen in the literature before being used to calculate the rigid-limit Q-band spectra

of AMUPol and TEKPol. The parameters used are summarized in Table 6.9. The calculated Q-band spectra have been used to make qualitative comparisons with the experimental data.

In Figure 6.14, the experimental data for a sample of PEO impregnated by swelling in 10 mM AMUPol in glycerol- $d_8$ /D<sub>2</sub>O/H<sub>2</sub>O (60/30/10 vol%), which exhibits relatively poor resolution and significant line shape distortion, is compared to the calculated Q-band spectrum of AMUPol.

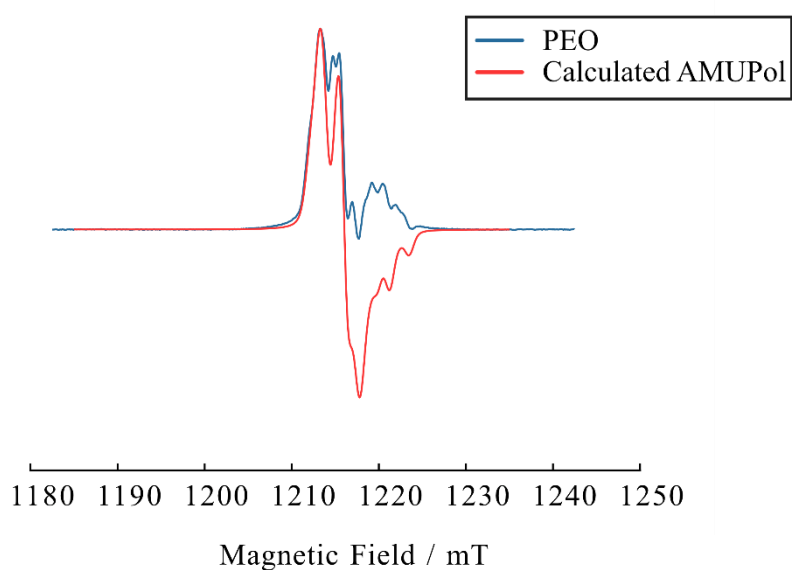


*Figure 6.14: Experimental data for PEO impregnated by swelling in a solution of 10 mM AMUPol in glycerol- $d_8$ /D<sub>2</sub>O/H<sub>2</sub>O (60/30/10 vol%) (Blue) and calculated spectrum of AMUPol based on HF EPR data (Red). The calculated spectrum shows the expected line shape for the first-derivative of the absorption spectrum, comparison with the experimental line shape demonstrates its significant distortion from the expected first-derivative of the absorption spectrum due to saturation effects. Intensities are normalized to the maximum amplitude.*

Comparing the features of the two spectra and disregarding the partial saturation of the experimental data, shows that the experimental spectrum is consistent with the literature parameters. This implies that the biradical is well dispersed in the polymer matrix. This result is expected as it is shown in Section 5.4, that this method of sample preparation results in good DNP enhancements which rely on a homogeneous radical distribution.

Comparing the spectrum of a sample of PEO impregnated with a  $9 \mu\text{mol g}^{-1}$  concentration of AMUPol in  $\text{scCO}_2$  with the sample prepared by swelling demonstrates a significant further reduction of resolution of the  $\text{scCO}_2$  sample. This can be seen in Figure 6.15 which shows a comparison of the experimental data for these two samples. Although the  $\text{scCO}_2$  spectrum shares some features with the swelling spectrum, overall the resolution is much poorer.

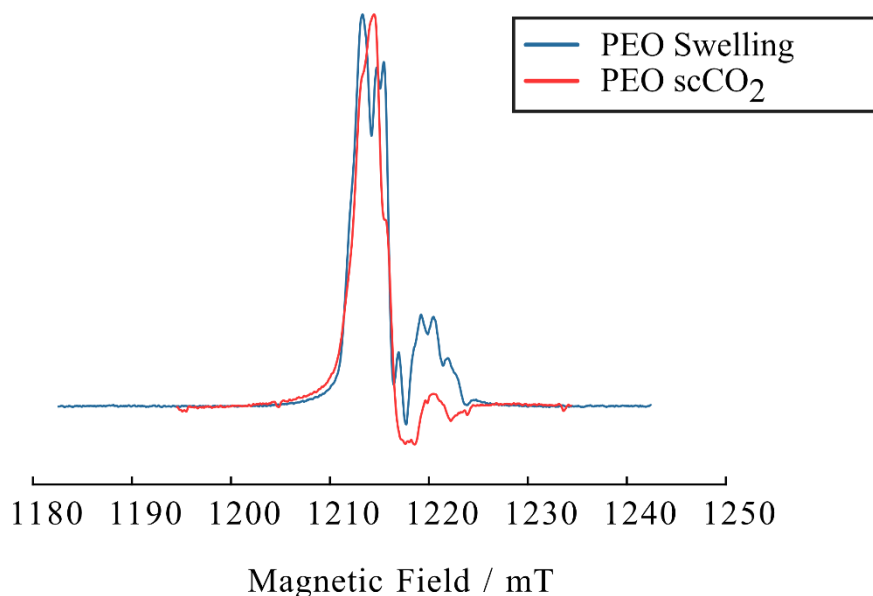


*Figure 6.15: Experimental spectra of PEO impregnated by swelling in a solution of 10 mM AMUPol in glycerol- $d_8$ /D<sub>2</sub>O/H<sub>2</sub>O (60/30/10 vol%) (Blue) and PEO impregnated with  $9 \mu\text{mol g}^{-1}$  concentration of AMUPol in  $\text{scCO}_2$  (Red). Although the  $\text{scCO}_2$  spectrum shares some features with the swelling spectrum there is overall much poorer resolution. Intensities are normalized to the maximum amplitude.*

The less resolved features of the  $\text{scCO}_2$  spectrum can be reproduced in the calculated Q-band spectrum by removing the *intra*-molecular e-e interactions from the model used (Figure 6.16).

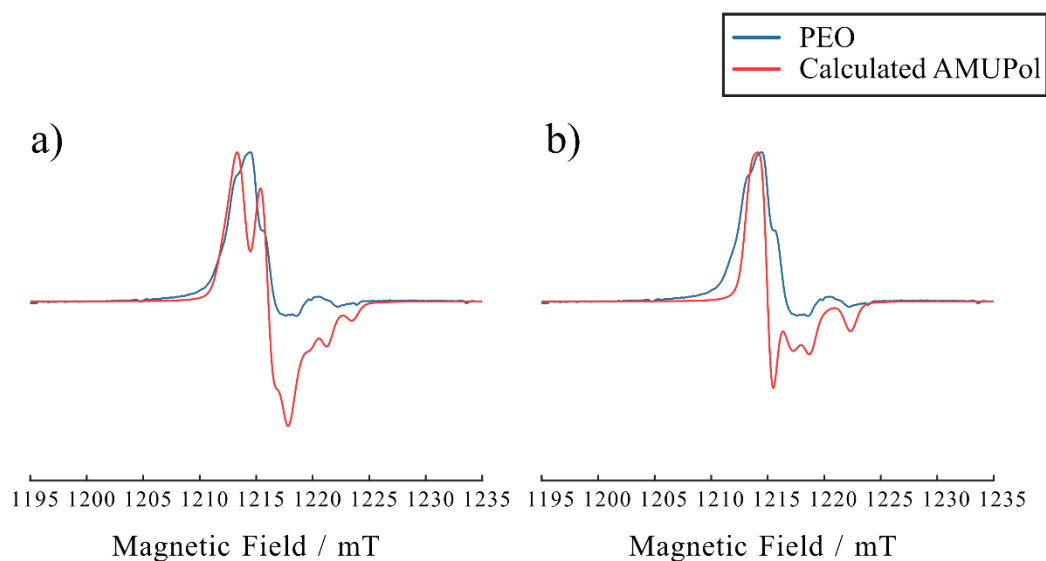


*Figure 6.16: Comparisons of the experimental data of the  $scCO_2$  impregnated PEO sample (Blue) and the calculated Q-band spectrum (Red) modelled a) with intra-molecular e-e interactions and b) without intra-molecular e-e interactions. In b) the features of the spectra around 1212 and 1220 mT are much better reproduced in the simulation without intra-molecular e-e interactions. Intensities are normalized to the maximum amplitude and the linewidth parameters are held constant to allow for comparison of a) and b).*

The need to remove the intra-molecular e-e interactions to better model the  $scCO_2$  experimental data implies that for this sample, *inter*-molecular e-e interactions dominate the spectrum. It therefore follows that there is likely some aggregation of the radical in this sample.

This observed inhomogeneity of radical may explain the poorer DNP enhancements seen for  $scCO_2$  impregnated samples, compared to samples impregnated by swelling (Section 6.4.1).

Comparisons of experimental spectra of PEO and PS impregnated with TEKPol in  $scCO_2$ , with the calculated Q-band spectrum of TEKPol modelled *with* e-e interaction shown in Figure 6.17, show better agreement than for AMUPol in Figure 6.16a. The calculated spectrum of TEKPol without the e-e intra-molecular interaction fails to reproduce the lowest field feature at 1213 mT seen in the experimental spectra of samples with TEKPol. Despite poor resolution, the line shape agreement of the calculated Q-band spectrum of TEKPol with the

e-e interaction shows that this interaction is partially resolved in the experimental spectra.

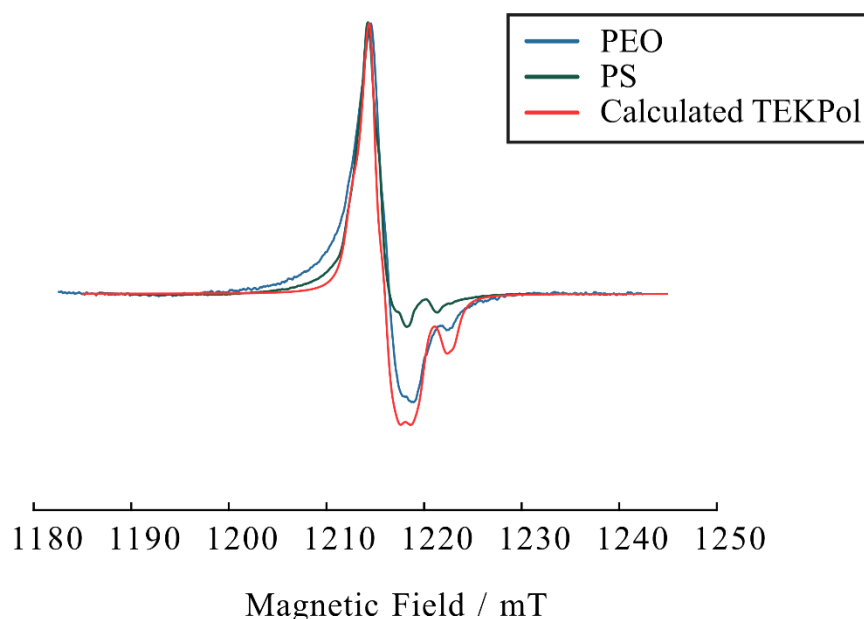


Figure 6.17: Experimental data for PEO impregnated with  $6 \mu\text{mol g}^{-1}$  concentration of TEKPol in  $\text{scCO}_2$  (Blue), experimental data for PS impregnated with  $5 \mu\text{mol g}^{-1}$  of TEKPol in  $\text{scCO}_2$  (Green), and the calculated Q-band spectrum of TEKPol, modelled with intra-molecular e-e interactions (Red). Intensities are normalized to the maximum amplitude.

The partial resolution of the intra-molecular e-e interaction in  $\text{scCO}_2$  samples impregnated with TEKPol suggests that there is *less* inter-molecular interaction in these samples than in the  $\text{scCO}_2$  sample impregnated with AMUPol, indicating that there is less aggregation of the radical.

The improved resolution of the intra-molecular e-e interaction in samples impregnated with TEKPol could be due to an improved homogeneity of the radical in the sample. Alternatively, it could be due to the lower expected radical concentration in these samples (samples prepared with 5 or  $6 \mu\text{mol g}^{-1}$  of TEKPol compared to  $9 \mu\text{mol g}^{-1}$  of AMUPol) which would result in a lower probability of inter-molecular interactions.

Radical	$g_1$ <sup>(a)</sup>	$g_2$	$g_3$	$A_1$ <sup>(b)</sup>	$A_2$	$A_3$	$\alpha$ <sup>(c)</sup>	$\beta$	$\gamma$	$J$ <sup>(d)</sup>	$D$ <sup>(e)</sup>	$\theta$ <sup>(f)</sup>	$\phi$
AMUPol	2.0092 (0.0008)	2.0061 (0.0003)	2.0020 (0.00012)	18	17	100	123.1	129.8	-46	+32	35	76	-174
TEKPol	2.0095 (0.00085)	2.0060 (0.00035)	2.0021 (0.00013)	18	16	98	-75.4	79.6	-58.6	+2	30.5	66	10

Table 6.9: Experimental HF EPR parameters for AMUPol and TEKPol radicals from Ref [203], used to calculate rigid-limit Q-band EPR spectra. a)  $g$ -tensors,  $g_i$  (the  $g$ -strains for these values in parenthesis). b)  $^{14}\text{N}$  hyperfine coupling,  $A_i$  given in MHz. c) Euler angles  $\alpha$ ,  $\beta$ , and  $\gamma$ , given in degrees with respect to the first  $g$ -tensor value. d) Isotropic exchange interaction,  $J$ , given in MHz. e) Dipolar coupling interaction,  $J$ , given in MHz. f) dipolar orientation,  $\theta$  and  $\phi$ , given in degrees.

### 6.4.3.1. EPR Relaxation

Longitudinal and transverse electron relaxation,  $T_{1e}$  and  $T_{2e}$ , of some samples prepared by scCO<sub>2</sub> and swelling impregnation were also measured to confirm that the scCO<sub>2</sub> treatment had not affected the structure or properties of the nitroxide radicals used.

Radical	Impregnation Method	$T_{1e}$	$T_{2e}$	$\epsilon_{DNP}$
AMUPol	Swelling	254 $\mu s$ 53 $\mu s$	1.70 $\mu s$	22.8
AMUPol	scCO <sub>2</sub>	470 $\mu s$ 99 $\mu s$	1.72 $\mu s$	4.7
TEKPol	scCO <sub>2</sub>	420 $\mu s$ 76 $\mu s$	1.66 $\mu s$ 0.31 $\mu s$	4.0

Table 6.10:  $T_{1e}$ ,  $T_{2e}$  and DNP enhancements for 3 samples of PEO impregnated with nitroxide radicals by different methods.

The  $T_{2e}$  is relatively consistent for all three samples. However, the  $T_{1e}$  of the samples prepared by scCO<sub>2</sub> are significantly longer than that of the sample impregnated by swelling. This observation can be rationalized by the lower radical concentration expected in the scCO<sub>2</sub> samples.<sup>204</sup> These relaxation measurements confirm that scCO<sub>2</sub> treatment has no detrimental effect on the radical and further support the recurring conclusion, that the radical concentration of samples impregnated *via* scCO<sub>2</sub> is too low.



## 6.5. Summary

The successful impregnation of polymers with DNP radicals in supercritical CO<sub>2</sub> has been demonstrated for three different polymer systems.

The impregnation of PEO with AMUPol and TEKPol resulted in good DNP enhancements for <sup>1</sup>H-<sup>13</sup>C CP experiments. The successful impregnation with both radicals is a positive sign that scCO<sub>2</sub> impregnation is a versatile technique. Although the scCO<sub>2</sub> impregnation conditions for PEO were not optimized, a comparison of this technique with the swelling impregnation technique, proved the benefits of scCO<sub>2</sub> impregnation as a ‘matrix-free’ sample preparation technique with a higher SNR and higher resolution spectrum. The EPR measurements of the scCO<sub>2</sub> and swelling sample suggest that there is a much poorer distribution of the radical in the scCO<sub>2</sub> sample. It is therefore likely that the DNP enhancements obtained on scCO<sub>2</sub> impregnated samples can be improved by optimization of the impregnation process, to increase the homogeneity of radical distribution.

Although the PS samples and PS:PMMA core-shell polymers did not exhibit very good DNP enhancements in this work, the recent publication from Le *et al.*<sup>188</sup> provides evidence that this lack of enhancement is largely due to the radical concentration being too low. Repetition of the experiments presented here with higher radical concentrations should be done to confirm whether this is the case, or alternatively there is some other improvement to the scCO<sub>2</sub> impregnation set-up or conditions that would improve the enhancements of scCO<sub>2</sub> impregnated polymers.

The PEO samples prepared in this work were also impregnated with lower initial radical concentrations however, the DNP enhancements observed for PEO are comparable to the enhancements achieved for PS with very high initial radical concentrations prepared by Le *et al.*<sup>188</sup> Measurements of radical concentration in the samples prepared in this work by EPR, and further investigations of the effect of high radical concentrations on the enhancements achieved for PEO are required to determine the reason for this. This may provide information on the specificity of impregnation conditions required for different materials.

The multi-component DNP build-up curves of samples prepared in this work indicate that there is not a homogeneous dispersion of the radical throughout the polymer matrix. There is evidence that the dispersion of the radical can be controlled by varying the pressure of scCO<sub>2</sub> used during the impregnation process.

Initial experiments investigating the SCREAM-DNP activity in PS:PMMA core-shell polymers show that the PMMA shell does experience methyl <sup>1</sup>H-<sup>13</sup>C cross-relaxation and that this cross-relaxation induced polarization can be transferred from the methyl <sup>13</sup>C to other PMMA carbon environments. Methyl groups of the PDMS-MA stabilizer used in PS synthesis were also shown to exhibit SCREAM-DNP activity. The build-up of cross-relaxation induced polarization of PS resonances is likely to originate from these methyl groups, rather than the PMMA shell. The presence of these methyl groups in the PS core limits the applicability of SCREAM-DNP in the measurement of core and shell domain sizes. However, if domain specific impregnation of the PMMA shell is accomplished, these methyl resonances in the PS domain may prove useful in the application of relayed DNP

## 7. Summary and Outlook

In this thesis, solid-state and DNP-enhanced solid-state NMR have been successfully applied to the structural and dynamic analysis of several materials which are at the forefront of the drive for more sustainable chemistry and materials.

Methylammonium lead halide perovskites,  $\text{MAPbX}_3$  ( $X = \text{Br}^-, \text{Cl}^-, \text{I}^-$ ) are important functional materials with promising applications in solar cells.  $\text{MAPbI}_3$  is an extensively studied perovskite with well understood properties. However, to increase the stability and photoconversion efficiency a more thorough understanding of defects present in the structure is required.  $\text{MAPbI}_3$  and  $\text{MAPbI}_3$  on  $\text{ZnO}$  were characterized by  $^1\text{H}$  NMR to identify possible structural defects which could indicate proton diffusion in these materials.  $^1\text{H}$  NMR investigations of  $\text{MAPbI}_3$  using both static and MAS VT NMR were used to demonstrate the phase change between tetragonal and pseudocubic  $\text{MAPbI}_3$ , but in this temperature range, it was not possible to detect diffusion of the MA ion. With the addition of spectral editing techniques to suppress the dominant  $\text{NH}_3$  and  $\text{CH}_3$  signals of  $\text{MAPbI}_3$ , it becomes clear that there are additional signals from some impurity at 0-2 ppm. These impurities are consistently present in spectra of  $\text{MAPbI}_3$  in the literature where they are assigned to water in the material. However, these signals are also present in  $^1\text{H}$  NMR spectra of several other purely inorganic perovskites and are assigned to interstitial and substitutional hydrogen defects. Intentional wetting of the  $\text{MAPbI}_3$  sample was used here to aid in the assignment of these signals and showed that although there is some overlap with the chemical shift of water on the surface and within the pores of  $\text{MAPbI}_3$ , these impurity signals remain largely unchanged by exposure to moisture and could be evidence of some other hydrogen impurity. Variable temperature experiments of  $\text{MAPbI}_3$  provide evidence that these impurity signals could be involved in some diffusion throughout the sample.

In combination with other analytical techniques, there are several approaches which could be taken to improve the understanding of these additional hydrogen species *via* solid-state NMR. Partial or complete deuteration of the MA ion

would simplify the  $^1\text{H}$  spectrum of  $\text{MAPbI}_3$  and  $\text{MAPbI}_3$  on  $\text{ZnO}$  and may assist in differentiating which signals are due to H impurities in  $\text{ZnO}$  and which are from  $\text{MAPbI}_3$ . Following the hydration and decomposition of the sample *via*  $^1\text{H}$  NMR of samples exposed to controlled humidity and water content could assist in assigning signals which may be due to water or  $\text{MAPbI}_3$  decomposition products. Increasing the temperature range of experiments would help identify if any signals are due to high temperature decomposition products. A better understanding of the properties of these species may also assist with their assignment. For this, a more thorough investigation of the potential diffusion of these species by *pulsed field gradient* (PFG) MAS NMR and further variable temperature measurements of  $T_1$  and  $T_2$  relaxation is required.

Plastic manufacturing and waste are major contributors to the current climate emergency and development of more sustainable polymers is a key step in improving the environmental outlook. The development of new sustainable polymers and plastics requires a detailed understanding of the structure-property relationship of existing and new materials. Solid-state NMR has played an important role in this endeavour, but it is limited by poor sensitivity. DNP-enhanced solid-state NMR has not had the same impact on improving the analysis of polymers, as it has other classes of materials, due to difficulties in the sample preparation of polymers. The swelling of polymers in a radical solution has been demonstrated here to be an important step in achieving a homogeneous distribution of radical throughout the polymer matrix which allows for good DNP enhancements to be achieved. The ability of amorphous polymers to act as ‘glass-formers’, negating the requirement for additional components, such as glycerol in the radical solution has also been demonstrated. Most vitally, the results presented in this thesis demonstrate the importance of considering all aspects of the sample preparation process when determining the optimal technique. It is essential that the impact of the sample preparation on the structure and conformation of the polymer itself is considered.

Additional improvements to DNP sample preparation *via* the swelling method could be made by improving the understanding of the effect of using glycerol in the sample preparation. This could identify the limits of certain polymers as glass-forming agents and maximize the potential enhancements in the absence

of glycerol. Additional investigations of polymers with different cross-linking densities may also provide more information on this. Further attempts to measure the extent of swelling using  $^1\text{H}$ - $^1\text{H}$  DQ or variable contact time CP experiments could also help identify the ideal sample preparation conditions.

A solvent-free method of polymer impregnation was also demonstrated. Supercritical  $\text{CO}_2$  was used to successfully impregnate several types of polymers with both AMUPol and TEKPol. The  $\text{scCO}_2$  impregnated samples presented modest DNP enhancements, but excellent SNR due to the significant increase in practical sample weight of these samples. The DNP enhancements observed in this work are likely restricted by low radical concentrations, and with further development of the  $\text{scCO}_2$  impregnation process these may be improved.

The future development and application of the  $\text{scCO}_2$  impregnation process hinges on the optimization of the impregnation and depressurization conditions to ensure a homogeneous dispersion of the radical in the polymer sample. Developing a deeper understanding of the solubility of the currently available DNP radicals in  $\text{scCO}_2$ , or development of new radicals which are designed to have the desired  $\text{scCO}_2$  solubility will also improve the radical homogeneity and any potential further DNP enhancements. A better understanding of radical solubility, diffusion, and dispersion in  $\text{scCO}_2$  may present excellent opportunities for domain specific impregnation in complex polymer morphologies such as core-shell systems or block copolymers. Domain specific impregnation has the potential to provide information on domain sizes by relayed or cross-relaxation DNP. Additionally, if the  $\text{scCO}_2$  impregnation mechanism is deemed to be suitable, the use of  $\text{scCO}_2$  impregnation could be expanded to other materials that present challenges for traditional sample preparation methods.

# References

- 1 E. Vartiainen, G. Masson, C. Breyer, D. Moser and E. Román Medina, *Prog. Photovoltaics Res. Appl.*, 2020, **28**, 439–453.
- 2 IEA, *Global Energy and Climate Model*, 2022.
- 3 L. L. Kazmerski, Best Research Cell Efficiencies, [http://www.nrel.gov/ncpv/images/efficiency\\_chart.jpg](http://www.nrel.gov/ncpv/images/efficiency_chart.jpg), (accessed 29 November 2022).
- 4 K. W. Kenyon and E. Kridler, *Auk*, 1969, **86**, 339–343.
- 5 D. K. A. Barnes, F. Galgani, R. C. Thompson and M. Barlaz, *Philos. Trans. R. Soc. B Biol. Sci.*, 2009, **364**, 1985–1998.
- 6 K. J. Groh, H. P. H. Arp, M. MacLeod and Z. Wang, *Environ. Sci. Process. Impacts*, 2023, **25**, 10–25.
- 7 C. Wilcox, E. Van Sebille, B. D. Hardesty and J. A. Estes, *Proc. Natl. Acad. Sci. U. S. A.*, 2015, **112**, 11899–11904.
- 8 J. Keeler, *Understanding NMR spectroscopy*, John Wiley and Sons, 2nd edn., 2010.
- 9 M.H. Levitt, *Spin dynamics: basic principles of nuclear magnetic resonance*, John Wiley & Sons, Chichester, 2nd ed., 2008.
- 10 M. J. Duer, *Solid-State NMR Spectroscopy Principles and Applications*, Blackwell Science, 2001.
- 11 D. C. Apperley, R. K. Harris and P. Hodgkinson, *Solid-state NMR : basic principles & practice*, Momentum Press, 1st edn., 2012.
- 12 A. W. Overhauser, *Phys. Rev.*, 1953, **92**, 415.
- 13 T. R. Carver and C. P. Slichter, *Phys. Rev.*, 1953, **92**, 213.
- 14 M. Abraham, M. A. H. McCausland and F. N. H. Robinson, *Phys. Rev. Lett.*, 1959, **2**, 451.

- 15 L. R. Becerra, G. J. Gerfen, R. J. Temkin, D. J. Singel and R. G. Griffin, *Phys. Rev. Lett.*, 1993, **71**, 3564.
- 16 E. Erb, J. L. Motchane and J. Uebersfeld, *C. R. Hebd. Seances Acad. Sci.*, 1958, **246**, 2121–2123.
- 17 A. Abragam and W. G. Proctor, *C. R. Hebd. Seances Acad. Sci.*, 1958, **246**, 2253–2256.
- 18 Y. Hovav, A. Feintuch and S. Vega, *J. Magn. Reson.*, 2010, **207**, 176–189.
- 19 C. F. Hwang and D. A. Hill, *Phys. Rev. Lett.*, 1967, **18**, 112.
- 20 C. F. Hwang and D. A. Hill, *Phys. Rev. Lett.*, 1967, **19**, 1014.
- 21 D. S. Wollan, *Phys. Rev. B*, 1976, **13**, 3685.
- 22 M. Borghini, *Phys. Rev. Lett.*, 1968, **20**, 421.
- 23 Q. Z. Ni, E. Daviso, T. V. Can, E. Markhasin, S. K. Jawla, T. M. Swager, R. J. Temkin, J. Herzfeld and R. G. Griffin, *Acc. Chem. Res.*, 2013, **46**, 1933–1941.
- 24 T. V. Can, M. A. Caporini, F. Mentink-Vigier, B. Corzilius, J. J. Walish, M. Rosay, W. E. Maas, M. Baldus, S. Vega, T. M. Swager and R. G. Griffin, *J. Chem. Phys.*, 2014, **141**, 064202.
- 25 T. V. Can, Q. Z. Ni and R. G. Griffin, *J. Magn. Reson.*, 2015, **253**, 23–35.
- 26 K. R. Thurber and R. Tycko, *J. Chem. Phys.*, 2012, **137**, 1–14.
- 27 A. Zagdoun, G. Casano, O. Ouari, M. Schwarzwälder, A. J. Rossini, F. Aussenac, M. Yulikov, G. Jeschke, C. Copéret, A. Lesage, P. Tordo and L. Emsley, *J. Am. Chem. Soc.*, 2013, **135**, 12790–12797.
- 28 C. Sauvée, M. Rosay, G. Casano, F. Aussenac, R. T. Weber, O. Ouari and P. Tordo, *Angew. Chemie - Int. Ed.*, 2013, **52**, 10858–10861.
- 29 A. B. Barnes, G. De Paëpe, P. C. A. van der Wel, K.-N. Hu, C.-G. Joo, V. S. Bajaj, M. L. Mak-Jurkauskas, J. R. Sirigiri, J. Herzfeld, R. J. Temkin

- and R. G. Griffin, *Appl. Magn. Reson.*, 2008, **34**, 237–263.
- 30 D. Le, G. Casano, T. N. T. Phan, F. Ziarelli, O. Ouari, F. Aussenac, P. Thureau, G. Mollica, D. Gigmes, P. Tordo and S. Viel, *Macromolecules*, 2014, **47**, 3909–3916.
- 31 A. Lesage, M. Lelli, D. Gajan, M. A. Caporini, V. Vitzthum, P. Miéville, J. Alauzun, A. Roussey, C. Thieuleux, A. Mehdi, G. Bodenhausen, C. Copéret and L. Emsley, *J. Am. Chem. Soc.*, 2010, **132**, 15459–15461.
- 32 H. Takahashi, D. Lee, L. Dubois, M. Bardet, S. Hediger and G. Depaëpe, *Angew. Chemie - Int. Ed.*, 2012, **51**, 11766–11769.
- 33 H. Takahashi, C. Fernández-De-Alba, D. Lee, V. Maurel, S. Gambarelli, M. Bardet, S. Hediger, A. L. Barra and G. De Paëpe, *J. Magn. Reson.*, 2014, **239**, 91–99.
- 34 E. L. Hahn, *Phys. Rev.*, 1950, **80**, 594.
- 35 K. Saalwächter, *J. Chem. Phys.*, 2004, **120**, 454–464.
- 36 O. N. Antzutkin and R. Tycko, *J. Chem. Phys.*, 1999, **110**, 2749–2752.
- 37 K. Saalwächter, P. Ziegler, O. Spyckerelle, B. Haidar, A. Vidal and J.-U. Sommer, *J. Chem. Phys.*, 2003, **119**, 3468–3482.
- 38 A. Pines, M. G. Gibby and J. S. Waugh, *J. Chem. Phys.*, 2003, **56**, 1777.
- 39 S. R. Hartmann and E. L. Hahn, *Phys. Rev.*, 1962, **128**, 2042–2053.
- 40 V. Aladin, M. Vogel, R. Binder, I. Burghardt, B. Suess and B. Corzilius, *Angew. Chemie - Int. Ed.*, 2019, **58**, 4863–4868.
- 41 A. A. Bakulin, O. Selig, H. J. Bakker, Y. L. A. Rezus, C. Müller, T. Glaser, R. Lovrincic, Z. Sun, Z. Chen, A. Walsh, J. M. Frost and T. L. C. Jansen, *J. Phys. Chem. Lett.*, 2015, **6**, 3663–3669.
- 42 T. Oku, in *Solar Cells - New Approaches and Reviews*, InTech, 2015.
- 43 D. M. Trots and S. V. Myagkota, *J. Phys. Chem. Solids*, 2008, **69**, 2520–2526.
- 44 D. Weber, *Zeitschrift für Naturforsch. B*, 1978, **33**, 1443–1445.



- 45 A. Kojima, K. Teshima, Y. Shirai and T. Miyasaka, *J. Am. Chem. Soc.*, 2009, **131**, 6050–6051.
- 46 M. Grätzel, *Nat. Mater.*, 2014, **13**, 838–842.
- 47 Y. Yamada, T. Nakamura, M. Endo, A. Wakamiya and Y. Kanemitsu, *Appl. Phys. Express*, 2014, **7**, 032302.
- 48 J. Mizusaki, K. Arai and K. Fueki, *Solid State Ionics*, 1983, **11**, 203–211.
- 49 H. J. Snaith, A. Abate, J. M. Ball, G. E. Eperon, T. Leijtens, N. K. Noel, S. D. Stranks, J. T. Wang, K. Wojciechowski and W. Zhang, *J. Phys. Chem. Lett.*, 2014, **5**, 1511–1515.
- 50 E. L. Unger, E. T. Hoke, C. D. Bailie, W. H. Nguyen, A. R. Bowring, T. Heumüller, M. G. Christoforo and M. D. McGehee, *Energy Environ. Sci.*, 2014, **7**, 3690–3698.
- 51 C. Eames, J. M. Frost, P. R. F. Barnes, B. C. O'Regan, A. Walsh and M. S. Islam, *Nat. Commun.*, 2015, **6**, 2–9.
- 52 J. Haruyama, K. Sodeyama, L. Han and Y. Tateyama, *J. Am. Chem. Soc.*, 2015, **137**, 10048–10051.
- 53 Y. Yuan, J. Chae, Y. Shao, Q. Wang, Z. Xiao, A. Centrone and J. Huang, *Adv. Energy Mater.*, 2015, **5**, 15000615.
- 54 Y. Yuan, Q. Wang, Y. Shao, H. Lu, T. Li and A. Gruverman, *Adv. Energy Mater.*, 2016, **6**, 1501803.
- 55 J. M. Frost, K. T. Butler, F. Brivio, C. H. Hendon, M. Van Schilfgaarde and A. Walsh, *Nano Lett.*, 2014, **14**, 2584–2590.
- 56 J. You, Y. (Michael) Yang, Z. Hong, T.-B. Song, L. Meng, Y. Liu, C. Jiang, H. Zhou, W.-H. Chang, G. Li and Y. Yang, *Appl. Phys. Lett.*, 2014, **105**, 183902.
- 57 K. D. Kreuer, *Solid State Ionics*, 1999, **125**, 285–302.
- 58 T. Norby, *Solid State Ionics*, 1999, **125**, 1–11.
- 59 K. Kreuer, S. J. Paddison, E. Spohr and M. Schuster, *Chem. Rev.*, 2004,

- 104**, 4637–4678.
- 60 D. A. Egger, L. Kronik and A. M. Rappe, *Angew. Chemie Int. Ed.*, 2015, **54**, 12437–12441.
- 61 J. C. Bourgoin and J. W. Corbett, *Phys. Lett.*, 1972, **38A**, 135–137.
- 62 Y. Liang, X. Cui, F. Li, C. Stampfl, S. P. Ringer and R. Zheng, *J. Phys. Chem. C*, 2022, **126**, 1721–1728.
- 63 Y. Chen, Y. Tsai, L. Hirsch and D. M. Bassani, *J. Am. Chem. Soc.*, 2017, **139**, 16359–16364.
- 64 S. Scheiner, *Biochim Biophys Acta .*, 2000, **1458**, 28–42.
- 65 V. Stojkovic and A. Kohen, *Israel J. Chem.*, 2009, **49**, 163–173.
- 66 Y. Feng, Y. Zhao, W. Zhou, Q. Li, W. A. Saidi, Q. Zhao and X. Li, *J. Phys. Chem. Lett.*, 2018, **9**, 6536–6543.
- 67 S. Sadhu, T. Buffeteau, S. Sandrez, L. Hirsch and D. M. Bassani, *J. Am. Chem. Soc.*, 2020, **142**, 10431–10437.
- 68 D. R. Ceratti, A. Zohar, R. Kozlov, H. Dong, G. Uraltsev, O. Girshevitz, I. Pinkas, L. Avram, G. Hodes and D. Cahen, *Adv. Mater.*, 2020, **32**, 2002467.
- 69 T. Buffeteau, L. Hirsch, D. Bassani, T. Buffeteau, L. Hirsch and D. Bassani, *Adv. Mater.*, 2021, **33**, 2007715.
- 70 D. R. Ceratti, A. Zohar, G. Hodes and D. Cahen, *Adv. Mater.*, 2021, **33**, 2102822.
- 71 D. J. Kubicki, S. D. Stranks, C. P. Grey and L. Emsley, *Nat. Rev. Chem.*, 2021, **5**, 624–645.
- 72 L. Piveteau, V. Morad and M. V. Kovalenko, *J. Am. Chem. Soc.*, 2020, **142**, 19413–19437.
- 73 R. E. Wasylishen, O. Knop and J. B. Macdonald, *Solid State Commun.*, 1985, **56**, 581–582.
- 74 O. Knop, R. E. Wasylishen, M. A. White, T. S. Cameron and M. J. M.

- Van Oort, *Can. J. Chem.*, 1990, **68**, 412–422.
- 75 C. Roiland, G. Trippé-Allard, K. Jemli, B. Alonso, J. C. Ameline, R. Gautier, T. Bataille, L. Le Pollès, E. Deleporte, J. Even and C. Katan, *Phys. Chem. Chem. Phys.*, 2016, **18**, 27133–27142.
- 76 D. J. Kubicki, D. Prochowicz, A. Hofstetter, P. Péchy, S. M. Zakeeruddin, M. Grätzel and L. Emsley, *J. Am. Chem. Soc.*, 2017, **139**, 10055–10061.
- 77 A. M. Askar, G. M. Bernard, B. Wiltshire, K. Shankar and V. K. Michaelis, *J. Phys. Chem. C*, 2017, **121**, 1013–1024.
- 78 J. V Milic, J. Im, D. J. Kubicki, A. Ummadisingu, J. Seo, Y. Li, M. A. Ruiz-preciado, M. I. Dar, S. M. Zakeeruddin, L. Emsley and M. Grätzel, *Adv. Energy Mater.*, 2019, **9**, 1900284.
- 79 D. J. Kubicki, D. Prochowicz, A. Hofstetter, M. Saski, P. Yadav, D. Bi, N. Pellet, J. Lewinski, S. M. Zakeeruddin, M. Gratzel and L. Emsley, *J. Am. Chem. Soc.*, 2018, **140**, 3345–3351.
- 80 T. Baikie, N. S. Barrow, Y. Fang, P. J. Keenan, P. R. Slater, R. O. Piltz, M. Gutmann, S. G. Mhaisalkar and T. J. White, *J. Mater. Chem. A*, 2015, **3**, 9298–9307.
- 81 W. M. J. Franssen and A. P. M. Kentgens, *Solid State Nucl. Magn. Reson.*, 2019, **100**, 36–44.
- 82 A. M. Askar, A. Karmakar, G. M. Bernard, M. Ha, V. V. Terskikh, B. D. Wiltshire, S. Patel, J. Fleet, K. Shankar and V. K. Michaelis, *J. Phys. Chem. Lett.*, 2018, **9**, 2671–2677.
- 83 A. Karmakar, A. M. Askar, G. M. Bernard, V. V. Terskikh, M. Ha, S. Patel, K. Shankar and V. K. Michaelis, *Chem. Mater.*, 2018, **30**, 2309–2321.
- 84 A. Senocrate, I. Moudrakovski, G. Y. Kim, T. Yang, G. Gregori, M. Gratzel and J. Maier, *Angew. Chemie*, 2017, **129**, 7863–7867.
- 85 W. M. J. Franssen, S. G. D. van Es, R. Dervisoglu, G. A. de Wijs and A. P. M. Kentgens, *J. Phys. Chem. C*, 2017, **8**, 61–66.

- 86 L.-Q. Wang, G. J. Exarhos, C. F. Windisch, C. Yao, L. R. Pederson and X.-D. Zhou, *Appl. Phys. Lett.*, 2007, **90**, 173115.
- 87 K. J. Alvine, M. Vijayakumar, M. E. Bowden, A. L. Schemer-Kohrn and S. G. Pitman, *J. Appl. Phys.*, 2012, **112**, 043511.
- 88 M. Wang, G. Yu, W. Ji, L. Li, W. Ding and L. Peng, *Chem. Phys. Lett.*, 2015, **627**, 7–12.
- 89 J. K. Cooper, S. B. Scott, Y. Ling, J. Yang, S. Hao, Y. Li, F. M. Toma, M. Stutzmann, K. V. Lakshmi and I. D. Sharp, *Chem. Mater.*, 2016, **28**, 5761–5771.
- 90 X. Xue, M. Kanzaki, D. Turner and D. Lorocho, *Am. Mineral.*, 2017, **102**, 519–536.
- 91 R. Nitta, Y. Kubota, A. Endo, H.-E. Lin, T. Kishi, S. Kitani, H. Kawaji and N. Matsushita, *Appl. Phys. Lett.*, 2022, **121**, 223302.
- 92 L.-Q. Wang, X.-D. Zhou, G. J. Exarhos, L. R. Pederson, C. Wang, C. F. Windisch and C. Yao, *Appl. Phys. Lett.*, 2007, **91**, 173107.
- 93 K. R. Thurber and R. Tycko, *J. Magn. Reson.*, 2009, **196**, 84–87.
- 94 W. M. J. Franssen, B. J. Bruijnaers, V. H. L. Portengen and A. P. M. Kentgens, *ChemPhysChem*, 2018, **19**, 3107–3115.
- 95 W. Xu, L. Liu, L. Yang, P. Shen, B. Sun and J. A. McLeod, *Nano Lett.*, 2016, **16**, 4720–4725.
- 96 A. Senocrate, I. Moudrakovski and J. Maier, *Phys. Chem. Chem. Phys.*, 2018, **20**, 20043–20055.
- 97 P. Heitjans, S. Indris and M. Wilkening, *Diffus. Fundam.*, 2005, **2**, 45.1–20.
- 98 P. Heitjans, A. Schirmer and S. Indris, *Diffus. Condens. Matter Methods, Mater. Model.*, 2005, 367–415.
- 99 D. Massiot, F. Fayon, M. Capron, I. King, S. Le Calvé, B. Alonso, J.-O. Durand, B. Bujoli, Z. Gan and G. Hoatson, *Magn. Reson. Chem.*, 2002, **40**, 70–76.

- 100 D. H. Fabini, T. A. Siaw, C. C. Stoumpos, G. Laurita, D. Olds, K. Page, J. G. Hu, M. G. Kanatzidis, S. Han and R. Seshadri, *J. Am. Chem. Soc.*, 2017, **139**, 16875–16884.
- 101 D. A. Egger, A. M. Rappe and L. Kronik, *Acc. Chem. Res.*, 2016, 49, 573–581.
- 102 E. A. Alharbi, A. Y. Alyamani, D. J. Kubicki, A. R. Uhl, B. J. Walder, A. Q. Alanazi, J. Luo, A. Burgos-Caminal, A. Albadri, H. Albrithen, M. H. Alotaibi, J. E. Moser, S. M. Zakeeruddin, F. Giordano, L. Emsley and M. Grätzel, *Nat. Commun.*, 2019, **10**, 1–9.
- 103 R. T. Wang, E. E. Liu, A. F. Xu, L. W. Yang, J. Y. Chen and G. Xu, *Crystals*, 2020, **10**, 162.
- 104 W. T. M. Van Gompel, R. Herckens, G. Reekmans, B. Ruttens, J. D’Haen, P. Adriaensens, L. Lutsen and D. Vanderzande, *J. Phys. Chem. C*, 2018, **122**, 4117–4124.
- 105 N. P. Jasti, G. E. Shter, Y. Feldman, D. R. Ceratti, A. Kama, I. Buchine, G. S. Grader and D. Cahen, *Adv. Funct. Mater.*, 2022, **32**, 2204283.
- 106 H. Wang, X. Zhang, T. Huang, Z. Lu, F. Gao, Z. Shi, L. Zhou, R. Li and G. Tang, *Opt. Mater. (Amst.)*, 2019, **89**, 375–381.
- 107 N. Sultana, A. Al Amin, D. Z. Metin and N. Gaston, *J. Mater. Sci.*, 2019, **54**, 13594–13608.
- 108 S. Bhattarai, A. Sharma and T. D. Das, in *AIP Conference Proceedings*, 2020, vol. 2269, p. 030071.
- 109 A. Janotti and C. G. Van de Walle, *Reports Prog. Phys.*, 2009, **72**, 126501.
- 110 C. G. Van de Walle, *Phys. Rev. Lett.*, 2000, **85**, 1012–1015.
- 111 A. Janotti and C. G. Van de Walle, *Nat. Mater.*, 2007, **6**, 44–47.
- 112 J. J. Lander, *J. Phys. Chem. Solids*, 1957, **3**, 87–94.
- 113 X. H. Huang, Z. Y. Zhan, K. P. Pramoda, C. Zhang, L. X. Zheng and S. J. Chua, *CrystEngComm*, 2012, **14**, 5163–5165.

- 114 J. K. Park, H. J. Kwon and C. E. Lee, *Sci. Rep.*, 2016, **6**, 1–8.
- 115 T. Li, M. Wang, X. Liu, M. Jin and F. Huang, *J. Phys. Chem. Lett.*, 2020, **11**, 2402–2407.
- 116 OECD, *Global Plastics Outlook, Policy Scenarios to 2060*, OECD Publishing, Paris, 2022.
- 117 Y. Zhu, C. Romain and C. K. Williams, *Nature*, 2016, 540, 354–362.
- 118 Z. Wang, M. S. Ganewatta and C. Tang, *Prog. Polym. Sci.*, 2020, **101**, 101197.
- 119 Z. Grubisic, P. Rempp and H. Benoit, *J. Polym. Sci.*, 1967, **5**, 753–759.
- 120 M. J. Richardson and N. G. Savill, *Rubber Chem. Technol.*, 1976, **49**, 224–232.
- 121 S. R. Sandler, W. Karo, J.-A. Bonesteel and E. M. Pearce, *Polym. Synth. Charact.*, 1998, **1**, 108–119.
- 122 J. Clauss, K. Schmidt-Rohr and H. W. Spiess, *Acta Polym.*, 1993, **44**, 1–17.
- 123 A. Buda, D. E. Demco, M. Bertmer, B. Blümich, B. Reining, H. Keul and H. Höcker, *Solid State Nucl. Magn. Reson.*, 2003, **24**, 39–67.
- 124 P. Selter and M. R. Hansen, in *NMR Methods for Characterization of Synthetic and Natural Polymers*, 2019, vol. 2019-Janua, pp. 363–386.
- 125 K. Landfester, C. Boeffel, M. Lambla and H. W. Spiess, *Macromolecules*, 1996, **29**, 5972–5980.
- 126 J. G. Filgueiras, M. F. Cobo, G. C. Faria, T. B. Moraes and E. R. De Azevedo, in *NMR Methods for Characterization of Synthetic and Natural Polymers*, 2019, vol. 2019-Janua, pp. 271–298.
- 127 F. G. Riddell, S. Arumugam, K. D. M. Harris, M. Rogerson and J. H. Strange, *J. Am. Chem. Soc.*, 1993, **115**, 1881–1885.
- 128 L. Abis, G. Floridi, E. Merlo, R. Pò and C. Zannoni, *J. Polym. Sci. Part B Polym. Phys.*, 1998, **36**, 1557–1566.

- 129 I. Nevares and M. Álamo-Sanza, in *Food Packaging and Preservation*, Elsevier Inc., 2018, vol. 1933, pp. 375–407.
- 130 R. P. Choudhury, J. S. Lee, R. M. Kriegel, W. J. Koros and H. W. Beckham, *Macromolecules*, 2012, **45**, 879–887.
- 131 S. R. Chaudhari, J. M. Griffin, K. Broch, A. Lesage, V. Lemaure, D. Dudenko, Y. Olivier, H. Siringhaus, L. Emsley and C. P. Grey, *Chem. Sci.*, 2017, **8**, 3126–3136.
- 132 X. Li, I. V. Sergeyev, F. Aussenac, A. F. Masters, T. Maschmeyer and J. M. Hook, *Angew. Chemie - Int. Ed.*, 2018, **57**, 6848–6852.
- 133 O. Ouari, T. Phan, F. Ziarelli, G. Casano, F. Aussenac, P. Thureau, D. Gigmes, P. Tordo and S. Viel, *ACS Macro Lett.*, 2013, **2**, 715–719.
- 134 F. Blanc, S. Y. Chong, T. O. McDonald, D. J. Adams, S. Pawsey, M. A. Caporini and A. I. Cooper, *J. Am. Chem. Soc.*, 2013, **135**, 15290–15293.
- 135 A. J. Rossini, A. Zagdoun, F. Hegner, M. Schwarzwälder, D. Gajan, C. Copéret, A. Lesage and L. Emsley, *J. Am. Chem. Soc.*, 2012, **134**, 16899–16908.
- 136 G. Mollica, D. Le, F. Ziarelli, G. Casano, O. Ouari, T. N. T. Phan, F. Aussenac, P. Thureau, D. Gigmes, P. Tordo and S. Viel, *ACS Macro Lett.*, 2014, **3**, 922–925.
- 137 Y. Matsuki, T. Maly, O. Ouari, H. Karoui, F. Le Moigne, E. Rizzato, S. Lyubenova, J. Herzfeld, T. Prisner, P. Tordo and R. G. Griffin, *Angew. Chemie Int. Ed.*, 2009, **48**, 4996–5000.
- 138 S. Tanaka, W. C. Liao, A. Ogawa, K. Sato and C. Copéret, *Phys. Chem. Chem. Phys.*, 2020, **22**, 3184–3190.
- 139 K. Saalwächter, P. Ziegler, O. Spycykerelle, B. Haidar, A. Vidal and J. U. Sommer, *J. Chem. Phys.*, 2003, **119**, 3468–3482.
- 140 W. Chassé, L. Valentín, G. D. Genesky and C. Cohen, 2011, **044907**, 1–11.
- 141 F. C. Schilling, A. E. Tonelli and A. L. Cholli, *J. Polym. Sci. Part B*

- Polym. Phys.*, 1992, **30**, 91–96.
- 142 D. J. Harris, T. J. Bonagamba, M. Hong and K. Schmidt-Rohr, *Macromolecules*, 2000, **33**, 3375–3381.
- 143 D. J. Harris, T. J. Bonagamba, M. Hong and K. Schmidt-Rohr, *Polymer (Guildf.)*, 2005, **46**, 11737–11743.
- 144 J. J. Shephard, P. J. Bremer and A. James McQuillan, *J. Phys. Chem. B*, 2009, **113**, 14229–14238.
- 145 D. Lee, S. R. Chaudhari and G. De Paëpe, *J. Magn. Reson.*, 2017, **278**, 60–66.
- 146 J. R. Yarava, S. R. Chaudhari, A. J. Rossini, A. Lesage and L. Emsley, *J. Magn. Reson.*, 2017, **277**, 149–153.
- 147 J. Chen and J. Shen, *J. Appl. Polym. Sci.*, 2000, **75**, 1331–1338.
- 148 A. Cupane, M. Levantino and M. G. Santangelo, *J. Phys. Chem. B*, 2002, **106**, 11323–11328.
- 149 J. Höpfner, G. Guthausen, K. Saalwächter and M. Wilhelm, *Macromolecules*, 2014, **47**, 4251–4265.
- 150 M. A. McHugh, V. J. Krukoniš and H. Brenner, in *Supercritical Fluid Extraction: Principles and Practice*, Elsevier, 2nd edn., 1994, pp. 1–16.
- 151 J. R. Williams and A. A. Clifford, *Supercritical Fluid Methods and Protocols*, Humana Press, New Jersey, 2000, vol. 13.
- 152 P. Raveendran and S. L. Wallen, *J. Am. Chem. Soc.*, 2002, **124**, 7274–7275.
- 153 P. Raveendran, Y. Ikushima and S. L. Wallen, *Acc. Chem. Res.*, 2005, **38**, 478–485.
- 154 M. Raventós, S. Duarte and R. Alarcón, *Food Sci. Technol. Int.*, 2002, **8**, 269–284.
- 155 C. Boyère, C. Jérôme and A. Debuigne, *Eur. Polym. J.*, 2014, **61**, 45–63.
- 156 W. C. V. Wang, E. J. Kramer and W. H. Sachse, *J. Polym. Sci. Part A-2*,



- Polym. Phys.*, 1982, **20**, 1371–1384.
- 157 R. G. Wissinger and M. E. Paulaitis, *J. Polym. Sci. Part B Polym. Phys.*, 1987, **25**, 2497–2510.
- 158 A. Bos, I. G. M. Pünt, M. Wessling and H. Strathmann, *J. Memb. Sci.*, 1999, **155**, 67–78.
- 159 I. Kikic and F. Vecchione, *Curr. Opin. Solid State Mater. Sci.*, 2003, **7**, 399–405.
- 160 K. F. Webb and A. S. Teja, *Fluid Phase Equilib.*, 1999, **158–160**, 1029–1034.
- 161 M. Tadesse Abate, A. Ferri, J. Guan, G. Chen and V. Nierstrasz, in *Advanced Supercritical Fluids Technologies*, IntechOpen, 2020, pp. 1–14.
- 162 M. L. Goñi, N. A. Gañán and R. E. Martini, *J. CO2 Util.*, 2021, **54**, 101760.
- 163 A. R. Berens, G. S. Huvard, R. W. Kormeyer and F. W. Kunig, *J. Appl. Polym. Sci.*, 1992, **46**, 231–242.
- 164 S. G. Kazarian, N. H. Brantley, B. L. West, M. F. Vincent and C. A. Eckert, *Appl. Spectrosc.*, 1997, **51**, 491–494.
- 165 J. M. Dobbs, J. M. Wong and K. P. Johnston, *J. Chem. Eng. Data*, 1986, **31**, 303–308.
- 166 J. M. Dobbs, J. M. Wong, R. J. Lahiere and K. P. Johnston, *Ind. Eng. Chem. Res.*, 1987, **26**, 56–65.
- 167 M. Champeau, J. Thomassin, T. Tassaing and C. Jérôme, *J. Control. Release*, 2015, **209**, 248–259.
- 168 A. López-Periago, A. Argemí, J. M. Andanson, V. Fernández, C. A. García-González, S. G. Kazarian, J. Saurina and C. Domingo, *J. Supercrit. Fluids*, 2009, **48**, 56–63.
- 169 A. S. Kopylov, V. A. Radtsig, N. N. Glagolev, A. B. Solovieva and V. N. Bagratashvili, *Russ. J. Phys. Chem. B*, 2015, **9**, 998–1004.

- 170 M. Champeau, J.-M. Thomassin, T. Tassaing and C. Jérôme, *J. Control. Release*, 2015, **209**, 248–259.
- 171 N. A. Chumakova, E. N. Golubeva, T. A. Ivanova, N. N. Vorobieva, P. S. Timashev and V. N. Bagratashvili, *Russ. J. Phys. Chem. B*, 2018, **12**, 1255–1260.
- 172 N. A. Chumakova, T. A. Ivanova, E. N. Golubeva and A. I. Kokorin, *Appl. Magn. Reson.*, 2018, **49**, 511–522.
- 173 O. I. Gromov, M. O. Kostenko, A. V. Petrunin, A. A. Popova, O. O. Parenago, N. V. Minaev, E. N. Golubeva and M. Y. Melnikov, *Polymers (Basel)*, 2021, **13**, 3059.
- 174 A. A. Akovantseva, V. N. Bagratashvili, N. A. Chumakova, E. N. Golubeva, O. I. Gromov, S. V. Kuzin, M. Y. Melnikov and P. S. Timashev, *Appl. Magn. Reson.*, 2018, **49**, 403–413.
- 175 E. N. Golubeva, O. I. Gromov, N. A. Chumakova, E. D. Feklichev, M. Y. Mel'nikov and V. N. Bagratashvili, *Russ. J. Phys. Chem. B*, 2016, **10**, 1229–1236.
- 176 A. Marchetti, J. Yin, Y. Su and X. Kong, *Magn. Reson. Lett.*, 2021, **1**, 28–70.
- 177 A. Pugliese, M. Tobyn, L. E. Hawarden, A. Abraham and F. Blanc, *Mol. Pharm.*, 2022, **19**, 3685–3699.
- 178 L. Zhao, A. C. Pinon, L. Emsley and A. J. Rossini, *Magn. Reson. Chem.*, 2018, **56**, 583–609.
- 179 D. Daube, V. Aladin, J. Heiliger, J. J. Wittmann, D. Barthelmes, C. Bengs, H. Schwalbe and B. Corzilius, *J. Am. Chem. Soc.*, 2016, **138**, 16572–16575.
- 180 T.-C. Ong, M. L. Mak-Jurkauskas, J. J. Walsh, V. K. Michaelis, B. Corzilius, A. A. Smith, A. M. Clausen, J. C. Cheetham, T. M. Swager and R. G. Griffin, *J. Phys. Chem. B*, 2013, **117**, 3040–3046.
- 181 P. Berruyer, L. Emsley and A. Lesage, in *Handbook of High Field*

- Dynamic Nuclear Polarization*, eds. V. K. Michaelis, R. G. Griffin, B. Corzilius and S. Vega, John Wiley & Sons, Ltd., 2020, pp. 337–352.
- 182 H. Takahashi, S. Hediger and G. De Paëpe, *Chem. Commun.*, 2013, **49**, 9479–9481.
- 183 D. Lee, S. Hediger and G. De Paëpe, *Solid State Nucl. Magn. Reson.*, 2015, **66**, 6–20.
- 184 Y. Zhang, K. K. Gangwani and R. M. Lemert, *J. Supercrit. Fluids*, 1997, **11**, 115–134.
- 185 L. N. Nikitin, M. O. Gallyamov, R. A. Vinokur, A. Y. Nikolaev, E. E. Said-Galiyev, A. R. Khokhlov, H. T. Jespersen and K. Schaumburg, *J. Supercrit. Fluids*, 2003, **26**, 263–273.
- 186 Y. Gushikem, E. V. Benvenuti and Y. V. Kholin, *Pure Appl. Chem.*, 2008, **80**, 1593–1611.
- 187 T. Maly, A. F. Miller and R. G. Griffin, *ChemPhysChem*, 2010, **11**, 999–1001.
- 188 D. Le, A. Frison, Y. Masmoudi, A. Bouledjoudja, P. Thureau, G. Mollica, E. Badens, F. Ziarelli and S. Viel, *Magn. Reson. Chem.*, 2022, **60**, 1171–1177.
- 189 A. J. Rossini, A. Zagdoun, F. Hegner, M. Schwarzwälder, D. Gajan, C. Copéret, A. Lesage and L. Emsley, *J. Am. Chem. Soc.*, 2012, **134**, 16899–16908.
- 190 A. J. Brady, H. Keskkula and D. R. Paul, *Polymer (Guildf.)*, 1994, **35**, 3665–3672.
- 191 J. Markarian, *Plast. Addit. Compd.*, 2004, **6**, 46–49.
- 192 G. Wu, J. Zhao, H. Shi and H. Zhang, *Eur. Polym. J.*, 2004, **40**, 2451–2456.
- 193 Q. B. Si, C. Zhou, H. D. Yang and H. X. Zhang, *Eur. Polym. J.*, 2007, **43**, 3060–3067.
- 194 M. R. Giles, J. N. Hay and S. M. Howdle, *Macromol. Rapid Commun.*,

- 2000, **21**, 1019–1023.
- 195 A. J. Haddleton, T. M. Bennett, X. Chen, R. L. Atkinson, V. Taresco and S. M. Howdle, *Polym. Chem.*, 2020, **11**, 5029–5039.
- 196 A. C. Pinon, U. Skantze, J. Viger-Gravel, S. Schantz and L. Emsley, *J. Phys. Chem. A*, 2018, **122**, 8802–8807.
- 197 T. Schäfer, S. Vowinkel, H. Breitzke, M. Gallei and T. Gutmann, *J. Phys. Chem. C*, 2019, **123**, 644–652.
- 198 A. C. Pinon, J. Schlagnitweit, P. Berruyer, A. J. Rossini, M. Lelli, E. Socie, M. Tang, T. Pham, A. Lesage, S. Schantz and L. Emsley, *J. Phys. Chem. C*, 2017, **121**, 15993–16005.
- 199 A. Zagdoun, A. J. Rossini, M. P. Conley, W. R. Grüning, M. Schwarzwälder, M. Lelli, W. T. Franks, H. Oschkinat, C. Copéret, L. Emsley and A. Lesage, *Angew. Chemie - Int. Ed.*, 2013, **52**, 1222–1225.
- 200 R. Harrabi, T. Halbritter, F. Aussenac, O. Dakhlaoui, J. van Tol, K. K. Damodaran, D. Lee, S. Paul, S. Hediger, F. Mentink-Vigier, S. T. Sigurdsson and G. De Paëpe, *Angew. Chemie - Int. Ed.*, 2022, **61**, 1–9.
- 201 V. Aladin and B. Corzilius, *Solid State Nucl. Magn. Reson.*, 2019, **99**, 27–35.
- 202 V. Aladin, A. K. Sreemantula, T. Biedenbänder, A. Marchanka and B. Corzilius, *Chem. – A Eur. J.*, 2023, e202203443.
- 203 F. Mentink-Vigier, A. L. Barra, J. Van Tol, S. Hediger, D. Lee and G. De Paëpe, *Phys. Chem. Chem. Phys.*, 2019, **21**, 2166–2176.
- 204 T. A. Siaw, M. Fehr, A. Lund, A. Latimer, S. A. Walker, D. T. Edwards and S. I. Han, *Phys. Chem. Chem. Phys.*, 2014, **16**, 18694–18706.